University of Warsaw
Faculty of Physics

Doctoral Thesis

Beta-decay studies of very neutron-rich indium isotopes

Author:
Monika Piersa-Siłkowska

Supervisor:
dr hab. Agnieszka Korgul

November 2021

PREFACE

This thesis presents the results of an experimental study of the β decay of neutron-rich indium isotopes ^{133}In, ^{134}In, and ^{135}In. Measurements were carried out at the CERN-ISOLDE facility as part of the IS610 experiment performed in two campaigns, in 2016 and 2018.

Chapter 1 gives a brief introduction to the field of study by first outlining the fundamental concepts behind the nuclear shell model and β decay and then describing distinctive features of atomic nuclei under study. The discussion is followed by a summary of the previous experimental studies and the motivation behind the present study. Chapter 2 outlines experimental methods used to produce the beams of interest and gives basic characteristics of the detection system. Chapter 3 presents the results of the analysis of the β decay of ^{133}In, ^{134}In, and ^{135}In. Chapter 4 provides an interpretation of experimental findings. A review of the new and previous experimental information on nuclei under study is presented together with a discussion of the results of various shell-model calculations.

The results presented in this thesis have been published open access (CC-BY 4.0) in the three articles listed below.

[A1] First β-decay spectroscopy of ^{135}In and new β-decay branches of ^{134}In, M. Piersa-Siłkowska, A. Korgul, J. Benito, L. M. Fraile *et al.* (IDS Collaboration), Phys. Rev. C **104**, 044328 (2021).

[A2] β decay of ^{133}In: γ emission from neutron-unbound states in ^{133}Sn, M. Piersa, A. Korgul, L. M. Fraile, J. Benito *et al.* (IDS Collaboration), Phys. Rev. C **99**, 024304 (2019).

[A3] Investigation of low-lying states in ^{133}Sn populated in the β decay of ^{133}In using isomer-selective laser ionization,
M. Piersa, A. Korgul, L. M. Fraile, J. Benito *et al.*,
Acta Phys. Pol. B **49**, 523 (2018).

Some preliminary results reported in the above articles were presented by me at nine international conferences as oral contributions, one of which was an invited presentation and three of which were awarded. For my doctoral research work, I was awarded two grants from the Polish National Science Centre.

The results of the analysis presented in this thesis were among the motivations behind three experimental proposals (IS632, IS662, and IS693) accepted by the ISOLDE and nTOF Experiments Committee, which aimed to investigate the β decay of neutron-rich indium isotopes further.

In addition, I have been involved in other research closely related to the topic presented in this thesis, the results of which are presented in the articles listed below.

[A4] β-delayed neutron emission of r-process nuclei at the $N = 82$ shell closure, O. Hall, T. Davinson, A. Estrade, J. Liu, G. Lorusso, F. Montes, S. Nishimura, V. H. Phong, P. J. Woods, J. Agramunt, ..., M. Piersa *et al.*, Phys. Lett. B **816** 136266 (2021).

[A5] Detailed spectroscopy of doubly magic ^{132}Sn, J. Benito, L. M. Fraile, A. Korgul, M. Piersa *et al.* (IDS Collaboration), Phys. Rev. C 102, 014328 (2020).

[A6] Observation of a μs isomer in $^{134}_{49}$In$_{85}$: Proton-neutron coupling "southeast" of $^{132}_{50}$Sn$_{82}$, V. H. Phong, G. Lorusso, T. Davinson, A. Estrade, O. Hall, J. Liu, K. Matsui, F. Montes, S. Nishimura, A. Boso, ..., M. Piersa *et al.*, Phys. Rev. C **100**, 011302(R) (2019).

During my doctoral studies, I participated in experimental projects that resulted in 20 peer-reviewed publications (since 2017), including articles in Nature, Phys. Rev. Lett., and Phys. Lett. B.

I acknowledge the funding support from the Polish National Science Center
under Grants No. 2019/33/N/ST2/03023 (PRELUDIUM)
and No. 2020/36/T/ST2/00547 (Doctoral scholarship ETIUDA).

ABSTRACT

The β decay of the indium isotopes ^{133}In, ^{134}In, and ^{135}In was investigated experimentally with the aim of providing new insights into the nuclear structure of neutron-rich nuclides from the ^{132}Sn region. Better understanding of these exotic nuclides is required for accurate modeling of the rapid neutron capture nucleosynthesis process (r process), due to the $A \approx 130$ peak in the r-process abundance pattern being linked to the $N = 82$ shell closure. Because a vast number of nuclei involved in the r-process are β-delayed neutron (βn) emitters, new experimental data that can verify and guide theoretical models describing βn emission are of particular interest. The effects of nuclear structure strongly affecting the competition between neutron emission and γ-ray deexcitation in the decay of neutron-unbound states were recently observed in the region southeast of ^{132}Sn. The capability of γ-ray deexcitation to compete with neutron emission well above the neutron-separation energy calls for further investigation, primarily due to its consequences for astrophysical r-process modeling. Neutron-rich indium isotopes constitute excellent cases to address this problem owing to their large β-decay energy windows for the population of neutron-unbound states in daughter nuclei (>10 MeV), as well as the simplicity of their structure within the shell model. In particular, ^{134}In and ^{135}In – being rare instances of experimentally accessible nuclides for which the β-delayed three-neutron decay is energetically allowed – constitute representative nuclei to investigate the competition between β-delayed one- and multiple-neutron emission as well as the γ-ray contribution to the decay of neutron-unbound states.

The β-delayed γ-ray spectroscopy measurement was performed at the CERN-ISOLDE facility. The indium isotopes were produced in neutron-induced fission of the uranium carbide target. Laser-ionized beams of ^{133}In, ^{134}In, and ^{135}In were on-line mass separated and transported to the ISOLDE Decay Station. Isomer-selective ionization provided for ^{133}In enabled two β-decaying states in this nucleus to be studied separately for the first time. Transitions following the β decay of indium isotopes were identified based on $\beta\gamma$ and $\beta\gamma\gamma$ coincidence data. Decay schemes of ^{135}In and two β-decaying states of ^{133}In were established for the first time, while the decay scheme of ^{134}In was expanded with two β-decay branches. Two indium isotopes, ^{134}In and ^{135}In, were identified to be β-delayed two-neutron emitters. The population of neutron-unbound states decaying via γ rays was identified in ^{134}Sn and ^{133}Sn at excitation energies exceeding the neutron separation energy by 1 MeV. The β-delayed one-neutron decay was observed to be the dominant β-decay branch of ^{134}In and ^{135}In even though the Gamow-Teller resonance is located substantially above the two-neutron separation energy of the daughter nucleus. The observed dominant one-neutron emission from these nuclei is predicted only by theoretical models, which, apart from the inclusion of first-forbidden transitions, also consider all possible decay paths of neutron-unbound states. Experimental level schemes of ^{133}Sn, ^{134}Sn, and ^{135}Sn are compared with shell-model predictions, including calculations considering particle-hole excitations across the $N = 82$ shell gap. Neutron-unbound states corresponding to the couplings of the valence particles to the neutron-core excitations were found to be an important component of the deexcitation pattern observed in daughter nuclei following the β decay of neutron-rich indium isotopes.

STRESZCZENIE

Temat rozprawy doktorskiej w języku polskim:

Badanie przemiany beta bardzo neutronowo-nadmiarowych izotopów indu

Eksperymentalne badanie przemiany β izotopów indu ^{133}In, ^{134}In oraz ^{135}In umożliwiło uzyskanie nowych informacji o strukturze jądrowej neutronowo-nadmiarowych nuklidów z rejonu ^{132}Sn. Własności tych egzotycznych nuklidów mają istotne znaczenie w modelowaniu astrofizycznego procesu syntezy pierwiastków na drodze szybkiego wychwytu neutronów (tzw. proces r), gdyż zamknięty charakter powłoki $N = 82$ uwidocznia się w rozkładzie rozpowszechnienia izotopów wynikającym z przebiegu tego procesu. Rozpad większości jąder atomowych biorących udział w procesie r zachodzi na drodze przemiany β z następującą po niej emisją neutronu (rozpad βn). Do weryfikacji i poprawy przewidywań modeli opisujących rozpad βn potrzebne są nowe informacje eksperymentalne o emiterach takich neutronów. Niedawno zaobserwowano nietypową konkurencję między dwiema drogami rozpadu stanów niezwiązanych w neutronowo-nadmiarowych jądrach atomowych położonych na mapie nuklidów poniżej ^{132}Sn. Za występowanie konkurencji między emisją neutronu oraz deekscytacją przez promieniowanie γ mogą odpowiadać szczegóły struktury jądrowej. Możliwość konkurowania ze sobą tych dwóch kanałów rozpadu przy energiach wzbudzenia przekraczających znacznie energię separacji neutronu wymaga dalszych badań, gdyż to zjawisko może mieć istotny wpływ na przewidywany przebieg astrofizycznego procesu r. Neutronowo-nadmiarowe izotopy indu to właściwe przypadki do badania tej konkurencji, gdyż w ich rozpadach dostępne są duże okna energetyczne (>10 MeV) na populację stanów niezwiązanych. Dodatkowo, te izotopy są w prosty sposób opisywane przez model powłokowy jądra atomowego, co sprzyja rozpoznaniu efektów struktury jądrowej prowadzących do wzmożonej emisji promieniowania γ ze stanów położonych powyżej energii separacji neutronu. Dwa izotopy indu, ^{134}In oraz ^{135}In, to szczególnie reprezentatywne jądra atomowe do eksploracji różnych dróg rozpadu stanów niezwiązanych, gdyż są one jednymi z nielicznych nuklidów będących w zasięgu badań eksperymentalnych, dla których warunki energetyczne dopuszczają emisję nawet trzech neutronów po przemianie β.

Własności promieniowania γ emitowanego w przemianie β ^{133}In, ^{134}In oraz ^{135}In zostały zbadane w laboratorium CERN-ISOLDE. Izotopy indu były produkowane w procesie rozszczepienia jąder uranu indukowanego przez neutrony. Wiązki jonów powstałe w wyniku jonizacji laserowej oraz separacji masowej były wysyłane do stacji rozpadowej ISOLDE. Jonizacja z selekcją stanu jądrowego została zastosowana dla ^{133}In, co umożliwiło niezależne zbadanie przemiany β stanu podstawowego i izomerycznego tego jądra. Przejścia γ towarzyszące przemianie β izotopów indu zidentyfikowano na podstawie korelacji $\beta\gamma$ oraz $\beta\gamma\gamma$. Dzięki tym koincydencjom udało się po raz pierwszy zbudować schematy rozpadu ^{135}In oraz dwóch stanów w ^{133}In – niezależnie dla izomeru oraz stanu podstawowego. Schemat rozpadu ^{134}In został rozbudowany o dwa kanały rozpadu. Zaobserwowano emisję dwóch neutronów po przemianie β ^{134}In oraz ^{135}In. Populacja stanów niezwiązanych emitujących promieniowanie γ została zaobserwowana w ^{134}Sn oraz ^{133}Sn, przy energiach wzbudzeń przekraczających o 1 MeV energię separacji neutronu. Mimo, że przejścia Gamowa-Tellera zasilają głównie poziomy powyżej energii separacji dwóch neutronów w izotopach cyny, rozpad z emisją jednego neutronu jest dominującym kanałem rozpadu ^{134}In oraz ^{135}In. Dominująca emisja jednego neutronu po przemianie β tych jąder jest przewidywana jedynie przez modele teoretyczne, które, poza rozważaniem przejść wzbronionych, uwzględniają także wszystkie możliwe drogi rozpadu stanów niezwiązanych. Eksperymentalne schematy poziomów w ^{133}Sn, ^{134}Sn oraz ^{135}Sn zostały porównane z przewidywaniami modelu powłokowego, w tym z obliczeniami w których uwzględniono wzbudzenia typu cząstka-dziura ponad przerwę energetyczną odpowiadającą powłoce $N = 82$. Uzyskane dane wskazują, że stany niezwiązane odpowiadające konfiguracjom angażującym jednocześnie neutrony walencyjne i wzbudzenia rdzenia neutronowego są istotnymi elementami ścieżki deeksytacji obserwowanej w izotopach cyny po przemianach β izotopów indu.

CONTENTS

CHAPTER

I

INTRODUCTION

1 Fundamentals

1.1 Shell model

Even though the discovery of the atomic nucleus took place more than a hundred years ago, our understanding of its structure remains elusive. The pursuit of a comprehensive description of all nuclei, explaining the variety of observed nuclear effects, is the long-standing goal of nuclear physics. Thus far, more than three thousand different ways that the attractive nuclear force can bind protons and neutrons together into a nucleus have been experimentally identified [1]. Similarly to noble gases among chemical elements, which stand out due to their distinct chemical and physical properties, some atomic nuclei, just by virtue of being composed of specific numbers of protons (Z) and neutrons (N), exhibit distinct nuclear properties. Those specific numbers of nucleons, namely N or $Z = 2$, 8, 28, 50, and 82, as well as 126 for neutrons, are termed *magic numbers* [2, 3]. Figure I.1 presents their distribution on the chart of nuclides.

Nuclei with magic numbers of both protons and neutrons are called *doubly magic*, and are particularly stable in comparison to similar systems that differ only by a few nucleons. Many distinctive features of doubly magic nuclides are explained by the shell model of the atomic nucleus in which, in analogy to electronic orbitals, nucleons occupy single-particle orbitals under the influence of a mean-field potential created by the other nucleons (see Figure I.2).

The nuclear many-body Hamiltonian H consisting of kinetic energy T and potential energy V,

$$H = T + V = \sum_{i=1}^{A} \frac{-\hbar^2}{2m_N} \nabla_i^2 + \sum_{\substack{i,j=1 \\ i<j}}^{A} v(\vec{r}_i, \vec{r}_j), \tag{I.1}$$

can be expressed in another form

$$H = \left[T + \sum_{i=1}^{A} v(\vec{r}_i) \right] + \left[V - \sum_{i=1}^{A} v(\vec{r}_i) \right] \equiv T + V_{MF} + V_{RES}, \tag{I.2}$$

where the mean-field potential V_{MF} and the residual interaction V_{RES} were introduced. The latter is presumed to be significantly reduced in strength compared to the original potential V [4]. In the above expressions, m_N is the mass of a nucleon and $\vec{r}_i$ are the coordinates of nucleon i. At this point, the mean-field approximation provides a simple picture of a nucleus consisting of A nucleons, in which each one moves in an external potential produced by the other $A - 1$ nucleons.

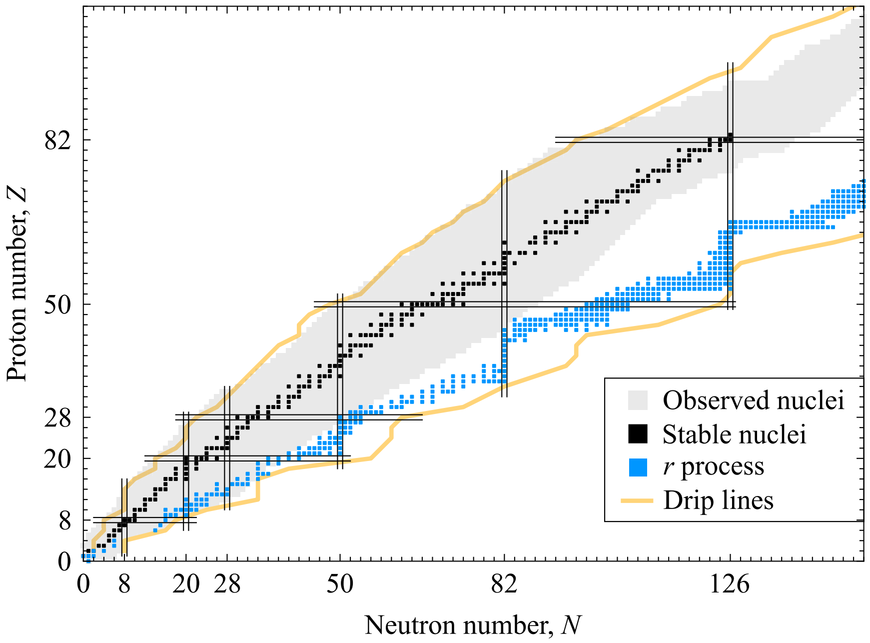

Figure I.1: Chart of nuclides presenting known nuclei (gray-shaded region) and those predicted to exist (region bound by the orange proton drip line from above and the neutron drip line from below). Nuclei with either magic number of protons or neutrons are narrowed by two straight solid lines. Picture was taken from Ref. [5] (changes were made under CC BY 4.0).

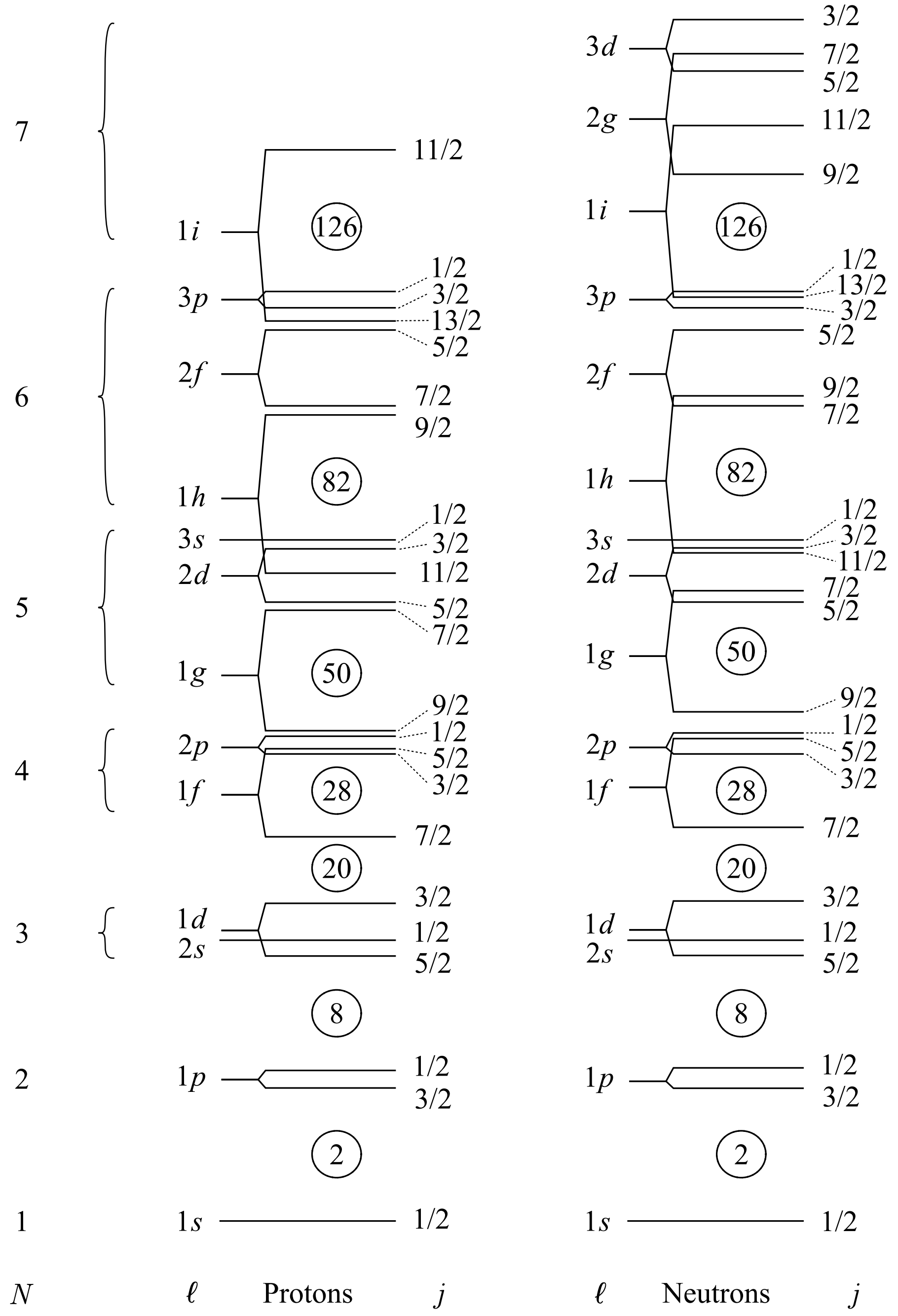

Figure I.2: Single-particle orbitals obtained with inclusion of spin-orbit coupling. Each of these discrete energy levels is described by three quantum numbers: $N-$ principal quantum number, $\ell-$ orbital angular momentum, and $j-$ total angular momentum. Magic numbers of either of the nucleons correspond to those configurations which fill all the orbitals up to the one separated by a sizable energy gap from the higher orbital. Single-particle orbitals in the lowest shells with $N = 1, 2$, and 3 are well separated from each other, which is a manifestation of magic numbers 2, 8, and 20. Energy gaps originating from spin-orbit interaction are responsible for other magic numbers: 28, 50, 82, and 126. The drawing was prepared following Ref. [6] (see Figure 1 therein).

A tremendous success in the shell-model description of nuclei was achieved when an additional term resulting from spin-orbit interaction was included in the nuclear mean-field potential [7, 8]. Because nucleons are characterized by spin $s = 1/2$, the spin-orbit coupling splits the levels of the same orbital angular momentum ℓ in two, with total angular momenta $j = \ell + 1/2$ and $j = \ell - 1/2$. This splitting reflects the fact that the force felt by the nucleon is dependent on the alignment of its spin and orbital angular momentum. An energy level with spin and orbital angular momentum aligned in parallel is energetically favored, in analogy to a classical magnetic dipole. The energy separation between these spin-orbit partners scales linearly with ℓ. The first considerable energy gap caused by spin-orbit interaction appears for the $1f$ shell ($\ell = 3$), above the $1f_{7/2}$ orbital. This effect makes the $1f_{7/2}$ orbital well-separated from both lower- and higher-lying single-particle orbitals. Sizable energy gaps appearing between successive orbitals are responsible for the effect of the shell closure (see Figure I.2). The numbers of nucleons that fill all single-particle orbitals situated below each of these gaps correspond to magic numbers. When all single-particle orbitals below the energy gap are filled with nucleons, they act together as a *core* with a spherically symmetric wave function.

Following the success of the shell model in reproduction of the magic nuclei properties, as was indicated from extensive experimental data, covering mainly ground-state properties [3], this theoretical approach has proven successful in predicting properties of low-energy levels in nuclei with numbers of protons and neutrons close to magic numbers. This is due to the aforementioned effect of the shell closure, which allows such nuclei to be described as a composite of a core and a few particles outside of it. The total angular momentum J of the level – commonly referred to simply as *spin* – results from the coupling of total angular momenta j of individual nucleons. Because the total angular momentum of all closed shells adds up to zero, the core contributes only $J^{\pi} = 0^{+}$ to the total angular momentum of low-lying levels. When only one or a few nucleons occupy single-particle orbitals outside the core, couplings of their angular momenta determine the spin of the state. The energy of such a state depends on the residual interaction among nucleons.

In the simplest case, for a nucleus with only one nucleon outside the core, the j value of the single-particle orbital occupied by the last nucleon corresponds to the spin J of the ground state. Excited states are formed by elevating the nucleon from this ground-state orbital to a higher orbital. Consequently, excitation energies reflect energy spacing between single-particle orbitals in a shell-model potential. Because this potential arises from nucleons composing the nucleus, single-particle energies are dependent on the nucleus mass. These energies may be differently affected by underlying filled shells due to the interaction of the valence nucleon with the closed shells [9]. It ought to be stressed that the sequence of neutron (ν) and proton (π) single-particle orbitals shown in Figure I.2 should be considered only as illustrating the single-particle levels arising from the shell-model approach.

In the shell-model picture of the nucleus with two or more particles outside the core, multinucleon configurations of valence particles are considered. Couplings of their individual j values result in a particular spin J of the state whose energy depends on the residual interaction among the nucleons occupying orbitals beyond closed shells. Mutual interaction of valence nucleons, which can be interpreted as making particles jump from one orbital to another, leads to configuration mixing that results in wave functions consisting of more than one configuration.

In the shell-model calculations, residual interaction most often appears in the form of the two-body matrix elements. Different types of two-body interactions are used [10, 11]. Those that are consistent with data obtained for two-nucleon systems are known as *realistic* interactions. Among them are interactions based on meson-exchange potentials and fitted *effective* interactions. The latter are adapted to the restricted basis as the two-body matrix elements are adjusted to reproduce available data. Shell-model calculations using effective interactions are likely to be successful only if the spectroscopic information on the regions of interest is available to fit-tune them. The structure of excited states in nuclei with only one or a few nucleons beyond shell closures provides experimental information of critical importance, enabling application and first validation of the shell-model approach in a particular model space.

1.2 β decay

Atomic nuclei are excellent objects with which to study three of the fundamental forces in nature. The most common radioactive decay mode of nuclei is β decay, which is a manifestation of the weak interaction. The β decay occurring in the many-body environment of the nucleus involves two isobars, which are often referred to as *parent* and *daughter* nuclei, as well as lepton and antilepton, both of electron flavor. In this process, the nuclear charge number Z changes by one unit due to the conversion of a neutron into a proton or vice versa. The Z number increases as a result of β^- decay:

$$(Z,N) \xrightarrow{\beta^-} (Z+1,N-1) + \mathrm{e}^- + \bar{\nu}_\mathrm{e} \tag{I.3}$$

or decreases as a result of β^+ decay:

$$(Z,N) \xrightarrow{\beta^+} (Z-1,N+1) + \mathrm{e}^+ + \nu_\mathrm{e}. \tag{I.4}$$

The probability of the β-decay transition resulting in a particular state in the daughter nucleus depends on the overlap between the initial and final wave functions. This nuclear structure information is contained in the Fermi and Gamow-Teller matrix elements. Decays associated with the vector part of the transition operator are called *Fermi* transitions, while those proceeding through its axial part are called *Gamow-Teller* (GT) transitions.

Fermi and GT β decays, in which final-state leptons are emitted in an s state relative to the nucleus, are classified together as *allowed* transitions. The following selection rules arise for these transitions from the conservation of angular momentum and parity:

$$J_f = J_i \text{ and } \pi_i \pi_f = +1 \text{ for Fermi transitions} \tag{I.5}$$

and

$$|J_f - J_i| = 0, 1 \ (0 \nrightarrow 0), \ \pi_i \pi_f = +1 \text{ for GT transitions,} \tag{I.6}$$

where f and i subscripts denote the spin and parity of the final state in the daughter nucleus and the initial state in the parent nucleus, respectively.

Another class of β decay, in which leptons with higher orbital angular momenta are emitted, corresponds to *forbidden* transitions. The term “forbidden” should not be taken literally because such β decays are only strongly hindered relative to the allowed ones. The initial and final nuclear states involved in forbidden transitions have opposite parities, i.e., $\pi_i \pi_f = -1$, or the difference of their spin values is greater than one. Forbidden transitions are divided into subgroups with successive levels of forbiddenness. Those with a higher degree of forbiddenness are least likely. Transitions involving p-wave leptons – termed *first-forbidden* (*ff*) transitions – are most often considered. They result in a change of parity and spin change up to two units.

The empirical classification of β decays into allowed and forbidden transitions, including their various degrees of forbiddenness, is performed in terms of $\log ft$ values [12]. In the case of allowed and *ff* transitions, these values depend exclusively on nuclear structure, which is contained in the β decay matrix elements [4]. Since $\log ft$ values are related to the experimental observables; this makes the β decay a powerful tool that allows us to probe the nuclear structure of the states involved.

Spin and parity are key properties of the β-decaying state of the parent nucleus, which serve as a starting point for discussing the structure of the ground and excited states populated in the daughter nucleus. High selectivity of the β decay, which results in feeding of levels with particular, “allowed” spin-parity values, conveys powerful information about configurations of the states involved in this process. This is especially emphasized in nuclei with only a few valence particles and/or holes relative to a doubly magic nucleus, as transitions can often be related to the simple wave functions of the states involved. Therefore, by studying their β decays, insight into the details of allowed and forbidden transitions is possible.

1.3 Decay of excited states

γ-ray deexcitation

The excited state populated in the daughter nucleus as a result of the β decay of the parent nucleus usually decays by emitting electromagnetic radiation. This process is much faster than the β decay governed by the weak interaction. Typical lifetimes of excited states are of the order of picoseconds or less. The γ ray emitted following the β decay appears with a β-decay half-life of the parent nucleus, but its energy reflects the energy level structure of the daughter nucleus. The properties of emitted γ rays – their energies, emission probabilities, and multipolarities – provide information on the energies, half-lives, spins, and parities of states involved in electromagnetic transition. All of these properties depend on the details of the wave functions of states and the transition operators for electromagnetic transitions. This essential information on the nuclear structure is contained in the *reduced transition probability*, which is also referred to as the transition strength, namely in the reduced matrix elements.

The electromagnetic decay process results from the interaction of the nucleus with an external electromagnetic field. To describe the decay of the nuclear excited state to its ground state, two states of the system consisting of the nucleus and field interacting weakly should be considered [4]. The unperturbed initial state of this system correspond to the nuclear excited state and electromagnetic field in its ground state, namely no photons. In the final state, there is a nuclear ground state and the electromagnetic field with one photon created in it. The transition between these two states is mediated by one of the multiple terms in the expansion of the electromagnetic radiation field. The sources of this field are either of electric (E) or magnetic (M) type.

When calculating the transition rate, it is useful to use expansion of the electromagnetic radiation field in multipoles in which the lower-order terms relate to the most probable transitions. The most likely transition is the one of the lowest multipolarity allowed by the angular momentum and parity conservation selection rules. For a λ-pole transition between the initial ($J_i^{\pi_i}$) and final ($J_f^{\pi_f}$) states, the selection rules are of the form:

$$|J_f - \lambda| \leq J_i \leq J_f + \lambda \tag{I.7}$$

and

$$\pi_i \pi_f = \begin{cases} (-1)^{\lambda} & \text{for } E\lambda, \\ (-1)^{\lambda-1} & \text{for } M\lambda. \end{cases} \tag{I.8}$$

When indicating the transitions with the lowest λ value as the most likely, it should be emphasized that there are no $E0$ or $M0$ γ-ray transitions. Their absence results from the form of the electric and magnetic tensor operators for $\lambda = 0$. With this multipolarity, the former is a constant, and the latter disappears.

Table I.1 presents a hierarchical classification of electromagnetic transitions, which is helpful in tracking the leading multipole responsible for the particular electromagnetic decay [4]. While selection rules often allow many transitions with different multipolarities, those with higher λ are generally without practical significance. Transitions with lower multipolarities can compete with each other. In practice, this competition mostly occurs between $E2$ and $M1$ transitions and is described by the mixing ratio, which is a measurable quantity. The dominance of the transition of higher multipolarity can be linked to a specific nuclear structure.

Table I.1: The most probable electromagnetic transitions between states with spin-parity values of $J_f^{\pi_f}$ and $J_i^{\pi_i}$.

$\Delta J = \|J_f - J_i\|$	0^*	1	2	3
$\pi_i \pi_f = -1$	$E1$	$E1$	$M2$	$E3$
$\pi_i \pi_f = +1$	$M1$	$M1$	$E2$	$M3$

* $0 \rightarrow 0$ not possible.

Internal conversion

Deexcitation via γ-ray emission is the most common decay mode of excited states. However, this process may be inhibited for some excited states (or forbidden for $E0$ transitions), and an alternative mechanism is possible – *internal conversion* – in which nuclear deexcitation energy is transferred to one of the bound electrons of the atom. As a result, an electron is ejected from the electron shell with kinetic energy corresponding to the energy difference of the initial and final nuclear states less the electron binding energy and the recoil energy. The emission of conversion electrons from each shell of the atom (K, L, M, ...) should be considered. The ratio of number of emitted conversion electrons and number of emitted γ rays is known as the internal-conversion coefficient, denoted by "α" symbol. This coefficient is the sum of the partial internal-conversion coefficients for each atomic shell (α_K, α_L, ...) and is often referred to as the total internal-conversion coefficient α_{tot} to distinguish it from the individual components. The α values vary considerably among different transition multipolarities. Since the excited state can decay via γ-ray emission and internal conversion, the total probability of transition between two nuclear states is a sum of the transition probabilities of these two competing processes.

β-delayed emission

When β decay populates states at excitation energies exceeding the energy required to separate one or a few nucleons from the daughter nucleus, emission of one or more particles may occur afterwards. Such β-delayed particle emission is mediated by the strong interaction and therefore is a process preferred to electromagnetic decay. However, there are some exceptions in which the hierarchy of these two forces is not manifested in the decay of unbound states [13]. Electromagnetic decay can compete with β-delayed proton emission when the Coulomb barrier defers the emission of charged particles. In the absence of this barrier, only the angular momentum barrier may hinder emission of neutrons, and thus γ-ray deexcitation can be enhanced. Because the transition probability depends on the overlap between the wave functions of the states involved in certain decay process, the unusual competition between neutron emission and γ-ray emission from unbound states demonstrates vital details of the nuclear structure.

The role of β-delayed particle emission is enhanced in nuclei with a large excess of neutrons or protons because separation energies decrease as the drip lines are approached. Due to the absence of Coulomb interaction between neutrons, which is repulsive for protons, the limit for the existence of such exotic nuclei lies on the neutron-rich side of the chart of nuclides much farther from the valley of β stability than on the proton-rich side (see Figure I.1 for comparison of the drip line locations) [14]. This constitutes a rough explanation of the fact that the vast majority of yet unexplored isotopes is neutron-rich, and β-delayed emission of one or more neutrons is their dominant decay branch.

The probability of β-delayed emission of x neutrons (P_{xn}) is an important β-decay property of nuclei with large neutron excess. This quantity is also referred to as the βxn-decay branching ratio, which should be understood as the probability of populating the ${}^{A-x}(Z+1)$ daughter nucleus in the β decay of the ${}^{A}Z$ parent nucleus. To distinguish a general decay mode via β-delayed neutron (βn) emission from its specific variants, additional labeling will be used to indicate β-decay branches with one ($\beta 1n$), two ($\beta 2n$), or more (βxn) neutrons. The β-decay branch of βn precursors, in which no neutrons are emitted, will be denoted by "$\beta\gamma$". Neutron-separation energy will be labeled analogously: the S_n symbol will stand for a general threshold energy for emission of any number of neutrons, while S_{1n} and S_{2n} indicate one- and two-neutron separation energies, respectively.

Figure I.3 shows energy windows considered for βn emitters. Energies of emitted neutrons (E_n), the neutron-emitting state fed by the β decay (E_i^*), and the state populated following neutron emission (E_f^*) are related according to the following formula:

$$E_n = \frac{A-1}{A}\left(E_i^* - S_n - E_f^*\right). \tag{I.9}$$

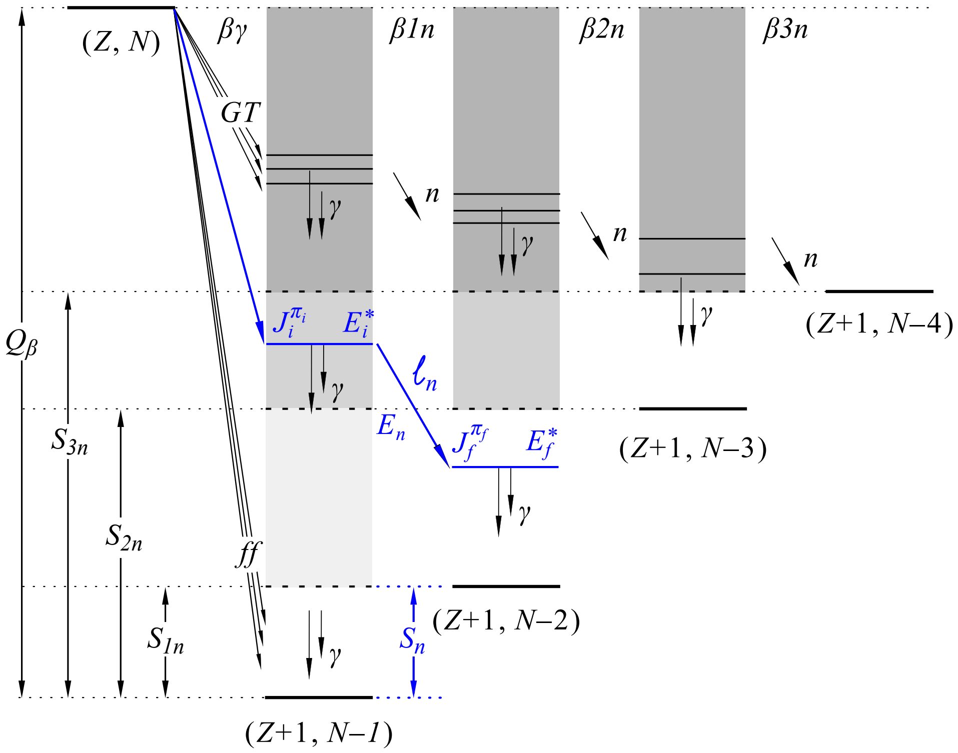

Figure I.3: Energy windows available for the population of neutron-unbound states (shaded regions) in the β decay of the nucleus that can emit up to three β-delayed neutrons. The left vertical scale shows the β-decay energy (Q_β) and (multi-) neutron separation energies (S_{xn}) with respect to the ground state of the daughter nucleus. An exemplary deexcitation pattern for the neutron-emitting state is shown in blue.

Conservation of angular momentum and parity leads to the differentiation between even and odd values of the orbital angular momentum of the emitted neutron (ℓ_n) depending on the parities of states involved in this process:

$$\vec{J_i} = \vec{J_f} + \vec{\ell_n} + \frac{\vec{1}}{2} \quad \text{and} \quad \pi_i = \pi_f \cdot (-1)^{\ell_n}. \tag{I.10}$$

2 *Physics cases*

New experimental information on the β decay of neutron-rich indium isotopes ^{133}In, ^{134}In, and ^{135}In that contain 18 ($N = 84$), 19 ($N = 85$), and 20 ($N = 86$) neutrons more than the heaviest stable indium isotope – more specifically primordial nuclide ^{115}In – is provided within the scope of this thesis. The β decay of these nuclei with proton number $Z = 49$ results in tin isotopes with the magic number of protons $Z = 50$ and only a few more neutrons more than the magic number $N = 82$. Owing to the distinctive properties of the $Z = 50$ and $N =$

82 shells, the studied isotopes constitute simple systems relevant for the shell-model description. These nuclei are located in the chart of nuclides in the vicinity of ^{132}Sn, which is the heaviest doubly magic nucleus far from the valley of β-decay stability (see Figure I.1).

Parent nuclei are situated in the quadrant south-east of ^{132}Sn, being the least explored part of the region around this doubly magic nucleus. Available experimental information on exotic nuclides from this region is mostly limited to ground-state properties. It is worth mentioning that the first mass measurements for ^{133}In and ^{134}In were reported very recently, in 2021 [15]. The mass of the more exotic isotope ^{135}In remains unknown, and only its extrapolation based on trends in measured masses of neighboring nuclides can be done [16].

Nuclei around ^{132}Sn are of great relevance for the development of the theoretical description of exotic nuclides with large neutron-to-proton ratios. Due to the robust nature of the ^{132}Sn core [17], tin isotopes above $N = 82$ offer a rare opportunity to investigate neutron-neutron components of effective interactions for heavy-mass nuclei with large neutron excess [18]. At present, the ^{132}Sn region is a unique part of the chart of nuclides, where spectroscopic information for neutron-rich nuclei with one and a few neutrons beyond the double-shell closure was obtained [18–20]. In another neutron-rich region, where lines indicating magic numbers intersect – the ^{78}Ni region – the first experimental information on excitation energies in the doubly magic nucleus was recently obtained [21], but excited states in isotopes that have more neutrons than ^{78}Ni remain unknown.

Understanding of the nuclear structure in the closest vicinity of the doubly magic ^{132}Sn is essential before extrapolating the nuclear properties towards more neutron-rich nuclides. With one neutron outside the ^{132}Sn core, ^{133}Sn provides unique information about neutron single-particle energies required in shell-model calculations in this mass region. Successive neutron single-particle orbitals between $N = 82$ and $N = 126$ shells determine the wave functions of states at low excitation energies in ^{133}Sn (see Figure I.2) [17]. With two neutrons more than ^{132}Sn, ^{134}Sn is a crucial case for testing the two-body matrix elements of effective interactions in this mass region. The more neutron-rich isotope ^{135}Sn, with an additional pair of neutrons compared to ^{133}Sn, is a relevant nucleus to investigate how single-particle states change with the addition of a pair of neutrons. Reproducing the structure of excited states in the nucleus with three valence neutrons should be a primary test of the predictive power of the shell-model calculations for more neutron-rich nuclei in this region.

One vital feature of ^{133}In, ^{134}In, and ^{135}In being located far away from the β-stability path is their large β-decay energy, $Q_\beta > 13$ MeV [16]. In conjunction with low S_n of daughter nuclei, it creates a wide energy window, exceeding 10 MeV, for the emission of one or more β-delayed neutrons (see Figure I.4). Therefore, the β decay of these neutron-rich indium isotopes may initiate a complex decay process involving two or more daughter nuclei. This conveniently grants us an experimental opportunity to investigate the nuclear structure of tin isotopes beyond $N = 82$ via different β decays, with various spin-parity values of parent nuclei.

Due to the simple structure of indium isotopes above $N = 82$, their β-decay study provides an excellent opportunity to probe the details of GT and *ff* transitions responsible for the β-decay properties of exotic nuclei located in the chart of nuclides below ^{132}Sn, i.e., with $Z < 50$ and $N \geq 82$. Of the two types of allowed β decays, only GT transitions may occur in nuclei from this region where single-particle orbitals are occupied with a strong imbalance of protons and neutrons. The lack of adequate single-particle orbitals in the last major proton and neutron shells precludes other allowed-type transitions (see Figure I.2). For neutron-rich nuclei with a proton hole below the $Z = 50$ shell gap, the highest-lying single-particle orbital in the $Z = 28-50$ shell plays a key role in the β decay, determining the transition rate and favoring the population of certain levels in daughter nuclei. The most favorable process leading to the filling of this proton hole can be probed by the β decay of indium isotopes above $N = 82$. This is facilitated by simple wave functions of states in isobars involved in β decays under study. Therefore, by studying the properties of radiation emitted following the β decay of neutron-rich indium isotopes, one can gain deeper insight into the structure of exotic nuclei from the ^{132}Sn region.

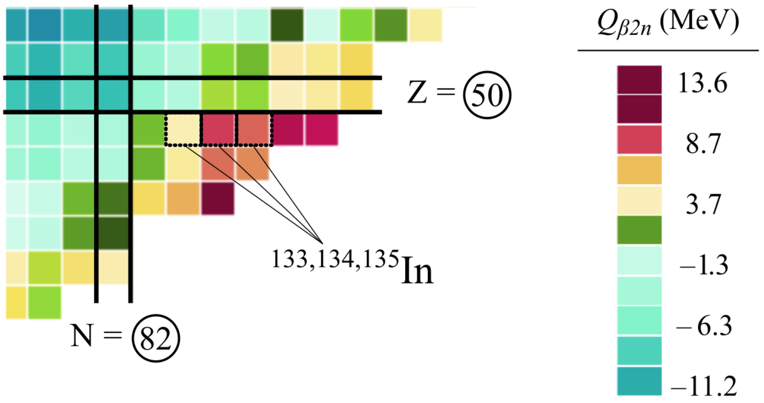

Figure I.4: Energy windows for β-delayed two-neutron emission ($Q_{\beta 2n}$) for nuclei in the ^{132}Sn region. The drawing was prepared using Ref. [22].

3 Previous studies

3.1 Parent nuclei

The discovery of ^{133}In and ^{134}In was reported in 1996 [1, 19, 23]. However, the first experiment using a beam of ^{133}In was performed more than a decade earlier [24]. The β decay of ^{133}In was studied using a detection system capable of measuring β particles, γ rays, and neutrons. One half-life of 180(2) ms was determined although the beam contained two β-decaying states of ^{133}In, the $(9/2^+)$ ground state and $(1/2^-)$ isomer. The parent nucleus proved to be a strong βn emitter, with a P_n value of 85(10)%. This dominant β-decay branch of ^{133}In became an obstacle to achieving the primary goal of the experiment, which was to identify excited states in ^{133}Sn. At that time, it was only possible to deduce positions of two neutron-unbound states in this daughter nucleus based on the energy spectrum of neutrons emitted from ^{133}In. One level was positioned at excitation energy of 3.7 MeV [19] while the other was found 2.5 MeV higher [24]. These two states were attributed to two-particle one-hole ($2p1h$) neutron configurations, with a hole in the $\nu 1h_{11/2}$ and $\nu 1g_{7/2}$ orbitals, respectively (assuming that Ref. [24] accidentally uses $\nu 1g_{11/2}$ instead of $\nu 1g_{7/2}$).

The strong βn-decay branch of the parent nucleus that acted as a bottleneck in the measurement with the ^{133}In beam proved to be an effective method to populate with appreciable intensity states in ^{133}Sn in a subsequent experiment using a beam of more neutron-rich ^{134}In [19]. Three transitions with energies of 854, 1561, and 2005 keV were attributed to ^{133}Sn based on observed coincidences with neutrons emitted from ^{134}In. They were interpreted as γ rays deexciting the neutron single-particle states $\nu 3p_{3/2}$, $\nu 1h_{9/2}$, and $\nu 2f_{5/2}$. Coincidence with neutrons was observed also for another two transitions, 354 and 802 keV, that were assigned to ^{133}Sn but not placed in its level scheme. The latter was mentioned as a possible candidate for γ ray deexciting the single-particle $\nu 3p_{1/2}$ state, decaying to the lower-lying $\nu 3p_{3/2}$ state. A half-life of 138(8) ms was reported for the parent nucleus. Information about the βn-decay branching ratio of ^{134}In was not reported in Ref. [19]. However, a value of ~65% attributed to that experiment appears in data evaluations [25, 26]. With already known energies of γ rays in ^{133}Sn deduced from the β-decay study of ^{134}In, it was possible to recognize these transitions as weak lines also in γ-ray spectra measured in the former experiment, using the ^{133}In beam.

The discovery of ^{135}In was reported in 2002 [1, 23, 27]. The measurement of neutrons emitted following the implantation of the ^{135}In ions yielded a half-life of 92(10) ms. No information was obtained on the population of states in tin isotopes. In the same experimental campaign, half-lives of the lighter indium isotopes were provided with improved precision. Values of 165(3) ms and 141(5) ms were reported for ^{133}In and ^{134}In, respectively [27].

Later β-decay studies of ^{133}In, ^{134}In, and ^{135}In reported only updated half-lives. The most recent results are as follows: 163(7) ms for ^{133}In, 126(7) ms for ^{134}In, and 103(5) ms for ^{135}In [28]. Half-lives of 165(3) ms, 136(4) ms, and 103(3) ms obtained for successive indium isotopes as averages over all previous results are recommended values [29]. Figure I.5 summarizes the information obtained to date on β decays of neutron-rich indium isotopes. Even though the population of states in five tin isotopes, from ^{131}Sn to ^{135}Sn, is energetically allowed in β-decay branches of ^{133}In, ^{134}In, and ^{135}In, previous β-decay studies provided insight into the structure of exited states only in ^{133}Sn. In total, three single-particle states and two neutron-emitting states were identified in this nucleus.

3.2 Daughter nuclei

3.2.1 ^{133}Sn

Among tin isotopes above $N = 82$, the most extensively studied was ^{133}Sn. The first confirmation of assignments resulting from the β-decay study of ^{134}In was in 1999. Attribution of the 1561-keV γ ray to the $(9/2^-)$ state in ^{133}Sn was supported by the spectroscopy of prompt γ rays emitted in the spontaneous fission of ^{248}Cf [30]. More transitions in ^{133}Sn were observed in three subsequent experiments based on the one-neutron transfer reaction [13, 17, 31, 32].

States in ^{133}Sn were studied via two reactions in inverse kinematics using the ^{132}Sn beam: ^{132}Sn$(d,p)^{133}$Sn in 2010 [17, 31] and ^{132}Sn(^{9}Be,^{8} Be)^{133}Sn in 2014 [32]. In the former, two transitions deexciting the $3/2^-$ and $5/2^-$ states in ^{133}Sn were confirmed. Moreover, new level at 1363(31) keV was reported, which was attributed to the $(1/2^-)$ state. Large spectroscopic factors were deduced for all observed states, revealing the purity of single-neutron excitations in ^{133}Sn. In the transfer reaction using a ^{9}Be target, all previously reported states in ^{133}Sn were identified. A new level was tentatively proposed at 2792 keV and attributed to the missing $\nu 1i_{13/2}$ state. A more precise energy of the $1/2^-$ state was provided: 1366.8(4) keV. A previously unobserved 513-keV γ ray deexcing this state to the $3/2^-$ state at 854 keV was identified. Although the 2792-keV transition was observed in coincidence with particles correlated with the ^{132}Sn(^{9}Be,^{8} Be)^{133}Sn reaction, its assignment to the $13/2^+$ state in ^{133}Sn was deemed inconclusive in Ref. [32].

More recently, states in ^{133}Sn were explored through a one-neutron knockout reaction in which ^{134}Sn ions impinged with relativistic energies on a carbon target [13]. Besides γ rays deexciting all previously known single-particle states in this nucleus, significant γ-ray strength was observed at energies exceeding the S_n of ^{133}Sn, at 2398.7(27) keV [16]. One prominent peak was seen in the energy range between 3.5 and 5.5 MeV. It was attributed to the 3570(50)-keV γ ray deexciting the neutron-unbound $(11/2^-)$ state. This level was previously positioned in ^{133}Sn at an excitation energy of $\sim$3.7 MeV based on the observation of 1.26-MeV neutrons following the ^{133}In β decay [19, 33].

After many experimental activities focused on ^{133}Sn, β decays of neutron-rich indium isotopes need re-examination, especially in view of new data on neutron-unbound states decaying via γ rays. The β-decay study seems to be a natural choice to investigate the nature of these states, because there is a large energy window for their population in the β decay of ^{133}In and ^{134}In. The enhanced emission of γ rays above S_n of ^{133}Sn hints at the prospect of finding the position of the single-particle $\nu 1i_{13/2}$ state, which has been hypothesized to be neutron unbound [30, 34]. Moreover, recent experimental developments enable the production of an isomer-selective beam of indium isotopes. In the case of ^{133}In, it offers the possibility of spin-selective population of states in ^{133}Sn, and identification of levels hitherto unobserved in β-decay study.

3.2.2 ^{134}Sn

The first information on excited states in ^{134}Sn was reported in 1997 from the measurement of γ rays emitted in spontaneous fission of ^{248}Cm [20]. Three transitions with energies of 174, 347, and 725 keV seen in coincidence were assigned to the 6^+, 4^+, and 2^+ levels in ^{134}Sn, respectively. The 6^+ state at 1246 keV was found to be an isomer with a half-life of 80(15) ns [20]. All levels identified in ^{134}Sn were assigned to the $\nu 2f^2_{7/2}$ multiplet. In a subsequent experiment involving the same fission reaction, levels previously ascribed to ^{134}Sn were confirmed. The 1262-keV γ ray was seen in coincidence with the 174, 347, and 725 keV transitions, indicating a new state with an excitation energy of 2509 keV [35]. This level was attributed to the $\nu 2f_{7/2}1h_{9/2}$ configuration with tentative spin and parity of 8^+. Based on angular correlation between the 725-keV and 347-keV γ rays, a stretched quadrupole character was deduced for both transitions. A more recent study of excited states in ^{134}Sn was reported in 2012 from an experiment aimed at searching for new isomers using in-flight fission of a ^{238}U beam [36]. Three known γ rays emitted from the isomeric 6^+ state in ^{134}Sn were identified. The half-life of this isomer was measured with improved precision and was reported to be 86(8) ns.

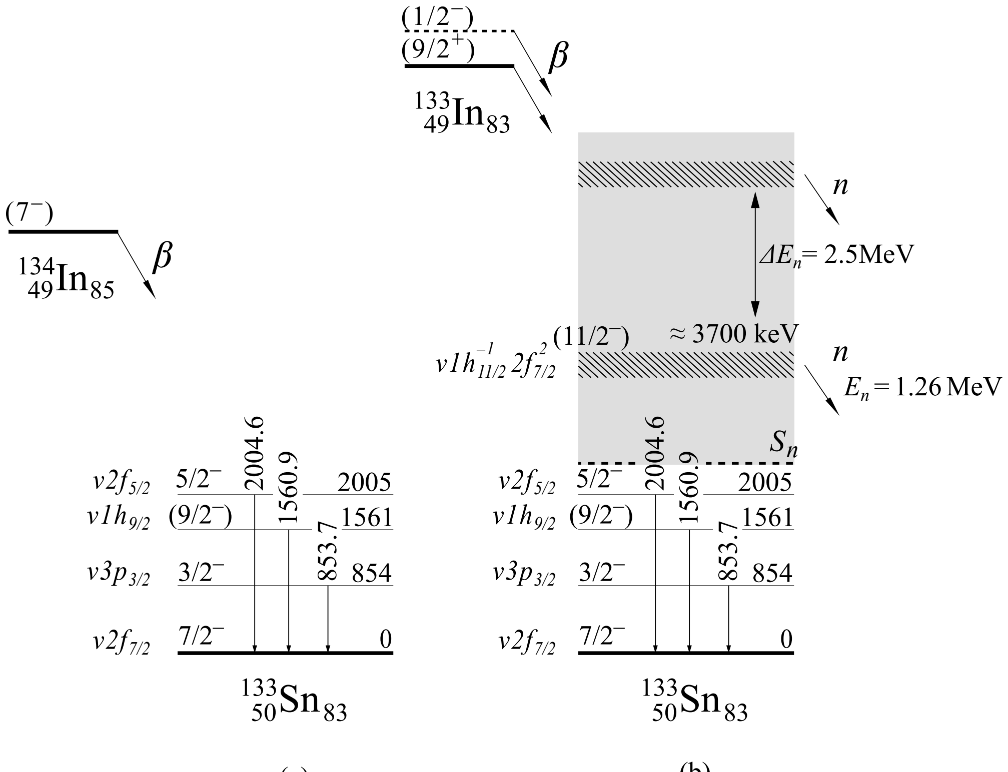

Figure I.5: Decay schemes obtained in the previous β-decay study of (a) ^{134}In and (b) ^{133}In [19, 33]. The scheme in panel (b) includes information also from a non-peer-reviewed report [24]. Spin-parity assignments for states in tin isotopes were taken from Refs. [13, 32].

Figure I.6 shows the level schemes of ^{133}Sn and ^{134}Sn established in previous experiments. To sum up, despite extensive studies, information on tin isotopes beyond $N = 82$ still appears to be scarce. A nucleus with only one neutron more than the doubly magic ^{132}Sn is the heaviest odd-A tin isotope for which excited states were reported so far. Even though ^{133}Sn was studied by various experimental methods, including β decay, fission, and three transfer reactions, the energy of one of the neutron single-particle states remains unknown. Moreover, significant γ-ray strength observed above the S_n of ^{133}Sn indicated the possibility to identify new, high-energy γ-ray emitting states in this nucleus. In the case of a nucleus with two neutrons more than doubly magic ^{132}Sn, only four excited states have been identified so far [35]. These known states correspond to only two different two-particle neutron configurations. A nucleus with three neutrons more than doubly magic ^{132}Sn represents presently the frontiers of experimental knowledge on excited states in neutron-rich tin isotopes.

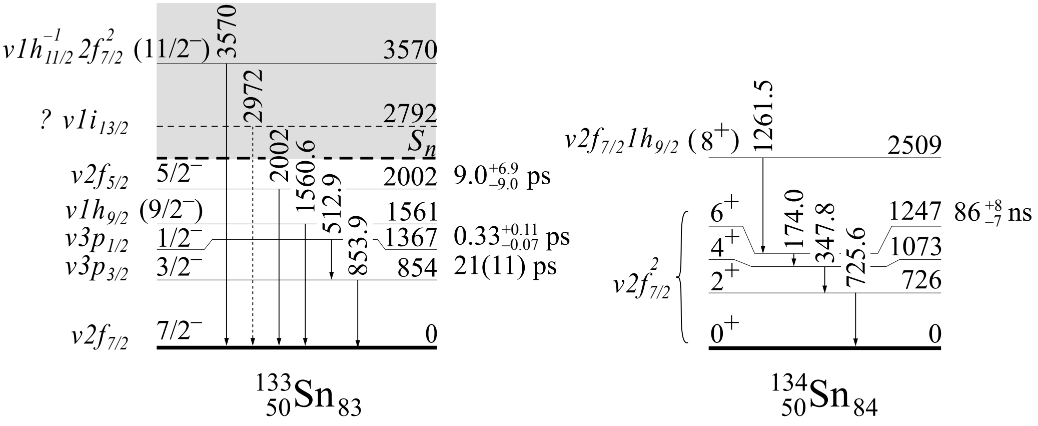

(a) (b)

Figure I.6: Summary of the experimental information on excited states in tin isotopes above $N = 82$, showing status prior to the publication of the results from this thesis. Level schemes, spin-parity assignments, and half-lives from the most recent studies reported in Refs. (a) [13, 32] and (b) [35, 36].

4 Motivation

Competition between γ-ray and neutron emission

Recently, a significant γ-ray decay branch for levels above the S_n was observed in ^{133}Sn [13, 37]. As reported in Ref. [13], the main factor hindering neutron emission from $2p1h$ states in ^{133}Sn is the small overlap of the wave functions of the initial and final states involved in the βn decay. It is expected that similar nuclear structure effects play a role for other nuclei southeast of ^{132}Sn [13]. Neutron-rich indium isotopes above $N = 82$ constitute excellent cases to address this problem owing to their large β-decay energy windows for the population of neutron-unbound states in daughter nuclei (>10 MeV). In particular, ^{134}In and ^{135}In – being rare instances of experimentally accessible nuclides for which the $\beta 3n$ decay is energetically allowed [16, 26] – constitute representative nuclei to investigate the competition between $\beta 1n$ and multiple-neutron emission as well as the γ-ray contribution to the decay of neutron-unbound states. Based on systematics, the energy windows for $\beta 3n$ emission from ^{134}In and ^{135}In are predicted to be 1.1(2) MeV and 5.2(3) MeV, respectively [16]. The particularly simple structure of excited states populated in tin isotopes following β decays of ^{133}In, ^{134}In, and ^{135}In allows for a thorough investigation of the nuclear structure effects that hinder the βn-decay branch.

At present, a precise understanding of the mechanism behind the βn emission remains elusive. Theoretical approaches use different assumptions about the capabilities of different decay branches, namely $\beta 1n$, $\beta 2n$, $\beta 3n$, ..., and $\beta\gamma$ decays, to compete with each other [38, 39]. A decisive validation of these approaches is currently unfeasible due to insufficient experimental information. Presently, there are only two known $\beta 2n$ emitters in the ^{132}Sn region for which P_{2n} values were measured [26, 40]: ^{136}Sb with $P_{2n} = 0.14(3)\%$ [41] and ^{140}Sb with $P_{2n} = 7.6(25)\%$ [42]. Thus, there is a pressing need for new experimental data that can verify and guide theoretical models describing βn emission for heavy-mass neutron-rich precursors.

Modeling of the r process

The properties of nuclei around ^{132}Sn are also important for modeling the rapid neutron capture nucleosynthesis process (r-process), which is responsible for the production of over half the elements heavier than iron. This process occurs in explosive astrophysical events producing or releasing neutrons with such high densities that neutron captures are faster than β decays of exotic nuclei. The optical characteristics of the kilonova associated with gravitational-wave signal GW170817 indicated that neutron-star mergers are vital, perhaps dominating, sites of r-process nucleosynthesis [43, 44]. Attempts to understand the observed r-process features are within the main focus of the entire field of astrophysics.

The astrophysical r-process involves multiple neutron captures by nuclei, sequentially repeated until β decay occurs. As a result, the atomic number increases, and the neutron capture sequence proceeds for the next isotopic chain, which is again terminated by the β decay, and the process continues recursively. Figure I.1 shows the predicted r-process path. Current experimental knowledge of neutron-rich nuclides on this path is extremely limited. The vast majority of r-process nuclei remain experimentally inaccessible, and their properties can be obtained only through theoretical means or through extrapolations of known properties from less exotic nuclei.

Since r-process nucleosynthesis is inextricably linked to the details of the nuclear structure, its accurate modeling requires knowledge of the β-decay properties of nuclei near and along the r-process path. Besides β-decay half-lives, the r-process pattern is also affected by the probabilities of βn emission because this process provides neutrons for late-time, non-equilibrium captures. In this way, βn emission shapes the fine details of the isobaric abundance distribution [45]. Formation of the rare earth peak and locations of the other main peaks in the r-process abundance pattern cannot be reproduced by the simulations without involvement of the late-time neutrons arising from βn emission.

Because a vast number of nuclei involved in the r-process are βn emitters, this makes βn decay a critical process that has to be described well by the nuclear models providing global nuclear-data sets used in astrophysical simulations. Therefore, new data for neutron-rich nuclei that decay through various β-decay modes are of particular importance because they guide the development of the theoretical models predicting β-decay properties for r-process nuclei beyond experimental reach.

Many of the βn emitters that have the greatest influence on the final r-process abundance features are located in the chart of nuclides in the ^{132}Sn region, near the $N = 82$ shell [45]. The distinctive nature of this closed shell is evident in the simulated dynamics of the r process. The magic neutron number $N = 82$ is responsible for the $A \approx 130$ peak in the r-process abundance pattern [46–49]. Therefore, better understanding of exotic nuclides in the ^{132}Sn region is needed for accurate modeling of the r process. Recently observed in this region enhanced emission of γ rays from neutron-unbound states calls for further investigation also due to its possible consequences for astrophysical r-process modeling. In particular, this enhancement of γ-ray emission may affect neutron capture rates of neutron-rich nuclei [38]. In an r-process sensitivity study, ^{134}In and ^{135}In were indicated to be among those βn emitters that have the greatest impact on the abundance pattern in cold wind r-process simulations [45]. Moreover, for neutron densities around 10^{25} cm^{-3}, where the r-matter flow has already broken through the $N = 82$ shell, the ^{135}In nuclide acts as an important "waiting-point" [27], i.e., the isotope for which successive neutron capture is limited by photodisintegrations, and at this point the r process "waits" for the β decay to take place.

CHAPTER

II

EXPERIMENT

1 Production

The experimental part of the research presented in this thesis was performed at the Isotope Separator On-Line Device (ISOLDE) [50], which is one of CERN's facilities. Indium isotopes – ^{133}In, ^{134}In, and ^{135}In – were produced as fission fragments via the Isotope Separation On-Line (ISOL) method using 1.4-GeV protons from the Proton Synchrotron Booster (PSB) (see Figure II.1). In order to produce these neutron-rich nuclei with the minimized formation of isobaric contamination, fission in a thick uranium carbide target was induced by neutrons. Protons from the PSB were directed onto a solid tungsten proton-to-neutron converter [51] mounted close to the ISOLDE target, producing spallation neutrons with MeV energies. With this production mechanism, the ratio of neutron-rich fission fragments to neutron-deficient isobars in the mass region of interest is higher than in the standard target configuration, in which the primary proton beam is sent directly to the target [52].

The indium atoms diffused out of the target material and subsequently effused via a transfer line into the hot cavity ion source, where they were selectively ionized by the Resonance Ionization Laser Ion Source (RILIS) [53]. The RILIS enhanced the ionization efficiency for indium, a surface-ionized element with an ionization potential of 5.7864 eV [54]. The ionization scheme for indium consisted of two steps. The resonant 304-nm excitation step provided element selectivity, and the 532-nm step was used for non-resonant ionization (see Figure II.2) [27, 55].

Two modes of RILIS operation were used that allowed either efficient selective ionization of indium or isomer-selective ionization of this element. The resonant transition was excited with frequency-tripled light from a titanium:sapphire (Ti:Sa) laser operated either in standard linewidth (broadband) or narrow linewidth (narrowband) modes [56]. For the latter, the fundamental linewidth is ~800 MHz. Measurements with RILIS in the broadband mode were made for ^{133}In, ^{134}In, and ^{135}In. For the lightest of these isotopes, studies were also performed with ions produced using the RILIS in narrowband mode.

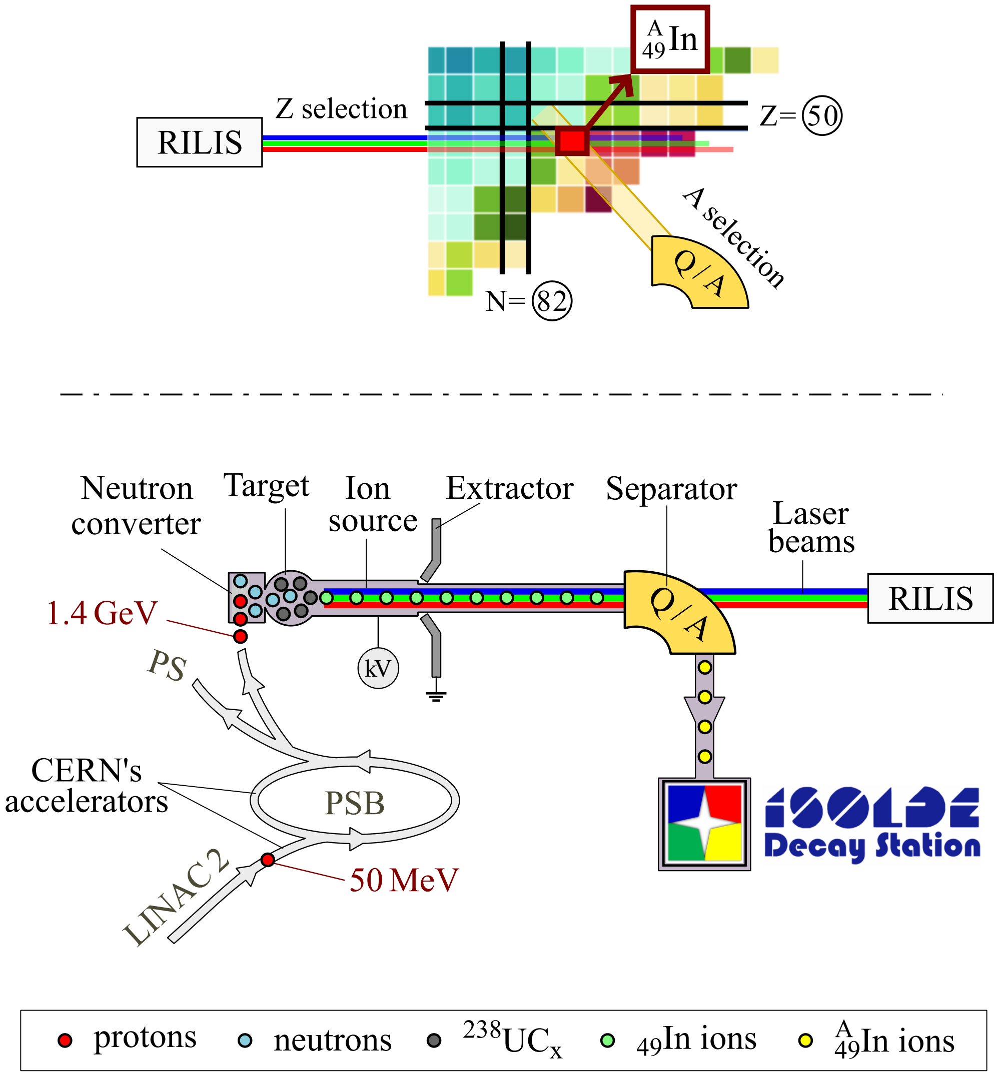

Figure II.1: Schematic drawings showing the key elements of ion beam production at ISOLDE. Element-selective ionization is provided by the Resonance Ionization Laser Ion Source (RILIS), while isotopic selectivity is achieved via electromagnetic mass separation.

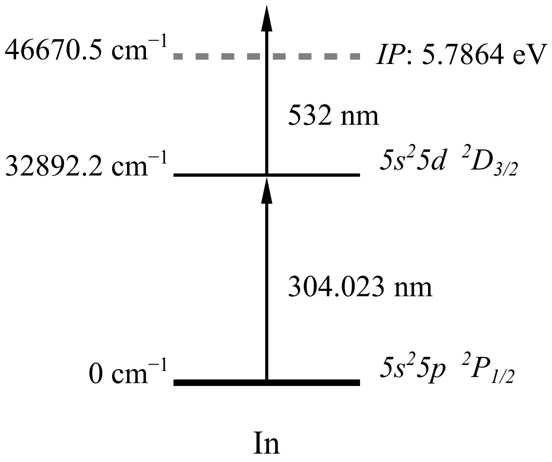

Figure II.2: Resonance laser ionization scheme for indium [55] with ionization potential (*IP*) of 5.7864 eV [54]. The RILIS was used to excite indium in two steps: selectively from the ${}^2P_{1/2}$ atomic ground state to the ${}^2D_{3/2}$ excited state and subsequently non-resonantly to the continuum.

RILIS is a sensitive tool that, owing to narrow-bandwidth lasers, is capable of resolving a hyperfine splitting of atomic lines caused by nucleon-electron spin interaction [57]. For odd-A indium isotopes, hyperfine splittings between electronic energy levels of the $9/2^+$ nuclear ground state and $1/2^-$ isomer are sufficiently large to be resolved by the narrowband Ti:Sa laser [53]. Laser wavelengths were optimized to selectively ionize indium atoms in the ground or isomeric state using a beam of a less exotic isotope ^{129}In with the goal of providing a minimum mixing ratio of β-decaying states of the parent nucleus (see Figure II.3). In summary, utilization of RILIS provided an enhanced population of the desired nuclear state in the produced beam of ^{133}In ions.

Once the RILIS had provided element selectivity for the ion beam, the next step was to achieve isotopic selectivity. The extracted ion beam was accelerated to an energy of 40 keV and transmitted to one of the ISOLDE mass separators, where indium isotopes were separated according to the mass-to-charge (A/Q) ratio. Because mostly singly charged ions are extracted and sent for mass selection, separator settings for a given A/Q ratio are commonly referred to as the settings for the given mass (A). Two ISOLDE mass separators with independent target-ion source systems were used in the experiment performed in two campaigns, in 2016 and 2018. In the former, the High-Resolution Separator (HRS) was used to produce the ^{133}In beam. In the latter, the $A = 134$ and $A = 135$ masses of interest were selected using the General-Purpose Separator (GPS). The key difference between these two separators is the mass-separation resolution. It amounts to approximately 800 and 6000 for GPS and HRS, respectively [54].

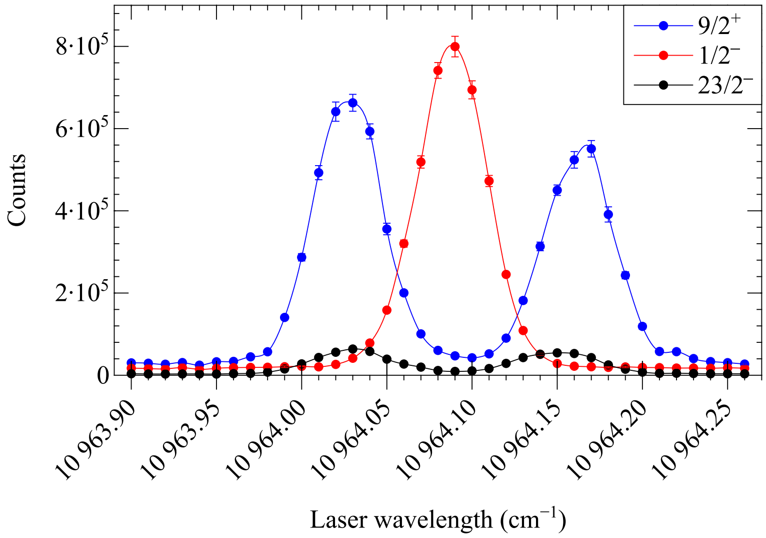

Figure II.3: The RILIS wavelength scan performed with the ^{129}In beam. The relative content of the ions of ^{129}In in the isomeric state versus those in the ground state was evaluated as a function of the laser wavelength. The beam composition was deduced from count rates for γ rays emitted from only one of the β-decaying states of ^{129}In. The complex hyperfine structure prevents the production of an isomerically pure beam. However, a significant enhancement of the fraction of one of the nuclear states in the produced ion beam is observed at certain laser frequencies.

2 Beam implantation

Mass-separated indium ions were transmitted to the ISOLDE Decay Station (IDS), which is a permanent detector setup at ISOLDE designed for decay spectroscopy [58, 59] (see Figure II.4). The ion beam passed through a variable aperture collimator and was implanted on an aluminized mylar tape inside a vacuum chamber at the center of the detection setup.

The time structure of ions reaching the IDS varied depending on the composition of the PSB supercycle, which is a continuously executed plan of cycles defined to satisfy beam requirements in the CERN accelerator complex. Individual cycles, multiples of 1.2 s in length, are attributed with desired beam characteristics to end beam users, including the ISOLDE facility. The supercycle structure changed during the experiment. Its length ranged from 26 to 34 cycles, corresponding to 31.2 and 40.8 s, respectively. The time intervals between successive proton pulses sent to the ISOLDE target also varied.

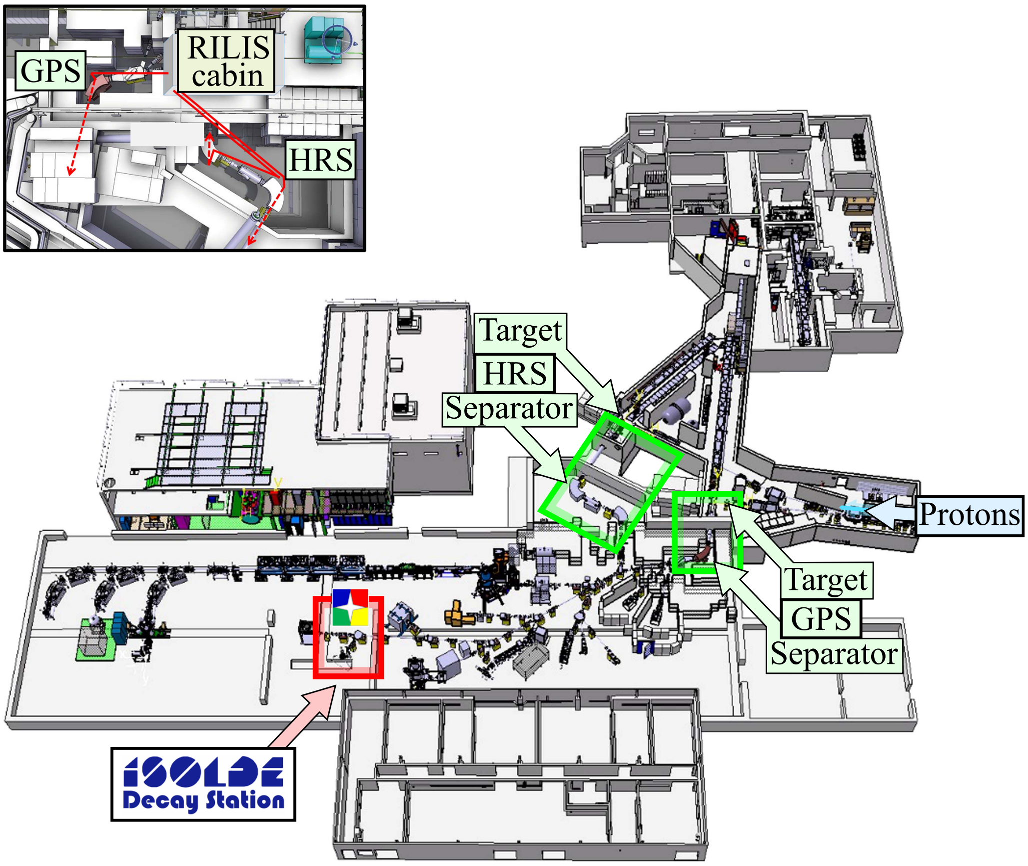

Figure II.4: Layout of the ISOLDE facility showing locations of target stations, mass separators, and the ISOLDE Decay Station in the experimental hall. The location of the laser laboratory (RILIS cabin) positioned on a platform above the ion beam lines is also shown. Pictures were taken from Refs. [50, 53] (changes were made under CC BY 3.0).

The time structure of ions transferred from the ISOLDE target to the beam line in the experimental area is controlled by an electrostatic deflector, which acts as a beam gate. When the beam gate is open, ions are transmitted to the beam line. The time of holding it open should be adjusted to the half-lives of the produced nuclei and possible contaminants present in the beam at a given mass. Delaying its opening after the proton pulse helps prevent entry to the experimental area of short-lived nuclei immediately ejected from the target material. Appropriate reduction of the beam gate length is applied to suppress transmission of possible contaminants having half-lives longer than the desired nuclei. When producing neutron-rich indium isotopes with half-lives of around a hundred ms, closing the beam gate between proton pulses occurring in multiples of 1.2 s helps to reduce implantation of cesium isomers. Those are released from the target as surface-ionized isobars, and their half-lives are in a timescale of hours.

Figure II.5 summarizes components for adjusting the time structure of the implanted ions. Various beam-gate settings were applied to achieve specific goals. For mass $A = 133$, measurements were performed with the beam gate open for 50, 200, and 600 ms immediately after the proton pulse. For mass $A = 134$, settings with both no delay and 5 ms delay were used. In the first option, the gate was open for 200 or 300 ms. In the second option, delayed extraction lasted for 200 or 500 ms. For mass $A = 135$, all measurements were performed with a 5-ms delay of the opening of the beam gate for 225 ms.

Data were collected at the IDS during beam extraction and subsequent decay of the isotopes of interest (see Figure II.5). To suppress long-lived activity arising from nuclei produced in the β-decay chain of indium isotopes, the tape on which ions were implanted was moved periodically. For most of the measurements, the movement took place after each PSB supercycle. A more effective operation mode of tape, with movement between each proton pulse, was used only in part of the experiment at mass $A = 134$. Supplementary measurements were made without tape movement to allow for the investigation of activity accumulated on it.

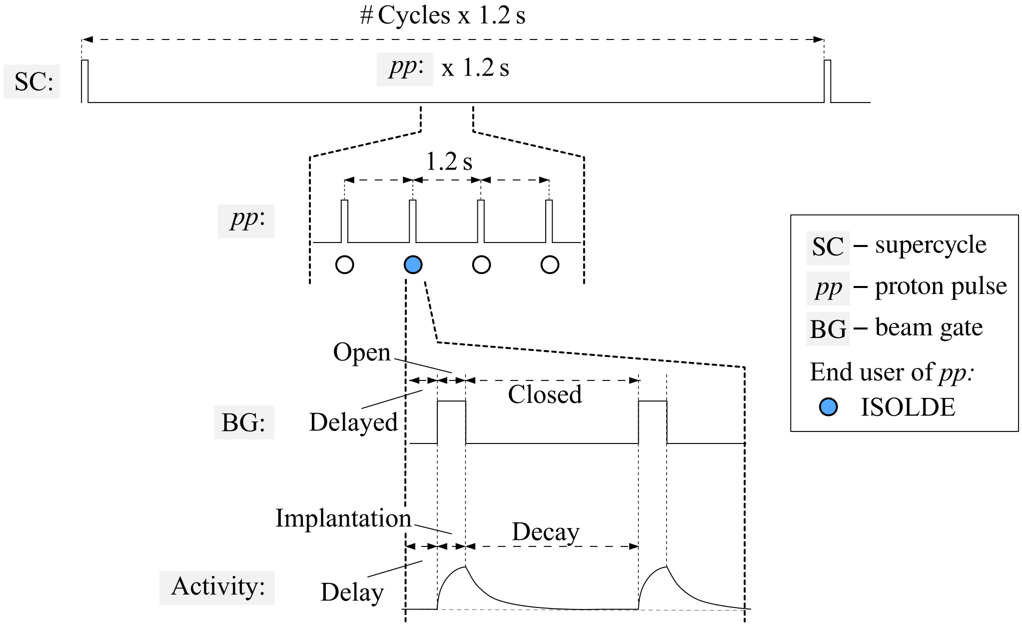

Figure II.5: An overview of the signals that contribute to the time structure of an ion beam produced at ISOLDE.

To enable a separate investigation of isobaric contaminants, additional implantations were performed at three masses with one of the RILIS lasers blocked. In such a laser-off mode, only surface-ionized elements reached the IDS, mostly cesium with low ionization potential (3.8939 eV [54]). In the laser-on mode, RILIS-ionized indium was additionally present in the beam. It should be noted that indium, with an ionization potential of 5.7864 eV [54], is also a surface-ionized element. Because ionization efficiency is significantly enhanced when the RILIS is used for its resonant ionization, comparison of the data collected in laser-on and laser-off modes allows identification of activity arising from the implantation of beam impurities.

3 Detection setup

The detection setup at IDS was adapted for the registration of γ rays and β particles. The arrangement of detectors around the beam implantation point is shown in Figure II.6. Signals from detectors carrying energy and time information on recorded events were processed by a digital data acquisition system commonly referred to as DAQ. The experimental setup was arranged to accommodate not only traditional γ-ray spectroscopy aimed at obtaining essential information about excitation energies in the studied nuclei but also fast-timing spectroscopy intended for the direct measurement of the lifetimes of nuclear levels [60–62]. Determination of half-lives from this experiment, mainly for the less exotic nuclei, was the purpose of the study described in another PhD thesis [63]. Details of the setup tailored for fast-timing spectroscopy can be found therein. This chapter focuses on the elements of the detection system that were dedicated for the γ-ray spectroscopic study. The same experimental setup was used at the IDS in the 2016 and 2018 campaigns. Only minor differences in detector positions and their operating parameters could be considered.

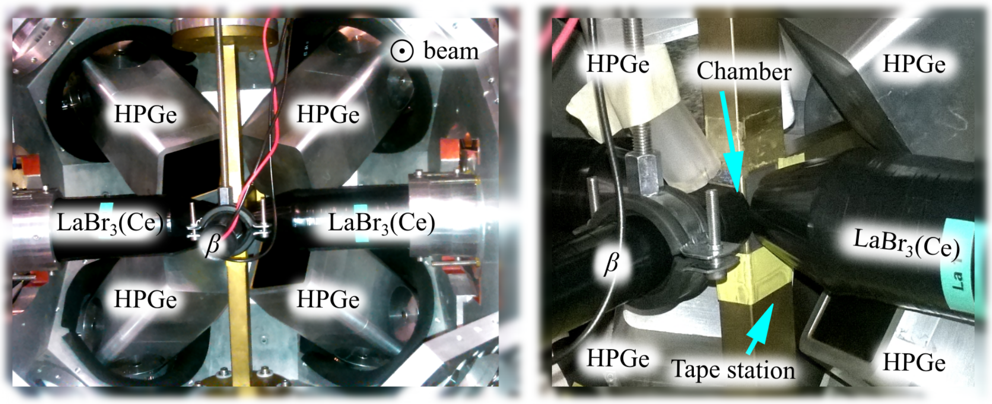

Figure II.6: Arrangement of detectors at the IDS. Indium ions were implanted on tape inside a vacuum chamber. The β detector was positioned just behind the ion collection point.

3.1 Detection of γ rays

The core of the IDS consisted of four high-purity germanium (HPGe) detectors, which are key instruments in γ-ray spectroscopy measurements, providing precise information about γ-ray energy. The arrangement of HPGe detectors at the IDS is shown in Figure II.6. These detectors were placed at a distance of around 75 mm from the implantation point, in the backward position with respect to the ion beam direction. They were evenly spaced azimuthally and directed toward the vacuum chamber where the indium ions were implanted.

Each HPGe detector contained four crystals of 50 mm diameter and 70 mm length mounted closely in a common cryostat. Such an assembly of HPGe detectors is referred to as a clover. More specifically, Euroball-type clovers manufactured by Canberra were used [64]. The advantage of the joint arrangement of HPGe segments versus their single configuration is improved detection efficiency due to the reduction of the material surrounding the crystals. Moreover, clover-type detectors offer the ability to reconstruct the full energy deposit for events in which γ rays scatter in one crystal and are absorbed in another adjacent segment of the same detector. This procedure is commonly known as “add-back” [65]. This reconstruction is particularly helpful in analyzing decays of exotic nuclei such as neutron-rich indium isotopes, for which low beam intensities impede the collection of adequate statistics in spectra. Another advantage of a composite detector comprising modest diameter crystals is improved resistance to neutron radiation damage compared with larger volume HPGe detectors [65]. This is an important feature in the case of measurements with strong neutron emitters, such as the indium isotopes under study.

Two of the clovers used at the IDS offered excellent performance for x-ray detection due to the carbon composite window at the entrance, which provides transmission to below 10 keV. The other two were equipped with a typical aluminum window, which has improved ruggedness, but worse detection capabilities below 30 keV. Clovers with aluminum windows have crystal positioned 13 mm deeper than those with carbon, which implies different solid angle coverage by these two detector models. More details about clovers being a permanent part of the IDS setup, including GEANT4 simulations, can be found in Refs. [59, 66].

3.2 Detection of β particles

Identification of events associated with β decay was provided by a compact plastic scintillator positioned directly behind the ion implantation point (see Figure II.6). This detector, shaped like a cylinder with 3 mm width and 25 mm diameter, was designed specifically for fast-timing applications [62]. In that case, deposition of only part of the energy of the incident β particle is needed to provide crucial information that β decay has occurred. Therefore, the β-particle detector should act mainly as a quick trigger.

The detector was made of EJ-232 plastic [67], characterized by 350 ps rise time and 1.6 ns decay time. Plastic was coupled to a high-speed response photomultiplier tube (PMT), with a short rise time of 7 ns. More specifically, the R5320 PMT model produced by Hamamatsu was used [68]. The efficiency of β-particle detection ranges between 10% and 30% and is determined mainly by geometry.

The use of a thin scintillator should ensure a time response almost independent of the energy of registered β particles because, in that case, energy deposited by incident radiation is expected to be relatively uniform. However, some complication arises from events for which the effective thickness of the absorbing medium is different. Effects dependent on the energy of incoming particles can occur because the amount of energy deposited in the detector material is dependent on the orientation of the scintillator plane with respect to the direction of the incident β particle.

3.3 Fast-response setup

Part of the setup dedicated to lifetime measurements comprised two additional γ-ray detectors with a $\mathrm{LaBr_3}$(Ce) scintillator. This material offers superior energy resolution to other scintillators commonly used for fast-timing applications [69, 70]. Truncated cone-shaped $\mathrm{LaBr_3}$(Ce) crystals with a height of 38.1 mm and bases of 38.1 and 25.4 mm produced by Saint-Gobain were used [71, 72]. They were coupled to a fast-time response PMT with a 51 mm diameter, the Hamamatsu R9779 model, with an anode rise time of 1.8 ns [73].

Two $\mathrm{LaBr_3}$(Ce) detectors combined with the plastic detector formed a fast-response system for studying coincidences involving γ rays and β particles. They were placed in close geometry around the beam implantation point, as shown in Figure II.6. The PMT anode signals from these detectors were processed by analog constant fraction discriminators and then sent to time-to-amplitude converters (TACs), which provided the time difference between coincident signals. This configuration made it possible to perform lifetime measurements for excited states using the advanced time-delayed $\beta\gamma\gamma(\mathrm{t})$ method, also known as the fast-timing technique [60–62]. Results of fast-timing analyses of data collected in the experiment are presented in Refs. [63, 74].

3.4 Data acquisition and online analysis

Signals from all detectors, along with outputs from TACs and the reference signal from the PSB, were acquired using the Nutaq VHS-ADC acquisition system [75, 76]. It consisted of three modules, each equipped with 16 channels. High-speed 14-bit ADCs were capable of a maximum sampling rate of 105 MHz. Data were collected in triggerless mode. A total data readout method [77] was employed in which all channels were read independently, timestamped with 10-ns precision using a 100 MHz clock signal, and then associated entirely in software to reconstruct events. Online analysis of the raw data stream was performed using the GRAIN software package [78]. Figure II.7 shows the successive stages of processing the collected data.

Events were reconstructed offline using `nutaq4ids` code [79]. Data were converted to the GASPware format, in which each event contains a header with timestamp and detector parameters. In this step, the configuration of detector signals processed by the DAQ was defined. Each detector received at least three parameters describing the event, one with energy information and two with time information. The time difference between each signal and the time centroid of the event was defined as high-resolution time, with 10 ns per channel. Another time parameter contained information about the time difference between the event and the pulse from the PSB, which is an essential reference signal for selecting β-decay events correlated with protons hitting the target. This parameter, referred to as low-resolution time, was given in a timescale of ms. At this stage, a time window for coincidence detection was also set. Window lengths of 200, 300, and 1000 ns were independently applied to various data sets. A number of coincidences between detectors required to trigger an event could also be specified. It was chosen that all events, including single-detector ones, should be considered in the analysis.

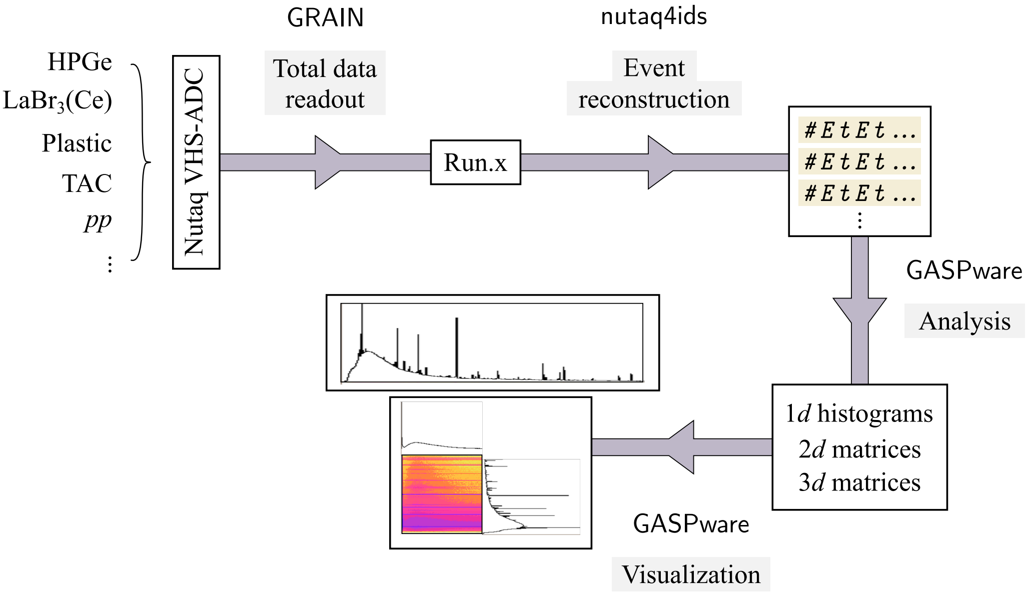

Figure II.7: A diagram depicting successive processing steps of data collected in the experiment. The following software was used: GRAIN [78], nutaq4ids [79], and GASPware [80].

3.5 Offline analysis

Further analysis of events was performed using the GASP Data Analysis Program Package [80]. At this stage, the main spectroscopic analysis of data collected in the experiment began. The GASP software allowed many operations on data to be executed. These included the following: the creation of a histogram from content read in a given channel in the DAQ, calibration of raw data, applying the add-back algorithm, creation of a one-dimensional spectrum of the given detector parameter, and production of many-dimensional coincidence matrices involving selected detector parameters. Various operations on parameters were performed during the sorting procedure to build matrices tailored for analysis. In this way, the selection of events meeting certain conditions was performed, commonly referred to as “gating”.

One of the most important tasks in the analysis was to select events recorded in coincidence in plastic detector and clovers, because they can be associated with β particles and γ rays arising from the same β-decay events. Then, by analyzing a symmetrized matrix comprising events recorded in coincidence in HPGe detectors, it can be determined whether the γ rays observed in coincidence with β particles belong to a known or yet unobserved γ-ray cascade. Based on their time distributions relative to the proton pulse, which acts as a tag of the beam implantation, it was possible to conclude whether these $\beta\gamma$ coincidences arise from the β decay under study.

3.6 Detection performance and calibrations

The purpose of the calibration measurements was to study the performance of the detection system and establish the characteristics required for it to determine the essential properties of radiation emitted in the β decays under study. In order to investigate discrete nuclear energy levels, precise information about γ-ray energy is needed. It is also necessary to determine how efficiently detectors record emitted radiation. Knowing the limitations of the detection system and corrections that have to be applied to measured quantities to obtain absolute emission rates is essential for inferring dominant decay paths of the nuclei under study.

Information on γ-ray energies was obtained from HPGe detectors with superior energy resolution to the other type of γ-ray detector used. Consequently, γ-ray emission rates were determined for transitions with precisely known energies. Efficiency characteristics of HPGe detectors provided the basis for their calculation. For β particles produced with a continuum of energies, information about their registration, without details of the energy deposit, was sufficient for the analysis. Applying a $\beta\gamma$ coincidence condition to events was required to suppress the background hindering the β-decay study of indium isotopes. Consequently, emission rates inferred from γ-ray spectra built with such a condition had to be corrected for the efficiency of β-particle detection.

Two types of radioactive sources were used in the calibration measurements. One type consisted of standard γ-ray sources: ^{133}Ba, ^{137}Cs, ^{152}Eu, and ^{140}Ba/^{140}La. For these nuclei, recommended decay data standards are available [81, 82]. These sources were used to collect reference data before and after the experiment, lasting several days. Independent data sets allowed us to check the stability of the detection setup. In addition, so-called "online" sources produced via the ISOL method were used. Additional collections of ion beams at masses $A = 88$ and 138 were made primarily to meet the needs of fast-timing analysis. They provided reference data on decays of surface-ionized ^{88}Rb and ^{138}Cs, respectively, which improved the energy and efficiency calibrations. The measurement at $A = 88$ was particularly useful because the response of the detectors to the 4.7-MeV γ rays could be investigated.

3.6.1 Energy calibration

The γ-ray energy calibration of HPGe detectors – the relation linking the channel number in the energy spectrum to the γ-ray energy – was established in several steps. Firstly, histograms resulting from the pulse-height analysis of signals read in individual DAQ channels connected to clover segments were analyzed. Such histograms, produced from data collected in a given DAQ channel, will be further referred to as projections. Calibration points covering the energy range from 0.1 to 4.4 MeV were established using three data sets collected in 2016. Data acquired in reference measurements were insufficient to provide calibration points at energies above 1.8 MeV. Therefore, those collected with the ^{132}In beam had to be included in the calibration of individual crystals. More data sets for calibration of clover segments are available from 2018. Calibration points were established between 0.1 and 4.7 MeV from energy projections measured with the following sources and samples produced online: ^{88}Rb, ^{138}Cs, ^{152}Eu, ^{140}Ba/^{140}La, and ^{134m}Cs. The latter corresponds to an isobaric contaminant produced abundantly at mass $A = 134$. Sixteen calibration curves were obtained in simple linear regression. The resulting equations were included in the offline analysis at the stage of creating matrices. The energy spectrum measured by all HPGe detectors was then constructed by summing the calibrated projections.

Combining information from all crystals was beneficial not only due to increased statistics in the resulting spectra but also because of the ability to apply the add-back procedure. Energy spectra created from data sets previously used to calibrate individual clover crystals were analyzed to assess the quality of joint calibration of all HPGe detectors and extend it with new data points. Background γ rays originating from neutron capture reactions in surrounding materials allowed energy calibration of clovers to be extended up to 7.6 MeV. The origin and components of this background are discussed in Section III 1.1.2. Figure II.8 displays the final calibration curve of HPGe detectors and deviations of calibration points from this curve. For points below 4 MeV, differences are less than 0.2 keV. For those at higher energies, deviations do not exceed 0.8 keV. Similar quality of energy calibration of clovers was achieved in 2016 and 2018.

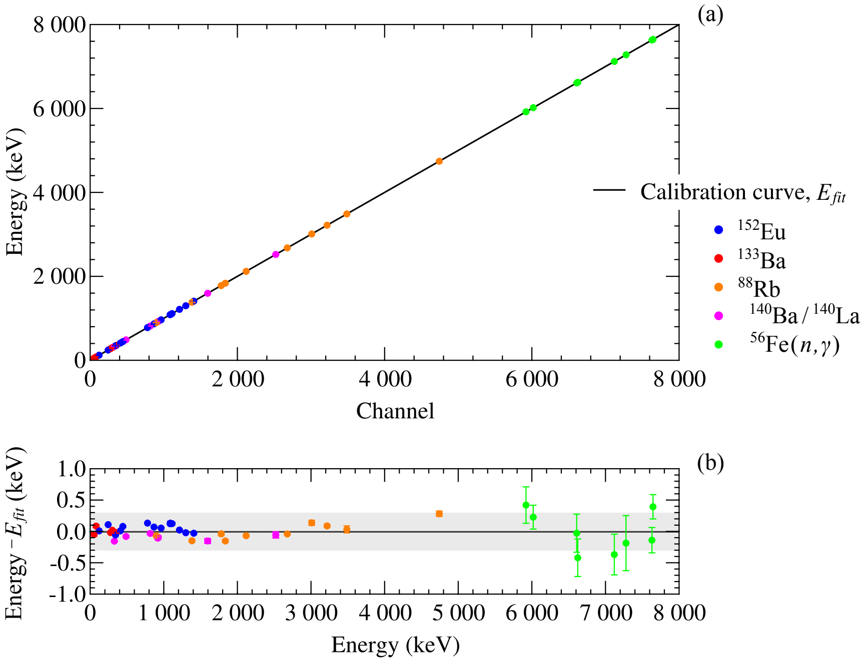

Figure II.8: Energy calibration of HPGe detectors from measurements in 2018. Calibration points were established in the energy range between 0.05 and 7.65 MeV. Differences between calibration points and the regression line are also presented.

3.6.2 Efficiency characteristics

γ-ray detection

Determination of absolute emission rates of γ rays observed in the experiment requires knowledge of the detection efficiency of HPGe detectors. Their calibration, with the aim of finding a relation describing this efficiency over a wide range of γ-ray energies, was performed in two steps. This two-stage approach was due to the use of two types of calibration sources, each requiring a different treatment. Energy spectra utilized in efficiency calibration were sorted following the same procedure that was applied for data collected with beams of indium isotopes, i.e., after adding up energy-calibrated projections and applying for the add-back procedure.

In the first step of the calibration procedure, only standard radioactive sources with known activity were included. Efficiencies were determined from spectra as ratios of counts in full-energy peaks to numbers of corresponding γ rays emitted by the source. Recommended decay data standards [81] were used to determine the latter. Once calibration points were established, a calibration curve relating γ-ray energy (E_γ) to detection efficiency (ϵ) was derived. A commonly used analytical function,

$$\epsilon(E_\gamma) = 1/E_\gamma \sum_{i=1}^{N} a_i (\log E_\gamma / 1 \text{ keV})^{i-1}, \tag{II.1}$$

was found to give a good representation of full-energy peak efficiencies using $N = 4$ [83]. The absolute efficiency characteristic for HPGe detectors was obtained in the energy range between 0.05 and 1.4 MeV. For the standard energy of 1333 keV, corresponding to the γ-ray emitted by ^{60}Co, the absolute detection efficiency of 3.4% was obtained.

In the second stage of the calibration procedure, data collected with calibration sources produced online were used. Determination of absolute γ-ray emission rates for samples implanted at the IDS was not possible. Only relative detection efficiencies were calculated, which correspond to the ratios of counts in the full-energy peak to the probability of emission of a given transition from the online source. Relative efficiencies shown as a function of γ-ray energy follow the shape of the calibration curve describing absolute detection efficiency of HPGe detectors. Factors were found to scale calibration points obtained with samples produced online to the efficiency calibration curve established using standard radioactive sources. Once relative efficiencies were scaled, the curve described by the previously used function $\epsilon(E_\gamma)$ (see Equation II.1) was fitted to calibration points covering the energy range between 0.05 and 4.7 MeV (see Figure II.9). For γ rays with energies lower than 4.5 MeV, detection efficiency was below 1.3%.

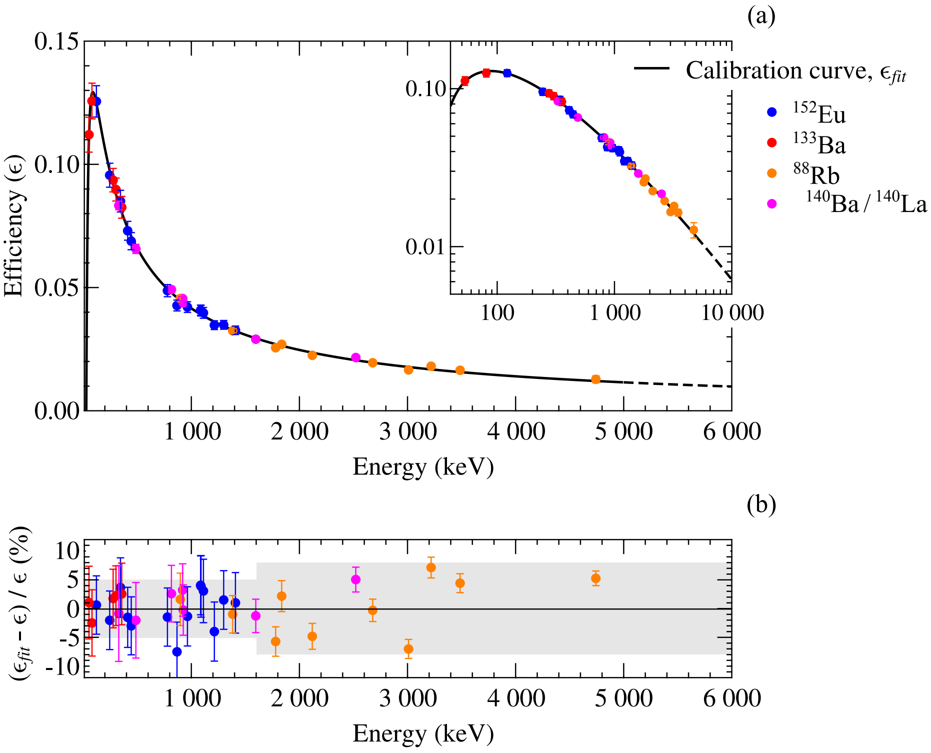

Figure II.9: Efficiency calibration of HPGe detectors from measurements in 2018. Calibration points were established in the energy range between 0.1 and 4.7 MeV. Differences between calibration points and values calculated using the function describing the calibration curve are also presented.

The accuracy of the efficiency calibration of HPGe detectors can be judged from deviations of calibration data from values calculated using the function describing the final calibration curve (see Figure II.9). From the observed spread of deviations, it can be concluded that the detection efficiency of γ rays with energies below 1.7 MeV is given with a relative uncertainty of around 5%. In the range between 1.7 and 5 MeV, the relative uncertainty is lower, not exceeding 8%. At higher energies, where no calibration points were available, at least 10% relative uncertainty should be considered. Similar quality of efficiency calibration of HPGe detectors was achieved in 2016 and 2018.

β-particle detection

In order to test the performance of the plastic detector, it was investigated how the number of counts in γ-ray spectra changes after imposing a $\beta\gamma$ coincidence condition. This was checked for the most intense γ rays emitted in β decays of various nuclei with different β-decay energies. Several data sets collected at different masses during the same experimental campaign were used, including those for less exotic indium isotopes, their daughter nuclei, and calibration sources. The observed change in the number of counts in the full-energy peak can be interpreted only as an apparent efficiency of β-particle detection. In order to evaluate absolute efficiencies, details of energy spectra of emitted β particles must be included in the considerations. Such information is available for only a few of the β decays for which data were collected.

Figure II.10 shows ratios of numbers of counts in the β-gated and singles γ-ray spectra for the most intense γ rays emitted in the β decay of nuclei with decay energies between 1.0 and 14.1 MeV. Transitions following the βn-decay branch were considered for two indium isotopes, ^{133}In and ^{134}In. For these two nuclei, energy windows for βn emission are considered respectively. As shown in Figure II.10, data collected with standard radioactive sources do not provide a good reference for measurements of β particles emitted in decays of exotic nuclei with large β-decay energy windows.

The application of $\beta\gamma$ coincidence leads to a different reduction in the number of counts in the γ-ray spectrum, ranging from ~0.1% for ^{140}Ba to ~24% for ^{134}In. Considering the counting geometry and assuming a 100% intrinsic efficiency of the plastic detector, an absolute β-particle detection efficiency of around 25% can be expected. This suggests that almost all β particles emitted from the most neutron-rich nuclei were registered if they only entered the detector. Significantly lower apparent efficiency was found when analyzing γ rays emitted from ^{132}In with similar β-decay energy to heavier indium isotopes. Its most dominant β-decay path results in β particles with average energies similar to those emitted from ^{131}In, for which comparable apparent efficiency of β-particle detection was observed. Figure II.10 also shows apparent detection efficiencies with respect to the average energies of β particles emitted in decays. Only the most intensively populated states in daughter nuclei were considered. Information on average β-particle energies was taken, if available, from Ref. [82]. Particles emitted in β decays with the lowest average energies were registered with the lowest apparent efficiency because some of their fraction did not reach the plastic detector or was missed due to the detection threshold used.

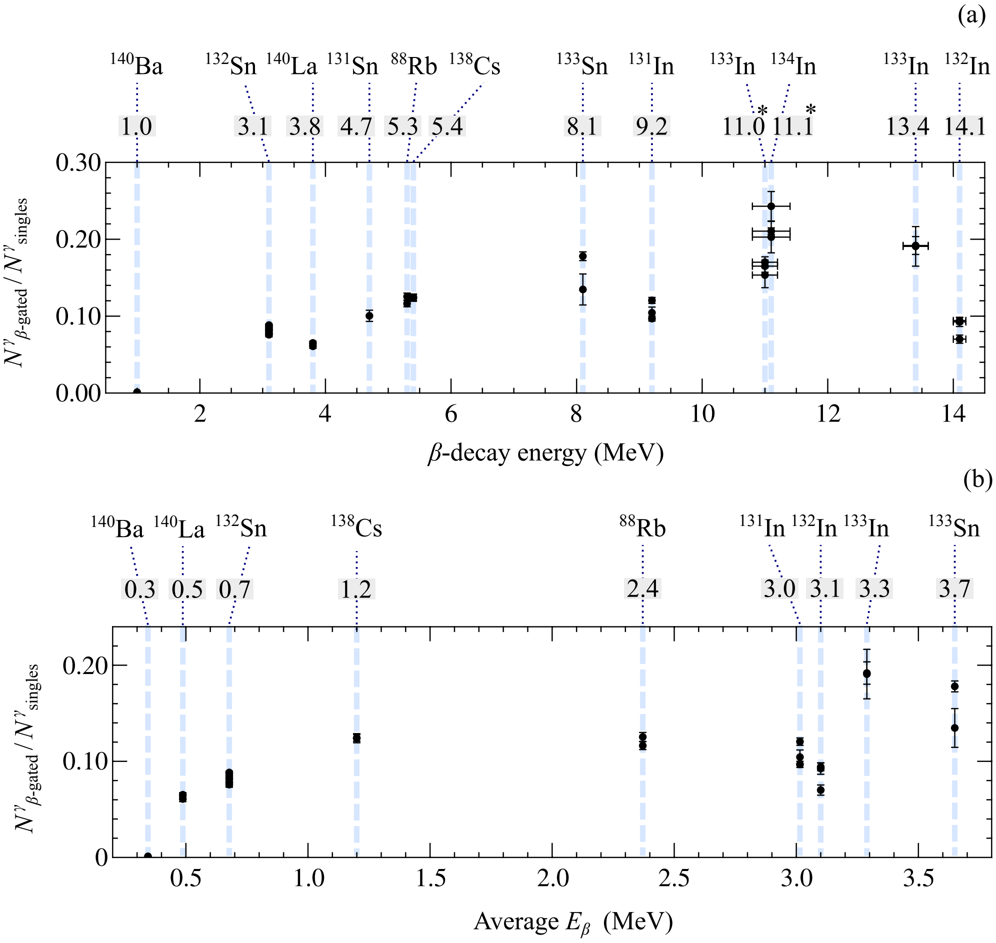

Figure II.10: Ratios of counts observed in the β-gated ($N^{\gamma}{}_{\beta\text{-gated}}$) and singles ($N^{\gamma}{}_{\text{singles}}$) γ-ray spectra for the most intense transitions emitted in various β decays. These ratios are presented with respect to (a) the β-decay energies taken from Ref. [16] and (b) the average energies of β particles (E_{β}) emitted in decays to the most intensely populated states in daughter nuclei, as stated in Ref. [82]. Asterisks indicate values corresponding to βn-decay energies.

CHAPTER

III

ANALYSIS AND RESULTS

1 β decay of ^{133}In

1.1 Background

1.1.1 Daughter nuclei

For the β-decay study of ^{133}In, a high-purity beam was obtained. In particular, it was free of isobaric contamination from readily surface-ionized cesium, the isotope of which is stable at mass $A = 133$. Figure III.1 shows the singles γ-ray spectrum acquired at mass $A = 133$. It presents data collected separately in narrowband and broadband modes of RILIS operation, using three different laser settings. Besides natural background lines, transitions that dominate this spectrum are associated with the ^{133}In implantation. However, most of them arise from β decays of daughter nuclei that produce a long-lived background hindering the β-decay study of the nucleus of interest. Figure III.2 shows the β-decay chain of ^{133}In, for which the half-life of 165(3) ms was reported as a weighted average from two experiments [84]. For its daughter nuclei, ^{133}Sn and ^{132}Sn, half-lives are one and two orders of magnitude longer, respectively.

The most intense lines in the singles γ-ray spectrum correspond to transitions in ^{132}Sb. These originate from the β decay of ^{132}Sn, being the daughter nucleus produced following βn emission from ^{133}In. Transitions in ^{132}Sn are also visible in this spectrum as strong lines. The 1561-keV γ ray in ^{133}Sn, which was reported to be the most intense transition observed in the $\beta\gamma$-decay branch of ^{133}In [19, 33], appears as a relatively weak line. It is enhanced in the spectrum when the $\beta\gamma$ coincidence requirement is applied. Figure III.1 displays the resulting β-gated γ-ray spectrum.

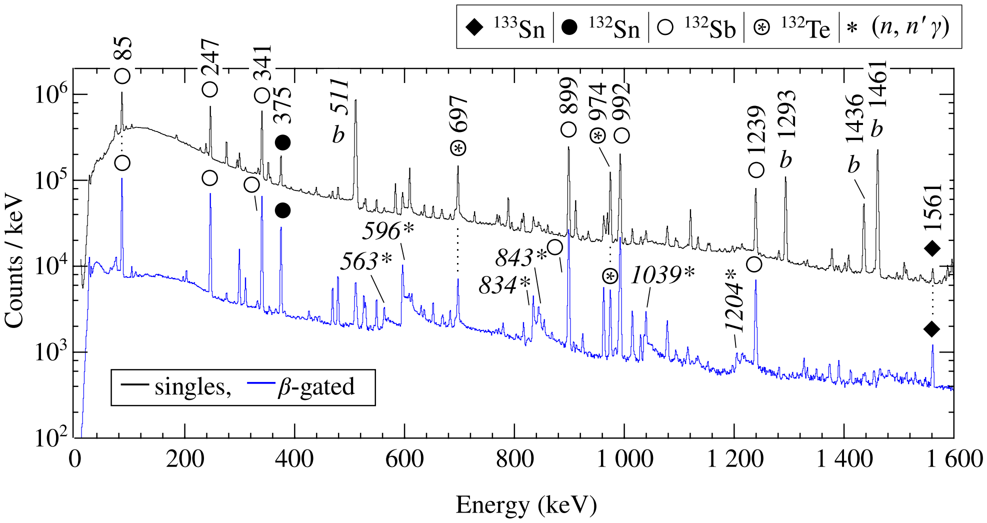

Figure III.1: Comparison of the singles (upper black curve) and β-gated (lower blue curve) γ-ray spectra obtained at mass $A = 133$ with three different RILIS settings. Transitions following the β decay of ^{133}In are indicated with filled symbols, while those arising from β decays of its daughter nuclei are indicated with open symbols. The most intense background lines are labeled with “b”. Neutron-induced peaks [85–90] are indicated with asterisks.

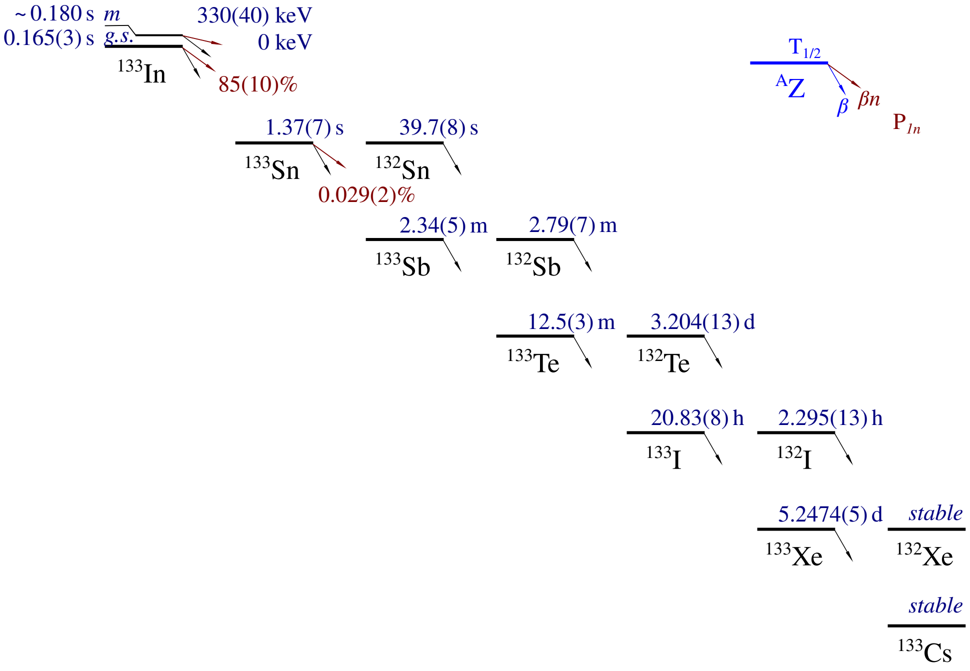

Figure III.2: Schematic drawing showing different time scales of the half-lives of nuclei produced in the ^{133}In β-decay chain. For readability, isomeric states known in some nuclei have been omitted. All data presented were taken from Refs. [29, 84], also for the parent nucleus (status prior to the publication of the results from this thesis).

1.1.2 Induced by neutrons

Fast neutrons emitted in the β decay

Gating on β particles revealed broad, triangular-shaped peaks in the γ-ray spectrum (see Figure III.1). The most prominent ones are at 596, 834, and 1039 keV. They arise from inelastic neutron scattering reactions in stable germanium isotopes inside the HPGe detectors [85–90]. Fast neutrons interacting with detector material were emitted from ^{133}In as β-delayed particles. The characteristic shape of the resulting peaks is due to the recoil of the atom in the scattering process. Recoil energy was additionally deposited in the HPGe detector, giving rise to a long-high-energy tail (see Figure III.1). Interactions of neutrons not only with detector material but also with surrounding elements should be considered. Identification of the resulting neutron-induced activity is generally not an issue because these interactions involve stable nuclei for which comprehensive experimental information is available.

Given that the nucleus under study is a strong neutron emitter, for which a P_n value of 85(10)% was previously reported [19, 33], the neutron-induced background appeared together with β-decay events and formed an inherent component of the γ-ray spectrum. Many background lines were identified based on several works investigating the fast-neutron-induced background under similar experimental conditions [85–88, 90]. Because this background was extensively described in Refs. [85–88, 90], the risk of the wrong assignment of neutron-induced transitions to the β decay under study appears to be low. Some strong lines arising from neutron interactions could hamper the identification of weaker transitions belonging to the β decay under study. For instance, two broad asymmetric peaks at 834 and 843 keV hinder the identification of the known 854-keV γ ray in ^{133}Sn.

Neutrons from the target area

An additional source of neutron-induced background in the experiment needs to be understood before analyzing the β-decay data for indium isotopes. Neutrons contributing to the background activity also arose from the target area, where they were produced by the proton-to-neutron converter and were emitted in fission. The resulting neutrons – time-correlated with protons hitting the ISOLDE target – interacted with surrounding materials by neutron capture or elastic and inelastic scattering, depending on their energy. Activity arising from the decay of neutron-activated products gives rise mainly to the long-lived background.

Figure III.3 shows the time distribution of events relative to the proton pulse measured in the HPGe detectors. The peak visible in the first tens of ms is due to the interactions of neutrons from the target area. Imposing the $\beta\gamma$ coincidence condition leads to its significant suppression. Then, some of the background components are still present because no growth typical of the implantation phase is seen in the first tens of ms. Neutron-induced activity from the target area was identified from the γ-ray spectrum in which a restrictive time gate was applied.

Figure III.4 displays the high-energy part of the γ-ray spectrum built by imposing a gate on the first 10 ms following the proton pulse. It shows background lines originating from thermal-neutron capture in iron. This background can be eliminated by considering events recorded only in a delayed period, for instance, 30 ms after the proton pulse or later. However, due to the short β-decay half-life of ^{133}In, using a stringent time constraint may not be optimal because it also lowers the statistics for the nucleus of interest. In general, the background induced by neutrons from the target area does not pose a significant problem in the β-decay study. Identification of its components is a helpful reference in the analysis of data for neutron-rich indium isotopes emitting fast neutrons as β-delayed particles.

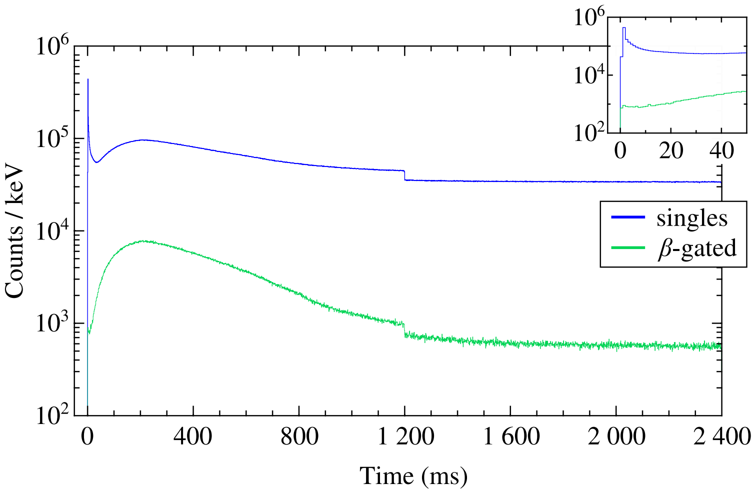

Figure III.3: Time distributions relative to the proton pulse of events recorded in the HPGe detectors at mass $A = 133$ with (green) and without (blue) $\beta\gamma$ coincidence requirement. Data collected with three different RILIS settings are presented together. The peak seen in the first 10 ms is due to the interactions of neutrons from the target area.

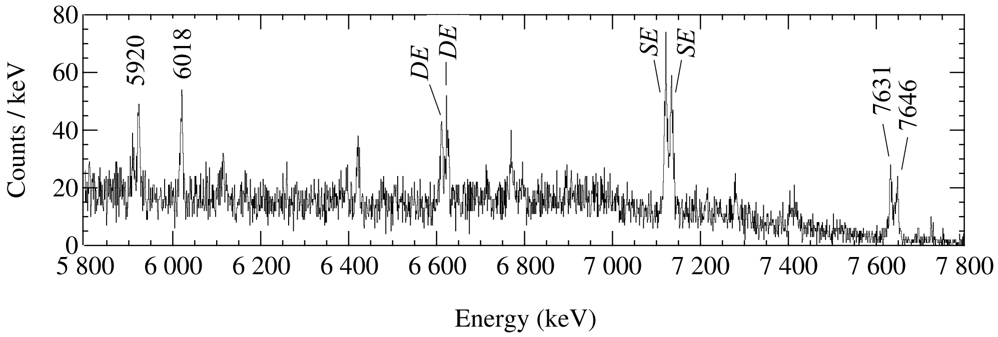

Figure III.4: The singles γ-ray spectrum obtained at mass $A = 133$ in the first 10 ms relative to the proton pulse. Lines originating from thermal-neutron capture in iron are labeled with energies in keV. The abbreviations *SE* and *DE* indicate single-escape and double-escape peaks, respectively.

1.2 Identification of γ rays following the decay

Transitions observed in a short time window after the proton pulse, of the order of hundreds of ms, can be associated with the ^{133}In β decay (see Figure III.2). Among them are lines corresponding to γ rays in daughter nuclei, ^{133}Sn and ^{132}Sn, and those resulting from inelastic scattering of fast neutrons emitted from the parent nucleus.

Transitions following the β decay of ^{133}In were identified based on the analysis of β-gated γ-ray spectra sorted with various conditions imposed on time relative to the proton pulse. If a time window matching two or three times the half-life of ^{133}In is used, the contribution from daughters' activities, with half-lives of 1.37(7) s for ^{133}Sn and 39.7(8) s for ^{132}Sn [29], is significantly reduced. The suppression effect is stronger when events recorded at later times are subtracted. The effectiveness of such an analysis method is shown in Figure III.5, which displays the β-gated γ-ray spectrum obtained in the first 500 ms after the proton pulse. The contribution of events recorded in the delayed interval, between 500 and 1000 ms, was subtracted from the presented data.

As shown in Figure III.5, selecting events recorded in a short period after the the proton pulse allows us to generate clean spectra of the ^{133}In β decay. If this time restriction is applied to the data collected in a narrowband mode of RILIS operation, with settings either for the ground state or isomer, unique transitions emitted in their β decays can be established. In the following sections, two β-decaying states of ^{133}In will be referred to using the notation ^{133g}In and ^{133m}In for the ground state and isomer, respectively.

The data collected at mass $A = 133$ provided new information about excited states in two daughter nuclei of ^{133}In, ^{133}Sn and ^{132}Sn. The structure of excited states populated in ^{132}Sn is beyond the scope of this thesis. Only the most intense transitions observed in the βn-decay branch are given when results are presented. Detailed γ-ray spectroscopy of ^{132}Sn from $\beta\gamma$ and βn decays of ^{132}In and ^{133}In, respectively, measured in the same experimental campaign was reported in Refs. [63, 74].

1.3 Observation of known γ rays following the decay

The quality of isomer selective ionization achieved for ^{133}In can be assessed based on γ rays reported from the first β-decay study of this nucleus [19, 33]. Previously, with a beam consisting of two β-decaying states of ^{133}In, a population of the $3/2^-$, $(9/2^-)$, and $5/2^-$ states in ^{133}Sn was observed. Transitions deexciting them were found as weak lines at 854 keV, 1561 keV, and 2005 keV, respectively [19, 33].

Figure III.6 displays portions of β-gated γ-ray spectra measured separately with different RILIS settings in narrowband mode. These spectra show relevant transitions in ^{133}Sn that were observed in the β decay of one of the states of ^{133}In.

An indication of the presence of the $(1/2^-)$ isomer in the beam is the detection of the 854-keV γ ray emitted from the $3/2^-$ state in ^{133}Sn. The 1561-keV line corresponding to the depopulation of the $(9/2^-)$ level in this nucleus is the signature of the $(9/2^+)$ ground-state content in the beam. Identification of the 513-keV γ ray deexciting the $1/2^-$ state in ^{133}Sn is hindered by a more intense 511-keV peak. The 513-keV line was found in the β-gated γ-ray spectrum in coincidence with the 854-keV transition (see Figure III.7). The 2005-keV γ ray, which was reported as deexciting the $5/2^-$ state in ^{133}Sn following the ^{133}In β decay, is not evident in the spectra acquired at $A = 133$ with any RILIS setting. Two transitions attributed tentatively to ^{133}Sn in the previous β-decay study of ^{133}In, 354 keV and 802 keV [19, 33], are also not observed.

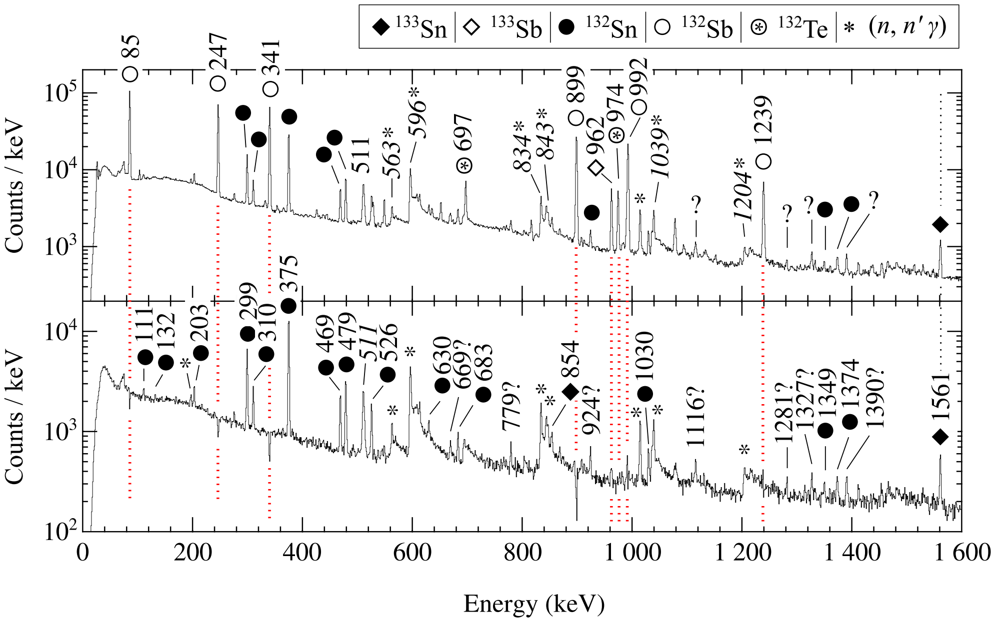

Figure III.5: Comparison of the β-gated γ-ray spectra obtained at mass $A = 133$ without (upper panel) and with (lower panel) an additional condition on time with respect to the proton pulse. The spectrum shown in the lower panel was sorted with a gate on 10-500 ms and subtraction of the background recorded between 500 and 990 ms. The presence of negative peaks is the consequence of subtracting the contribution from daughter nuclei. The presented data were collected separately with three RILIS settings, in narrowband and broadband. Transitions following the β decay of ^{133}In are indicated with filled symbols, while those arising from β decays of its daughter nuclei are indicated with open symbols. The strongest lines that are eliminated once the time gate is applied are indicated in red. Transitions labeled with a question mark remain unassigned.

A weak peak at 1561 keV in the γ-ray spectrum acquired with RILIS settings for ^{133m}In is due to the impurity of the isomeric beam (see the lower panel of Figure III.6). In order to evaluate the content of this admixture, count rates in the 1561-keV peak observed under different conditions can be compared.

The count rate of 0.14(3)/min was obtained with RILIS settings for ^{133m}In, while 1.6(1)/min were recorded with RILIS settings for ^{133g}In. For comparison, the count rate of 2.40(8)/min was registered during the measurement with RILIS in broadband mode. These frequencies are given as the average rates, estimated from the β-gated γ-ray spectra without accounting for the γ-ray and β-particle efficiencies (i.e., extracted as peak areas). The experimental conditions, such as the proton current on the target, varied slightly during the measurements. This could affect the count rates observed with different RILIS settings.

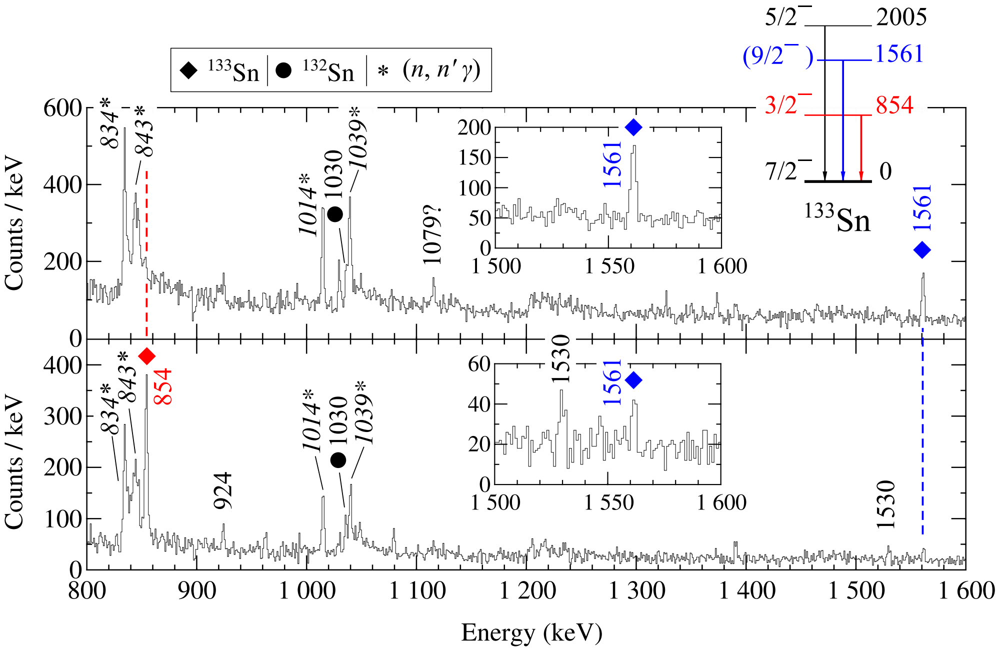

Figure III.6: Portions of the β-gated γ-ray spectra obtained at $A = 133$ with RILIS settings for ^{133g}In (upper panel) and for ^{133m}In (lower panel), time-correlated with the proton pulse. A time window of 10-500 ms was used, and long-lived background was subtracted. The 854-keV and 1561-keV γ rays in ^{133}Sn, which are emitted as unique transitions in the β decay of the $(9/2^+)$ ground state and $(1/2^-)$ isomer, respectively, are indicated. The presented level scheme includes states in ^{133}Sn that were observed in the previous β-decay study of ^{133}In [19, 33].

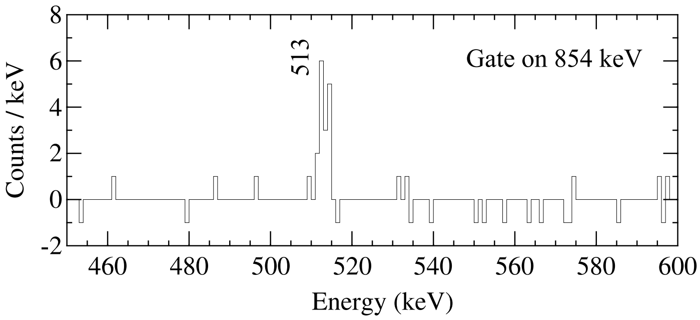

Figure III.7: The background-subtracted β-gated γ-ray spectrum in coincidence with the 854-keV transition in ^{133}Sn observed in the $\beta\gamma$ decay of ^{133m}In.

In the γ-ray spectrum collected with RILIS settings for ^{133g}In, identification of a peak arising from the isomer presence in the beam is hindered by a complex neutron-induced background at 834 and 843 keV. A weak line can be recognized at 854 keV, but a reliable estimation of its intensity to deduce admixture content is impeded (see Figure III.6). Coincidence relations indicative of a population of the $1/2^-$ state in ^{133}Sn were not found, suggesting that possible isomer content in the ^{133g}In beam may be negligibly small.

Although isomeric purity cannot be guaranteed for samples of ions implanted when the RILIS was operated in narrowband mode, an indication of the β-decaying state of ^{133}In to which a given transition belongs is well grounded. Assignment can be made by comparing relative γ-ray intensities, which were significantly influenced when RILIS was set to provide ^{133g}In versus ^{133m}In. From the comparison of spectra measured with different RILIS settings (see Figures III.6 and III.8), transitions belonging to the β decay of ^{133g}In and ^{133m}In were identified. These transitions are summarized in Table III.1.

1.4 Decay schemes

1.4.1 Ground state

Figure III.9 shows the β-decay scheme of ^{133g}In established using the $\beta\gamma$ and $\beta\gamma\gamma$ coincidence data. Among the known levels in ^{133}Sn, only the 1561-keV $(9/2^-)$ and 3564-keV $(11/2^-)$ states are fed by the ^{133g}In β decay. In comparison to the previous β-decay study of ^{133}In, four new transitions were assigned to the $\beta\gamma$-decay branch of this nucleus: 3181, 3564, 4110, and 6088 keV. Three of them, 3181, 4110, and 6088 keV, deexcite newly identified states in ^{133}Sn. For the known $(11/2^-)$ state in ^{133}Sn, improved accuracy of its excitation energy is provided, 3563.9(5) keV. All new γ rays attributed to the ^{133g}In $\beta\gamma$-decay branch depopulate levels above S_n of ^{133}Sn, 2398.7(27) keV [16].

Given the lack of $\gamma\gamma$ and $\beta\gamma\gamma$ coincidence relations for the 3181-, 4110-, and 6088-keV transitions, their alternative assignment to the daughter nucleus populated in the βn-decay branch of ^{133g}In cannot be supported. A γ ray that does not belong to any $\gamma\gamma$ cascade cannot be placed in the level scheme of ^{132}Sn below the excitation energy of 4041 keV, which corresponds to the energy of the first excited state in this nucleus. Therefore, the 3181- and 3564-keV transitions were assigned to ^{133}Sn. For the 4110-keV γ ray, with only slightly higher energy than the energy of the 2^+ state in ^{132}Sn, the same justification can apply. Additional support for assigning the 4110-keV γ ray to the level scheme of ^{133}Sn arises from the β-decay data collected with the ^{134}In beam (see Section III 2.5). Transition with consistent energy was attributed to the ^{134}In β decay, indicating that the 4110-keV state in ^{133}Sn is fed by the $\beta\gamma$- and βn-decay branches of two indium isotopes. For transitions observed in the ^{133g}In β decay with energies higher than 4 MeV that do not have $\gamma\gamma$ coincidence relations, assignment to the βn-decay branch can also be considered implausible. For instance, the population of the 6-MeV level in ^{132}Sn that would decay directly to the 0^+ ground state, with no γ-ray decay branches to known, lower-lying levels, is unlikely.

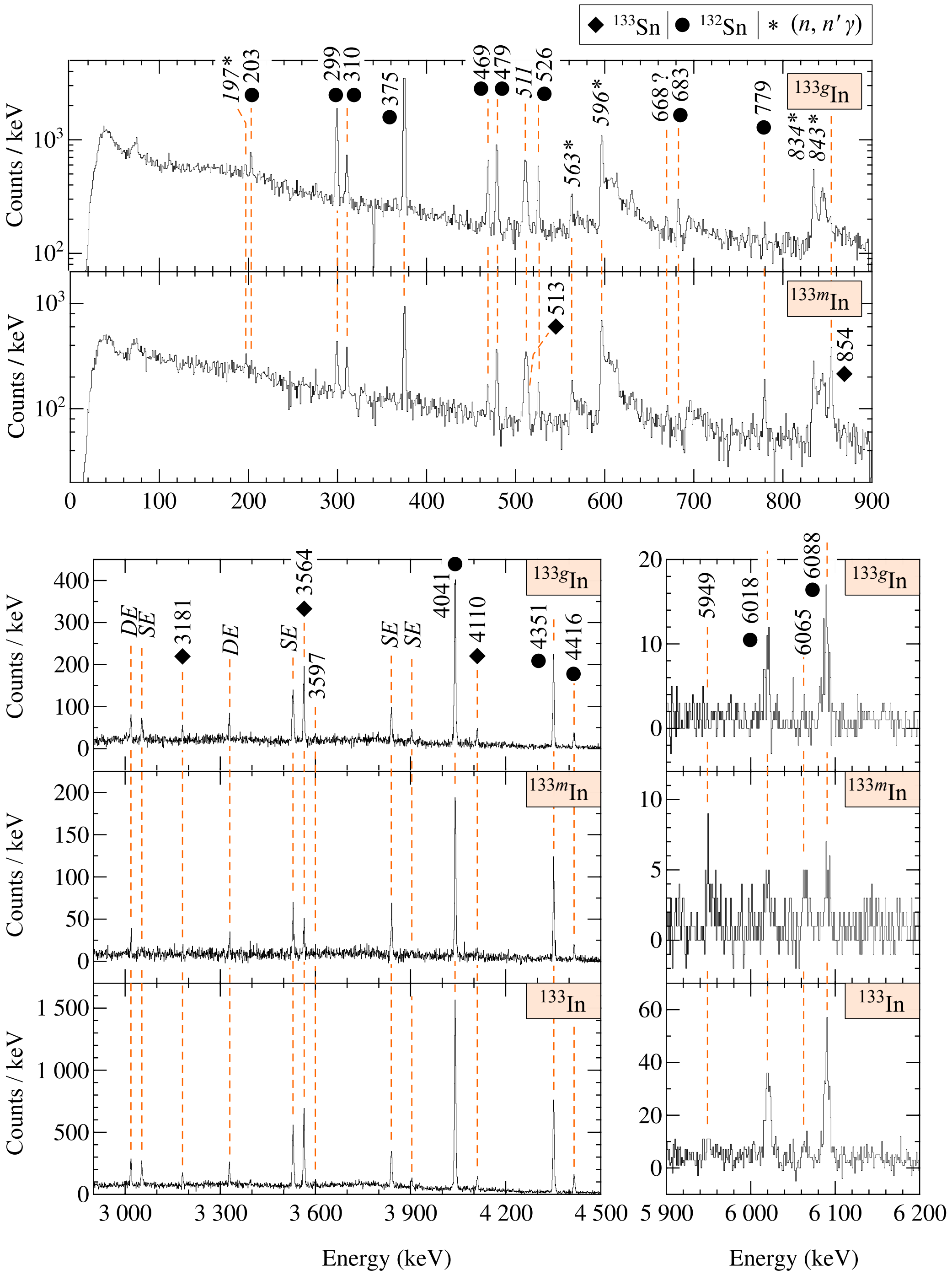

Figure III.8: Portions of the β-gated γ-ray spectra obtained separately at $A = 133$ with RILIS settings for ^{133g}In or ^{133m}In, time-correlated with the proton pulse. A time window of 10-500 ms was used, and long-lived background was subtracted. Portions of the spectrum sorted from all data collected for ^{133}In, both in narrowband and broadband modes, are shown in the high-energy range. To guide the eye, dashed lines indicate the labeled energies.

Table III.1: Energies and relative intensities of the transitions observed in the β decay of ^{133g}In and ^{133m}In. Total γ-ray and internal-conversion intensities are normalized to the intensity of the 4041-keV transition. For intensity per 100 decays of ^{133g}In and ^{133m}In, relative intensities should be multiplied by 0.049(5) and 0.043(5), respectively [74].

Decay branch	Daughter nucleus	Energy (keV)	Relative intensity	
			^{133g}In	^{133m}In
β	^{133}Sn	513(1)	[b]	[c]
β	^{133}Sn	854.3(5)	1.1(7)	33(2)
β	^{133}Sn	1561.2(5)	7.3(7)	3.0(7)
β	^{133}Sn	3181.1(5)	4.1(8)	1.8(8)
β	^{133}Sn	3563.9(5)	38(4)	14(2)
β	^{133}Sn	4110.3(5)	7(1)	4(1)
β	^{133}Sn	6018(2)	5.2(6)	4.5(7)
β	^{133}Sn	6088(2)	7.2(8)	4.3(8)
βn[a]	^{132}Sn	111.0(5)	2.5(3)[d]	2.5(9)[d]
βn	^{132}Sn	132.4(5)	3.9(8)[d]	[b]
βn	^{132}Sn	203.0(5)	5.7(5)[d]	2.9(5)[d]
βn	^{132}Sn	299.4(5)	28(2)[d]	13(1)[d]
βn	^{132}Sn	310.4(5)	7.9(6)	11.0(9)
βn	^{132}Sn	375.1(5)	77(4)[d]	43(2)[d]
βn	^{132}Sn	469.0(5)	12.8(9)	5.8(7)
βn	^{132}Sn	478.9(5)	19(1)	18(1)
βn	^{132}Sn	526.0(5)	10.5(9)	6.9(7)
βn	^{132}Sn	630.1(5)	< 3	< 3
βn	^{132}Sn	683.1(5)	5.6(5)	1.7(7)
βn[a]	^{132}Sn	779.4(5)	1.4(5)	8(1)
βn	^{132}Sn	913.1(5)	1.6(3)	[b]
βn[a]	^{132}Sn	924.1(5)	4.0(6)	5(1)
βn	^{132}Sn	1029.8(5)	3.9(8)	2.4(7)
βn	^{132}Sn	1035.8(5)	3.5(5)	6(1)
βn[a]	^{132}Sn	1281.4(8)	1.2(5)	[b]
βn	^{132}Sn	1349.6(5)	1.3(4)	1.0(7)
βn	^{132}Sn	1373.9(5)	2.3(5)	1.9(4)
βn[a]	^{132}Sn	1390.6(5)	2.3(5)	4.7(7)
βn	^{132}Sn	4041.1(5)	100(11)	100(11)
βn	^{132}Sn	4351.5(5)	54(6)	69(8)
βn	^{132}Sn	4416.2(5)	10(1)	8(1)
βn[a]	^{132}Sn	5132(1)	1.8(5)	6(1)

Unassigned transitions

Energy (keV)	Relative intensity		Energy (keV)	Relative intensity	
	^{133g}In	^{133m}In		^{133g}In	^{133m}In
669.5(5)	3.0(7)	8(1)	3597(1)	3.5(9)	[b]
1115.6(5)	2.1(5)	3.0(5)	5437(1)	[b]	9(1)
1327.3(5)	2.3(5)	1.9(5)	5949(2)	[b]	7.7(9)
1529.9(5)	1.3(3)	2.9(9)	6065(2)	[b]	5.5(8)
1649.5(5)	1.7(7)	6(1)			

Continuation of Table III.1

[a] Assignment to this branch from Refs. [63, 74]

[b] Line not observed.

[c] Seen only in coincidence with the 854-keV transition.

[d] Relative intensities were corrected for internal conversion $\alpha_{\mathrm{tot}}^{\sigma L}$ assuming σL character:

$\alpha_{\mathrm{tot}}^{M1}$(111 keV)= 0.414(6),
$\alpha_{\mathrm{tot}}^{E2}$(132 keV)= 0.589(9),
$\alpha_{\mathrm{tot}}^{M1}$(203 keV)= 0.0797(12),
$\alpha_{\mathrm{tot}}^{E2}$(299 keV)= 0.0356(5), and
$\alpha_{\mathrm{tot}}^{E2}$(375 keV)= 0.01739(25).
Values taken from Ref. [91].

A new level at 6018 keV in ^{133}Sn is proposed tentatively. Identification of the 6018-keV line as a transition belonging to ^{133g}In is uncertain because a peak arising from the neutron-induced background may appear at the same energy (see Figures III.4 and III.8).

The β decay of ^{133g}In is dominated by βn emission. The 4041-keV γ ray deexciting the 2^+ state in ^{132}Sn was found to be the strongest transition. The population of states up to an excitation energy of 5790 keV is observed in this daughter nucleus. Based on $\beta\gamma\gamma$ coincidences with previously known transitions, several new γ rays were assigned to ^{132}Sn. More information on states observed in the βn-decay branch of ^{133g}In is provided in Refs. [63, 74].

In order to determine the ^{133g}In β-decay half-life, three of the most intense transitions were considered: two from the βn-decay branch, 375- and 4041-keV γ rays in ^{133}Sn, and one from the $\beta\gamma$-decay branch, the 3564-keV γ ray in ^{133}Sn. Their time distributions relative to the proton pulse were constructed from $\beta\gamma$ coincidence events. The contribution from the background area of a peak on which gate was applied to create time projection was subtracted. Figure III.10 displays the decay curves of these three transitions. A function composed of a single exponential component was fitted in the time range between 200 and 1200 ms. The weighted average of 162(2) ms from the results obtained for individual transitions was adopted as the ^{133g}In half-life. This value is consistent with two recent results, 165(3) ms [27] and 163(7) ms [28].

Several other transitions were observed in the ^{133g}In β decay that could not be assigned to any daughter nucleus. Analysis of the $\beta\gamma\gamma$ and $\gamma\gamma$ matrices did not reveal any coincidence relations for them. These unassigned γ rays are listed in Table III.1.

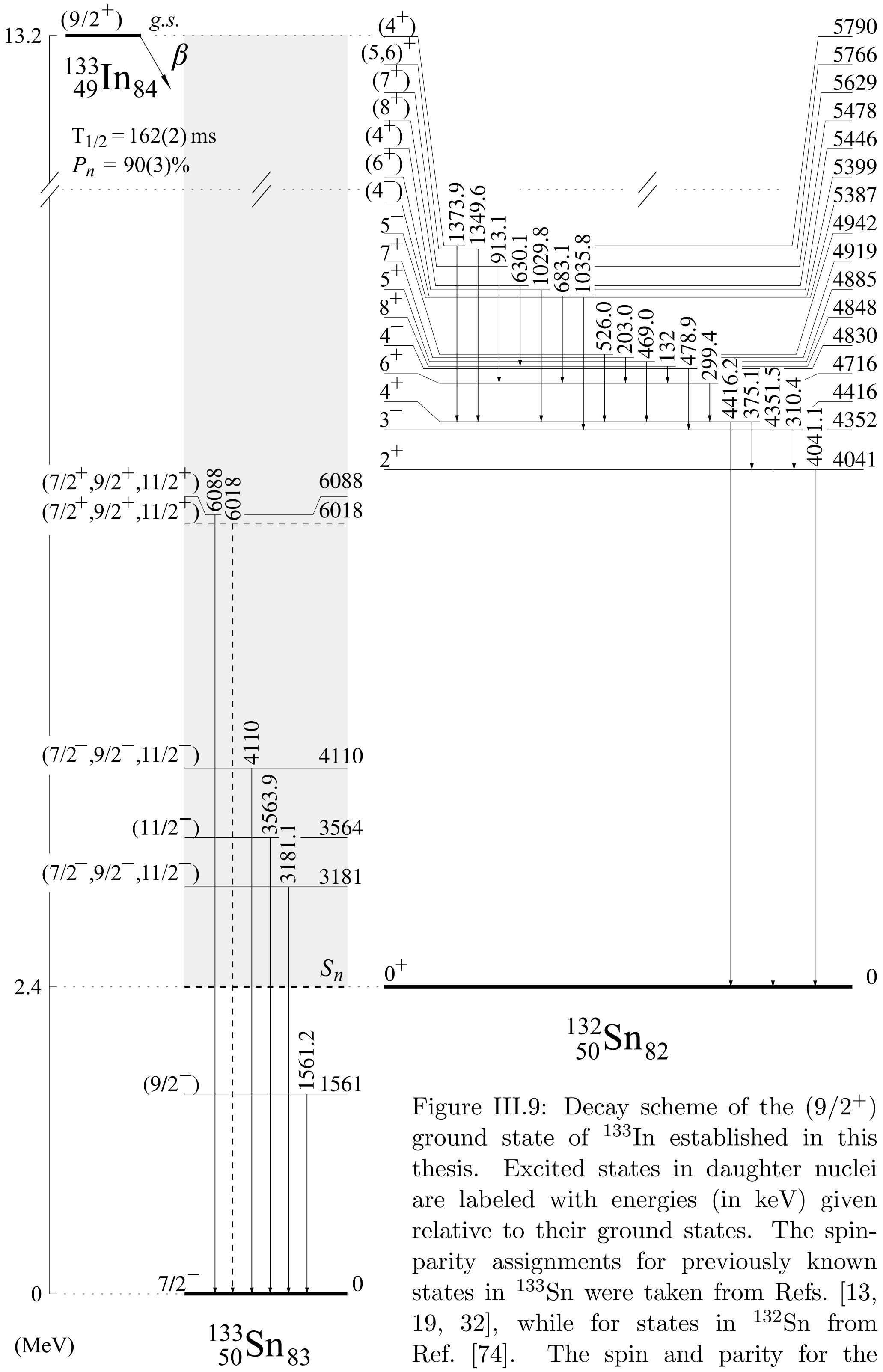

Figure III.9: Decay scheme of the $(9/2^+)$ ground state of ^{133}In established in this thesis. Excited states in daughter nuclei are labeled with energies (in keV) given relative to their ground states. The spin-parity assignments for previously known states in ^{133}Sn were taken from Refs. [13, 19, 32], while for states in ^{132}Sn from Ref. [74]. The spin and parity for the parent nucleus are based on systematics [29]. The shaded regions represent energy windows for the population of neutron-unbound states. Note that there is an energy gap in the left vertical scale (in MeV). The Q_β and S_n values were taken from Ref. [16].

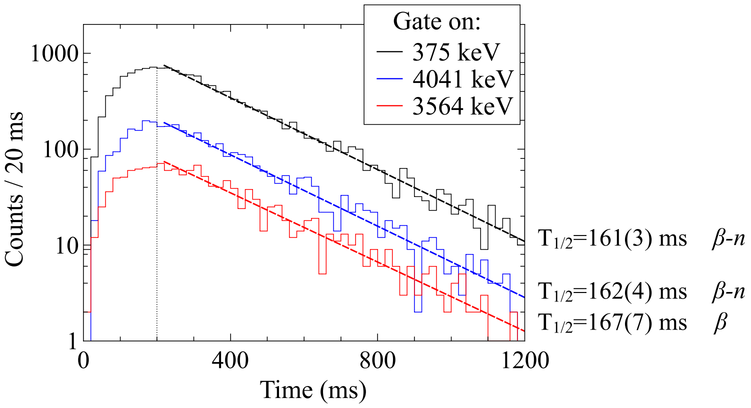

Figure III.10: Time distributions with respect to the proton pulse of the 375-, 4041-, and 3564-keV γ rays in coincidence with β particles observed in two β-decay branches of ^{133g}In. The vertical line indicates the end of the beam implantation. A function composed of an exponential decay was fitted in the range of 200-1200 ms.

1.4.2 Isomeric state

Figure III.11 displays the β-decay scheme of ^{133m}In established using the $\beta\gamma$ and $\beta\gamma\gamma$ coincidence data. Among the known levels in ^{133}Sn, only the $3/2^-$ and $1/2^-$ states were observed in the ^{133m}In β decay. Transitions deexciting them, 854 keV and 513 keV, form the $1/2^- \rightarrow 3/2^- \rightarrow 7/2^-_{g.s.}$ cascade that has not been observed to date in the β-decay study. An 802-keV γ ray tentatively attributed to the $1/2^-$ state in ^{133}Sn from the β decay of ^{133}In and ^{134}In [19, 33] was not confirmed in the present study.

Similar to the β decay of the ^{133}In ground state, the β decay of the isomer is dominated by βn emission. The 4041-keV γ ray deexciting the 2^+ state in ^{132}Sn is the most intense transition following this decay. Most of the γ rays assigned to this daughter nucleus from the ^{133g}In β decay were also identified in the ^{133m}In β decay. More information on states observed in the βn-decay branch of ^{133m}In is provided in Refs. [63, 74].

Only one transition that is unique to the ^{133m}In β decay can be used to determine the isomer half-life. Due to the impurity of the ^{133m}In beam, the contribution of the ground-state β decays to the intensity of strong lines corresponding to transitions in ^{132}Sn is possible. Therefore, γ rays that are not unique to the ^{133m}In β decay should not be used in the half-life analysis. Figure III.12 shows the time distribution of the 854-keV transition in coincidence with β particles. A half-life of 167(11) ms was obtained from a series of fits using differently generated time spectra for the 854-keV γ ray. Time projections were built by gating on the 854-keV peak and subtracting the contribution from the background area. This line

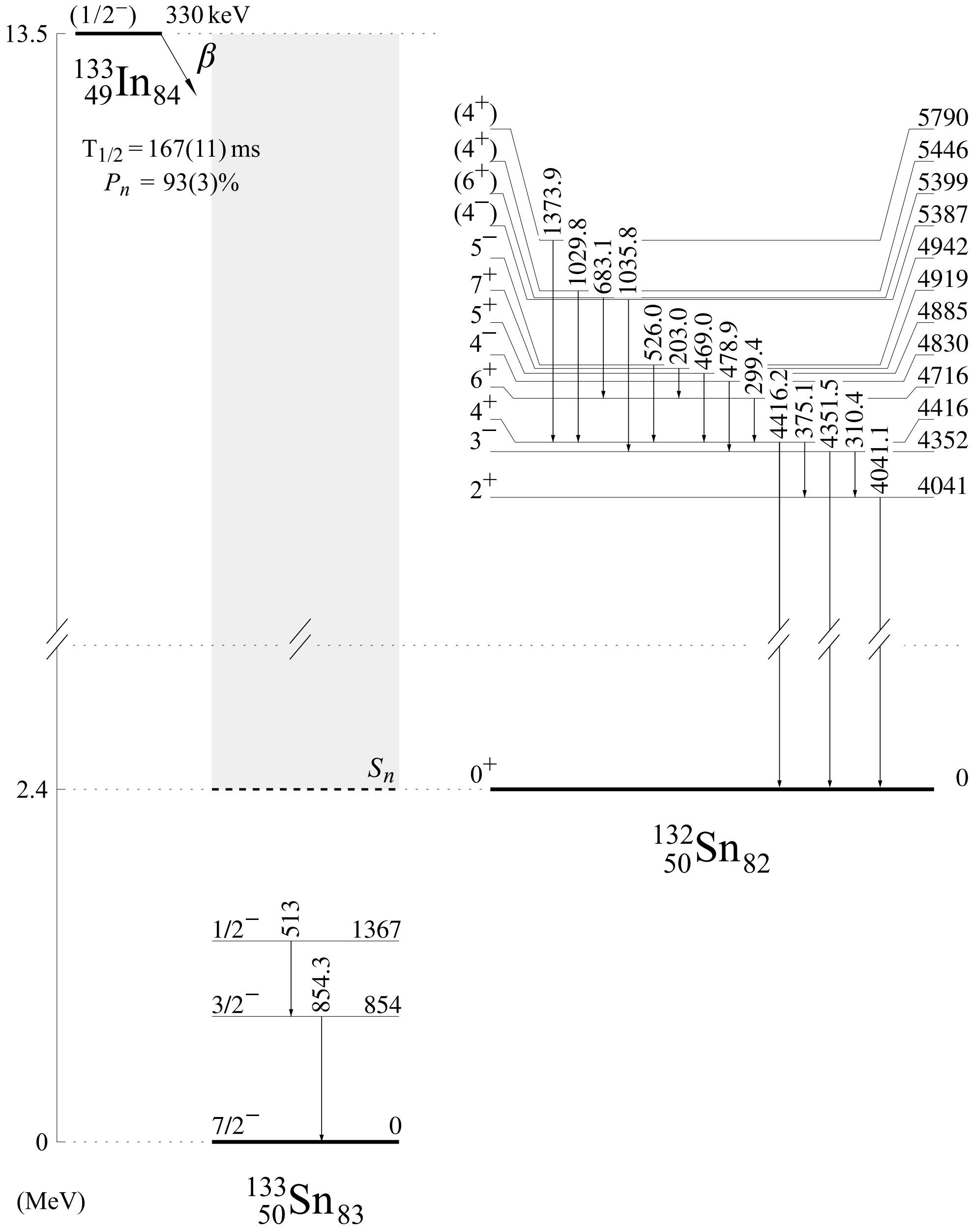

Figure III.11: Decay scheme of the (1/2⁻) isomer in ^{133}In established in this thesis. Excited states in the daughter nuclei are labeled with energies (in keV) given relative to the ground state of each tin isotope. Their spin-parity assignments were taken from Refs. [32, 74]. The spin and parity of the isomer are based on systematics [29]. The shaded regions represent energy windows for the population of neutron-unbound states. Note that there is an energy gap in the left vertical scale (in MeV). The Q_β and S_n values were taken from Ref. [16].

appears on triangular-shaped, neutron-induced peaks at 834 keV and 843 keV. Neutron inelastic scattering results in transitions having time characteristics like lines originating from the β decay under study. However, these background lines can also arise from the impurity in the ^{133m}In beam. The energy range that can be used for gating on the background area of the 854-keV peak is almost outside the energy range where two neutron-induced peaks extend. Thus, the subtracted background may not represent well the background component in the 854-keV peak.

Several new transitions were attributed to the ^{133m}In β decay, but there is no additional information that would allow to assign them to a particular daughter nucleus. In particular, no $\gamma\gamma$ coincidence relations were observed for them. These γ rays are listed in Table III.1. High-energy transitions observed only in the ^{133m}In β decay should be investigated as potential γ rays in ^{132}Sn. Contrary to the βn decay of the $(9/2^+)$ ^{133}In ground state, the βn decay of the $(1/2^-)$ isomer may populate states in ^{132}Sn that deexcite directly to the 0^+ ground state. Such states cannot be fed by the β decay of the lighter isotope ^{132}In with the (7^-) ground state.

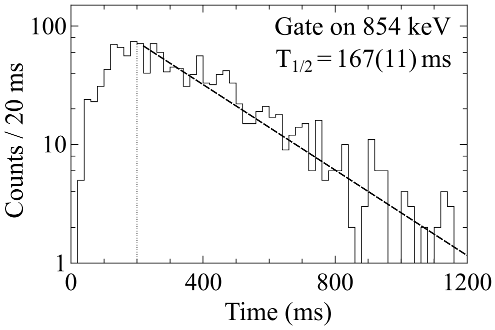

Figure III.12: Time distribution with respect to the proton pulse of the 854-keV γ rays in coincidence with β particles observed in the β decay of ^{133m}In. The vertical line indicates the end of implantation. A function composed of an exponential decay and a constant background was fitted in the range of 200-1200 ms.

1.5 *Relative transition intensities*

Most of the transitions assigned to the β decay of ^{133}In are not visible in the singles γ-ray spectrum, which is dominated by γ rays in daughter nuclei (see Figure III.1). In addition, some of the lines that can be recognized in this spectrum have broadened peaks, indicating a possible contribution of background lines to their intensities. For these reasons, the β-gated γ-ray spectrum was used to determine the intensities of transitions assigned to the ^{133}In β decay. For the strongest lines originating from two β-decay branches of ^{133}In, it was evaluated how the number of counts recorded in the spectrum changes when $\beta\gamma$ coincidence is required. Reduction factors of 0.29(2), 0.25(1), and 0.25(1) were obtained for the 1561-, 375-, and 4041-keV transitions, which are consistent with the expected performance of the β detector. Therefore, it was assumed that the ^{133}In β-decay events associated with the population of low-energy states in two daughter nuclei lead to similar energy deposits in this detector.

Intensities of transitions assigned to the ^{133}In β decay were determined as peak areas corrected for γ-ray detection efficiency and internal conversion. They were normalized with respect to the most intense 4041-keV transition. Two sets of relative intensities, extracted from spectra measured separately with RILIS settings for ^{133g}In and ^{133m}In, are shown in Table III.1.

Several lines attributed to the β decay under study were visible in spectra collected only with RILIS settings for ^{133m}In. This suggests that the isomer content in the ^{133g}In beam was negligibly small. In the case of the ^{133m}In beam, the presence of ground-state admixture is manifested in the spectra through known γ rays deexciting high-spin states, $(9/2^-)$ at 1561 keV and $(11/2^-)$ at 3564 keV, that cannot be populated in the β decay of the $(1/2^-)$ isomer. In the broadband mode of RILIS operation, the ratio of γ-ray detection-efficiency corrected counts in peaks at 1561 keV and 854 keV was found to be about 7. It is worth noting that intensity estimates for the 854-keV transition are hampered because this line is located in the energy range where two triangular-shaped background peaks appear.

For the set of intensities extracted from spectra collected with RILIS settings for ^{133m}In, a non-negligible contribution from the ground-state β decays must be taken into account. This is particularly important for the γ rays emitted in the strong βn-decay branch of the isomer – beam impurity can affect their intensities. In the $\beta\gamma$-decay branch, two β-decaying states of ^{133}In populate unique levels in ^{133}Sn. Therefore, intensities observed for γ rays deexciting them originate solely from the decay of one of the β-decaying states of ^{133}In.

1.6 βn-decay branching ratio

With known absolute intensities of transitions emitted in β decays of daughter nuclei of ^{133}In, ^{133}Sn and ^{132}Sn, it was possible to determine the βn-decay branching ratio for the parent nucleus using the γ-ray counting method [92]. The following transitions and their absolute intensities were used: the 962-keV γ ray in ^{133}Sb emitted in 12(2)% of ^{133}Sn β decays [93] and the 341-keV γ ray in ^{132}Sb emitted in 48.8(12)% of ^{132}Sn β decays (see Figure III.13).

For the 962-keV γ ray, the determination of the number of counts from the singles γ-ray spectrum is hindered by the complex background on which this peak occurs. Its energy and width are slightly higher than expected, indicating possible background contribution to the intensity of the line around 962 keV. The 2791- and 5149-keV transitions also following the ^{133}Sn β decay, reported with intensities about 50 and 30 times lower than the 962-keV γ ray [94], were not visible in the singles γ-ray spectrum. Firm identification of both 962- and 341-keV transitions was possible only in the spectrum of γ rays in coincidence with β particles. For this reason, transition intensities for the P_n calculation were extracted from the β-gated γ-ray spectrum. However, the consequent drawback of considering $\beta\gamma$ coincidences is that intensities determined from the β-gated γ-ray spectrum have to be corrected for β-particle detection efficiency.

Efficiency characteristics of the plastic detector used in the experiment are difficult to obtain for the β-decay study of the nucleus of interest with large β-decay energy. In order to estimate β-particle detection efficiency for events associated with the population of states in ^{133}Sb and ^{132}Sb deexciting via 962- and 341-keV γ rays, data collected in the same experimental campaign with ^{134}In and ^{132}In beams were utilized, respectively. Among daughter nuclei produced by β decays of these indium isotopes, ^{133}Sn and ^{132}Sn can be distinguished. The γ-ray intensity reduction after applying the $\beta\gamma$ coincidence requirement was evaluated for the 962- and 341-keV lines from spectra acquired at masses $A = 134$ and $A = 132$, respectively. The β-particle detection efficiency used in the P_n calculation for ^{133}In was taken as the ratio of counts for considered transitions in the β-gated and singles γ-ray spectra.

Transition intensities obtained from the β-gated γ-ray spectrum as peak areas corrected for γ-ray and β-particle detection efficiencies, as well as internal conversion, were further corrected for the missing activity due to the tape movement at the end of each PSB supercycle. The length and structure of the supercycle varied over measurements at mass $A = 133$, introducing changes in the tape movement frequency. Decays of daughter nuclei originating from implantation of ^{133}In ions at various stages of the supercycle were recorded in different periods. In particular, there was more time to capture the activity arising from protons hitting the ISOLDE target at the beginning than in the later phase of the supercycle, prior to the tape movement.

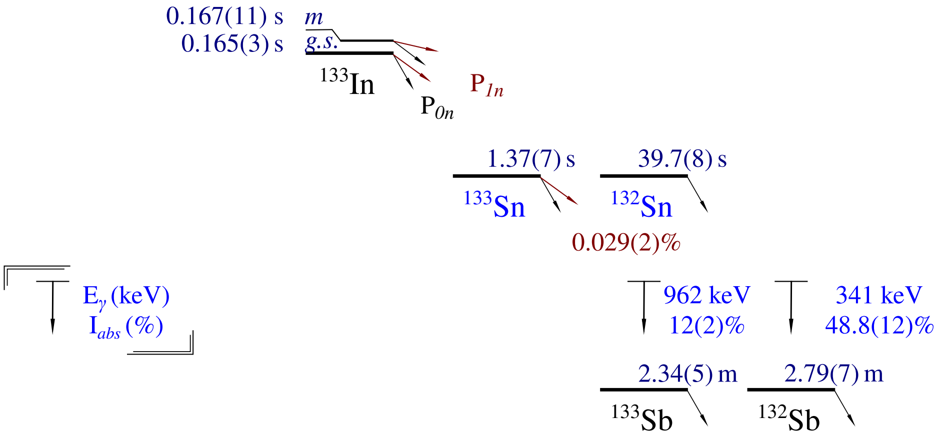

Figure III.13: Experimental information on β decays of daughter nuclei of ^{133}In, which was used to determine the βn-decay branching ratio for two states of the parent nucleus. Data taken from Refs. [93, 95], except for half-lives of two β-decaying states of ^{133}In.

An exemplary supercycle pattern is shown in Figure III.14. In the presented sequence, all nuclei produced in correlation with the first proton pulse had decayed before the tape moved, except for ^{132}Sn, for which only about 48% of all the decays had occurred in front of the HPGe detectors. In the case of nuclei correlated with the last proton pulse delivered to the ISOLDE target, about 80%, 10%, and 7% of all β decays of ^{134}In, ^{134}Sn, and ^{133}Sn, respectively, had occurred before the tape moved. From such a reconstruction of the supercycle, intensity corrections were deduced for the 962-keV and 341-keV transitions. On average, 91% and 25% of β decays of ^{133}Sn and ^{132}Sn occurred, respectively, before the tape was moved. Subsequently, after applying the abovementioned corrections to the intensities of the 962- and 341-keV transitions, the numbers of ^{133}Sn and ^{132}Sn nuclei produced in the β decay of ^{133}In were calculated. Finally, from the ratio of the number of daughter nuclei produced in the βn-decay branch to the total number of both daughter nuclei, the P_n values of 90(3)% and 93(3)% were deduced for ^{133g}In and ^{133m}In, respectively.

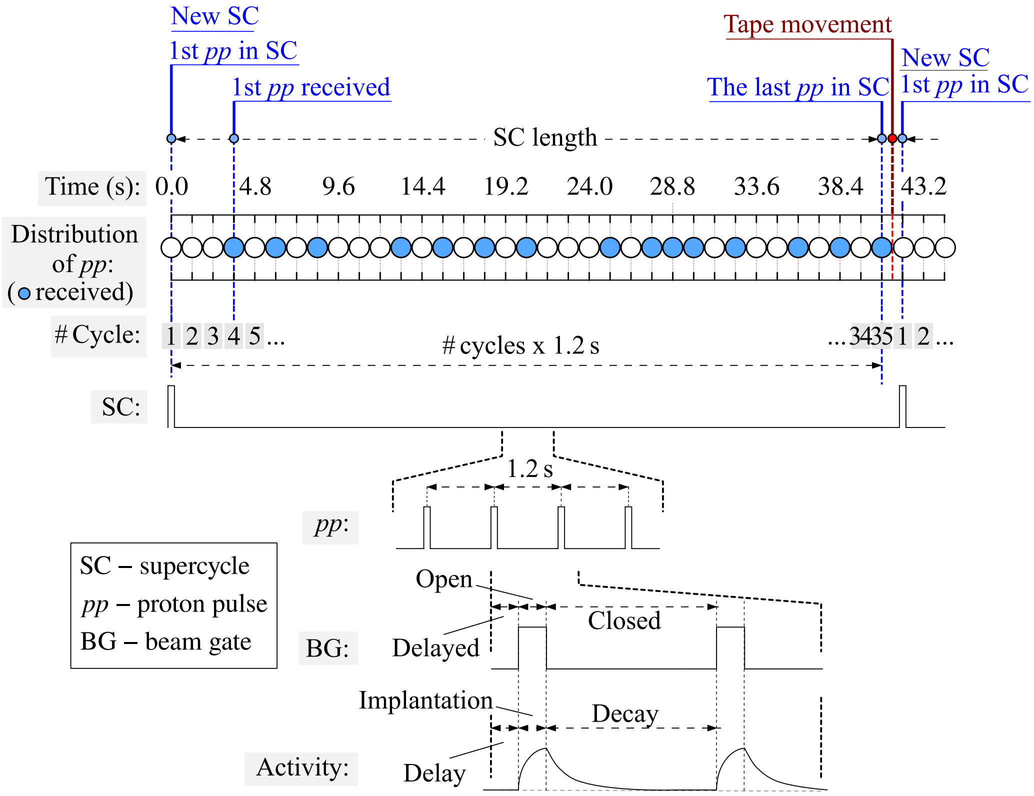

Figure III.14: Schematic representation of proton pulses grouped in a plan termed "supercycle", sequentially executed by the PSB. Elements relevant for operating tape movement in supercycle mode are highlighted.

2 β decay of ^{134}In

2.1 Contamination of the A=134 beam and background

In the beam at mass $A = 134$, surface-ionized ^{134}Cs appeared as an isobaric contamination. The most intense line in the singles γ-ray spectrum shown in Figure III.15 originates from the decay of the 139-keV isomeric state in ^{134}Cs with a half-life of 2.912(2) h [29]. With a decay pattern involving low-energy transitions, ^{134m}Cs does not cause a substantial background that could hinder the β-decay study of ^{134}In, even though the production yield of the nucleus of interest is a few orders of magnitude lower than that of the isobaric contaminant [96, 97].

As can be seen in Figure III.15, applying a gate on β particles leads to almost complete reduction of unwanted activity from ^{134}Cs and background. This condition is sufficient to generate a relatively clean γ-ray spectrum of the ^{134}In β decay, which is dominated by the 1561- and 962-keV γ rays in $\beta 1n$-decay daughter and granddaughter nuclei, ^{133}Sn [19, 33] and ^{132}Sb [93], respectively.

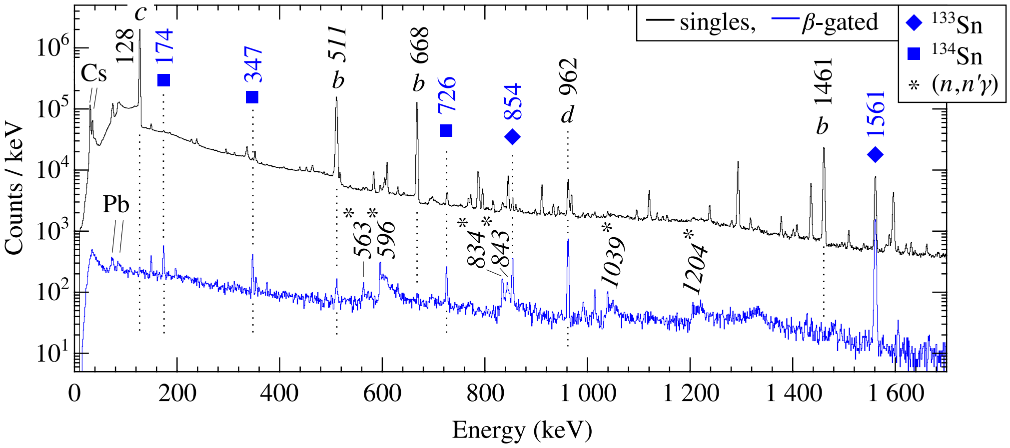

Figure III.15: Comparison of the singles (upper black curve) and β-gated (lower blue curve) γ-ray spectra obtained at mass $A = 134$ in 2018. The most intense transition in the singles γ-ray spectrum, the 128-keV line labeled with "*c*", belongs to isobaric contaminant ^{134m}Cs. The most intense background lines are indicated by "*b*". The most prominent lines in the β-gated γ-ray spectrum correspond to γ rays following the ^{134}In β decay. The peak marked with "*d*" originates from the β decay of the daughter nucleus ^{133}Sn. Wide triangular-shaped peaks arise from inelastic neutron scattering in the HPGe detectors [85–90].

Figure III.16 displays the time distributions of γ rays recorded in coincidence with β particles, which were acquired separately with two different tape movement modes. Both time spectra show a dominant short-lived decay component consistent with expectations for ^{134}In, for which the half-life of 136(4) ms was reported as a weighted average from three experiments [29]. Spectra measured with moving tape after each proton pulse have almost completely reduced background after 1.2 s. The peak visible at 1.7 s is due to a tape arrangement that brings the section on which the beam was previously implanted back into the detector area. In the measurements with tape movement following each supercycle, which ranged from 31.2 to 40.8 s, long-lived background originating from β decays of successive daughter nuclei was also recorded (see Figure III.17).

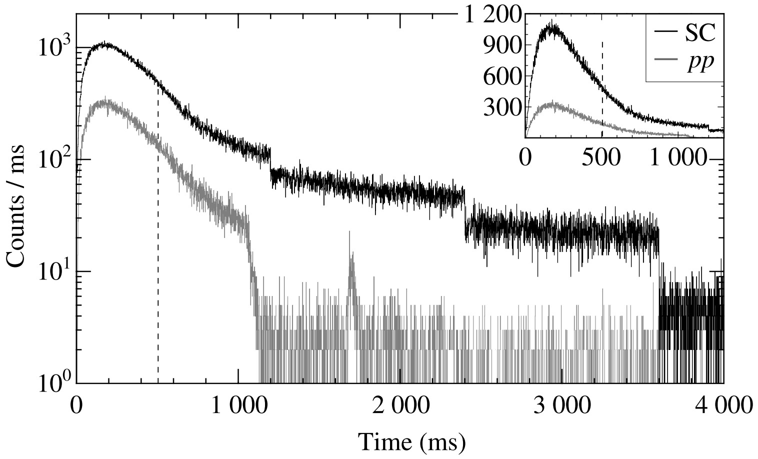

Figure III.16: Time distributions with respect to the proton pulse of the events recorded in HPGe detectors in coincidence with β particles, which were obtained separately at mass $A = 134$ in 2018 using different tape movement modes: after each supercycle (SC, black curve) or proton pulse (*pp*, gray curve). The vertical dashed line indicates the end of beam implantation after the proton pulse.

2.2 Comparison of the 2016 and 2018 data

Figure III.18 shows the singles and β-gated γ-ray spectra collected in the 2016 and 2018 measurements. From the intensity of the most prominent 1561-keV γ ray emitted in the ^{134}In β decay, it was estimated that roughly seven times more ^{134}In ions were implanted in 2018 than in 2016.

The integration of the two data sets to gain the statistics was not performed because some differences in the background lines were observed, in particular in the singles γ-ray spectra (see Figure III.18). These differences can be associated with the use of different mass separators, beam gate settings, and tape movement modes. Moreover, runs at mass $A = 134$ in 2016 and 2018 were preceded by implantation of different indium isotopes; hence, various long-lived activities may have been accumulated on the tape. For this reason, the primary data set presented in the thesis is that of 2018. Further on in this thesis, when the ^{134}In β-decay data are given without indicating the year, the results from the 2018 measurements are presented.

2.3 Observation of known γ rays following the decay

The most intense transitions observed in the previous β-decay study of ^{134}In, depopulating the 854-, 1561-, and 2005-keV states in the $\beta 1n$-decay daughter nucleus [19, 33], are confirmed in this thesis. In the singles γ-ray spectrum shown in Figure III.15, the corresponding peaks at 854, 1561, and 2004 keV appear as relatively weak lines. With the $\beta\gamma$ coincidence requirement, a significant enhancement of these lines with respect to the peaks originating from the beam impurities and background was achieved. As a result, the previously reported transitions in ^{133}Sn appear as the most intense lines. In particular, the 1561-keV line dominates the β-gated γ-ray spectrum.

Apart from γ rays that can be assigned to the ^{134}In β decay, gating on the β particles revealed wide, triangular-shaped peaks. These arise from inelastic scattering of fast neutrons [85–90] emitted from ^{134}In as β-delayed particles. This neutron-induced background was also observed in spectra measured with the ^{133}In beam (see Section III 1.1.2).

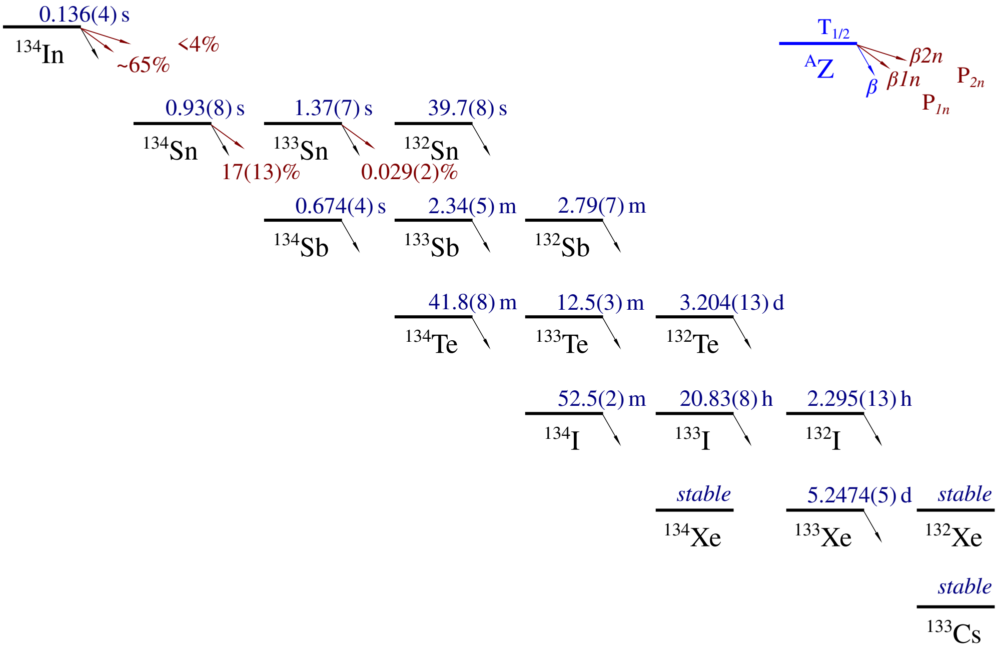

Figure III.17: Schematic drawing showing different time scales of the half-lives of nuclei produced in the ^{134}In β-decay chain. For readability, isomeric states known in some nuclei have been omitted. All data presented were taken from Ref. [29], also for the nucleus studied in this thesis (status shown prior to the publication of the results from this thesis).

The most intense transition observed in the β-gated γ-ray spectrum was used to determine the β-decay half-life of ^{134}In. For other relatively strong lines attributed to the ^{134}In β decay, the statistics was not adequate for detailed half-life analysis. Time distributions gated on the 1561-keV γ ray, which were acquired with two different beam gate settings, 200 or 500 ms for implantation, were analyzed. A shorter beam gate provides better conditions for the determination of the half-life of the order of a hundred ms. However, in the singles γ-ray spectrum collected with this setting, the number of counts in the 1561-keV peak is about ten times lower than in the spectrum acquired with the 500-ms beam gate. Therefore, data collected with both settings were considered in the half-life analysis.

Various fitting ranges as well as gates on the peak and background areas were tested, using γ-ray spectra with and without the $\beta\gamma$ coincidence requirement. Weighted average values for half-lives obtained from all the analyzed decay patterns were determined for the two beam gate settings. As a result, the ^{134}In half-life of 118(6) ms was deduced. The maximum uncertainty obtained in individual fits was taken as the uncertainty of the final value. Exemplary time distributions used in the half-life analysis are shown in Figure III.19. The determined half-life is consistent with the one measured recently at RIKEN, 126(7) ms [28], and slightly differs from the values previously reported in Ref. [19], 138(8) ms, and in Ref. [27], 141(5) ms.

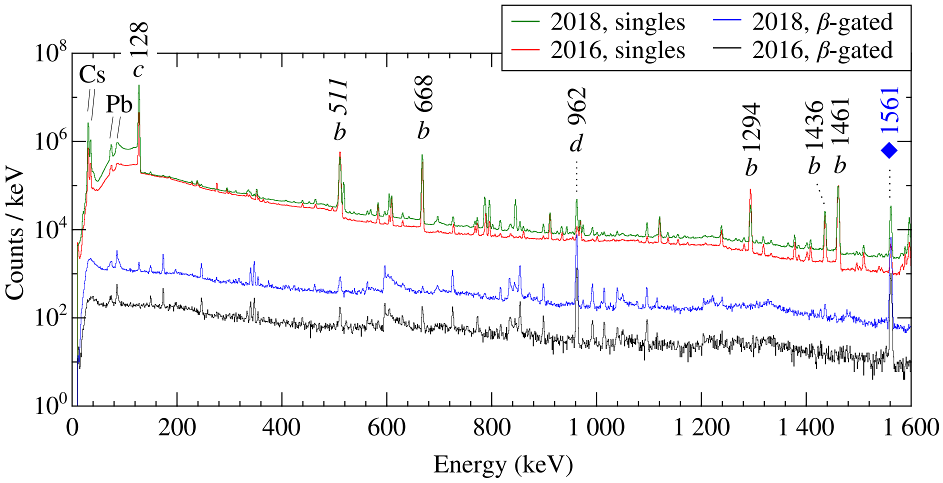

Figure III.18: Overview of the singles and β-gated γ-ray spectra obtained at mass $A = 134$ in the 2016 and 2018 measurements. The most intense transitions in the β-gated spectra, at 962 and 1561 keV, follow the ^{133}Sn and ^{134}In β decays, respectively. The most intense background lines are indicated by "*b*". The 128-keV peak labeled with "*c*", originates from the isobaric contaminant ^{134m}Cs.

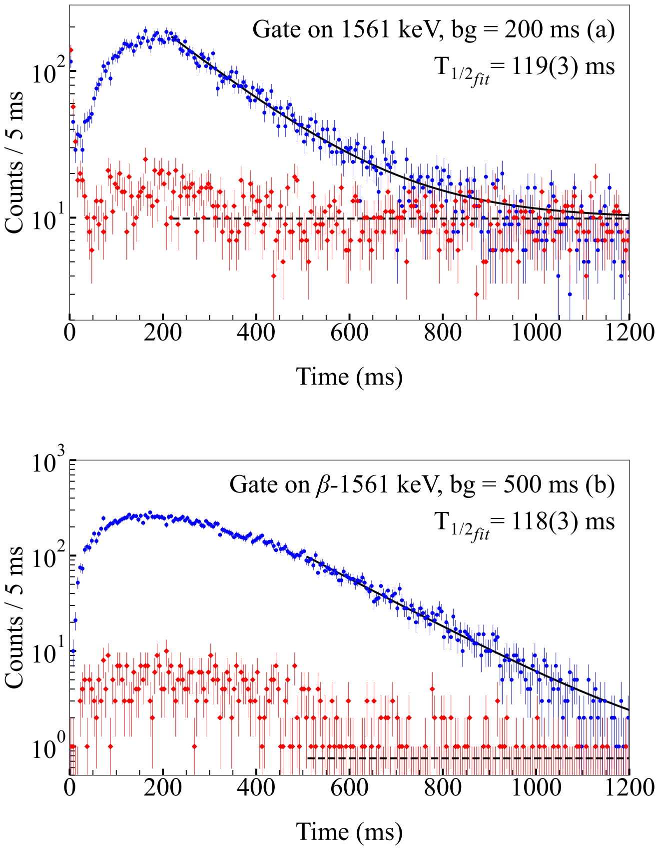

Figure III.19: Time distributions with respect to the proton pulse of the 1561-keV γ rays (blue circles) and the background area (red diamonds) recorded in the HPGe detectors: (a) with 200 ms beam gate and (b) in coincidence with β particles, with 500 ms beam gate. A function composed of an exponential decay and a constant background (solid line) was fitted in the range (a) 220-1200 ms and (b) 510-1200 ms, respectively. Background curves are also presented (dashed line).

2.4 Identification of γ rays following the decay

The possibility of correlating events with the proton pulse allows identification of other transitions emitted in the ^{134}In β decay. Figure III.17 shows schematically the subsequent β decays of the daughter nuclei produced in the β-decay chain of ^{134}In. Half-lives of successively produced nuclides are much longer than the ^{134}In half-life, so adequately chosen time gates allow transitions to be established that can be assigned to the β decay of the nucleus of interest, even if the obtained statistics do not allow their detailed half-life analysis.

Transitions following the β decay of ^{134}In were identified by comparing β-gated γ-ray spectra sorted using various conditions on the time of the event with respect to the proton pulse. Lines that can be attributed to γ rays in daughter nuclei are enhanced when this time window is limited to a few hundred ms.

Figure III.20 shows the β-gated γ-ray spectrum obtained at mass $A = 134$ during the first 400 ms following the proton pulse. Long-lived background recorded in the interval of 800-1200 ms after the proton pulse was subtracted from the data presented. With these conditions, neutron-induced lines are also enhanced because neutron interactions in the HPGe detectors follow the emission of β-delayed particles from ^{134}In.

2.5 New γ rays assigned to the $\beta 1n$-decay branch

The $\beta 1n$-decay branch of ^{134}In was expanded with three transitions depopulating states above S_n of ^{133}Sn, 2398.7(27) keV [16]. They are visible in Figure III.20 at 2434, 3563, and 4110 keV. Two new γ rays observed in the ^{134}In β decay, 3563 and 4110 keV, were also identified in the β-decay study of ^{133g}In, in which their energies were provided with better precision (see Section III 1.4.1). The 2434-keV transition was also seen in the β decay of more exotic ^{135}In (see Section III 3.4).

The 3563-keV line corresponds to the 3563.9(5)-keV γ ray depopulating the $(11/2^-)$ state in ^{133}Sn. The peak visible at 4110 keV can be associated with the 4110.3(5)-keV transition assigned to ^{133}Sn also from the ^{133g}In β-decay data. The absence of $\gamma\gamma$ coincidence relations hindered its attribution to a particular daughter nucleus of ^{133}In. However, after recent detailed γ-ray spectroscopy of ^{132}Sn, investigated in the β decay of ^{132}In [74, 98] as well as the βn decay of ^{133}In [74], it is highly unlikely that this transition belongs to ^{132}Sn. An observation of the 4110-keV line in β decays of both ^{133}In and ^{134}In provides support for its assignment to ^{133}Sn. No $\gamma\gamma$ coincidence relations were found in the ^{134}In β-decay data for the 3563- and 4110-keV transitions attributed to ^{133}Sn.

In the energy range corresponding to the predicted excitation energy of the $13/2^+$ state in ^{133}Sn, 2511(80) keV [34] or between 2360 and 2600 keV [99], one relatively intense transition was registered at 2434 keV (see Figure III.20). No $\beta\gamma\gamma$ and $\gamma\gamma$ coincidence relationships were observed for this line, making its attribution to either ^{134}Sn or ^{132}Sn unlikely and thus providing an argument for its assignment to ^{133}Sn. The 2792-keV transition, discussed in Ref. [32] as a possible candidate for γ-ray depopulating of the $13/2^+$ state in ^{133}Sn, was not observed in the β decay of ^{134}In.

Among the known low-lying levels in ^{133}Sn, only the $1/2^-$ state [17, 32, 37] was not seen in the ^{134}In β decay. The 354-keV transition that was identified in the previous β-decay study of ^{134}In but remained unassigned despite being registered in coincidence with β-delayed neutrons [19, 33], is confirmed in this thesis. No $\beta\gamma\gamma$ and $\gamma\gamma$ coincidence relations were found for this transition, making its attribution to any of the daughter nuclei impossible. The 802-keV transition, which was also reported to be in coincidence with neutrons emitted from ^{134}In [19, 33], was not seen in the spectra measured at mass $A = 134$.

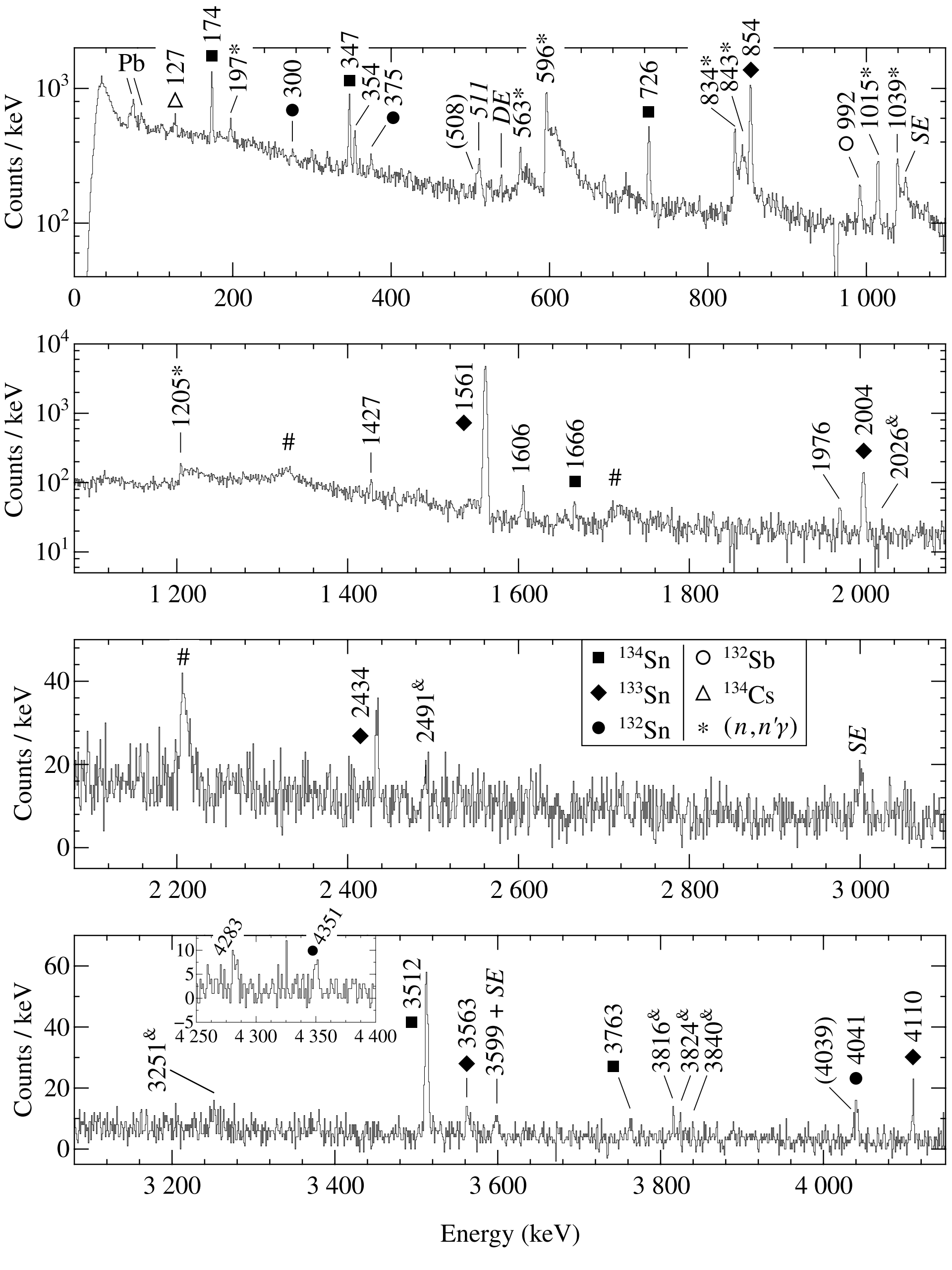

Figure III.20: The β-gated γ-ray spectrum obtained at mass $A = 134$ in the first 400 ms relative to the proton pulse from which long-lived background was subtracted. Transitions assigned to the daughter nuclei of ^{134}In are labeled with filled symbols, while those attributed to daughter or contaminant nuclei are marked with open symbols. Transitions that can be assigned to the ^{134}In β decay but not to a specific β-decay branch are indicated by energy only. Lines marked with an ampersand indicate possible weak transitions whose identification is uncertain. Energies of possible peaks, which might correspond to artifacts due to the background subtraction procedure, are given in parentheses. The presence of a negative peak at 962 keV is the consequence of subtracting the contribution from the daughter nucleus [93]. Neutron-induced peaks [85–90] are indicated with asterisks. The abbreviations *SE* and *DE* indicate single-escape and double-escape peaks, respectively. Broad peaks marked with a hash symbol remained unidentified.

2.6 *First observation of the $\beta\gamma$-decay branch*

The $\beta\gamma$-decay branch of ^{134}In, leading to the population of excited states in ^{134}Sn, was observed for the first time in this study. Figure III.20 shows the presence of the 174-, 347-, and 726-keV transitions that were assigned to ^{134}Sn from the ^{248}Cm fission data [20, 35]. These three γ rays are emitted in a cascade decay of an isomeric 6^+ state at 1247 keV for which the half-life of 86^{+8}_{-7} ns was previously reported [36]. Population of the (8^+) state in ^{134}Sn, decaying via the 1262-keV γ ray to the 6^+ state at 1247 keV [35], was not observed in the ^{134}In β decay.

Analysis of $\beta\gamma\gamma$ coincidences reveals three new transitions in ^{134}Sn. The 1666-, 3512-, and 3763-keV lines are seen in spectra of γ rays in coincidence with previously known transitions in this nucleus. Figure III.21 displays the γ-ray spectra in coincidence with the 1666-, 3512-, and 3763-keV transitions assigned to the daughter nucleus produced in the $\beta\gamma$-decay branch of ^{134}In. Two of them depopulate neutron-unbound states at excitation energies exceeding the S_n of ^{134}Sn, 3631(4) keV [16], by more than 1 MeV.

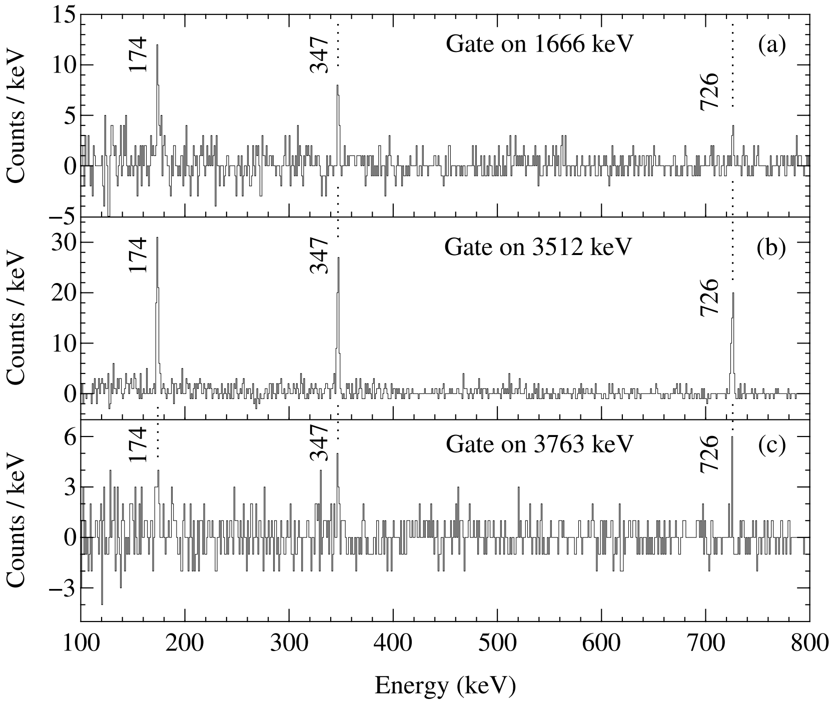

Figure III.21: Background-subtracted γ-ray spectra in coincidence with (a) 1666-, (b) 3512-, and (c) 3763-keV transitions that depopulate new levels in ^{134}Sn following the $\beta\gamma$ decay of ^{134}In. Vertical dotted lines indicate energies of previously known transitions in ^{134}Sn.

2.7 First observation of the $\beta 2n$-decay branch

The $\beta 2n$-decay branch of ^{134}In, leading to the population of states in ^{132}Sn, was observed for the first time. Transitions depopulating the 2^+, 3^-, 4^+, and 6^+ states in ^{132}Sn [100], with energies of 4041, 4351, 375, and 300 keV, respectively, were identified (see Figure III.20). Coincidence relationships observed for γ rays in the daughter nucleus produced in the $\beta 2n$-decay branch of ^{134}In are shown in Figure III.22. Observation of the 4041-keV transition in coincidences with the 300- and 375-keV γ rays constitutes clear evidence of the first observation of this exotic β-decay branch of ^{134}In.

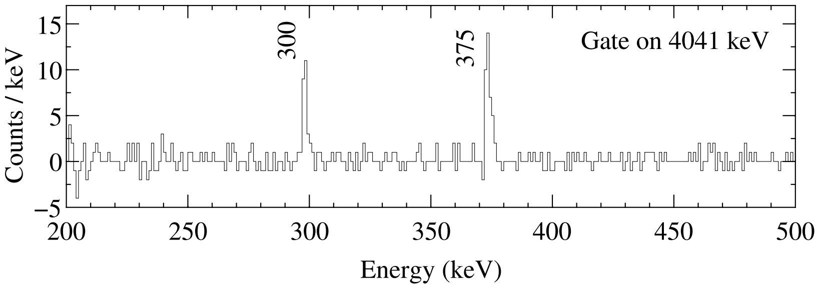

Figure III.22: Background-subtracted γ-ray spectrum in coincidence with the 4041-keV transition in ^{132}Sn observed in the $\beta 2n$ decay of ^{134}In.

2.8 Decay scheme

Transitions assigned to the $\beta\gamma$-, $\beta 1n$-, and $\beta 2n$-decay branches of ^{134}In are summarized in Table III.2. Several additional transitions were observed with a time pattern consistent with the ^{134}In β-decay half-life. However, due to the lack of $\beta\gamma\gamma$ and $\gamma\gamma$ coincidence relationships, they could not be assigned to a particular β-decay branch of the parent nucleus. These transitions are also listed in Table III.2. The β-decay scheme of ^{134}In established in this thesis is shown in Figure III.23. The previously reported scheme [19] is now complemented by the $\beta\gamma$- and $\beta 2n$-decay branches, with 13 new transitions assigned to this β decay. Neutron-unbound states decaying via γ rays were identified in two daughter nuclei, ^{134}Sn and ^{133}Sn.

It should be emphasized that presumably only a partial β-decay scheme is established in this thesis, because the β-decay energy of ^{134}In is large, $Q_\beta = 14.5\,\mathrm{MeV}$ [16], and the contribution of γ-ray deexcitation to the decay of neutron-unbound states in two daughter nuclei was found to be significant. High-energy transitions feeding from above low-lying states in tin isotopes can be missed by the HPGe detectors, introducing problems with reliable determination of β-decay feeding to states observed in the ^{134}In β decay. Such a scenario was confirmed in the ^{78}Ni region in the β-decay study of neutron-rich ^{83}Ga, which was performed with high-efficiency detectors allowing registration of γ rays up to energy of 11 MeV [101]. It was revealed that γ rays emitted from neutron-unbound

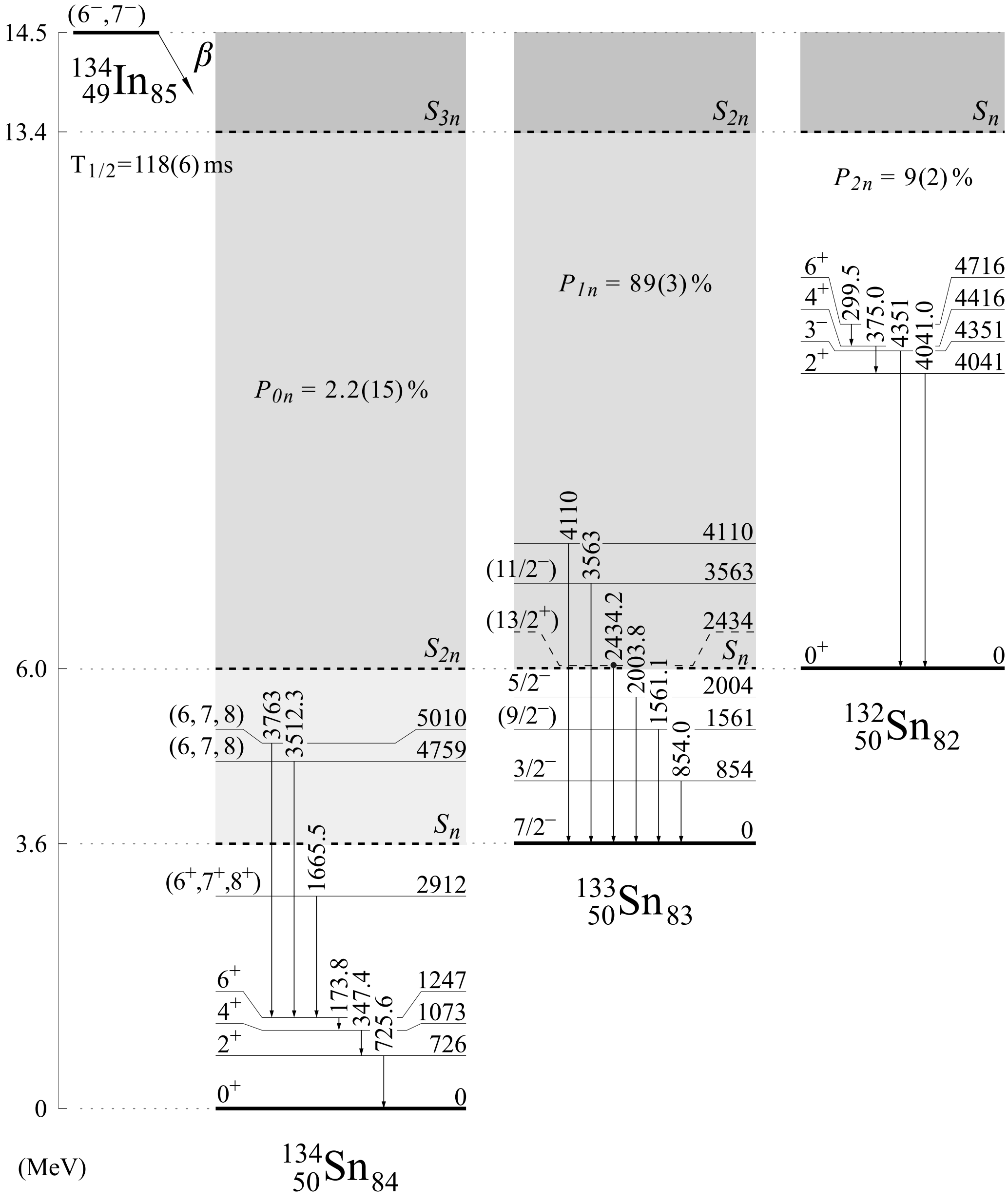

Figure III.23: Decay scheme of ^{134}In established in this thesis. Excited states in the daughter nuclei are labeled with energies (in keV) given relative to the ground state of each tin isotope. The spin-parity assignments for previously known states in tin isotopes were taken from Refs. [13, 19, 20, 100]. The ground-state spin and parity of ^{134}In were proposed based on experimental findings reported in this thesis. Shell-model predictions and systematics discussed in Section IV 1.2 favor the 7^- assignment. The left vertical scale (in MeV) shows the excitation energy and (multi-) neutron separation energies with respect to the ^{134}Sn ground-state. The shaded regions represent energy windows for the population of (multi-) neutron-unbound states. The Q_β, S_{1n}, S_{2n}, and S_{3n} values were taken from Ref. [16].

states account for a large part of the β-decay feeding previously attributed to the low-lying states in the daughter nucleus from measurements employing high-resolution γ-ray detectors. Enhanced emission of γ rays from neutron-unbound states in ^{134}Sn and ^{133}Sn following the ^{134}In β decay, which was registered by high-resolution HPGe detectors, suggest that such an effect may also occur in the β decay under study. This means that determined intensities of the transitions assigned to the ^{134}In β decay may not reflect real β-decay feeding to states in daughter nuclei. Therefore, the determination and interpretation of quantities such as $\log ft$ were found not to be well founded.

2.9 Relative transition intensities

Relative intensities of transitions following the ^{134}In β decay, shown in Table III.2, were determined from the β-gated γ-ray spectrum. These intensities, normalized to the most intense 1561-keV γ ray, agree with those reported in the previous β-decay study of ^{134}In [19, 33]. Because two sets of inconsistent relative intensities were provided in Refs. [19, 33], it is worth specifying that the results provided in this thesis are consistent with the intensities previously obtained from the spectrum of γ rays registered in coincidence with both β particles and neutrons. Relative intensities reported in Refs. [19, 33] as extracted from the β-gated γ-ray spectrum are higher than those determined in the present study. By comparing the previously reported values [19, 33] with those presented in this thesis, factors of 2.2(2) and 7(1) are obtained for the 854-keV and 2004-keV transitions, respectively, observed in β-gated γ-ray spectra.

For three γ rays emitted in the cascade from the isomeric 6^+ state in ^{134}Sn, 174, 347, and 726 keV, a correction to the intensity extracted from the β-gated γ-ray spectrum due to an isomer half-life of 81.7(12) ns [63] was included. The $\beta\gamma$ correlation time was chosen to be 200 ns, so around 82% of isomeric transitions were captured in this spectrum.

The transition intensities determined from the β-gated γ-ray spectrum as peak areas corrected for efficiency and internal conversion were found to be equal for the 174-, 347-, and 726-keV transitions, suggesting that the 2^+ and 4^+ states in ^{134}Sn are not fed directly in the β decay of ^{134}In within the intensity uncertainties. This is further confirmed by the analysis of the γ-ray spectrum in coincidence with the 347-keV transition, where the ratio of transition intensities for the 174- and 726-keV lines was deduced to be 1.0(1). These observations points to the lack of direct β-decay feeding to the 2^+ and 4^+ states in ^{134}Sn and consequently provides an argument for the high spin value of the ground state of the parent nucleus, which can be 6^- or 7^-.

Table III.2: Energies and relative intensities of the transitions observed in the ^{134}In β decay. Total γ-ray and internal-conversion intensities are normalized to the intensity of the 1561-keV transition, for which the absolute intensity is deduced to be 10.8(6)% per β decay of ^{134}In.

Decay branch	Daughter nucleus	Energy (keV)	Relative intensity
$\beta\gamma$	^{134}Sn	173.8(3)	4.9(3)[a]
$\beta\gamma$	^{134}Sn	347.4(3)	4.9(3)[a]
$\beta\gamma$	^{134}Sn	725.6(3)	4.9(4)
$\beta\gamma$	^{134}Sn	1665.5(3)	0.6(1)
$\beta\gamma$	^{134}Sn	3512.3(3)	2.7(3)
$\beta\gamma$	^{134}Sn	3763(1)	0.5(1)
$\beta 1n$	^{133}Sn	854.0(3)	10.4(7)
$\beta 1n$	^{133}Sn	1561.1(3)	100(5)
$\beta 1n$	^{133}Sn	2003.8(3)	3.7(3)
$\beta 1n$[b]	^{133}Sn	2434.2(3)	1.4(2)
$\beta 1n$	^{133}Sn	3563(1)	0.6(2)
$\beta 1n$	^{133}Sn	4110(1)	0.7(2)
$\beta 2n$	^{132}Sn	299.5(3)	0.4(2)
$\beta 2n$	^{132}Sn	375.0(3)	0.48(7)
$\beta 2n$	^{132}Sn	4041.0(5)	0.9(2)
$\beta 2n$	^{132}Sn	4351(1)	0.5(1)

Unassigned:

Energy (keV)	Relative intensity	Energy (keV)	Relative intensity
354.3(3)	1.5(2)	3599(2)	0.4(1)[d]
1427.4(3)	0.7(2)	3816(1)[c]	< 0.4
1605.8(3)	1.0(2)	3824(1)[c]	< 0.4
1976.3(3)	0.8(1)	3840(1)[c]	< 0.4
2026(1)[c]	< 0.5	4283(1)	0.5(1)
3251(1)[c]	< 0.4		

[a] Relative intensities were corrected for internal conversion assuming $E2$ character: α_{tot}(174 keV)=0.227(4) and α_{tot}(347 keV)=0.0221(4) [91].

[b] See the discussion section IV 5 for more details on this assignment.

[c] The identification is uncertain due to insufficient data.

[d] Upper limit; this intensity includes a contribution from the SE peak.

2.10 βn-decay branching ratios

The probabilities of $\beta 1n$ and $\beta 2n$ emission from ^{134}In were determined from the ratio of daughter nuclei produced in a given β-decay branch to the total number of all daughter nuclei, using γ rays emitted in their β decays. These were determined proceeding analogously to the analysis performed for ^{133}In (see Section III 1.6). The only difference is that the transition intensities used in the $P_{1n,2n}$ calculation for ^{134}In were determined from the singles γ-ray spectrum. This overcomes the problem of reproducing the β-particle detection efficiency for events originating from high-energy β decays.

Decays of daughter nuclei considered in the $P_{1n,2n}$ calculation for ^{134}In are shown in Figure III.24. The following transitions and their absolute intensities were used: 872 keV in ^{134}Sb from the ^{134}Sn β decay with 6(3)% [102], 341 keV in ^{132}Sb from the ^{132}Sn β decay with 48.8(12)% [95, 103], and 962 keV in ^{133}Sb from the ^{133}Sn β decay with 12(2)% [93]. For the latter, both the β decay of ^{133}Sn and the βn decay of ^{134}Sn contribute to the intensity. For the βn-decay branch of ^{134}Sn, information on the 1.4% feeding of the 962-keV state in ^{133}Sb reported in Ref. [102] was employed. Corrections to the recorded activity of daughter nuclei due to tape movement were included based on the reconstructed average supercycle structure. In this way, the following branching ratios for the β decay of ^{134}In were obtained: $P_{0n} = 2.2(15)\%$, $P_{1n} = 89(3)\%$, and $P_{2n} = 9(2)\%$. For the uncertainty analysis, the Monte Carlo method was used [104]. The P_{1n} value obtained in our estimate is larger than the βn-decay branching ratio evaluated from the previous β-decay study of ^{134}In, $P_n \approx 65\%$ [19, 25, 26]. The previous result was not given directly in Refs. [19, 33], but appears in evaluations and databases [25, 26].

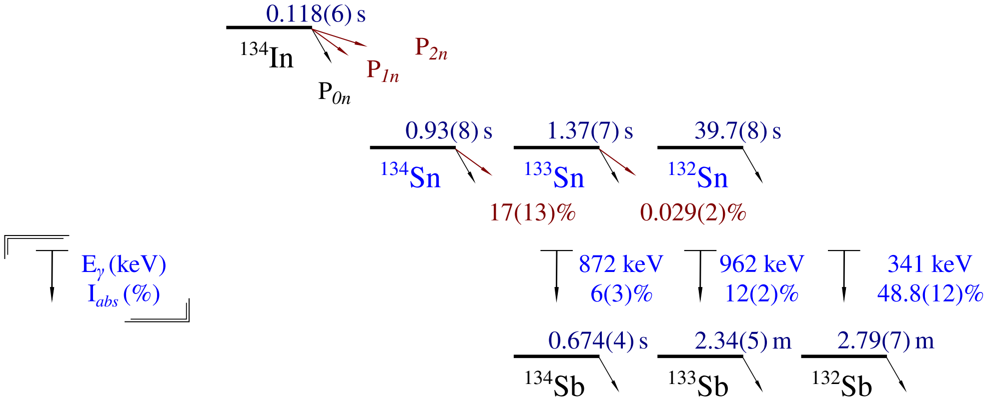

Figure III.24: Experimental information on β decays of daughter nuclei of ^{134}In, which was used to determine the βn-decay branching ratios for the parent nucleus. Half-life values were taken from Ref. [29], excluding the one for ^{134}In. Information on β decays of tin isotopes is from Refs. [93, 95, 102, 103].

Using the reconstructed total number of all daughter nuclei produced in the β decay of ^{134}In, an absolute intensity of 10.8(8)% per decay was obtained for the most intense 1561-keV transition. This value is consistent with the absolute intensity of (5-10)% per decay reported for the same transition in the previous β-decay study of ^{134}In [19]. Because βn-decay branching ratios determined for ^{134}In stem from β-delayed γ rays and include the imprecise $P_{1n} = 17(13)\%$ [102, 105] value for ^{134}Sn, a direct measurement of the βn probabilities would be desirable.

3 β decay of ^{135}In

3.1 Contamination of the A=135 beam and background

Identification of the transitions following the β decay of the most exotic indium isotope studied in this work was hindered by a severe contamination of the beam at mass $A = 135$. A significant content of long-lived impurities is evident from the time distribution of the events with respect to the proton pulse, which is shown in Figure III.25. The decay component corresponding to the short-lived nucleus of interest, with a half-life of the order of a hundred milliseconds [29], is not visible in the distribution, which appears to be almost flat.

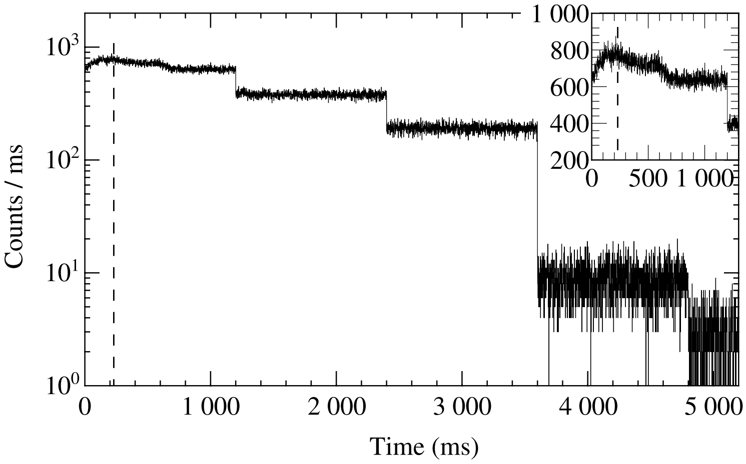

Figure III.25: Time distribution with respect to the proton pulse of the events recorded in HPGe detectors in coincidence with β particles, which was obtained at mass $A = 135$ with an RILIS-ionized indium beam. The vertical dashed line indicates the end of the beam implantation after the proton pulse.

Spectra acquired at mass $A = 135$ are dominated by the decay of the readily surface-ionized ^{135}Cs. Figure III.26a shows a comparison of the singles and β-gated γ-ray spectra measured when RILIS was applied to ionize indium. The 787- and 846-keV γ rays emitted in the decay of the isomeric state of ^{135}Cs [106] (see Figure III.26b) overwhelm these two spectra, affecting also the lower energy range, where a significant Compton background appears. As can be seen in Figure III.26a, identification of γ rays below $\approx$850 keV is hindered. A 518-keV transition observed in the singles γ-ray spectrum may be due to the presence of the isomeric state of another cesium isotope, ^{136}Cs [107]. No transitions were observed in coincidence with this γ ray, supporting its assignment to ^{136m}Cs. The peak visible in Figure III.26a at 668 keV corresponds to a transition in ^{132}Xe, which is confirmed by observed coincidence with 630- and 773-keV γ rays and many others, consistent with Ref. [108]. The presence of these lines in the γ-ray spectrum is due to the accumulation on the tape of the activity of successive daughter nuclei produced in earlier measurements with beams of lighter indium isotopes, in particular ^{132}In.

Imposing a requirement for registration of the coincident β particle does not solve the problem of isobaric contamination in γ-ray spectra, even though the emission of γ rays from the isomeric state of ^{135}Cs is not associated with β decay (see Figure III.26). After applying a gate on the β particles, a considerable attenuation of the activity originating from ^{135m}Cs, of an order of 10^{-3}, is obtained. However, it might be insufficient if one wants to study the decay of the nucleus being simultaneously produced with an intensity over four orders of magnitude lower [96, 97]. The 668-keV transition, belonging to the ^{132}I decay, also remains visible in the β-gated γ-ray spectrum. For the 518-keV γ ray that can be attributed to the ^{136m}Cs decay, a complete suppression of its intensity is observed after imposing the $\beta\gamma$ coincidence condition.

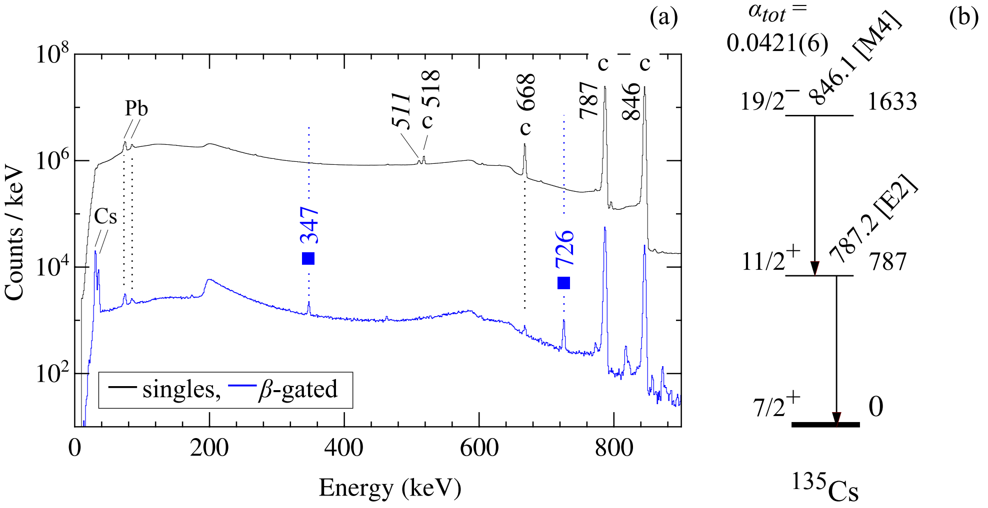

Figure III.26: (a) Comparison of the singles (upper black curve) and β-gated (lower blue curve) γ-ray spectra obtained at mass $A = 135$ when RILIS was used to ionize indium. Both spectra are dominated by the 787- and 846-keV γ rays emitted in the decay of the isobaric contaminant ^{135m}Cs [106, 109]. The most prominent transitions assigned to the ^{135}In decay are labeled with squares, while those attributed to beam contamination are marked with "*c*". (b) Decay scheme of the isomeric state of ^{135}Cs with half-life of 53(2) min [29, 106, 109].

Two effects may be responsible for the presence of substantial isobaric background in the β-gated γ-ray spectrum obtained at $A = 135$. The conversion electrons accompanying the 846-keV $M4$ transition following the decay of ^{135m}Cs [106] can be registered by the plastic detector, resulting in random $\beta\gamma$ coincidences. It is also possible that γ rays emitted in the ^{135m}Cs decay scatter in the β detector, with the effect of producing a background for detecting real β-decay events. Because the isotope of interest is produced along with an overwhelming quantity of isobaric cesium, such random coincidences constituted a severe source of background for the detection of γ rays emitted in the ^{135}In β decay.

Beam impurities can be identified in the γ-ray spectra collected when one of the RILIS lasers was blocked. Only elements with low ionization potential, such as cesium (3.89 eV), were then ionized. It should be noted that indium, with an ionization potential of 5.78 eV, also becomes surface ionized at a typical hot cavity operating temperature, but with lower efficiency than cesium. In a short measurement (~2 h) performed when one of the RILIS lasers was disabled, no transitions that could be attributed to the ^{135}In β decay were observed, indicating a small or even negligible contribution from surface ionization to the ionization of indium achieved with the use of the RILIS.

The β-gated γ-ray spectrum obtained at mass $A = 135$ in the laser-off mode is shown in Figure III.27a, in which the dominating contribution from the ^{135m}Cs decay is visible. Observation of γ rays following the decay of another cesium isotope, ^{138}Cs [110, 111], indicated the presence of a molecular beam contamination. Analysis of $\gamma\gamma$ coincidences confirms the identification of ^{138}Cs (see Figure III.27b). Nonetheless, by comparing spectra collected in the laser-on and laser-off modes, peaks corresponding to beam impurities and activities of long-lived nuclei accumulated on tape during the experimental campaign can be identified. Due to the limited statistics of the data acquired in the laser-off mode, such identification is possible in the energy range up to about 1 MeV. The use of other approaches for recognizing peaks originating from unwanted activities is therefore desirable.

3.2 First observation of γ rays following the decay

Figure III.28 shows a comparison of the β-gated γ-ray spectra measured in laser-on and laser-off modes. Despite strong isobaric contamination of the RILIS-ionized beam, transitions following the ^{135}In β decay were identified for the first time. The two most intense lines seen only in the spectrum collected when RILIS was used to ionize indium, at 347 and 726 keV, correspond to γ rays in ^{134}Sn.

The β-decay half-life of ^{135}In was determined from the time distributions of the 347- and 726-keV transitions, which yielded 89(10) ms and 90(9) ms, respectively. Various gates on the peak and background areas were tested, using spectra with the $\beta\gamma$ coincidence requirement. Two exemplary fits are shown in Figure III.29. The weighted average of 89(7) ms is in agreement with the half-life previously determined at ISOLDE by measuring the β-delayed neutrons, 92(10) ms [27], and slightly lower than the half-life of 103(5) ms measured at RIKEN [28]. Based on the systematics of the lighter odd-A indium isotopes, a β-decaying isomer in ^{135}In is expected to exist, with a half-life similar to the ground state [112]. However, no evidence for its presence was found in this work.

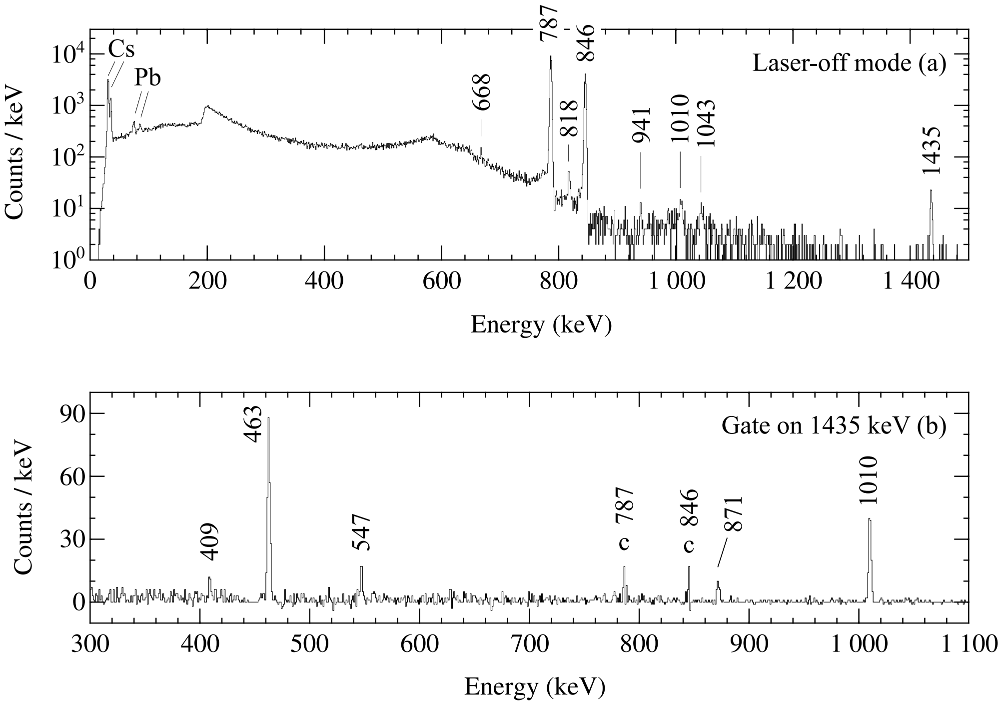

Figure III.27: (a) The β-gated γ-ray spectrum obtained at mass $A = 135$ when one of the RILIS lasers was disabled. Some of the most prominent transitions are labeled with their energies. Peaks present in this spectrum originate from beam contamination. (b) Background-subtracted γ-ray spectrum in coincidence with the 1435-keV transition following the decay of the ^{138}Cs contaminant. The labeled peaks, except those marked with "c", correspond to known transitions in ^{138}Cs [111].

3.3 Background suppression

Suppression of the background observed at $A = 135$ was crucial for the identification of other transitions following the ^{135}In β decay. Two approaches were used independently in the analysis to reduce contaminants. Figures III.30 and III.31 show the comparisons of γ-ray spectra built using different β-gating conditions. These spectra demonstrate the effectiveness of the suppression methods on the example of the known transitions in ^{134}Sn.

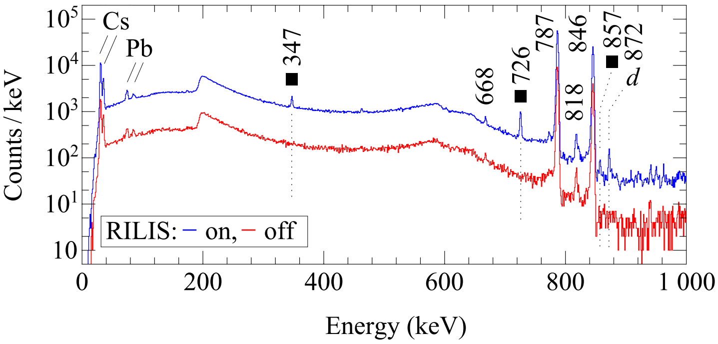

Figure III.28: The β-gated γ-ray spectrum obtained at mass $A = 135$ when RILIS was applied to ionize indium (upper blue curve) and when one of the RILIS lasers was blocked (lower red curve). Some of the most prominent transitions are labeled with their energies (in keV). Peaks present in both spectra originate from the beam contaminants, while those appearing only in the RILIS-on mode can be attributed to the β decay of ^{135}In (square) or its daughter nucleus (marked with "*d*").

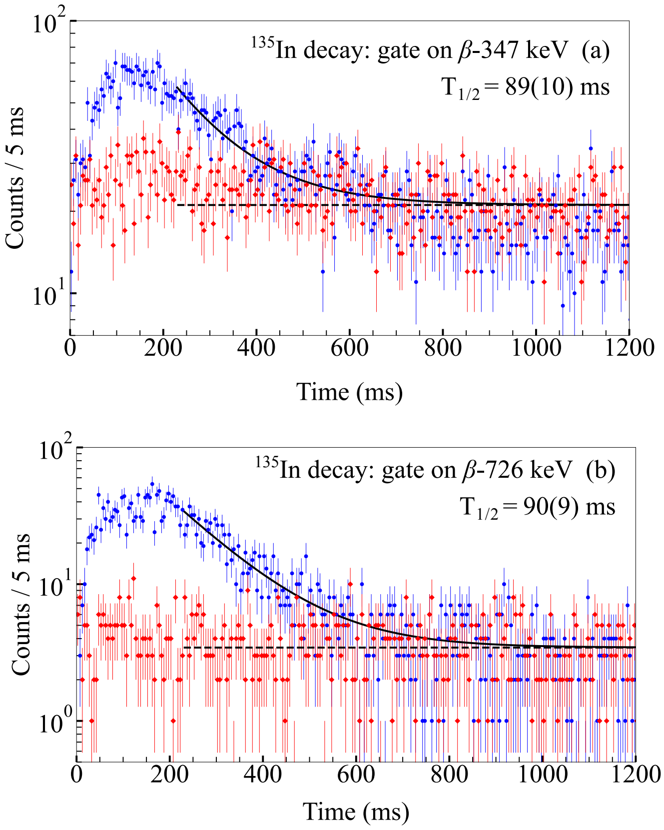

Figure III.29: Time distributions relative to the proton pulse of the (a) 347-keV and (b) 726-keV γ rays (blue circles) and the background areas (red diamonds) observed in coincidence with β particles at mass $A = 135$ in the laser-on mode. A function composed of an exponential decay and a constant background was fitted (solid line) in the 230-1200 ms time range. The curve corresponding to the background component is also presented (dashed line). A Bayesian approach was applied in the statistical analysis of the data [113, 114].

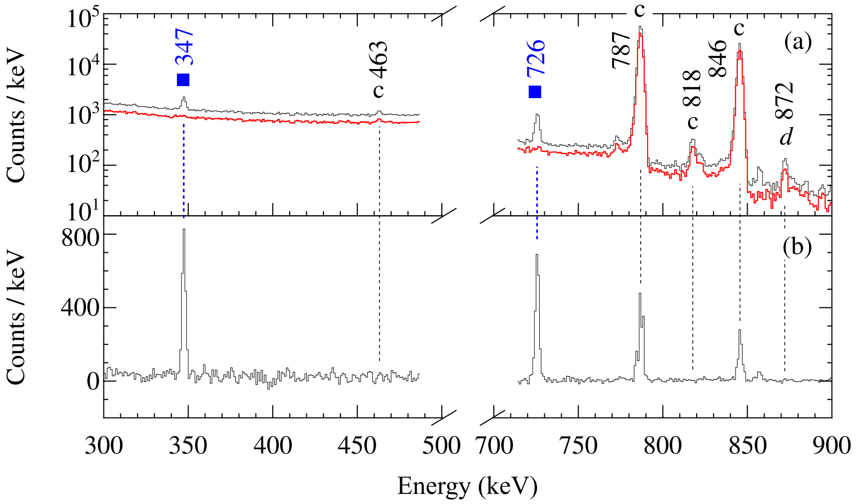

Figure III.30: Portions of the β-gated γ-ray spectra obtained at mass $A = 135$ with RILIS-ionized beam, which were built with different conditions applied on the time of the event with respect to the proton pulse. (a) Spectrum without the time restriction is shown by the black curve, while the spectrum gated on delayed period, later than 600 ms after the proton pulse, is presented by the red curve. (b) Spectrum gated on the interval of 0-500 ms, in which the long-lived background registered between 500 and 1000 ms has been subtracted.

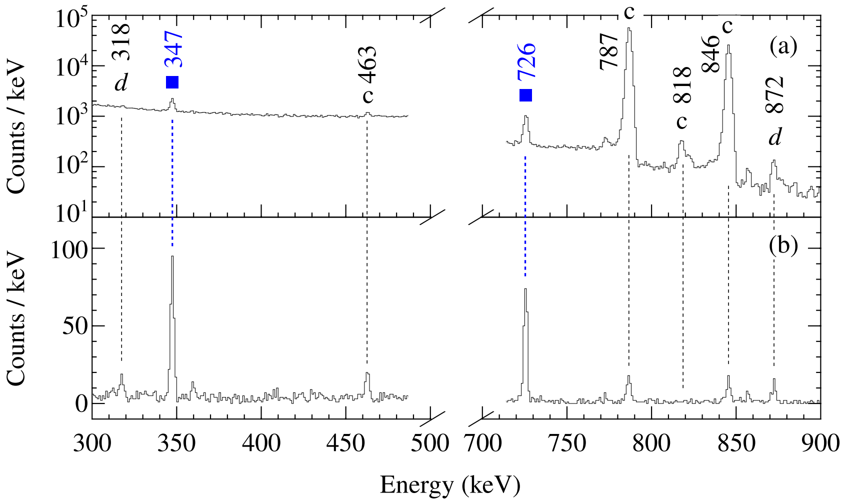

Figure III.31: Portions of the β-gated γ-ray spectra obtained at mass $A = 135$ with RILIS-ionized beam, which were built (a) without any condition imposed on the events recorded by the plastic detector and (b) with gate on the highest energy deposit in the plastic detector.

One strategy for reducing long-lived background exploits information about the time of the event with respect to the proton pulse. Because the β-decay half-life of ^{135}In is short compared to the timescale of proton pulses (multiples of 1.2 s) as well as the β-decay half-lives of daughter nuclei (see Figure III.32), it is possible to distinguish events that may be attributed to its β decays. The γ-ray spectra were gated using various periods relative to the proton pulse to identify transitions having time distribution consistent with the β-decay half-life of ^{135}In (see of Figure III.30). Transitions visible in the time-delayed β-gated γ-ray spectra, for example registered later than 600 ms after the proton pulse, were assigned to the background arising from either daughter or contaminant nuclei. Gating on the first few hundred milliseconds after the proton pulse resulted in enhancement of γ rays following the ^{135}In decay with respect to those arising from the background. Figure III.30 displays the β-gated γ-ray spectrum recorded in the first 500 ms after the proton pulse, in which events recorded at delayed interval were subtracted. As a result, a substantial decrease in contamination from 53(2)-min ^{135m}Cs [29, 106, 109] and a reduction of the activity of daughter nuclei were achieved.

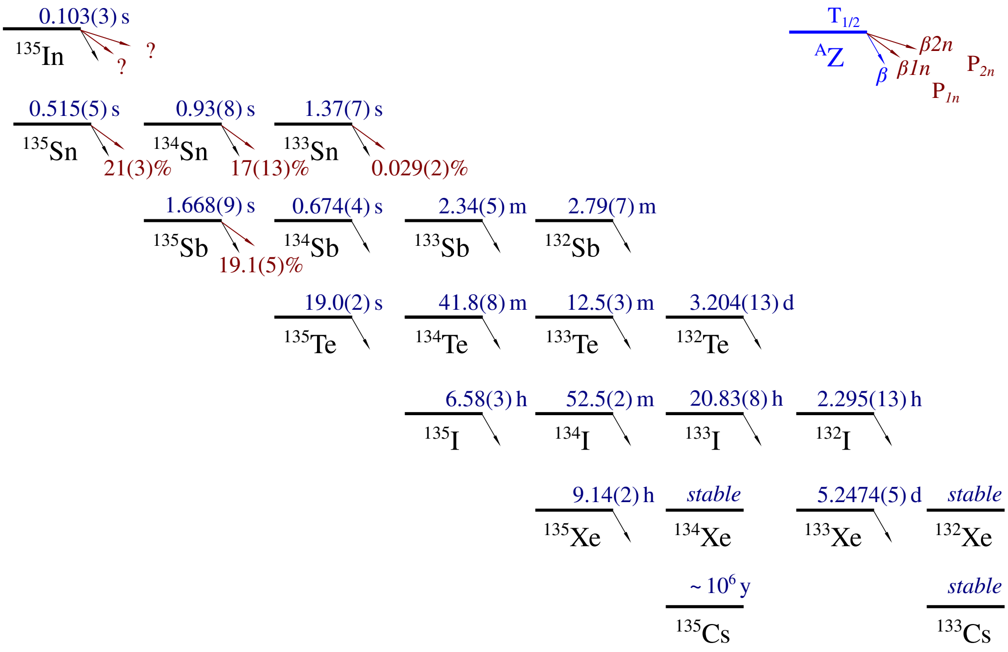

Figure III.32: Schematic drawing showing different time scales of the half-lives of nuclei produced in the ^{135}In β-decay chain. For readability, isomeric states known in some nuclei were omitted. All data presented were taken from Ref. [29], also for the parent nucleus (status prior to the publication of results from this thesis).

The second approach allowing for the reduction of unwanted activities was to study γ rays observed in coincidence with the highest-energy deposit in the plastic detector, in order to preferentially select ^{135}In β decays. This restriction reduced random events registered in the β-particle detector, mainly due to scattering of γ rays, that were wrongly interpreted as β-decay events. Energy spectra measured by the plastic detector in the laser-on and laser-off modes are shown in Figure III.33. The energy deposit extended to higher energies when RILIS-ionized indium was present in the $A = 135$ beam. From spectra registered in coincidence with 787- and 846-keV γ rays following the ^{135m}Cs decay, an optimal threshold for energy deposit in the plastic detector was determined. It was found that gating on channels higher than 184 led to a significant reduction of the intensities of the 787- and 846-keV transitions in the γ-ray spectrum and, at the same time, provided adequate data to search for γ rays emitted in the ^{135}In β decay. However, lines corresponding to the decay of another cesium contaminant, ^{138}Cs, were still visible.

After applying the high-energy threshold for the energy deposit in the β detector, known transitions in ^{134}Sn were found then to be the most intense ones in the β-gated γ-ray spectrum (see Figure III.31). Similar enhancement was also observed for several other γ rays seen in the β-gated γ-ray spectrum gated on short intervals after the pulse. Transitions following the β decay of ^{134}Sn – the daughter nucleus produced in the $\beta 1n$ decay of ^{135}In – were also present (318-, 554-, and 872-keV γ rays [115]).

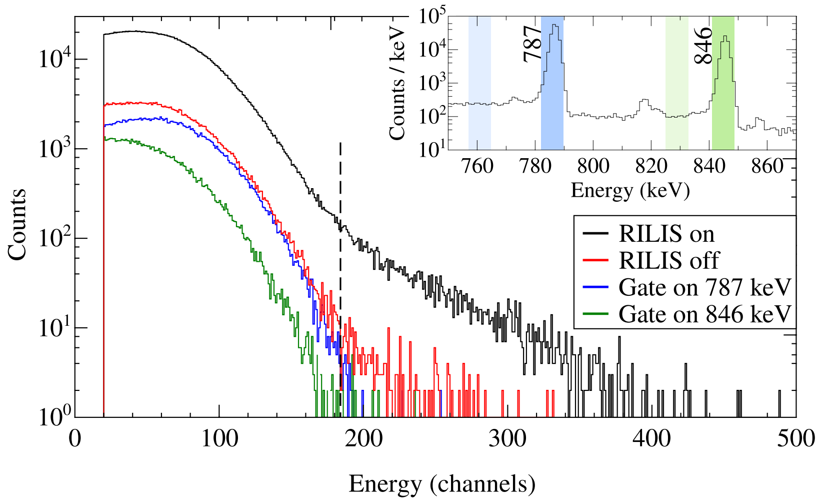

Figure III.33: Energy spectra measured by the plastic detector at mass $A = 135$. The black curve shows the spectrum measured when the RILIS was used to ionize indium, while the red curve shows the spectrum measured when one of the RILIS lasers was blocked. Spectra in coincidence with 787- and 846-keV γ rays are shown in blue and green curves, respectively. The vertical dashed line indicates the optimal channel for applying a high-energy threshold for β particles that results in suppression of unwanted activity from ^{135m}Cs. Inset shows a portion of the β-gated γ-ray spectrum measured at mass $A = 135$ in the laser-on mode, where regions selected for the gating on relevant peaks and on their background areas are presented.

3.4 Identification of γ rays following the decay

Figures III.34, III.35, and III.36 provide a detailed overview of the γ-ray spectra built using different β-gating conditions. By comparing these spectra, transitions following the ^{135}In β decay were established. Their energies and relative intensities are provided in Table III.3.

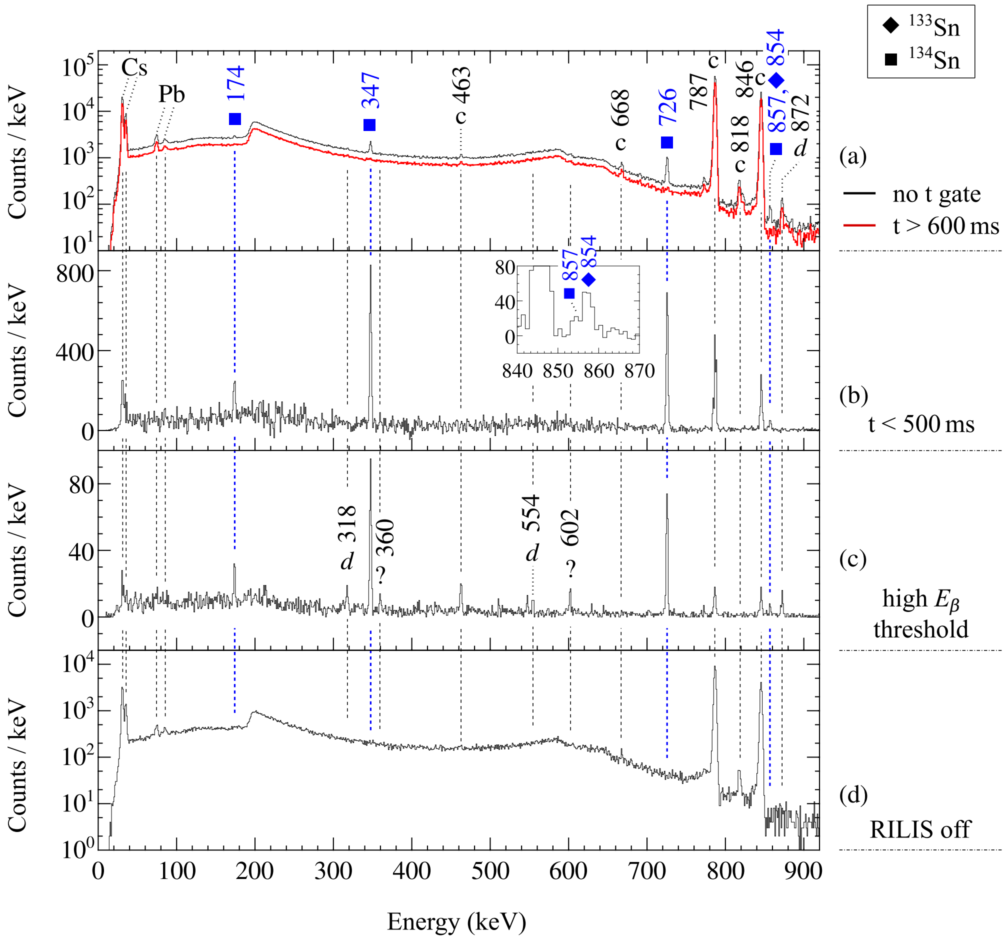

Figure III.34: β-gated γ-ray spectra obtained at mass $A = 135$ in the laser-on [(a), (b), and (c)] and laser-off (d) modes.

(a) The spectrum shown in red was gated at times later than 600 ms with respect to the proton pulse, while the one shown in black was built without any additional condition imposed on $\beta\gamma$ coincidence events. (b) Spectrum recorded in the first 400 ms relative to the proton pulse from which long-lived background was subtracted. (c) Spectrum built with an increased energy threshold for β particles.

Transitions attributed to the $\beta 1n$- and $\beta 2n$-decay branches of ^{135}In are marked with squares and diamonds, respectively. Peaks that can be assigned to the ^{135}In β decay are indicated by energy only, while those attributed to daughter or contaminant nuclei are marked with "*d*" and "c", respectively. Unassigned peaks in panel (c) are marked with a question mark.

The most intense transitions observed in the ^{135}In β decay, at 174, 347 and 726 keV, belong to the yrast $6^+ \rightarrow 4^+ \rightarrow 2^+ \rightarrow 0^+_{g.s.}$ γ-ray cascade in ^{134}Sn [20, 35]. Three lines that can be attributed to the γ rays in ^{133}Sn, 854, 1561, and 2004 keV, were identified at consistent energies. The 2434-keV line, which was seen in the ^{134}In β decay (see Section III 2.5), was also observed in the ^{135}In β decay and is a plausible candidate for a new transition in ^{133}Sn. As for the possible $\beta 3n$-decay branch of ^{135}In, a slight excess of counts over background appears in the γ-ray spectrum at around 4041 keV (see Figure III.37), corresponding to the energy of the first-excited state in ^{132}Sn [74, 100]. The inadequate data do not allow us to firmly establish whether the $\beta 3n$-decay branch has been observed for ^{135}In.

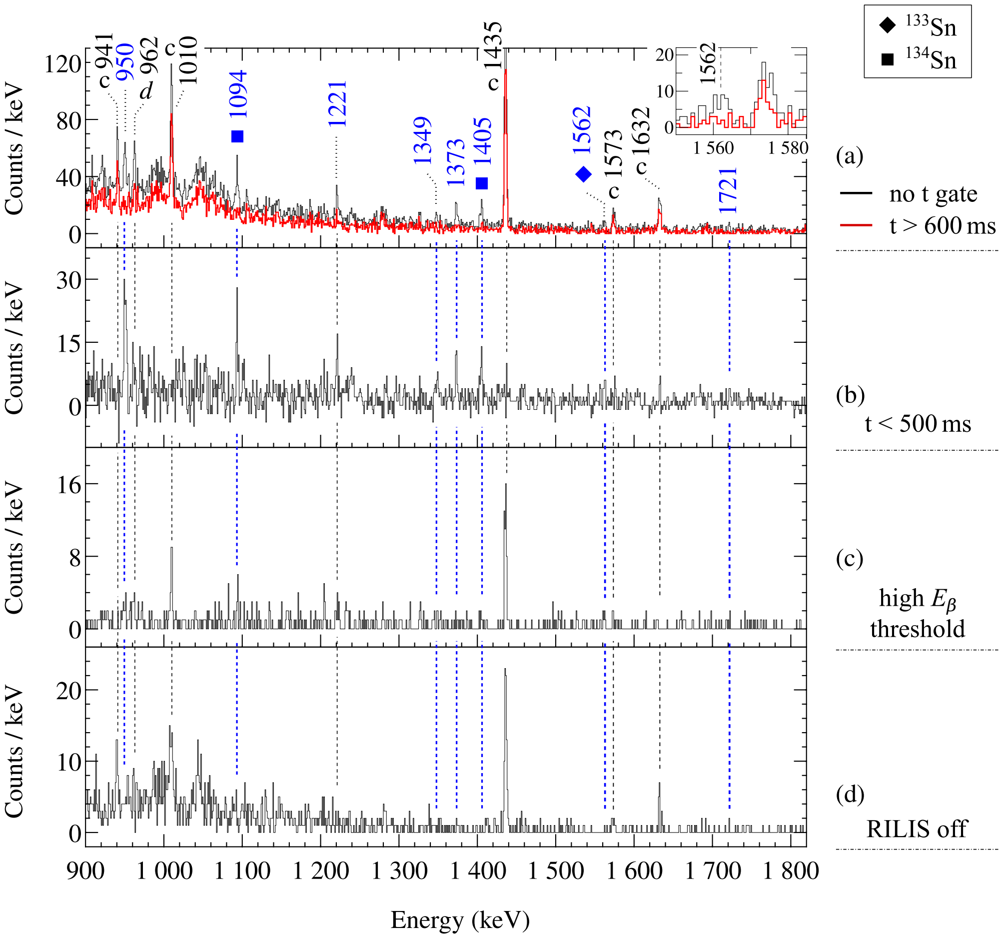

Figure III.35: Caption the same as in Figure III.34.

3.5 Analysis of $\beta\gamma\gamma$ coincidences

Using $\beta\gamma\gamma$ coincidence data, the population of the 2^+, 4^+, and 6^+ states in ^{134}Sn was confirmed by the observation of the 174-, 347, and 726-keV γ rays in coincidence [20, 35]. Figure III.38 displays the β-gated γ-ray spectra in coincidence with the 347- and 726-keV transitions that reveal three new γ rays in ^{134}Sn, with energies of 857, 1094, and 1405 keV. The absence of the 174-keV line in spectra of γ rays in coincidence with the 857-, 1094-, and 1405-keV transitions, shown in Figure III.39, indicates that they deexcite states at 1930, 2167, and 2478 keV, respectively. Tentative assignment to ^{134}Sn was made for the 595-keV transition, which was found in coincidence with that at 726 keV but was not observed in the γ-ray spectra sorted with two different β-gating conditions (see Figure III.34).

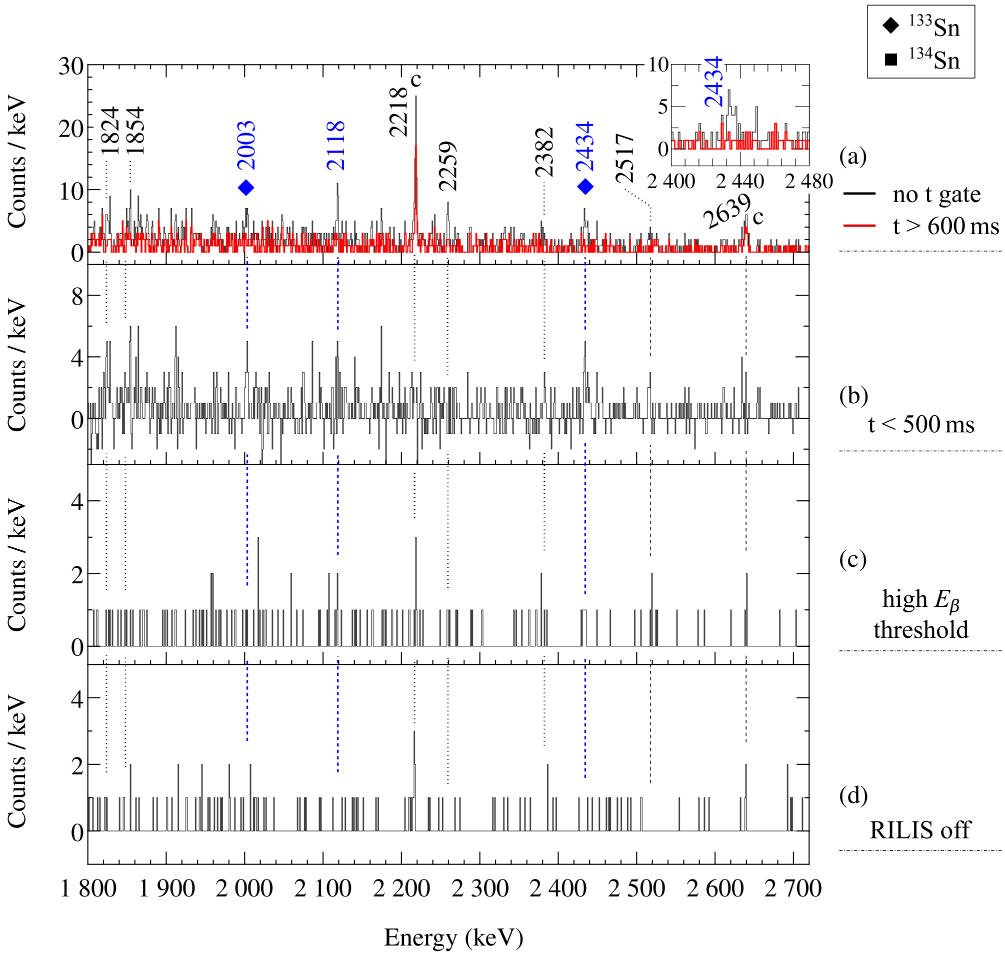

Figure III.36: Caption the same as in Figure III.34.

Table III.3: Energies and relative intensities of transitions observed in the ^{135}In β decay. Total γ-ray and internal-conversion intensities are normalized to the intensity of the 726-keV transition.

Decay branch	Daughter nucleus	Energy (keV)	Relative intensity
$\beta\gamma$[a]	^{135}Sn	950.3(3)	7(1)
$\beta\gamma$[a]	^{135}Sn	1220.9(3)	4.0(9)
$\beta 1n$	^{134}Sn	173.8(3)	25(5)[b]
$\beta 1n$	^{134}Sn	347.4(3)	74(5)[b]
$\beta 1n$[a]	^{134}Sn	595(1)[c]	11(5)[d]
$\beta 1n$	^{134}Sn	725.6(3)	100(6)
$\beta 1n$	^{134}Sn	857.2(3)	7(1)
$\beta 1n$	^{134}Sn	1093.8(6)	6(1)
$\beta 1n$	^{134}Sn	1404.8(6)	3.9(8)
$\beta 2n$	^{133}Sn	854.0(8)	1.6(9)
$\beta 2n$	^{133}Sn	1562.4(8)	2.0(6)
$\beta 2n$	^{133}Sn	2003.3(8)	1.8(6)
$\beta 2n$[e]	^{133}Sn	2434.2(7)	2.6(7)

Unassigned:

Energy (keV)	Relative intensity	Energy (keV)	Relative intensity
1349.2(9)	2.4(7)	1853.1(8)	2.2(7)
1372.9(3)	3.3(8)	2118.3(6)	2.5(7)
1720.9(8)	1.2(5)	2259.3(8)	1.8(6)
1824.0(8)	2.0(7)	2516.1(8)	1.5(5)

[a] Tentatively assigned to this β-decay branch of ^{135}In.

[b] Relative intensities were corrected for internal conversion assuming $E2$ character: α_{tot}(174 keV)=0.227(4) and α_{tot}(347 keV)=0.0221(4) [91, 116].

[c] Transition observed only in $\beta\gamma\gamma$ coincidence.

[d] Intensity obtained from coincidences.

[e] See the discussion section III 5 for more details on this assignment.

3.6 Decay scheme

Figure III.40 shows the β-decay scheme of ^{135}In established in this thesis. Several new lines, which were not observed in the β decays of the lighter indium isotopes, were seen in the ^{135}In β decay. They are listed in Table III.3. Based on the available experimental information on daughter nuclei produced in the $\beta 1n$- and $\beta 2n$-decay branches of ^{135}In, at least two of them can be considered as transitions in ^{135}Sn. For ^{134}Sn, identification of new levels below the excitation energy of the 6^+ state (at 1247 keV) is unlikely [20, 35, 36]. For ^{133}Sn, new levels below 2004 keV are also not expected [13, 19, 31–33, 37, 117]. Therefore, the 950- and 1221-keV lines, being the most intense ones in the considered energy range and for which no coincident γ rays were observed, were attributed to deexcitations in ^{135}Sn. Due to the higher excitation energies of other transitions as well as the lack of $\beta\gamma\gamma$ and $\gamma\gamma$ coincidences for them, it was not possible to attribute them to either ^{135}Sn or ^{134}Sn.

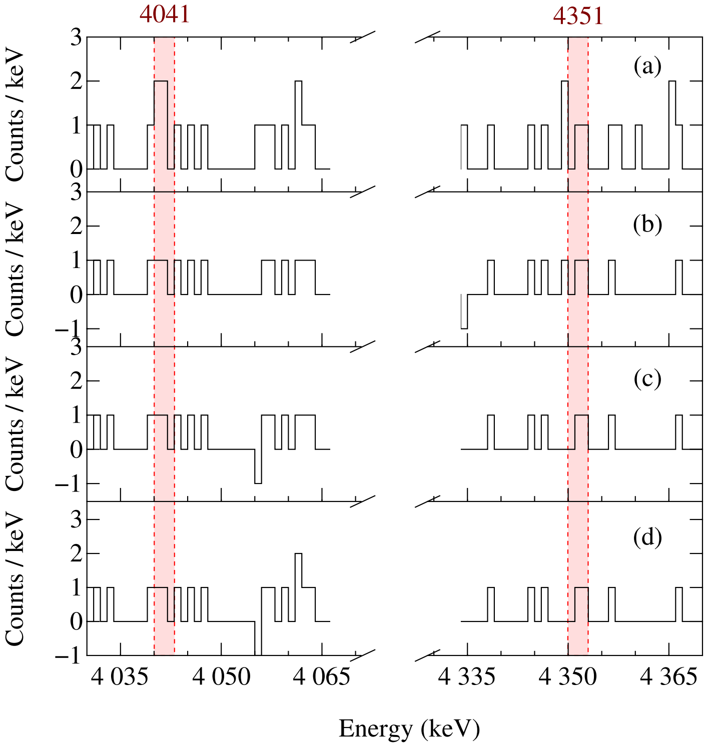

Figure III.37: Portions of the β-gated γ-ray spectra obtained at mass $A = 135$ with an RILIS-ionized beam, which are relevant in the search for transitions depopulating excited states in ^{132}Sn. These four spectra were built with different time conditions relative to the proton pulse: (a) no restriction, or gated on the following intervals: (b) 0-400 ms (events registered in the range of 700-1100 ms were subtracted), (c) 0-450 ms (events registered in the range of 550-1000 ms were subtracted), (d) 0-500 ms (events registered in the range of 500-1000 ms were subtracted).

3.7 Relative transition intensities

Relative intensities of transitions assigned to the ^{135}In β decay, presented in Table III.3, were determined from the β-gated γ-ray spectrum. The values provided for the 174-, 347-, and 726-keV transitions emitted in cascade from the isomeric 6^+ state in ^{134}Sn with a half-life of 81.7(12) ns [63], were corrected to account for the events not registered in the β-gated γ-ray spectrum due to the time window of 300 ns used for the $\beta\gamma$ coincidence. Under these conditions, around 92% of all the decays of the 6^+ isomer were captured.

Due to the overwhelming long-lived background in the singles and β-gated γ-ray spectra acquired at $A = 135$, evaluation of the transition intensities that would allow reconstruction of the number of daughter nuclei produced in the ^{135}In β decay was not possible. Thus, absolute intensities of transitions assigned to the β decay of ^{135}In as well as its βn-decay branching ratios could not be determined. Based on relative intensities, it can only be concluded that the ^{135}In β decay is dominated by the $\beta 1n$ emission.

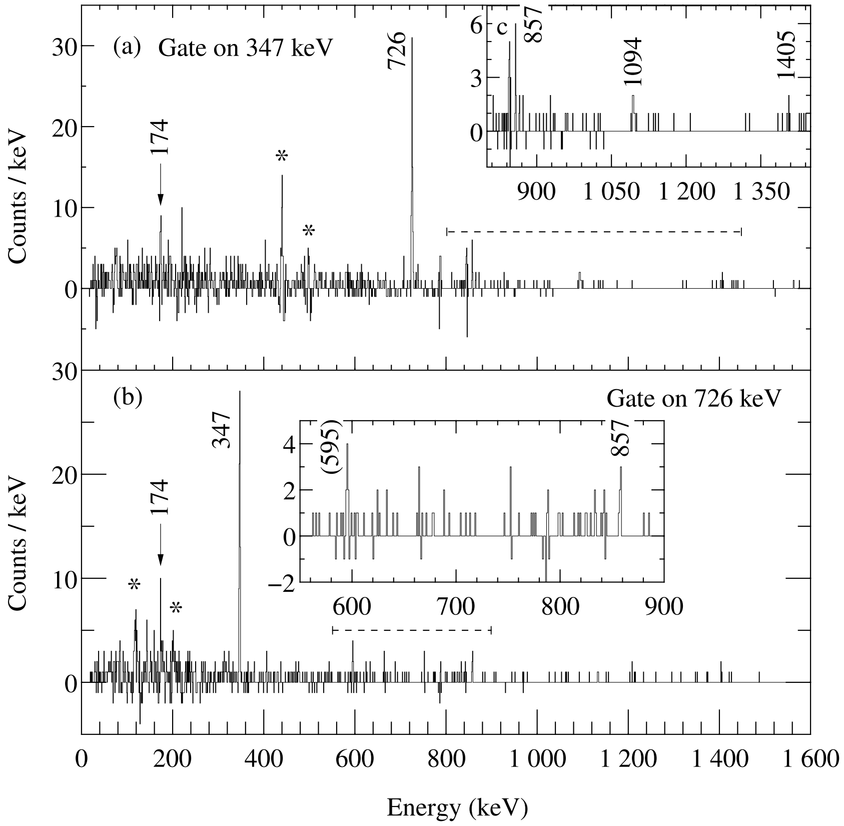

Figure III.38: Background-subtracted β-gated γ-ray spectra in coincidence with the (a) 347- and (b) 726-keV γ rays that depopulate previously known levels in ^{134}Sn following the $\beta 1n$ decay of ^{135}In. Peaks that can be attributed to ^{134}Sn are labeled with their energies (in keV). Tentative assignment is marked with additional parentheses. Asterisks indicate artifacts due to the background subtraction procedure. Insets display expanded regions whose ranges are indicated with dashed lines.

The unknown β-decay feedings to ground states of tin isotopes produced in the ^{135}In β decay preclude the approximate estimate of the βn-decay branching ratios from relative transition intensities. In the analogous β decay of the $(9/2^{+})$ ground state of ^{133}In, a significant β-decay feeding to ground states of the two daughter nuclei, ^{133}Sn with $7/2^{-}_{g.s.}$ and ^{132}Sn with $0^{+}_{g.s.}$, was deduced. Making approximate estimates of $P_{1n,2n}$ for ^{135}In assuming the lack of ground-state β-decay feedings in daughter nuclei is therefore not well founded.

Apparent $\beta 1n$-decay feedings ($I^{app}_{\beta 1n}$) to excited states in ^{134}Sn were calculated assuming that the intensity of the 726-keV transition reflects the total β-decay feeding in this daughter nucleus. The resulting values, shown in Figure III.41, suggest that the three lowest excited states receive comparable feeding. However, the $I^{app}_{\beta 1n}$ values should be treated as approximate, because only a partial β-decay scheme of ^{135}In was obtained in this work. The $\beta 1n$-decay energy is large, $Q_{\beta 1n} = 11.25(30)$ MeV [16], and therefore it is likely that some of the high-energy γ rays feeding from above low-lying states in ^{134}Sn were overlooked by high-resolution γ-ray detectors.

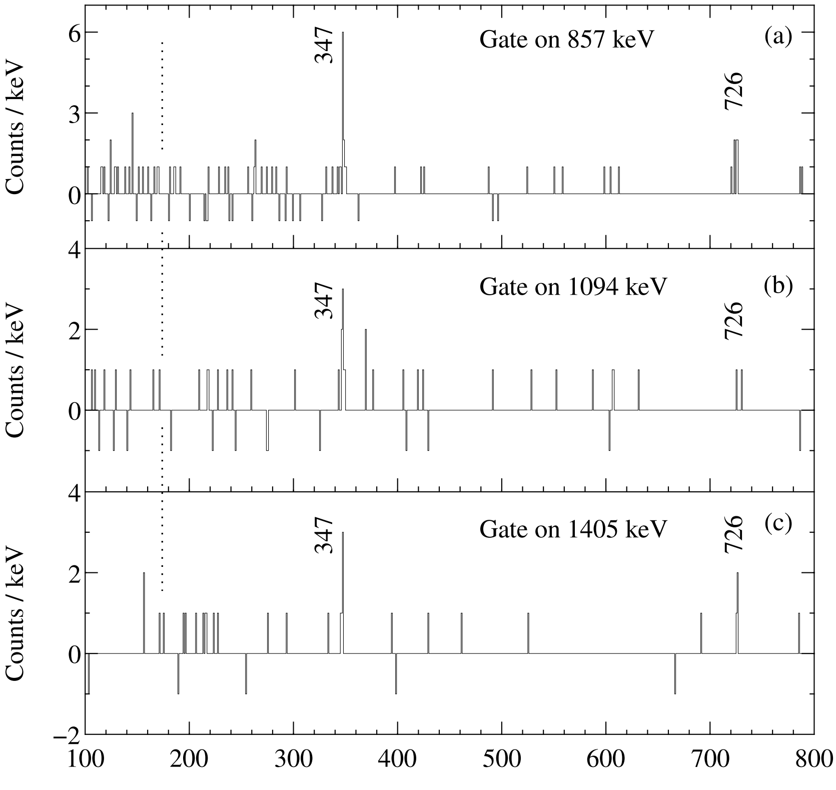

Figure III.39: Background-subtracted β-gated γ-ray spectra in coincidence with new transitions in ^{134}Sn observed in the $\beta 1n$ decay of ^{135}In. The dotted line indicates the energy of the known 174-keV transition in ^{134}Sn.

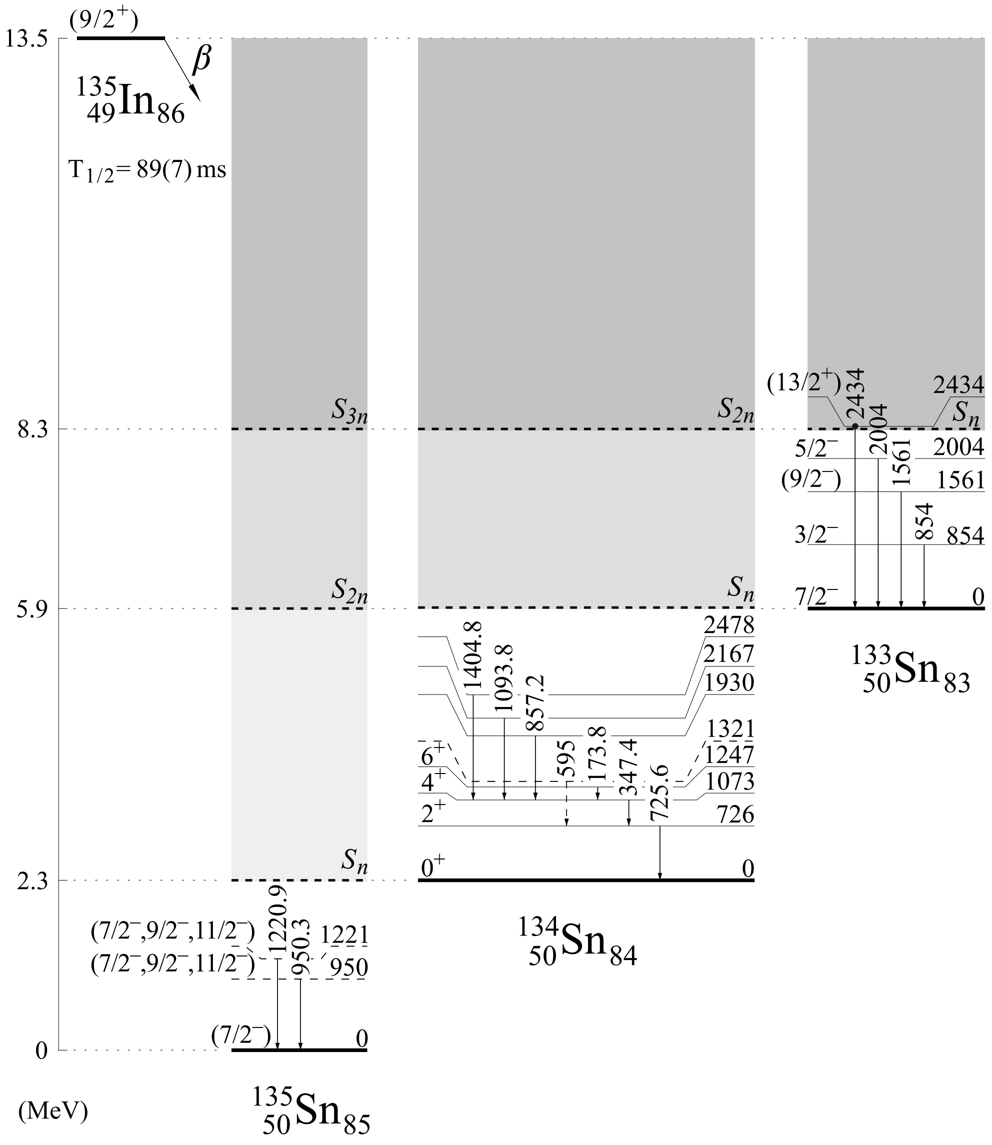

Figure III.40: Decay scheme of ^{135}In established in this work. Excited states in daughter nuclei are labeled with energies (in keV) given relative to the ground state of each tin isotope. Levels tentatively proposed in ^{135}Sn and ^{134}Sn are indicated with dashed lines. The spin-parity assignments for previously known states in ^{134}Sn and ^{133}Sn were taken from Ref. [19, 20]. The ground-state spin and parity of ^{135}Sn and ^{135}In are based on systematics [29]. The left vertical scale (in MeV) shows the excitation energy and (multi-) neutron separation energies with respect to the ^{135}Sn ground state. The shaded regions represent energy windows for the population of neutron-unbound states. The Q_β, S_n, S_{2n}, and S_{3n} values were taken from Refs. [16].

The possible presence in the $A = 135$ beam of a low-spin isomer in ^{135}In was considered. In such a scenario, the deduced transition intensities should be treated as obtained for the mixture of two β-decaying states. However, in a series of short optimization runs at mass $A = 133$ with RILIS in the broadband mode, preceding the implantation of ^{135}In ions, no peak corresponding to the unique 854-keV transition following the β decay of the $(1/2^-)$ isomer in ^{133}In was observed. Therefore, it can be expected that in the measurement at $A = 135$ in which RILIS lasers operated in the same broadband mode, transitions arising from the β decay of only one state of the parent nucleus were observed.

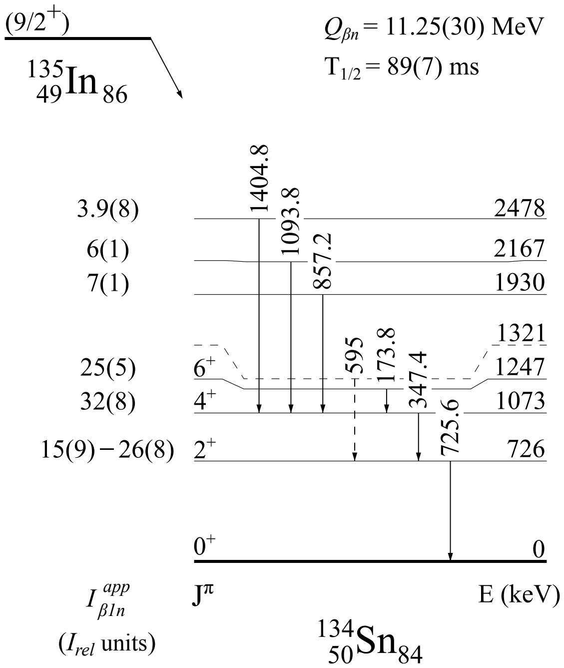

Figure III.41: Partial β-decay scheme of ^{135}In showing apparent $\beta 1n$-decay feedings ($I^{app}_{\beta 1n}$) to excited states in ^{134}Sn calculated solely from relative transition intensities. Two $I^{app}_{\beta 1n}$ values are provided for the 726-keV level, with or without the inclusion of the tentative 595-keV transition.

CHAPTER

IV

DISCUSSION

1 Ground-state spin-parity assignments for parent nuclei

Ground-state spins and parities of indium isotopes beyond $N = 82$ have not yet been experimentally determined. There are, however, experimental and theoretical indications that allow us to indicate the most probable spin-parity values for ground states of ^{133}In, ^{134}In, and ^{135}In as well as the isomeric state in ^{133}In.

This section summarizes experimental and theoretical arguments supporting tentative spin-parity values for β-decaying states of parent nuclei that have already been referenced in this thesis. Further arguments for the spin-parity assignments for ^{133g}In, ^{133m}In, and ^{134}In result from the observed β-decay feeding patterns to the states in tin isotopes with well-established spins and parities. By combining these results with experimental information on analogous multiplets in the lighter indium isotopes, the most favored spin-parity values for β-decaying states of parent nuclei were inferred. These assignments serve as the foundation for discussing GT and *ff* decays of neutron-rich indium isotopes, in which the spin and parity of the initial state imply a particular preference for final states being populated via a given type of β decay.

1.1 Odd-A ^{133}In and ^{135}In

The ground-state configurations of odd-even ^{133}In and ^{135}In, with $N = 84$ and $N = 86$, respectively, are based on the coupling of a proton hole in the $\pi 1g_{9/2}$ orbital and two or four neutrons in the $\nu 2f_{7/2}$ orbital, respectively. In an isomeric state of ^{133}In, the proton hole is located on a deeper bound orbital $\pi 2p_{1/2}$. Schematic representations of the ground- and isomeric-state configurations are shown in Figure IV.1.

Since pairing interaction favors nucleon pairs in the same single-particle orbital to be coupled to spin zero, neutrons do not contribute to the structure of low-lying levels in ^{133}In and ^{135}In. Properties of the β-decaying states in these isotopes are driven by the nature of the proton orbital in which the hole is located. Therefore, odd-A indium isotopes beyond $N = 82$ are expected to have similar features to lighter odd-A indium isotopes for which more experimental data are available. Laser spectroscopy measurements confirmed spin-parity values for the $9/2^+$ ground and $1/2^-$ isomeric states of odd-A indium isotopes from ^{113}In up to ^{131}In [29, 118]. Therefore, based on the systematics of the $Z = 49$ nuclei, the $9/2^+$ ground-state spin-parity assignment can be proposed for both ^{133}In and ^{135}In. Analogously, the $1/2^-$ isomer is expected in these nuclei. So far, it has been identified only in ^{133}In.

In the previous β-decay study of ^{133}In, a dominant β-decay feeding to the $(9/2^-)$ state at 1561 keV in ^{133}Sn was deduced [19, 33]. This observation suggested that the spin of the parent nucleus is high, and the $9/2^+$ assignment was tentatively proposed. However, the presence of a mixture of the two β-decaying states in the ^{133}In beam was inferred from the observation of the 854-keV transition attributed to the $3/2^-$ level in ^{133}Sn. The results presented in this thesis, from measurements at $A = 133$ with isomer-selective ionization of indium, support the high-spin assignment for the ^{133}In ground state. Besides the prevalent population of the $(9/2^-)$ state in ^{133}Sn, a significant β-decay feeding to the 3564-keV level with tentative spin-parity assignment of $11/2^-$ was also observed in the ^{133g}In β decay. In contrast, the population of these two levels was disfavored in the β decay of the isomeric state of ^{133}In. In this case, only low-spin states were fed in ^{133}Sn, $3/2^-$ at 854 keV and $1/2^-$ at 1367 keV, as expected for the β-decaying $1/2^-$ state. It is worth highlighting that low-lying states in ^{133}Sn were investigated in several experiments, including three one-neutron transfer reactions (see Section I 3.2.1) [13, 17, 32]. With more reliable information about the nature of these states, the observed preference for a population of high- or low-spin states appeared to be a strong argument in the discussion of spin-parity assignments for β-decaying states of ^{133}In.

In the case of ^{135}In, there is no definite information about excited states populated in ^{135}Sn. Levels with well-established spins and parities are populated via the βn-decay branches of ^{135}In, in ^{134}Sn and ^{133}Sn. However, inferring a spin-parity value for the parent nucleus from βn-decay population patterns assuming low angular momenta for neutrons may not be appropriate. This limitation is evident from a wide range of spin-parity values of states populated in daughter nuclei following the βn emission from the lighter indium isotopes. In the βn decay of the $(9/2^+)$ ground state of ^{133}In, a significant feeding to the 0^+ ground state of ^{132}Sn was deduced [74], corresponding to the large angular momentum of emitted neutrons, $\ell_n = 5$. In the $\beta 1n$ decay of ^{134}In with the (7^-) ground state, a wide range of spins, from $3/2^-$ to $(11/2^-)$, for the states populated in ^{133}Sn was concluded.

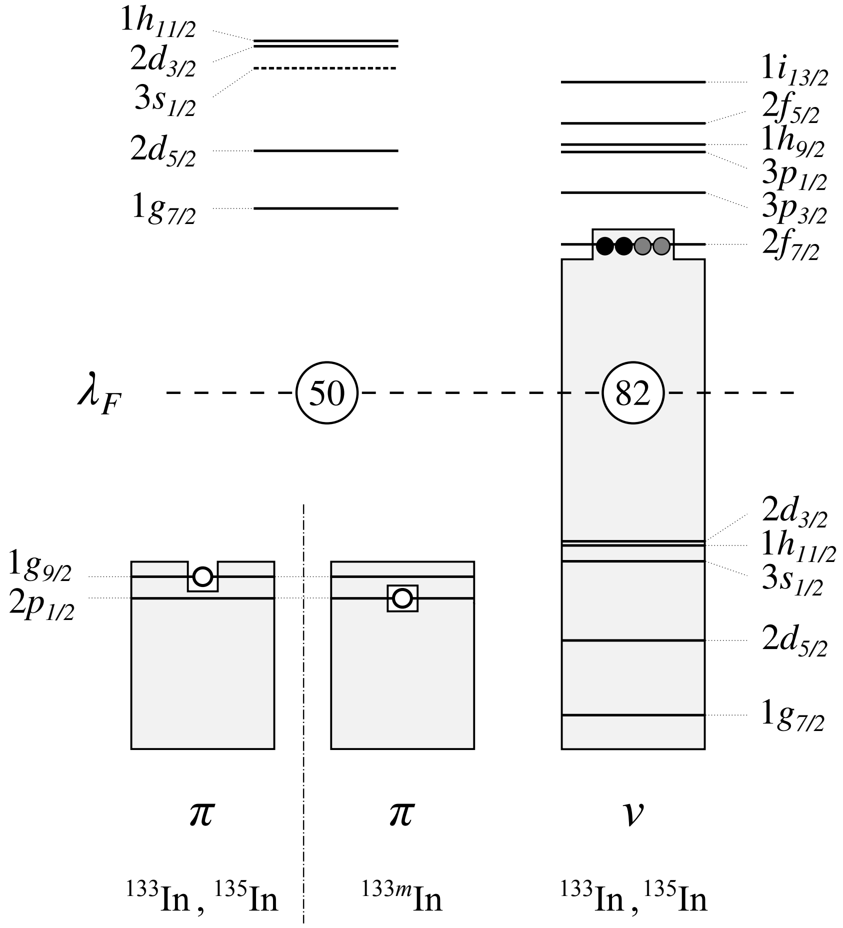

Figure IV.1: Schematic representation of the ground- and isomeric-state configurations for ^{133}In and ^{135}In. The open circle indicates the location of a proton hole for the ground and isomeric states, while the filled circles indicate the location of two (in black for ^{133}In) or four (in gray for ^{135}In) valence neutrons. In order to eliminate the Coulomb energy difference between proton and neutron orbitals, their positions were set with respect to the middle of the shell gap (λ_F). The drawing was prepared following Ref. [119] (see Figure 2 therein).

1.2 Even-A ^{134}In

The ground-state configuration of odd-odd ^{134}In, with $N = 85$, is based on the coupling of a proton hole in the $\pi 1g_{9/2}$ orbital and three neutrons in the $\nu 2f_{7/2}$ orbital. Its schematic representation is shown in Figure IV.2. For the lowest-lying levels, two neutrons can be expected to be coupled to spin zero. Consequently, these states should form a multiplet similar to the one in ^{132}In, arising from the $\pi 1g_{9/2}^{-1}\nu 2f_{7/2}$ configuration. Spin and parity of the ^{132}In ground state are tentatively proposed as 7^- [29], with strong experimental arguments pointing to this value. The β-decay feeding intensity to the 6^- excited state in ^{132}Sn was found to be predominant, with 41.6(4)% [74, 98, 100]. Thus, it can be expected that in ^{134}In, the lowest multiplet of states belonging to the $\pi 1g_{9/2}^{-1}\nu 2f_{7/2}^{3}$ configuration forms a Paar's parabola [120] with 7^- also being the lowest-lying member [121].

In the previous β-decay study of ^{134}In, expected spin-parity values for the parent nucleus were restricted to a range from 4^- to 7^-, with 7^- being favored. This assignment was inferred from the observed $\beta 1n$-decay feeding to excited states in ^{133}Sn [19]. In this thesis, the dominant $\beta 1n$-decay feeding to the $(9/2^-)$ state at 1561 keV was confirmed. Transitions deexciting other states in tin isotopes have at least ten times lower intensity. Furthermore, preference for the population of high-spin levels in daughter nuclei is evident from the observation of the neutron-unbound $(11/2^-)$ state in ^{133}Sn.

The $\beta\gamma$-decay branch of ^{134}In, identified for the first time in this thesis, provides another argument for a high spin of the parent nucleus. Among the levels involved in the well-known yrast $6^+ \to 4^+ \to 2^+ \to 0^+_{g.s.}$ cascade in ^{134}Sn [20, 35, 36], only the 6^+ state was observed to be fed by the β decay. The lack of the β-decay feeding to the lower energy 2^+ and 4^+ levels indicates the high-spin value for the ^{134}In ground state, which can be 6^- or 7^-.

Admittedly, relying on γ-ray intensities deduced using HPGe detectors for the decay of a nucleus with large β-decay energy, $Q_\beta = 14.5$ MeV [16], and significant contribution of γ-ray emission from neutron-unbound states might be considered unreliable. Moreover, spins and parities of the parent and daughter nuclei involved in GT decays of ^{134}In are conducive to the population of high-energy states that can decay via fast $E1$ transitions to low-lying levels in ^{134}Sn. These γ rays may be able to compete with neutron emission. Such an effect has been reported in the ^{78}Ni region for neutron-rich ^{83}Ga [101]. If this effect also occurs for ^{134}In, then it is possible that the 6^+ state is not fed via *ff* decays but instead through high-energy $E1$ transitions from GT-fed levels not seen by high-resolution γ-ray detectors. However, even in this scenario, assuming significant β-decay feeding to the high-energy states deexciting through unobserved γ rays to low-lying levels in ^{134}Sn (pandemonium effect [122]), the 7^- assignment for the ^{134}In ground state remains valid. In that case, only fast transitions feeding the 6^+ state from above, resulting in a spin change of only one unit, should be considered.

Further support for the 7^- ground-state spin-parity assignment for ^{134}In is provided by the recent discovery of a microsecond isomeric state in this nucleus [123]. Its identification allowed the first verification of the shell-model predictions for ^{134}In. The new level was interpreted as a yrast 5^- state decaying via $E2$ isomeric transition to the 7^- ground state. Since the shell-model calculations reproduce well the microsecond isomer [123], the predicted 7^- ground state of ^{134}In becomes more plausible.

To conclude, by combining the experimental observations presented in this thesis with the arguments from previous studies, the most likely spin-parity value for the ^{134}In ground state was found to be 7^-. Further in this thesis, only this spin-parity assignment is considered.

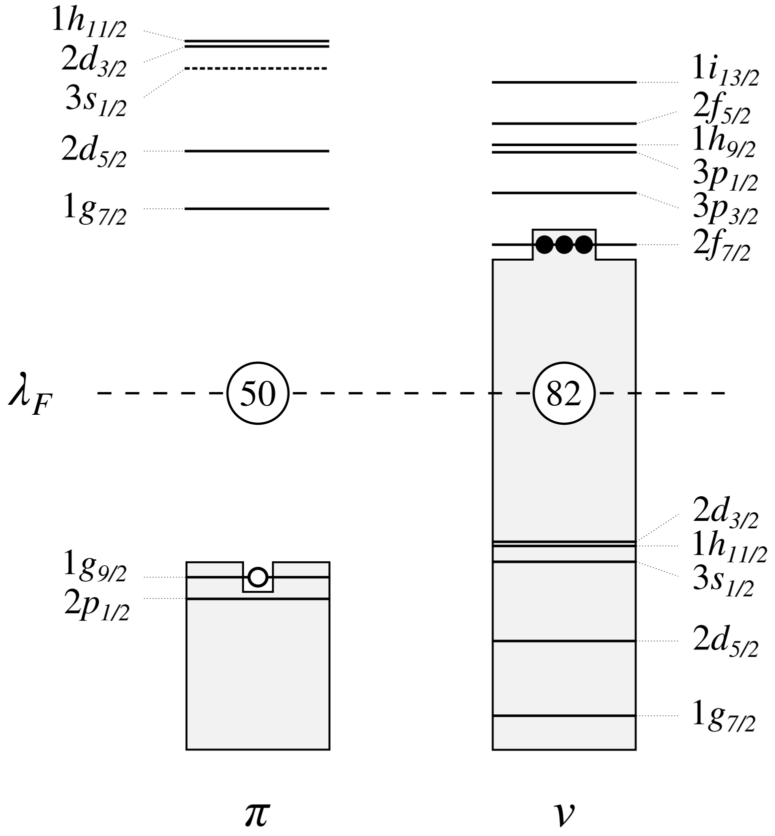

Figure IV.2: Schematic representation of the ground-state configuration for ^{134}In. The open circle indicates the location of the proton hole, while the filled circles indicate the location of three valence neutrons. In order to eliminate the Coulomb energy difference between proton and neutron orbitals, their positions were set with respect to the middle of the shell gap (λ_F). The drawing was prepared following Ref. [119] (see Figure 2 therein).

2 Gamow-Teller β decays

Figure IV.3 shows the positions of single-particle orbitals within major proton and neutron shells involved in GT decays of neutron-rich indium isotopes with $N \geq 82$. The β decay of these nuclei is dominated by the $\nu 1g_{7/2} \rightarrow \pi 1g_{9/2}$ transition [124–126], which is the only possible GT-type β decay that can occur for spin-orbit partner orbitals of the $Z = 28 - 50$ and $N = 50 - 82$ major shells. Therefore, this transition determines the β-decay properties of nuclei with $Z < 50$ and $N \geq 82$, including those of importance for the r-process simulations [49, 127]. This dominant GT transition results in a population of states in daughter nuclei based on couplings of a neutron hole in the $\nu 1g_{7/2}$ orbital and a few neutrons occupying the $\nu 2f_{7/2}$ orbital. Since the $\nu 1g_{7/2} \rightarrow \pi 1g_{9/2}$ transition involves deeply bound neutrons in the ^{132}Sn core, the energies of resulting excitations are larger than the size of the $N = 82$ shell gap.

In the β decay of the lighter odd-odd ^{132}In, a 6^- state in ^{132}Sn arising from the $\nu 1g_{7/2}^{-1} 2f_{7/2}$ configuration populated by a strong GT transition, with $\log ft = 4.6$, was identified at 7211 keV [74, 100]. Analogous allowed β decay of odd-odd ^{134}In should populate the state of the $\nu^{-1}\nu^3$ nature in ^{134}Sn at comparable excitation energy. Due to the even-odd effect in the GT strengths [128], the $\nu^{-1}\nu^2$ and $\nu^{-1}\nu^4$ states in ^{133}Sn and ^{135}Sn populated by the $\nu 1g_{7/2} \rightarrow \pi 1g_{9/2}$ transition of odd-even ^{133}In and ^{135}In are expected at lower excitation energies than identified for the corresponding $\nu^{-1}\nu$ state in ^{132}Sn.

Other GT transitions relevant to neutron-rich indium isotopes correspond to energetically less favorable proton excitations across the $Z = 50$ shell gap. These transitions involve spin-orbit partner orbitals within major neutron and proton $50 - 82$ shells (see Figure IV.3) [125]. They result in $\nu^n \nu^{-1} \pi \pi^{-1}$ configurations in daughter nuclei. States arising from such multiplets appear at high excitation energies, reflecting the sum of shell gap energies at $Z = 50$ and $N = 82$.

Because β-decay energies of ^{133}In, ^{134}In, and ^{135}In are large ($Q_\beta > 13$ MeV), these nuclei provide an excellent opportunity to obtain experimental information about GT transitions that determine the properties of neutron-rich nuclei in the astrophysically relevant ^{132}Sn region. The three isotopes studied in this thesis have predominant βn-decay branches, indicating that the overwhelming majority of the β-decay feeding is located well above the S_n in daughter nuclei. In the following sections, information on GT-fed states populated in β decays of ^{133}In, ^{134}In, and ^{135}In is provided.

2.1 ^{133}In

The ground-state β decay of ^{133}In offers a great opportunity to investigate the $\nu 1g_{7/2} \to \pi 1g_{9/2}$ transition. The lowest level in ^{133}Sn populated via this GT transition has a configuration with two neutrons in the $\nu 2f_{7/2}$ orbital coupled to spin zero and a proton hole in the $\pi 1g_{9/2}$ orbital (see Figure IV.3). Establishing the relative position of the resulting $\nu 1g_{7/2}^{-1} 2f_{7/2}^{2}$ state with respect to the $\nu 2f_{7/2}$ ground state of ^{133}Sn is a first step towards studying systematic trends for more neutron-rich nuclei.

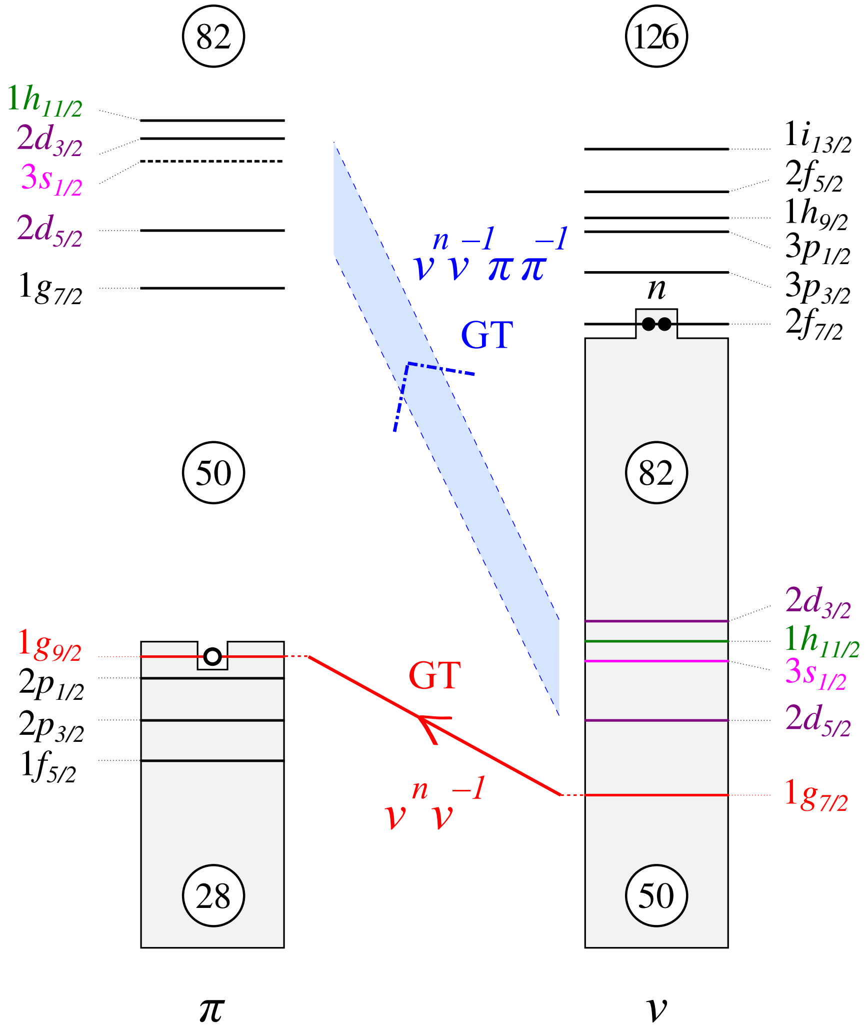

Figure IV.3: A schematic representation of GT transitions relevant to the ground-state β decay of neutron-rich indium isotopes with n neutrons more than the magic number of 82. The $\nu 1g_{7/2} \to \pi 1g_{9/2}$ transition shown in red dominates β decays of these nuclei. A group of other possible GT transitions involving proton particle-hole excitations across the $Z = 50$ shell gap is symbolically indicated in blue. The type of configuration of the state populated via a given GT transition is indicated.

Figure IV.4 shows a schematic interpretation of the ground-state ^{133}In β decay, with dominant GT transitions indicated. Given the expected $9/2^+$ ground-state spin and parity of the parent nucleus, allowed β decays populate $7/2^+$, $9/2^+$, and $11/2^+$ states in the daughter nucleus. The position of the lowest GT-fed level in ^{133}Sn can be estimated from energies of the analogous 6^- and 7^- states in ^{132}Sn, 7211 keV and ~7550 keV [74, 100, 129], respectively, which provide empirical information about the $\nu 1g^{-1}_{7/2}2f_{7/2}$ interaction. Using these values together with known single-particle and single-hole energies from the ^{132}Sn region, the energy of the first $7/2^+$ state arising from the $\nu 1g^{-1}_{7/2}2f^2_{7/2}$ configuration in ^{133}Sn was calculated to be around 6.1 MeV. This excitation energy exceeds the S_n of ^{133}Sn. However, there are favorable circumstances to observe γ-ray deexcitation of neutron-unbound states in this nucleus even at such high energies, which are 3.7 MeV above S_n [16].

Due to the high excitation energy of the first-excited state in ^{132}Sn, 4041 keV [74, 130], the 0^+ ground state is the only state that can be fed in ^{132}Sn following neutron emission from neutron-unbound states in ^{133}Sn located below 6.4 MeV (see Figure IV.5). For high-spin states up to 6.4 MeV in ^{133}Sn, neutron emission is hindered by the angular momentum barrier, allowing γ rays to contribute to their decays. For instance, neutron emission from the $7/2^+$ level located below 6.4 MeV proceeds with $\ell_n = 4$. This means that the γ-ray deexcitation of the GT-fed $7/2^+$ state in ^{133}Sn with an estimated energy of about 6.1 MeV is likely to be observed.

The aforementioned considerations support the interpretation of the 6088-keV transition observed in the ground-state β decay of ^{133}In as deexciting the $7/2^+$ state arising from the $\nu 2f^2_{7/2}1g^{-1}_{7/2}$ configuration in ^{133}Sn. The predicted spectrum of neutrons emitted in the β decay of ^{133g}In [125] and preliminary results from the neutron-spectroscopy measurement of this nucleus [126] yield consistent energy of the $7/2^+$ state populated by the $\nu 1g_{7/2} \rightarrow \pi 1g_{9/2}$ decay. The 6018-keV transition tentatively assigned to the ^{133g}In β decay is a candidate for the γ ray depopulating state in ^{133}Sn belonging to the same multiplet.

It is important to stress that β-decay feedings deduced from the high-resolution β-delayed γ-ray spectroscopy measurement for ^{133g}In cannot be taken as a reliable indicator of the type of the β decay populating given state in the daughter nucleus. In particular, the γ-ray intensity observed for transitions deexciting neutron-unbound states in ^{133}Sn provides information only about a portion of their real β-decay feeding because these states decay dominantly via neutron emission. Therefore, apparent logft values exceeding those expected for the GT-type transition should not be used as an argument to rule out this type of β decay.

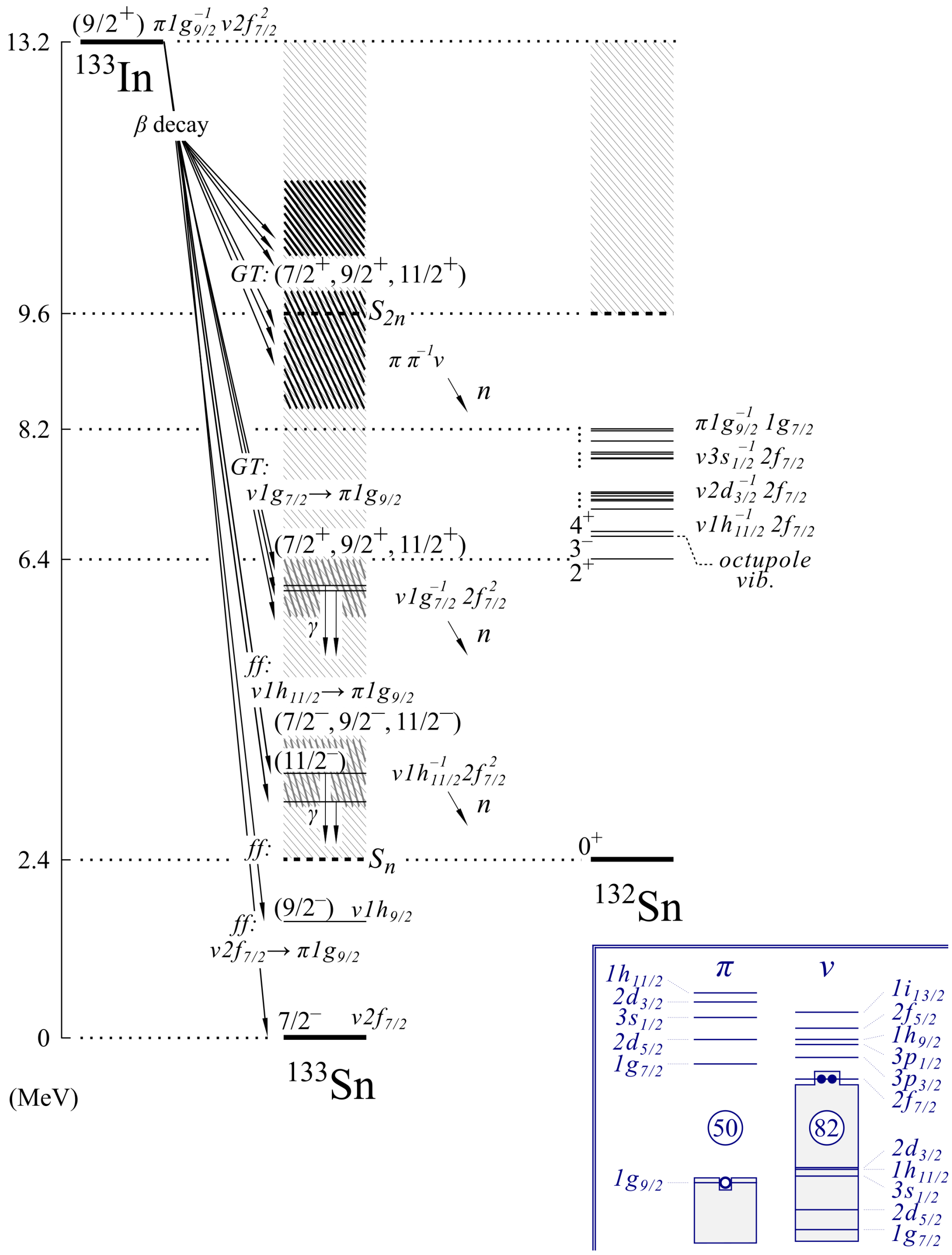

Figure IV.4: Schematic β-decay scheme of ^{133g}In showing GT and *ff* transitions populating neutron-unbound (gray striped areas) and bound states in the daughter nuclei. The expected excitation energies of states built on core excitations are indicated by black striped areas. Neutron-unbound states for which decay via γ-ray emission was observed are indicated. The spin-parity assignments for previously known states in daughter nuclei were taken from Refs. [13, 32, 100]. Schematic representation of proton and neutron orbitals relevant for the β decay of ^{133g}In is shown in blue. The ground-state configuration of the parent nucleus is schematically represented by circles indicating the location of valence neutrons (full circles) and proton hole (open circle) relative to the ^{132}Sn core.

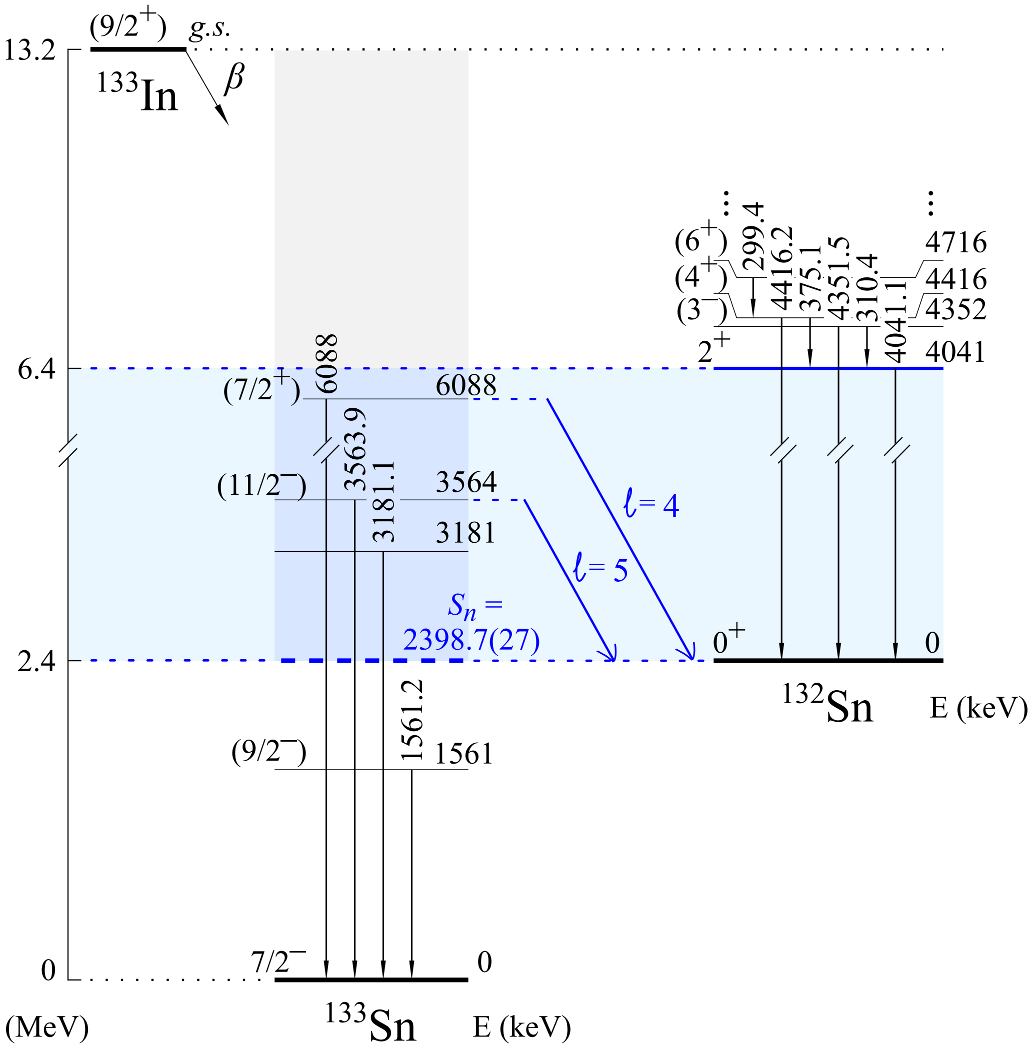

Figure IV.5: Partial β-decay scheme of the ^{133}In ground state showing in blue the βn-decay energy window in which only the ground state of ^{132}Sn can be populated. The βn emission from the $7/2^+$ and $11/2^-$ states located below 6.4 MeV in ^{133}Sn proceed with $\ell = 4$ and $\ell = 5$, respectively. Due to centrifugal barrier hindering the neutron from leaving the nucleus, γ-ray emission can contribute to decays of these neutron-unbound states. The Q_β and S_n values were taken from Ref. [16].

The observed population of excited states in ^{132}Sn up to 5.8 MeV reveals that the βn decay of ^{133g}In proceeds through neutron-unbound states in ^{133}Sn located at energies exceeding 8.2 MeV (see Figure IV.4). Such high-energy levels in ^{133}Sn can be fed by GT decays involving proton orbitals above the $Z = 50$ shell gap. This interpretation arises from the observation of almost the same transitions in ^{132}Sn following the βn decay of the isomeric $(1/2^-)$ state in ^{133}In. Given the different locations of the proton hole below the $Z = 50$ shell gap for the two β-decaying states of the parent nucleus, the population of levels corresponding to proton particle-hole excitations in ^{132}Sn, attributed to the $\pi 1g_{9/2}^{-1} 1g_{7/2}$ configuration [74], following both ^{133g}In and ^{133m}In βn decays can be ascribed to the contribution of proton orbitals above this shell gap.

2.2 ^{133m}In

In the case of the isomeric state of ^{133}In, there is no spin-orbit partner for the $\pi 2p_{1/2}$ orbital in the $N = 50 - 82$ shell to allow any GT transition to occur (see Figure IV.3). The only possible GT decays involve proton orbitals above the $Z = 50$ shell gap. These transitions lead to high-energy excitations in ^{133}Sn, reflecting the sizes of the shell gaps at $Z = 50$ and $N = 82$. Large β-decay energy of ^{133}In, $Q_\beta = 13.2$ MeV [16], makes their population in the $\beta\gamma$-daughter nucleus possible. Observation of the γ rays deexciting the 5.8-MeV state in ^{132}Sn following the ^{133m}In βn decay indicates that neutron-unbound states at energies exceeding 8.2 MeV in ^{133}Sn are fed. As mentioned in the previous section, identification of almost the same levels to be populated in ^{132}Sn via βn decays of both ^{133g}In and ^{133m}In suggests that they are fed from neutron-emitting states in ^{133}Sn built on configurations involving proton particle-hole excitations across the $Z = 50$ shell gap.

2.3 ^{134}In

Figure IV.6 shows a schematic interpretation of the ^{134}In β decay in which transitions populating states in daughter nuclei over a wide β-decay energy window ($Q_\beta = 14.5$ MeV [16]) are indicated. Given the most likely spin-parity assignment of 7^- for the parent nucleus, GT-type β decays populate the 6^-, 7^-, and 8^- states in ^{134}Sn. The dominant $\nu 1g_{7/2} \rightarrow \pi 1g_{9/2}$ transition results in a strong β-decay feeding to states based on the coupling of a neutron hole in the $\nu 1g_{7/2}$ orbital and three neutrons in the $\nu 2f_{7/2}$ orbital.

The β-decay feeding pattern of ^{134}In can be expected to be similar to that observed for ^{132}In, with only a pair of neutrons less. However, deexcitation paths in their $\beta\gamma$-decay daughter nuclei, ^{134}Sn and ^{132}Sn, are different. Allowed β decays of more neutron-rich ^{134}In populate states in ^{134}Sn at energies greatly exceeding the S_n. In the case of ^{132}In, the major β-decay feeding strength by the $\nu 1g_{7/2} \rightarrow \pi 1g_{9/2}$ transition is located below the S_n of ^{132}Sn [74, 98].

In the energy range around 7 MeV, where one might search for a GT-fed state in ^{134}Sn guided by the energy of the analogous level in ^{132}Sn, no transition that can be assigned to the ^{134}In β decay was observed. This suggests that neutron-unbound states in ^{134}Sn populated via dominant GT decay have a negligible γ-ray deexcitation branch. Neutron emission from these states is not limited by kinematic conditions to a particular final state in ^{133}Sn, as is the case for some neutron-unbound states in ^{133}Sn populated following the ^{133g}In β decay.

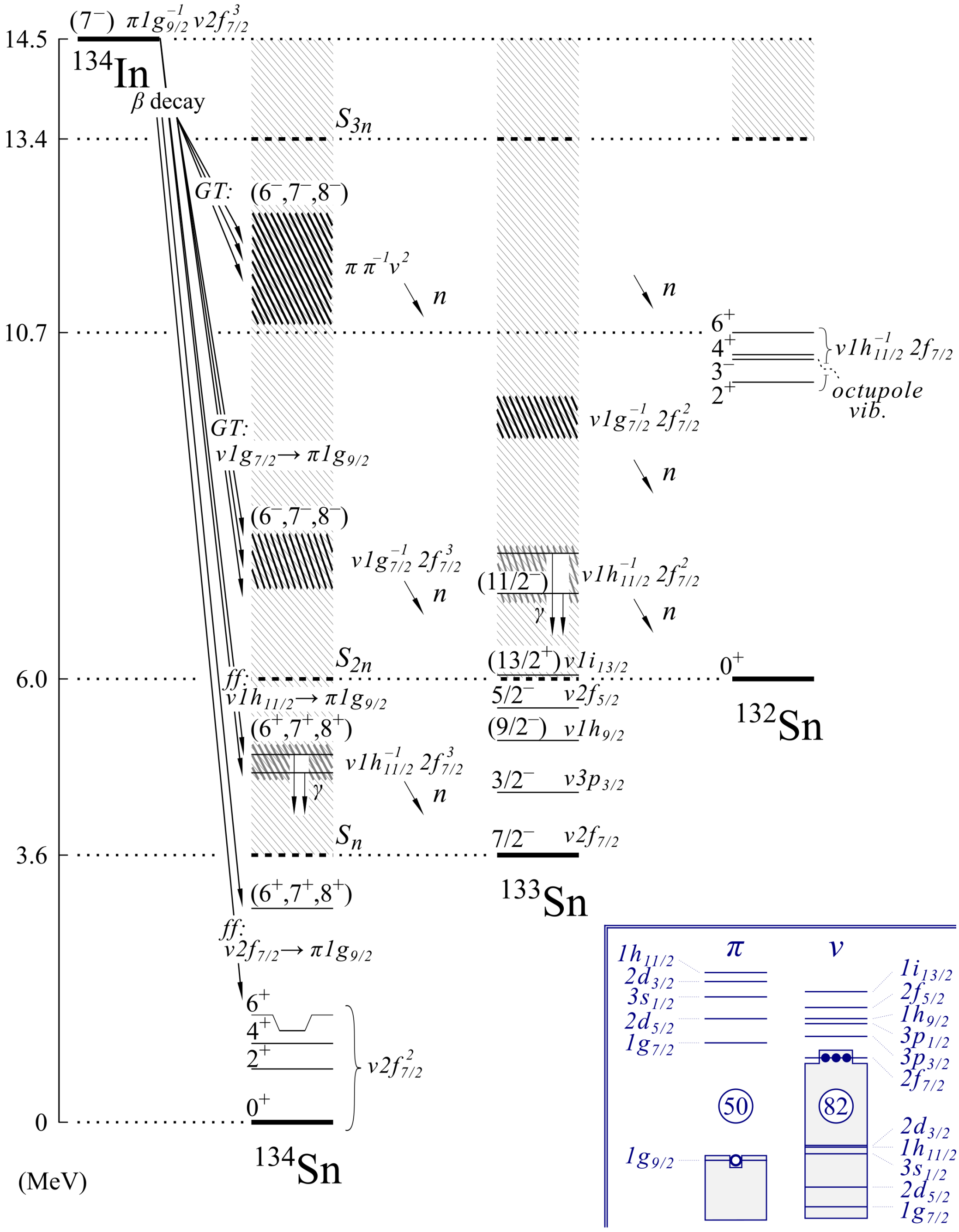

Figure IV.6: Schematic β-decay scheme of ^{134}In showing GT and *ff* transitions populating neutron-unbound (gray striped areas) and bound states in the daughter nuclei. The expected excitation energies of states having core-excited configurations are indicated by black striped areas. Neutron-unbound states for which decay via γ-ray emission was observed are indicated. The spin-parity assignments for previously known states in daughter nuclei were taken from Refs. [13, 19, 20, 100]. Schematic representation of proton and neutron orbitals relevant for the β decay of ^{134}In is shown in blue. The ground-state configuration of the parent nucleus is schematically represented by circles indicating the location of valence neutrons (full circles) and proton hole (open circle) relative to the ^{132}Sn core.

Although the prevalent $\nu 1g_{7/2} \rightarrow \pi 1g_{9/2}$ GT transition feeds neutron-unbound states in ^{134}Sn at energies exceeding the S_{2n}, the $\beta 1n$ emission dominates the ^{134}In β decay, with $P_{1n} = 89(3)\%$. Moreover, the observed population of the 6^+ state at 4716 keV in ^{132}Sn indicates that there is significant β-decay feeding to the levels in ^{134}Sn at energies exceeding 10.7 MeV, which is more than 4.7 MeV above the S_{2n} (see Figure IV.6). This β-decay strength most likely originates from GT transitions involving proton particle-hole excitations across the $Z = 50$ shell gap (see Figure IV.3). Their contribution to the βn emission was also revealed in the ^{133}In β decay.

2.4 ^{135}In

The β-decay feeding pattern of $N = 86$ ^{135}In should be similar to that observed for $N = 84$ ^{133}In. An interpretation of the ^{135}In β decay is proposed in Figure IV.7 following the discussion of GT decays of the lighter indium isotope. An additional pair of neutrons in ^{135}In compared to ^{133}In results in a higher density of possible GT-fed levels in ^{135}Sn than ^{133}Sn. The lowest-lying state populated via the $\nu 1g_{7/2} \rightarrow \pi 1g_{9/2}$ transition in ^{135}Sn is expected at energy around 6 MeV, at which the analogous state in ^{133}Sn was identified and tentatively attributed to this GT transition. This energy is close to the S_{2n} of ^{135}Sn, $S_{2n} = 5901(4)$ keV [16]. Therefore, the ^{135}In β decay is dominated by βn-decay branches. In particular, $\beta 1n$ decays are the most prevalent. Identification of transitions depopulating levels above 2 MeV in the $\beta 2n$-decay daughter nucleus, ^{133}Sn, indicates that there is a β-decay feeding to neutron-unbound states in ^{135}Sn at energies exceeding 8 MeV. This β-decay strength can be attributed to GT transitions involving proton particle-hole excitations across the $Z = 50$ shell gap (see Figure IV.3), as it was also concluded for the lighter indium isotopes.

3 First-forbidden β decays

Decays via *ff* transitions involve more orbitals in the $Z = 28 - 50$ and $N = 50 - 82$ major shells than GT transitions. Figure IV.8 shows single-particle states contributing to *ff* decays of neutron-rich indium isotopes. One of these is the $\nu 2f_{7/2} \rightarrow \pi 1g_{9/2}$ transition in which the proton hole in the $\pi 1g_{9/2}$ orbital is filled and the ground state of the daughter nucleus is populated. Other *ff* decays involving the low-lying orbital $\nu 2f_{7/2}$ are energetically less favorable transitions in which proton orbitals above the $Z = 50$ shell gap participate. The $\nu 1h_{11/2} \rightarrow \pi 1g_{9/2}$ decay, with a contribution of deeply bound neutrons in the ^{132}Sn core, is the one that dominates the ground-state *ff* decays of neutron-rich indium isotopes and, in general, nuclei in this mass region [124, 129]. Transitions involving orbitals with low orbital angular momentum located below the $N = 82$ shell gap are relevant to the *ff* decays of isomeric states of odd-A indium isotopes. In these decays, the proton hole in the $\pi 2p_{1/2}$ orbital is filled through the $\nu 2d_{3/2} \rightarrow \pi 2p_{1/2}$ or $\nu 3s_{1/2} \rightarrow \pi 2p_{1/2}$ transitions.

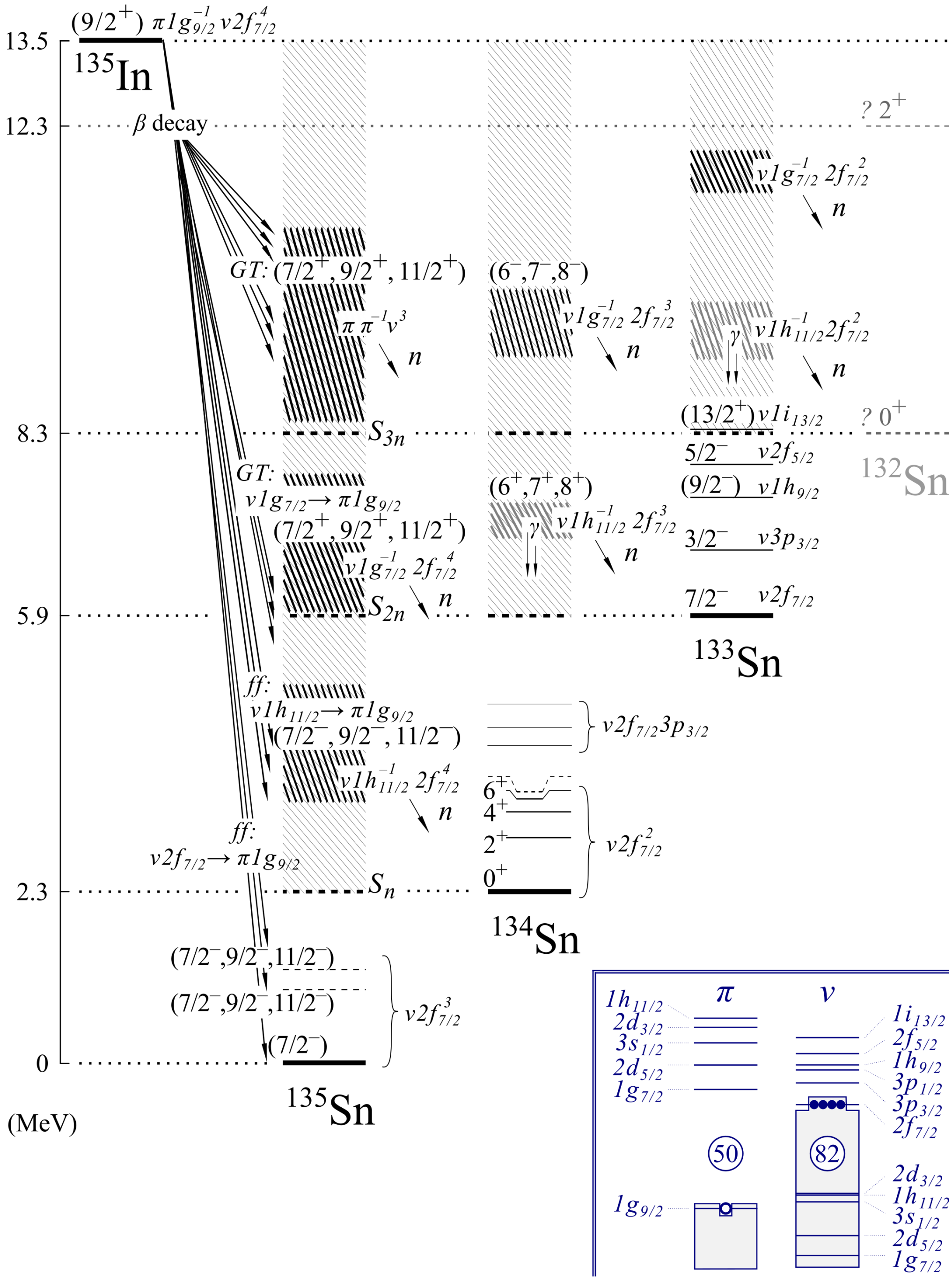

Figure IV.7: Schematic β-decay scheme of ^{135}In showing GT and *ff* transitions populating neutron-unbound (gray striped areas) and bound states in the daughter nuclei. The expected excitation energies of states built on core excitations are indicated by black striped areas. The spin-parity assignments for previously known states in daughter nuclei were taken from Refs. [13, 32, 100]. Schematic representation of proton and neutron orbitals relevant for the β decay of ^{135}In is shown in blue. The ground-state configuration of the parent nucleus is schematically represented by circles indicating the location of valence neutrons (full circles) and proton hole (open circle) relative to the ^{132}Sn core.

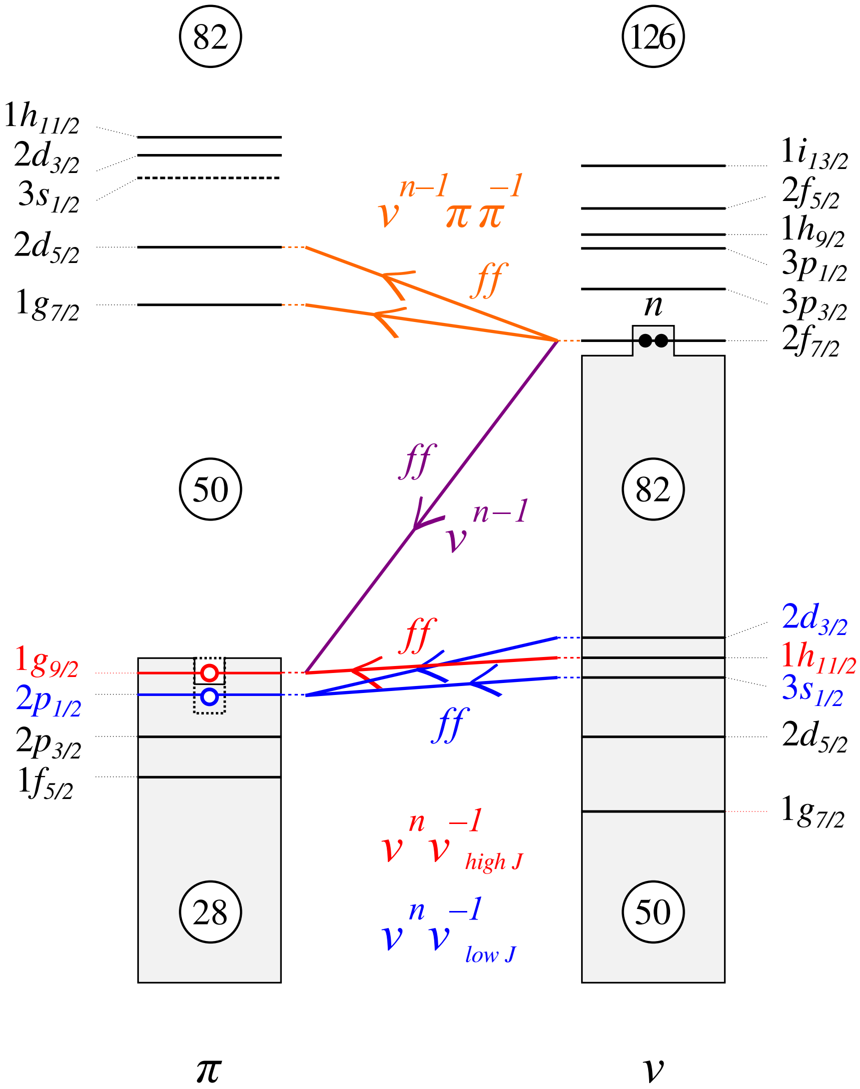

Figure IV.8: A schematic representation of *ff* transitions relevant to the ground- and isomeric-state β decay of neutron-rich indium isotopes with n neutrons more than the magic number of 82. The $\nu 1h_{11/2} \rightarrow \pi 1g_{9/2}$ transition shown in red dominates *ff*-type ground-state β decays. The $\nu 2d_{3/2} \rightarrow \pi 2p_{1/2}$ and $\nu 3s_{1/2} \rightarrow \pi 2p_{1/2}$ transitions shown in blue dominate *ff*-type isomeric-state β decays. Other possible *ff* transitions are also shown. The type of configuration of the state populated via a given *ff* transition is indicated.

The aforementioned *ff* decays of neutron-rich indium isotopes lead to the population of either the ground state or states built on the $\nu^n\nu^{-1}$ or $\nu^{n-1}\pi\pi^{-1}$ configurations in the daughter nucleus (see Figure IV.8). Due to the involvement of orbitals deeply bound in the $N = 82$ ^{132}Sn core or those above the $Z = 50$ shell gap, such excitations appear at high excitation energies, exceeding S_n.

Examining systematic trends of levels with neutron-hole configurations in the odd-A tin isotopes with $N < 82$ allows us to estimate relative positions of states of this nature in more neutron-rich tin isotopes. Excitation energies of the considered levels, shown in Figure IV.9, follow a smooth trend. The three lowest states, having configurations with a neutron hole in the $\nu 2d_{3/2}$, $\nu 1h_{11/2}$, and $\nu 3s_{1/2}$ orbitals, are located within a 300-keV range. They lie around 2 MeV below the GT-fed state with a neutron hole in the $\nu 1g_{7/2}$ orbital. Similar relative positions between analogous levels are expected for heavier odd-A tin isotopes.

States at low excitation energies in tin isotopes beyond $N = 82$, corresponding to excitations of neutrons in the $N = 82 - 126$ major shell, can be populated only via *ff*-type β decays of neutron-rich indium isotopes. Properties of these states reflect the nature of neutron orbitals above the $N = 82$ shell closure. Large β-decay energies of neutron-rich indium isotopes, combined with a dominance of their GT and *ff* decays populating levels above $S_{1n/2n}$ of daughter nuclei, hinder the β-decay feeding to low-energy states in tin isotopes. Nevertheless, for each parent nucleus studied in this thesis, these *ff*-fed states were observed (^{133}Sn and ^{134}Sn) or tentatively identified (^{135}Sn) in daughter nuclei.

With information on the population of low-energy states in ^{133}Sn and ^{134}Sn, having well-established spin-parity assignments, it was possible to infer the properties of β-decaying states of parent nuclei and some of neutron-unbound states. Although the identification of the *ff*-type of β decay does not warrant a certain spin-parity determination, a simple structure of tin isotopes as well as fairly well-studied single-particle and single-hole states in the ^{132}Sn region make tentative spin-parity assignments possible is some cases. In the next sections, information on *ff*-fed states populated following β decays of ^{133}In and ^{134}In is provided.

3.1 ^{133}In

In the β decay of ^{133}In, the population of states in ^{133}Sn below the excitation energy of 6 MeV, where the GT resonance is expected, is solely due to *ff* transitions (see Figure IV.4). Two β-decaying states of ^{133}In, differing significantly in spin values, provide a great opportunity to exploit *ff*-decay selectivity to investigate separately the lower and higher spin states in ^{133}Sn, and thus to probe independently various single-particle excitations as well as states of the $2p1h$ nature built on excitations of the ^{132}Sn core (see Figure IV.10).

The *ff* decays of the $(9/2^+)$ ground state of ^{133}In lead to a population of $(7/2^-)$, $(9/2^-)$, and $(11/2^-)$ states. The $\nu 1h_{11/2} \rightarrow \pi 1g_{9/2}$ transition is the most favorable one (see Figure IV.8). In the *ff* decays of the $(1/2^-)$ isomer, the $(1/2^+)$

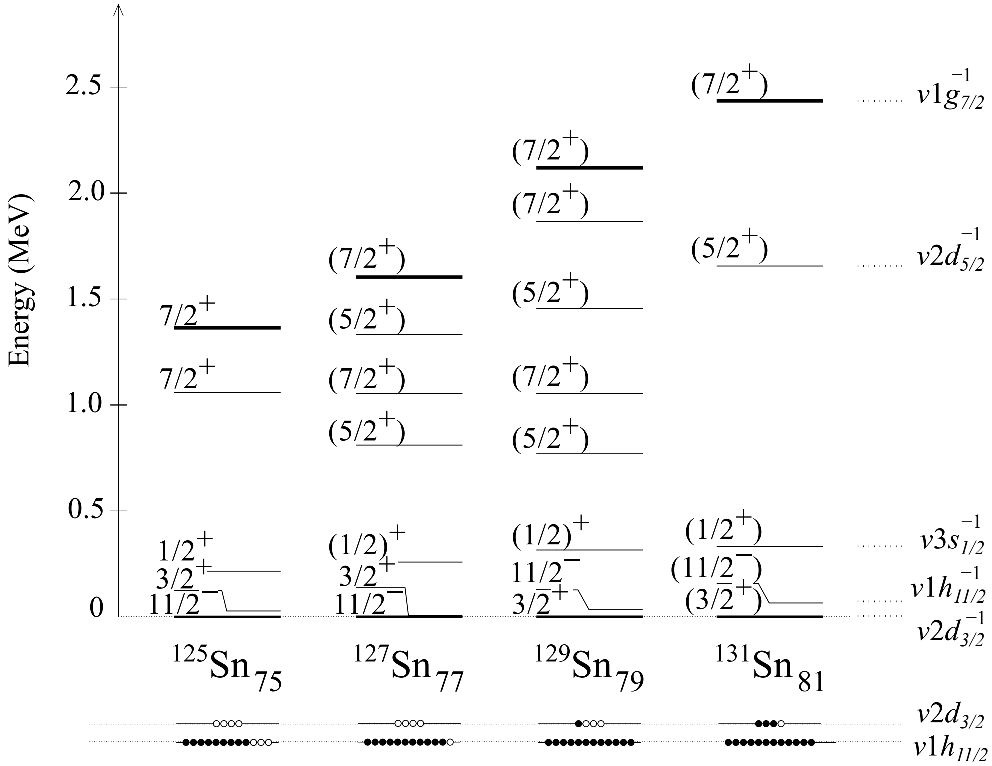

Figure IV.9: Systematics of the low-lying $1/2^+$, $3/2^+$, $5/2^+$, $7/2^+$, and $11/2^-$ levels in odd-A $^{125-131}$Sn observed in the β decay of $^{125-131}$In [131–133]. The $7/2^+$ states indicated by bold lines receive the biggest feedings in the β decay of the $9/2^+$ ground states of indium isotopes.

and $(3/2^+)$ levels are fed through the $\nu 3s_{1/2} \rightarrow \pi 2p_{1/2}$ and $\nu 2d_{3/2} \rightarrow \pi 2p_{1/2}$ transitions. According to the systematics of odd-A $^{125\text{-}131}$Sn, the two lowest-lying states of neutron-hole nature in ^{133}Sn should be the $3/2^+$ and $11/2^-$ levels (see Figure IV.9). Their positions in ^{131}Sn are less than 100 keV apart. It can be expected that corresponding excitations in ^{133}Sn also appear in a similar energy range.

In the analogous β decay of the $(9/2^+)$ ground state of ^{131}In, the $(11/2^-)$ level in ^{131}Sn, with configuration $\nu 1h_{11/2}^{-1}$, is the only state of neutron-hole nature populated below the GT-fed state $(\nu 1g_{7/2}^{-1})$ [131]. Taking as a reference the 6088-keV level in ^{133}Sn interpreted as arising from the $\nu 2f_{7/2}^{2} 1g_{7/2}^{-1}$ configuration, the $3/2^+$ and $11/2^-$ states are expected about 2 MeV lower in energy (see energy spacing between corresponding excitations in ^{131}Sn in Figure IV.9). Three levels were identified in the β decay of the $(9/2^+)$ ground state of ^{133}In in a consistent energy range, 2−3 MeV below the considered GT-fed state in ^{133}Sn. Although they are located above S_n of the daughter nucleus, their deexcitation via γ rays was observed, as the neutron emission is hindered by the centrifugal barrier (see Figure IV.5).

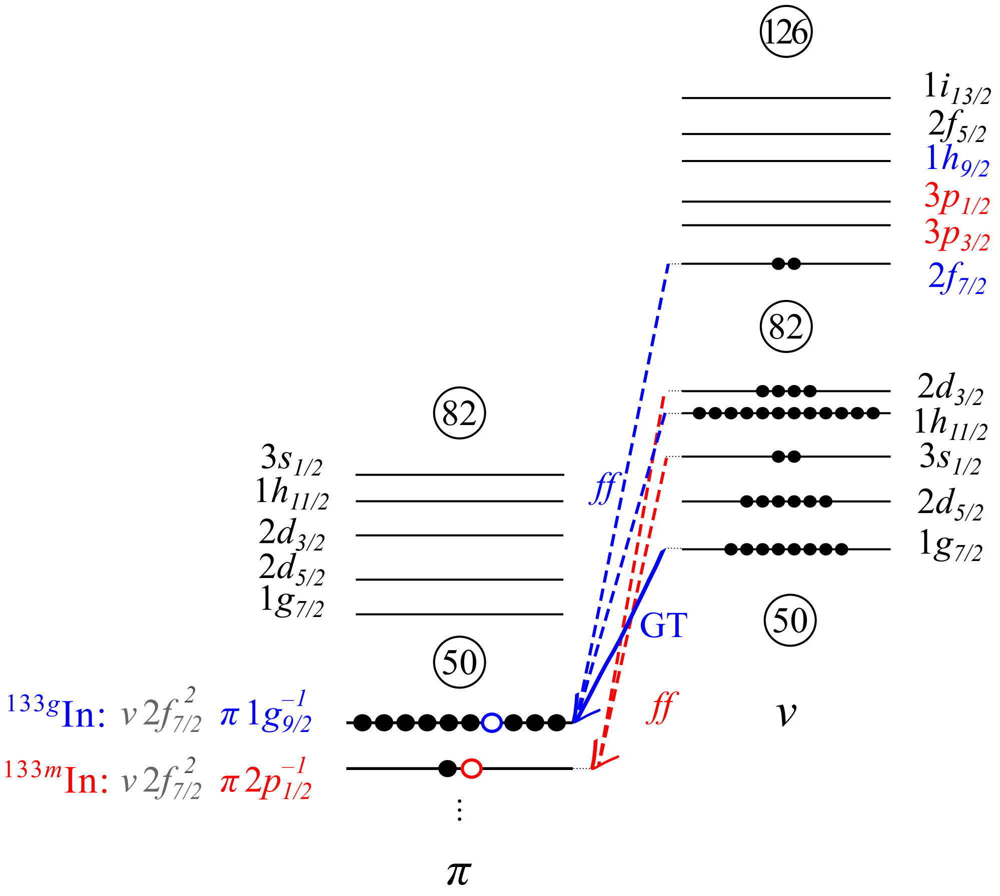

Figure IV.10: Schematic view of proton and neutron orbitals involved in the dominant *ff* decays of the ground and isomeric states of ^{133}In.

One of these, the 3564-keV level, corresponds to the previously reported neutron-hole $(11/2^-)$ state, which is populated via the $\nu 1h_{11/2} \rightarrow \pi 1g_{9/2}$ transition [13, 19]. The energy spacing between levels assigned to configurations with a neutron hole in the $\nu 1h_{11/2}$ and $\nu 1g_{7/2}$ orbitals is the same in ^{131}Sn and ^{133}Sn. In the β decay of the isomeric $(1/2^-)$ state of ^{133}In, no high-energy transitions were identified that could be attributed to *ff* transitions resulting in configurations with a neutron hole in the $\nu 2d_{3/2}$ or $\nu 3s_{1/2}$ orbitals. Due to low spin values of the corresponding levels and, consequently, the absence of a centrifugal barrier, their deexcitation by γ rays is not expected.

Thanks to the large spin difference of the two β-decaying states in ^{133}In, it is possible to probe independently different *ff* transitions populating single-particle states in ^{133}Sn. Three known transitions deexciting the $1/2^-$ $(\nu 3p_{1/2})$, $3/2^-$ $(\nu 3p_{3/2})$, and $(9/2^-)$ $(\nu 1h_{9/2})$ levels in ^{133}Sn were identified as unique lines, observed in the β decay of only one state of ^{133}In. In contrast, the β-decay feeding to the $5/2^-$ $(\nu 2f_{5/2})$ level was not evident in the β decay of the $(9/2^+)$ ground state or the $(1/2^-)$ isomer. The $13/2^+$ state was also not identified.

3.2 ^{134}In

The population of states below the excitation energy of 7 MeV in ^{134}Sn, where the first GT-fed level should appear, is due to *ff* decays of ^{134}In (see Figure IV.6). The $\nu 1h_{11/2} \rightarrow \pi 1g_{9/2}$ transition is the one that has a major contribution to this β-decay feeding (see Figure IV.8). Two new states found in ^{134}Sn at excitation energies of 4759 and 5010 keV are most likely populated via this *ff* transition, resulting in the $\nu 1h^{-1}_{11/2} 2f^{3}_{7/2}$ configuration. These levels are expected to be analogous to the $(11/2^{-})$ state at 3564 keV in ^{133}Sn fed via the same *ff* transition (see Section IV 3.1). Such assignment is supported by the shell-model calculations with core excitations, which predict the first state from this multiplet at around 5 MeV in ^{134}Sn [134] (more details in Section IV 7.3.2).

Only two states below S_n are fed in ^{134}Sn following the ^{134}In β decay. One is a well-known 6^{+} level at 1247 keV belonging to the yrast cascade [20, 35], while the other is a newly identified state at 2912 keV. Observation of the β-decay feeding to only one member of the $\nu 2f^{2}_{7/2}$ multiplet allows us to infer the ground-state spin and parity of the parent nucleus, benefiting from the selectivity of the *ff* decays (see Section IV 1.2).

A particular remark should be made about the 354-keV transition, which is confirmed in this work as following the β decay of ^{134}In [19]. Due to the lack of $\beta\gamma\gamma$ or $\gamma\gamma$ coincidence relations, its assignment to one of the daughter nuclei is not possible. A state decaying directly to the ground state cannot be placed at such a low excitation energy in the level scheme of ^{133}Sn or ^{134}Sn. In view of the enhanced contribution of γ-ray deexcitation to the decay of levels above S_n of daughter nuclei of ^{134}In, one might consider the possibility that the 354-keV γ ray is emitted from a neutron-unbound state for which the centrifugal barrier hinders neutron emission. Once a γ ray has been emitted with the associated angular-momentum transfer, the level that has been fed could subsequently decay via neutron emission.

3.3 ^{135}In

The $\beta\gamma$-decay branch of ^{135}In is based entirely on tentative assignment. Taking into account the most probable $9/2^{+}$ ground-state spin and parity of the parent nucleus, the two transitions at 950 keV and 1221 keV are proposed in ^{135}Sn with spin-parity values of $7/2^{-}$, $9/2^{-}$, or $11/2^{-}$. With such excitation energies, they can be attributed to levels arising only from *ff* decays. In analogous β decay of the $(9/2^{+})$ ground state of ^{133}In, only two bound states in ^{133}Sn were observed: the $7/2^{-}$ $(\nu 2f_{7/2})$ ground state and the $(9/2^{-})$ $(\nu 1h_{9/2})$ excited state. The contribution of *ff* transitions to the β decay of ^{135}In is expected to be similar to that observed for ^{133}In. However, it should be stressed that the structure of the three-valence-particle nucleus is more complex than the one-valence-particle nucleus. Therefore, more bound states can be populated via *ff* transitions in ^{135}Sn than in ^{133}Sn.

4 β-delayed neutron emission

Determination of βn-decay branching ratios for ^{133}In and ^{134}In as well as identification of the dominant β-decay branch of ^{135}In allow for verification of the predictions of the models used for calculating β-decay properties of r-process nuclei beyond experimental reach. Experimental $P_{1n,2n}$ values obtained in this thesis are compared with theoretical predictions based on quasiparticle random phase approximation (QRPA) [135], the relativistic Hartree-Bogoliubov (RHB) model with the proton-neutron relativistic QRPA (RQRPA) [39], as well as the phenomenological effective density model (EDM) [136] (see Table IV.1). For the QRPA, it is possible to compare three successively extended models, some of which take into account not only GT transitions but also *ff* transitions and competition between all available decay modes of neutron-unbound states [38, 135, 137, 138].

In the case of ^{133}In, for which only one βn-decay branch was observed, calculations consistently indicate a dominance of the $\beta 1n$ emission. The QRPA predictions are the closest to the measured value, while the other two models underestimate the P_{1n} value, especially RHB+RQRPA. Incorporating further effects in the QRPA-based models introduces little change in the predicted values. The inclusion of *ff* transitions in the second version of the QRPA predictions, QRPA-2 [137], leads to a reduction in the P_{1n} value by only 7%. The latest version of the QRPA calculations, QRPA+HF [38, 138], yields practically the same result for ^{133}In as the previous one.

More interesting is the comparison for ^{134}In, for which two competing βn-decay branches were observed. The inclusion of *ff* transitions in the QRPA-2 leads to an increase in the P_{1n} value for this nucleus by a factor of about ten with respect to the QRPA-1, in which only GT transitions were considered. A larger contribution of the $\beta 1n$ emission from ^{134}In is predicted by RHB+RQRPA, which accounts for both GT and *ff* transitions. However, in the RHB+RQRPA calculations, the total probability of βn emission ($P_{n,tot}$) is lower ($\approx$ 66%) than in the two first variants of the QRPA calculations, where $P_{n,tot}$ exceeds 90%. Besides, the predicted branching ratio of the $\beta 1n$ decay remains lower than the experimental result. The dominant contribution of the $\beta 1n$ emission from ^{134}In is predicted by the most recent QRPA calculations, QRPA+HF, in which the statistical Hauser-Feshbach (HF) model [38] is incorporated to address competition between one- and multiple-neutron emission as well as γ-ray deexcitation in the decay of neutron-unbound states. The P_{1n} value predicted by the QRPA+HF, which also accounts for *ff* transitions, is the closest to the experimental value for ^{134}In among the models considered. In the case of the P_{2n}, the experimental value is well reproduced only by the EDM. This approach also accounts for the competition between one- and multiple-neutron emission as well as γ-ray deexcitation above the S_n. If the cutoff method is applied to the EDM, so that the decay of states above S_{1n} (S_{2n}) proceeds only via emission of one (two) neutron(s), the calculated probabilities change significantly; $P_{1n} = 28\%$ and $P_{2n} = 39\%$ [139].

Table IV.1: Comparison of predicted and experimental values of $P_{1n,2n}$ (%) for ^{133}In, ^{134}In, and ^{135}In. Results of calculations using three successively improved approaches based on QRPA: QRPA-1 [135], QRPA-2 [137] and QRPA+HF [38, 138] as well as based on RQRPA [39] and EDM [136, 139] are presented. Data were taken from Ref. [40]. Predictions of the EDM model after applying the cutoff model (EDM$_{cutoff}$) [136, 139] are also presented.

Nucleus	^{133}In		^{134}In		^{135}In	
Method	P_{1n}	P_{2n}	P_{1n}	P_{2n}	P_{1n}	P_{2n}
QRPA-1	99.6	0.4	0.60	99.4	86.2	8.3
QRPA-2	92.7	0.2	6.5	86.7	23.5	64.3
QRPA+HF	93	0	78	15	86	10
RHB+RQRPA	67.2	0.4	18.9	46.8	49	41.2
EDM	84.3	0	64.5	2.2	52.4	1.2
EDM$_{cutoff}$	–	–	28	39	–	–
Experiment:	90(3)	–	89(3)	9(2)	–	–

A comparison of the different $P_{1n,2n}$ calculations for ^{134}In shows that the best reproduction of the experimental values is achieved when *ff* transitions and all possible deexcitation paths of neutron-unbound states are taken into account. Indeed, the inclusion of competition between the emission of one and multiple neutrons as well as γ rays following the ^{134}In β decay is relevant, because the $\beta 1n$-decay branch of ^{134}In was observed to be dominant even though the GT resonance is located substantially above the S_{2n} of ^{134}Sn. Moreover, neutron-unbound states decaying via γ rays were observed in the two daughter nuclei of ^{134}In, ^{134}Sn and ^{133}Sn. In the previous study, it was estimated that around 25%−35% of the decays of neutron-unbound states populated in ^{133}Sn following the one-neutron knockout from ^{134}Sn proceed via γ-ray emission [13]. The enhanced γ-ray deexcitation of states above S_n was explained by the small spectroscopic overlap between states involved in neutron emission.

A similar nuclear structure effect is expected to play a role in the β decay of ^{134}In, both in $\beta\gamma$- and $\beta 1n$-decay branches. The GT decays of neutrons from the $N = 82$ ^{132}Sn core result in the population of states in ^{134}Sn formed by couplings of the valence neutrons to core excitations ($\nu^{-1}\nu^3$ or $\pi\pi^{-1}\nu^2$, see Figure IV.3). The wave functions of the states populated following neutron emission have little spectroscopic overlaps with the low-lying states in ^{133}Sn, having a single-particle nature [17]. For this reason, γ rays are able to compete with neutron emission well above S_n. Similar structure effects leading to the hindrance of neutron emission were identified in other βn emitters [101, 140, 141]. Interestingly, the QRPA+HF calculations estimate a minor change, below 3%, in the calculated P_{1n} values if an increase of one order of magnitude to the γ-ray strength function is assumed [38]. However, such γ-ray emission enhancement would have a larger effect on the neutron capture rates of neutron-rich nuclei.

For the most neutron-rich indium isotope studied in this thesis, it was not possible to determine the $P_{1n,2n}$ values. However, it was possible to indicate the $\beta 1n$-decay branch as the dominant one. This qualitative finding provides valuable information because ^{135}In is the lightest odd-A indium isotope for which models predict a significant contribution of the $\beta 2n$ decay (compare predictions for ^{133}In and ^{133}In; shown in Table IV.1). The contribution of this β-decay branch is overestimated by two models, namely QRPA-2 and RHB+RQRPA. In general, it can be concluded that QRPA-2, RHB+RQRPA, and EDM calculations underestimate the P_{1n} value for ^{135}In.

5 *Single-particle* $\nu 1i_{13/2}$ *state*

The β decay of ^{134}In offers favorable conditions to search for the missing single-particle $\nu 1i_{13/2}$ state in ^{133}Sn. The the ground-state spin of the parent nucleus is expected to be high, most likely 7^-, and the $\beta 1n$-decay branch populating states in this tin isotope practically dominates the decay. The high excitation energies of the predicted multiplets in ^{134}Sn involving the $\nu 1i_{13/2}$ orbital are also advantageous (more details in Section IV 7.3.2). The lowest-lying state arising from the $\nu 2f_{7/2}1i_{13/2}$ configuration is expected at an excitation energy of around 4−5 MeV [142] or 3.2 MeV [143], where negative-parity neutron $2p1h$ excitations are also predicted. Due to the high density of negative-parity levels in ^{134}Sn with a contribution of the $\nu 1i_{13/2}$ orbital, there is a chance that they are mixed with $2p1h$ states. Such admixtures would increase the overlap of the wave functions of states involved in the $\beta 1n$ decay of ^{134}In in which the $13/2^+$ state in ^{133}Sn can be populated. Because spins of the states identified in ^{133}Sn following this $\beta 1n$ decay cover a wide range of values, from $3/2^-$ at 0.85 MeV to $(11/2^-)$ at 3.56 MeV, the population of the $13/2^+$ level does not seem to be hindered in terms of the angular momentum for neutron emission.

The excitation energy of the first $13/2^+$ state in ^{133}Sn was estimated to be 2511(80) keV [34] or between 2360 and 2600 keV (more details in Section IV 7.3.1). The 2434-keV γ ray observed in the ^{134}In β decay, being the only one registered in the energy range between 2100 and 3500 keV, is therefore a natural candidate for a transition depopulating the $13/2^+$ level in ^{133}Sn. Alternative assignment to ^{134}Sn may be excluded due to the large difference between the ^{134}In and ^{134}Sn ground-state spin values. Direct or indirect feeding to an excited state in ^{134}Sn that decays to the 0^+ ground state is unlikely in the β decay of ^{134}In with (7^-) ground state. The 2434-keV transition was also observed in the ^{135}In β decay, in which other states in ^{133}Sn are populated in the $\beta 2n$-decay branch. The same arguments may be used to explain the population of the $13/2^+$ state in ^{133}Sn via the $\beta 2n$ decay of ^{135}In as outlined for its population via the $\beta 1n$ decay of ^{134}In.

The decay of the $13/2^+$ state to the $7/2^-$ ground state in ^{133}Sn can proceed via an $E3$ transition with an expected lifetime of around 2 ns. Its decay via a cascade of $M2$ and $M1$ transitions, through the $(9/2^-)$ state at 1561 keV, can also be anticipated. In the analogous nucleus in the ^{208}Pb region with one neutron above the core, ^{209}Pb, a $15/2^-$ level corresponding to the $\nu 1j_{15/2}$ single-particle state decays via an $E3$ transition to the $9/2^+$ ground state ($\nu 2g_{9/2}$) and via an $M2$ transition to the $11/2^+$ excited state ($\nu 1i_{11/2}$) [144, 145]. The observed relative intensities of these two transitions are 100(2) and 11(1), respectively. Relying on the similarity of the corresponding excitations in the ^{132}Sn and ^{208}Pb regions [34, 93, 94, 146–148], the $E3$ transition is anticipated to dominate the decay of the $13/2^+$ state in ^{133}Sn, as is the case in the decay of the analogous $15/2^-$ state in ^{209}Pb. Therefore, the non-observation of an $M2$-$M1$ cascade from the 2434-keV level is consistent with the γ-ray branching ratios deduced for the $15/2^-$ state in ^{209}Pb.

For the sake of completeness, it is worth mentioning that a 2434-keV transition was identified in ^{131}Sn [131]. However, an excited state with that energy cannot be populated in ^{131}Sn following the ^{134}In β decay due to an insufficient β-decay energy window.

6 Spin-parity assignments for daughter nuclei

In this section, experimental observations from different β-decay branches of neutron-rich indium isotopes are brought together to provide key information obtained in this thesis on excited states in ^{133}Sn, ^{134}Sn, and ^{135}Sn. These observations are combined with interpretations already discussed, arising from the selectivity of the β-decay process, experimental systematics of the lighter tin isotopes, and expected analogies to β decays of less exotic indium isotopes.

6.1 ^{133}Sn

Experimental information on states in ^{133}Sn was obtained in total from four β decays: $\beta\gamma$-decay branches of the ground and isomeric states of ^{133}In as well as $\beta 1n$- and $\beta 2n$-decay branches of ^{134}In and ^{135}In, respectively. Figure IV.11 shows the level scheme of ^{133}Sn established in this thesis. In total, four new excited states were identified, and one tentative state was proposed. Different spins and parities of indium isotopes, namely $(1/2^-)$, $(9/2^+)$, and (7^-), made it possible to investigate states in ^{133}Sn over a wide range of their spin-parity values. For the latter two β-decaying states of parent nuclei, angular momentum carried by β-delayed neutrons also contributes, expanding the population possibilities in βn-decay branches compared to *ff* transitions.

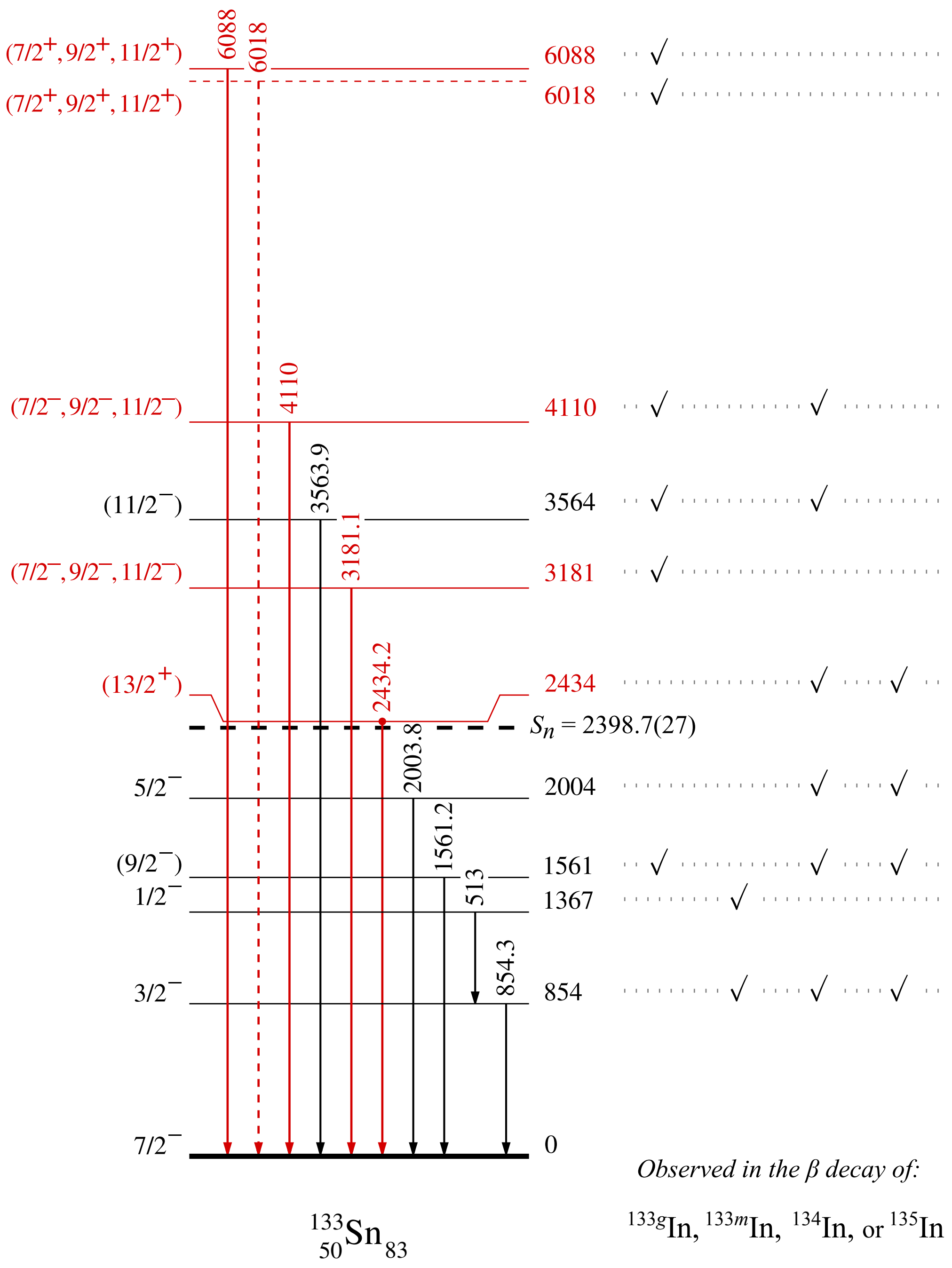

Figure IV.11: Experimental level scheme of ^{133}Sn. New states reported in this thesis are shown in red. The β decays of indium isotopes in which a particular transition was observed are labeled on the right. The experimental spin-parity assignments for previously known states were taken from Refs. [19, 32]. The S_n value was taken from Ref. [16].

All known single-particle states in ^{133}Sn were observed, and consistent information relevant to their spin-parity assignments was obtained. In the case of the ^{133}In β decay, the low-spin single-particle states, $3/2^-$ at 854 keV and $1/2^-$ at 1367 keV, were observed solely in the $(1/2^-)$ isomer decay, while the high-spin single-particle $(9/2^-)$ state at 1561 keV was identified only in the $(9/2^+)$ ground-state decay. The single-particle $5/2^-$ state at 2005 keV, which was previously reported to be populated in the β decay of ^{133}In [19], was not observed for any of the β-decaying states of this nucleus. The lack of its observation is consistent with the forbiddenness category of transition leading to the population of this state. Similarly, no candidate was observed for the single-particle $13/2^+$ state because its population starting from the $(9/2^+)$ ground state of ^{133}In would proceed as a second-forbidden β decay.

The $3/2^-$, $(9/2^-)$, and $5/2^-$ states in ^{133}Sn were populated through the $\beta 1n$ and $\beta 2n$ decays of ^{134}In and ^{135}In, respectively. In addition, the 2434-keV γ ray being a candidate for the transition depopulating the missing single-particle $13/2^+$ state was seen in these β decays. The resulting 2434-keV level in ^{133}Sn is located slightly above S_n ($\approx$ 35 keV). Its observation in β decays of both ^{134}In and ^{135}In provides a solid argument for the placement in the level scheme of ^{133}Sn, but its interpretation as the single-particle $13/2^+$ state is based entirely on empirical estimates of the last missing neutron single-particle energy in the ^{132}Sn region (see Section IV 7.3.1).

Four new neutron-unbound states decaying via γ-ray emission were identified in ^{133}Sn. In addition, one such level was proposed as tentative. Two of these new states were observed in the $\beta\gamma$- and $\beta 1n$-decay branches of indium isotopes. One is the previously identified $(11/2^-)$ level, which was attributed to the $\nu 2f^2_{7/2} 1h^{-1}_{11/2}$ configuration [13, 19].

For states populated in ^{133}Sn following the $(9/2^+)$ ground-state β decay of ^{133}In, spin values of 7/2, 9/2, or 11/2 are the most probable. These spin values are large compared to the 0^+ ground state of ^{132}Sn, which is the only level that can be fed in the $\beta 1n$-decay daughter nucleus from neutron-emitting states in ^{133}Sn at energies up to 6.4 MeV. Thus, decays of these neutron-unbound states via neutrons are associated with a large centrifugal barrier that makes competing decays via γ-ray emission possible.

Parities of the states in ^{133}Sn were proposed based on the systematics of neutron-hole states in lighter odd-A tin isotopes (see Figure IV.9) and considering the excitation energy of the GT-fed state in ^{132}Sn identified in the ^{132}In β decay [74, 100]. Taking into account the even-odd effect in the GT strengths [128], this energy in ^{132}Sn served as a reference to indicate the expected energy of about 6 MeV for an analogous GT-fed state in ^{133}Sn. On this basis, the 6088-keV level was attributed to the GT decay of $^{133\mathrm{g}}$In, and consequently, its positive parity was proposed. A similar interpretation was suggested for the tentative state at 6018 keV. All levels populated in the ^{133g}In β decay at energies lower than 6 MeV in ^{133}Sn should arise from *ff* transitions, so their negative parity is expected.

6.2 ^{134}Sn

Experimental information on states in ^{134}Sn is obtained from β decays of two indium isotopes, ^{134}In and ^{135}In, through the $\beta\gamma$- and $\beta 1n$-decay branches. These decays, with (7^-) and $(9/2^+)$ ground-state spins and parities of parent nuclei, respectively, give access mainly to high-spin states in ^{133}Sn. Neutron angular momentum introduces more spin population variants to the $\beta 1n$ decay of ^{135}In than those possible via *ff* decays of ^{134}In.

Figure IV.12 shows the level scheme of ^{134}Sn established in this thesis. In total, six new states were identified and one tentative state was proposed in this nucleus. Three levels above 2.9 MeV were assigned from the $\beta\gamma$-decay branch of ^{134}In, while new levels below this energy were deduced from the $\beta 1n$-decay branch of ^{135}In.

Among the four known excited states in ^{134}Sn, only the (8^+) state at 2509 keV identified from the ^{248}Cm fission data [35] was not observed. The yrast cascade built on the 6^+ isomer at 1247 keV was seen in β decays of two indium isotopes. Different β-decay feedings were deduced to the 2^+, 4^+, and 6^+ states involved in this cascade. In particular, the 6^+ state was identified to be the only one that receives β-decay feeding from ^{134}In. Because this state has well-established spin and parity, this observation allowed the expected spin-parity value for the ground state of the parent nucleus to be narrowed down to 7^- (see Section IV 1.2). Consequently, relying on the selectivity of the β decay, it enabled the spins of the newly identified levels in ^{134}Sn fed by the ^{134}In β decays to be proposed as 6, 7, or 8. For new states in ^{134}Sn assigned from the ^{135}In $\beta 1n$ decay, the γ-ray decay branch only to the 4^+ level at 1073 keV was observed. A low spin can be expected for a tentatively proposed state at 1321 keV, which decays via the 595-keV transition to the 2^+ state at 726 keV.

After recent identification of high-energy neutron-unbound states decaying via γ-ray emission in ^{133}Sn [13], ^{134}Sn was found to be another isotope in which this phenomenon occurs. Such states were observed in the ^{134}In β decay, so high-spin values of 6, 7, or 8 can be attributed to them. These states are expected to be analogous to the $(11/2^-)$ level of the neutron $2p1h$ nature in ^{133}Sn.

For new states in ^{134}Sn located below S_n, positive parity resulting from the nature of low-lying neutron orbitals above the $N = 82$ shell gap can be proposed (see Figure IV.6). An additional argument arises from the population pattern by GT and *ff* decays. The position of the first GT-fed state in ^{134}Sn is expected to be comparable to the location of the analogous state known in ^{132}Sn, which is fed by the same GT transition [100]. Such a state was identified in ^{132}Sn at 7 MeV [100]. Based on this energy and systematics of neutron-hole states in lighter odd-A tin isotopes (see Figure IV.9), it is possible to indicate relative energies at which states of neutron-hole nature populated via *ff* transitions should appear in ^{134}Sn. These considerations imply the expected positive parity for all levels below 7 MeV in ^{134}Sn. In particular, levels at around 5 MeV can be interpreted as positive-parity states arising from the neutron $3p1h$ configuration.

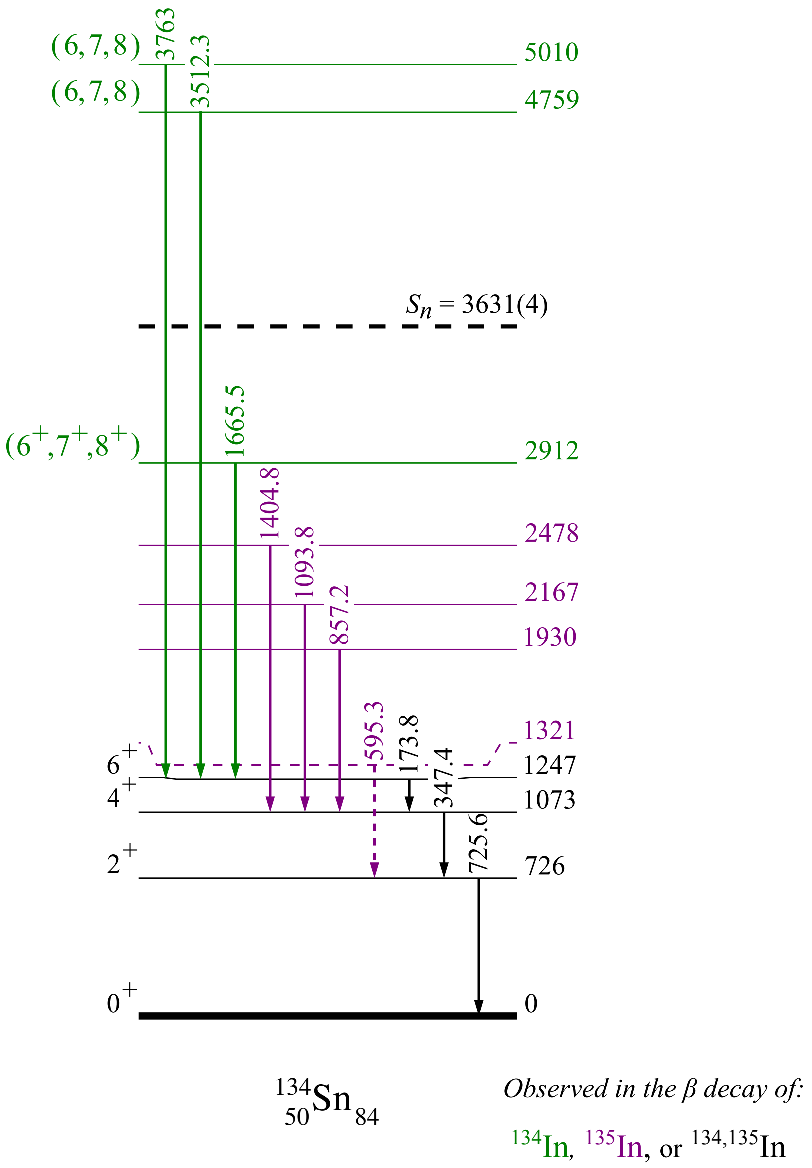

Figure IV.12: Experimental level scheme of ^{134}Sn. New states reported in this thesis are shown in colors. Transitions observed solely in the ^{134}In β decay are shown in green, while those observed only in the ^{135}In β decay are shown in violet. Transitions observed in both β decays are shown in black. The experimental spin-parity assignments for previously known states were taken from Refs. [20, 35]. The S_n value was taken from Ref. [16].

6.3 ^{135}Sn

Experimental information on excited states in ^{135}Sn is based entirely on a tentative assignment from the $\beta\gamma$-decay branch of ^{135}In. Two transitions, 950 keV and 1221 keV, were placed in the level scheme as decaying to the ($7/2^-$) ground state (see Figure IV.13). At such low excitation energies, only *ff* transitions can populate states in this nucleus. Taking into account the most probable $9/2^+$ ground-state spin and parity of the parent nucleus, these two levels were proposed as $7/2^-$, $9/2^-$, or $11/2^-$.

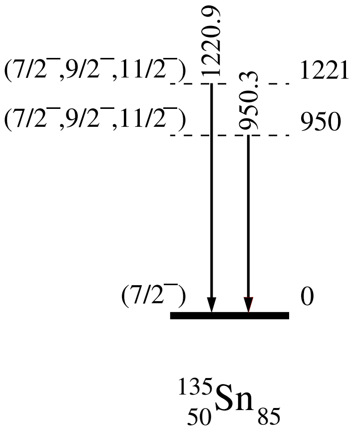

Figure IV.13: Excited states tentatively proposed in ^{135}Sn. The ground-state spin-parity assignment is based on systematics of the $Z = 50$ isotopes [29].

7 Shell-model predictions

7.1 Shell-model description

Neutron-rich tin isotopes with a proton magic number $Z = 50$ and a few more neutrons than the neutron magic number $N = 82$ represent excellent cases of nuclei for which the simplest possible theoretical description can be applied. Within the shell-model framework, these isotopes can be described using the ^{132}Sn nucleus as an inert core and only one or a few neutrons outside this core. The applicability of the shell-model approach to interpret the structure of nuclei around ^{132}Sn arises from the doubly magic nature of this nucleus. Such nature is evident from the high energy of the first-excited state in ^{132}Sn (4041 keV [100, 130]), low S_n values for nuclei in its closest vicinity [16], and large spectroscopic factors (≈ 1) determined for low-lying states in ^{133}Sn, which revealed the purity of single-neutron excitations in this one-valence-neutron nucleus [17].

Figure IV.14 shows a typical model space used in the shell-model calculations for nuclei in the ^{132}Sn region having one or a few more nucleons than magic numbers $Z = 50$ and $N = 82$. This model space is built on the ^{132}Sn core consisting of single-particle orbitals below shell closures at $Z = 50$ and $N = 82$, which are filled with particles and considered to be inert in the mean-field approximation. Valence nucleons occupy successive single-particle states outside the core. In general, five proton and six neutron orbitals are taken into account, which, once filled with nucleons, correspond to the next major shell closures at $Z = 82$ and $N = 126$. The nature of filled valence orbitals determines the properties of low-energy states in the considered nuclei.

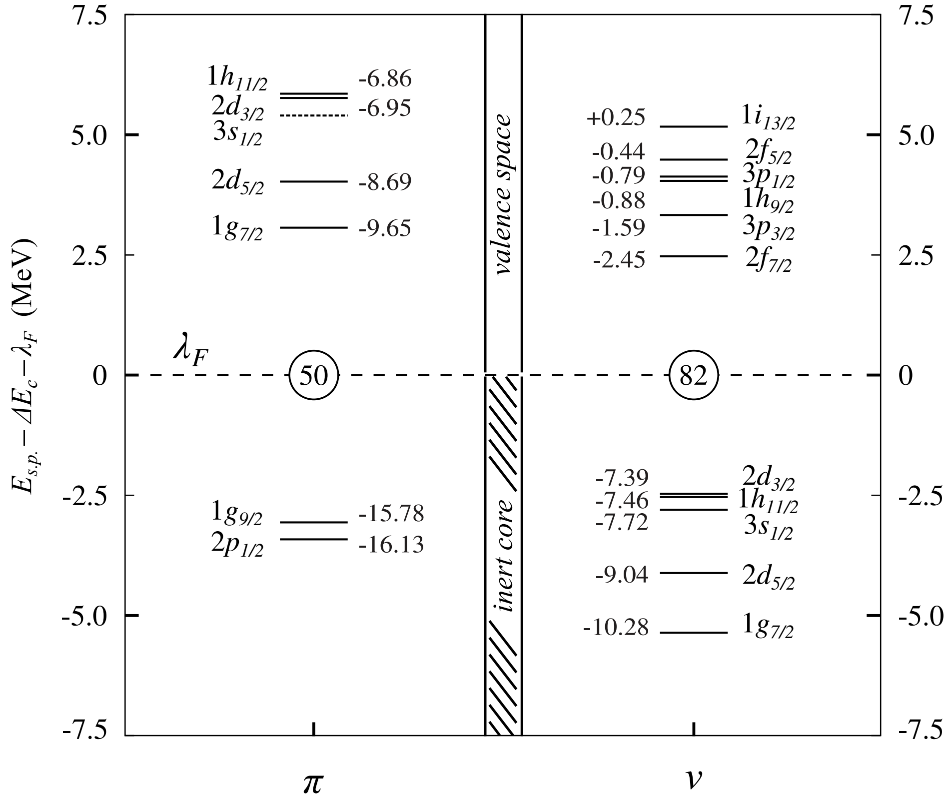

Figure IV.14: Experimental single-particle energies ($E_{s.p.}$) of proton (π) and neutron (ν) orbitals for the doubly magic ^{132}Sn. In order to eliminate the Coulomb energy difference (ΔE_c) between proton and neutron orbitals, energies are normalized to the middle of the shell gap (λ_F). Proton and neutron orbitals frozen in the core and those forming valence space in most of the shell-model calculations for neutron-rich nuclei in the ^{132}Sn region are indicated. The figure was prepared following Ref. [119] (see Figure 2 therein).

In tin isotopes beyond $N = 82$, states were identified not only at low excitation energies, by which is meant below their S_n values, but also at those comparable to or even higher than the $N = 82$ shell gap energy ($\approx$ 4 MeV [142, 149]). For ^{133}Sn and ^{134}Sn, new levels at energies up to around 5−6 MeV were observed, which are attributed to *ff* and GT transitions involving deeply-bound neutrons in the $N = 82$ ^{132}Sn core. This means that the typical shell-model space used in calculations for nuclei from the ^{132}Sn region is insufficient for studying the resulting high-energy excitations.

In order to investigate the entire deexcitation pattern observed in tin isotopes beyond $N = 82$ following β decays of neutron-rich indium isotopes, an extended valence space is required, allowing the two types of excitations to be studied. One class covers excitations of valence particles while the second one corresponds to excited states formed by couplings of the valence particles to core excitations. The extended valence space should be understood therefore as the one that involves more single-particle orbitals than the typical model space employed in the ^{132}Sn region (see Figure IV.14).

Shell-model calculations using extended valence space for heavy nuclei are computationally challenging, especially the diagonalization of the Hamiltonian matrix due to its extremely large size. Computational effort increases rapidly as the number of single-particle orbitals forming the valence space enlarges. The size of the adopted model space is therefore limited by the present computational capabilities, hindering a comprehensive understanding of the structure of all excited states. For this reason, a computationally optimal core must be chosen, which is realized in practice by the opening of only a few single-particle orbitals just below shell closures. Constraints on interpretation due to the core approximation become apparent as the excitation energy of the states under study increases because orbitals deeply bound in the core or those located well above it are needed to explain high-energy excitations.

7.2 Overview of the calculations

A brief overview of the shell-model calculations available for neutron-rich tin isotopes is provided in this section. These calculations use different valence spaces as well as various nucleon-nucleon (NN) interactions. Identifying the differences between the various shell-model variants is essential to understand the limitations of each approach and to explain possible differences in their predictions.

7.2.1 Extended valence spaces

For nuclei in the ^{132}Sn region, shell-model calculations with extended valence spaces were reported in several studies [134, 150–154]. Various restrictions on the model space were made, for instance, ^{116}Sn ($Z = 50$, $N = 66$) [134], ^{110}Zr ($Z = 40$, $N = 70$) [153, 155], or ^{78}Ni ($Z = 28$, $N = 50$) [150] were employed as cores. Among these calculations, only one study focuses on neutron-core excitations in neutron-rich tin isotopes [134].

H. Jin *et al.* presented the results of large-scale shell-model calculations, further referred to as Jin2011 [134], in which an extended pairing-plus-quadrupole model with monopole corrections (EPQQM) was employed to determine two-body interaction matrix elements [156]. The valence space used in the EPQQM calculations included five proton orbitals between $Z = 50$ and 82: $\pi 1g_{7/2}$, $\pi 2d_{5/2}$, $\pi 3s_{1/2}$, $\pi 2d_{3/2}$, and $\pi 1h_{11/2}$, five neutron orbitals above $N = 82$: $\nu 2f_{7/2}$, $\nu 3p_{3/2}$, $\nu 3p_{1/2}$, $\nu 1h_{9/2}$, and $\nu 2f_{5/2}$, as well as two neutron orbitals below $N = 82$: $\nu 1h_{11/2}$ and $\nu 1d_{3/2}$. With such a model space, it was possible to investigate core-excited states with a neutron hole in the $\nu 1h_{11/2}$ or $\nu 1d_{3/2}$ orbitals. It is worth noting that the $\nu 1i_{13/2}$ orbital from the $N = 82 - 126$ shell was not included in the valence space. Particle-hole excitations of protons in the $Z = 50$ ^{132}Sn core were also not considered. In the Jin2011 calculations, the experimental energies of states in nuclei with one valence particle or hole with respect to the doubly magic ^{132}Sn core, ^{133}Sb, ^{133}Sn, and ^{131}Sb, were not taken directly as single-particle energies, as is usually done. Energies for the shell-model basis were determined by comparing the EPQQM calculations for known states in these nuclei and in the $A = 134$ isobars containing two valence particles, such as, ^{134}Te, ^{134}Sn, and ^{134}Sb. In this way also the proton-proton, neutron-neutron, and proton-neutron interactions were obtained.

H. Naïdja *et al.* performed shell-model calculations in which couplings between core excitations and valence particles were also considered [155]. In their study, further referred to as Naid2015, a realistic interaction was derived from the charge-dependent Bonn (CD-Bonn) NN potential [157, 158] renormalized through the V_{low-k} approach [159]. The renormalized CD Bonn interaction is also referred to in the literature as RCDB. In Naid2015, empirical corrections were introduced to the V_{low-k} interaction to ensure the reproduction of the single-particle energies in ^{133}Sn and ^{133}Sb and their masses. Two versions of the interactions were tested: the original (NNS110) and the modified one that incorporates corrections to the pairing strength (NNS110P). In the chosen valence space, containing seven neutron orbitals: $\nu 1h_{11/2}$, $\nu 2f_{7/2}$, $\nu 3p_{3/2}$, $\nu 3p_{1/2}$, $\nu 1h_{9/2}$, $\nu 2f_{5/2}$, and $\nu 1i_{13/2}$, and five proton orbitals: $\pi 1g_{9/2}$, $\pi 1g_{7/2}$, $\pi 2d_{5/2}$, $\pi 2d_{3/2}$, and $\pi 3s_{1/2}$, ^{110}Zr acts as a core nucleus. This means that core excitations are restricted to the opening of the $\nu 1h_{11/2}$ and $\pi 1g_{9/2}$ orbitals below $N = 82$ and $Z = 50$ shell gaps, respectively. Despite the relevant valence space, high-energy states arising from the core excitations are not discussed in Naid2015. The presented results are limited to a discussion of the structure of low-lying levels, including the effect of core opening on reduced transition probabilities.

7.2.2 Typical valence space

Shell-model calculations taking into account only one type of excitation, the one involving valence particles, were reported for neutron-rich tin isotopes in several studies [142, 143, 160–166]. Previously known low-energy excitations in these isotopes were shown to be fairly well described using various effective interactions, derived mainly from the CD-Bonn NN potential [157, 158] and various model spaces.

A. Covello *et al.* presented shell-model predictions on excited states in neutron-rich tin isotopes in several works, in 2002 [143], 2007 [161], and 2011 [162]. Their last published results for ^{134}Sn and ^{135}Sn [162], further referred to as Cov2011, were obtained using a realistic effective interaction derived without any adjustable parameter, starting from the CD-Bonn NN potential, which was renormalized following the V_{low-k} approach [159]. It is worth mentioning that the interaction used in these calculations is often referred to in the literature as Napoli interaction. As a valence space, six neutron orbitals of the $N = 82 - 126$ shell were adopted: $\nu 2f_{7/2}$, $\nu 3p_{3/2}$, $\nu 3p_{1/2}$, $\nu 1h_{9/2}$, $\nu 2f_{5/2}$, and $\nu 1i_{13/2}$. An earlier study by this group, presenting predictions for ^{135}Sn, is further referred to as Cor2002 [143].

Kartamyshev *et al.* performed large-scale shell-model calculations for heavy tin isotopes [142] using realistic effective interactions obtained from the CD-Bonn potential through the G matrix renormalization method [167]. In their work, further referred to as Kart2007, valence space consisted of neutron single-particle states: $\nu 2f_{7/2}$, $\nu 3p_{3/2}$, $\nu 1h_{9/2}$, $\nu 3p_{1/2}$, $\nu 2f_{5/2}$, and $\nu 1i_{13/2}$. The results of their calculations are discussed using a generalized seniority approach.

C. Yuan *et al.* reported shell-model calculations for neutron-rich tin isotopes [160], further referred to as Yuan2016, in which proton-proton and neutron-neutron interactions were also derived from the CD-Bonn renormalized G matrix, while the proton-neutron interaction across two major shells was obtained from the monopole-based universal interaction V_{MU} [168] plus the M3Y spin-orbit force [169]. The Hamiltonian used in the Yuan2016 calculations operates in the particle-particle model space. It is worth mentioning that interactions used in these calculations are often referred to in the literature as jj45pna, CWG, and VMU+LS(M3Y) for proton-proton, neutron-neutron, and proton-neutron interactions, respectively. Single-particle orbitals for protons in the $Z = 28-50$ shell: $\pi 1f_{5/2}$, $\pi 2p_{3/2}$, $\pi 2p_{1/2}$, and $\pi 1g_{9/2}$ and for neutrons in the $N = 82 - 126$ shell: $\nu 2f_{7/2}$, $\nu 3p_{3/2}$, $\nu 3p_{1/2}$, $\nu 1h_{9/2}$, $\nu 2f_{5/2}$, and $\nu 1i_{13/2}$ formed the valence space. Single-particle energies used in these calculations were fitted to the experimental energies of corresponding proton-hole and neutron-particle states in ^{131}In and ^{133}Sn, respectively. These energies were not taken directly as the single-particle energies in the Hamiltonian but were modified by the residual proton-proton and proton-neutron interactions.

Although proton orbitals below the typical $Z = 50$ ^{132}Sn core are considered in Yuan2016, the valence space used in these calculations was not classified as extended compared to the most commonly used one, involving proton orbitals between $Z = 82$ and 126. The inclusion of single-particle orbitals below $Z = 50$

in model space practically does not affect the predictions for tin isotopes for which neutron orbitals are key to the interpretation.

A. Kumar *et al.* performed shell-model calculations in which residual interaction based on the CD-Bonn renormalized G matrix was variously modified [163, 164]. Changes were made to the position of the $\nu 1i_{13/2}$ orbital and/or to the diagonal and non-diagonal two-body matrix elements. Calculations were carried out in the valence space between $N = 82$ and 126 using experimental single-particle energies for the following orbitals: $\nu 2f_{7/2}$, $\nu 3p_{3/2}$, $\nu 3p_{1/2}$, $\nu 1h_{9/2}$, $\nu 2f_{5/2}$, and $\nu 1i_{13/2}$. Predictions reported for ^{134}Sn in the recent work, further referred to as Kum2017, were obtained either with or without modifications to the initial interaction. The resulting sets of data were compared with the results of the generalized seniority calculations.

S. and M. S. Sarkar presented shell-model calculations for ^{135}Sn with modified CW5082 interaction [166], originally derived from the ^{208}Pb region [170]. Modifications were introduced to this interaction to reproduce available experimental data in the region of interest. In their work, further referred to as Sar2004, the valence space includes five proton orbitals, $\pi 1g_{7/2}$, $\pi 2d_{5/2}$, $\pi 2d_{3/2}$, $\pi 3s_{1/2}$, and $\pi 1h_{11/2}$, and six neutron orbitals, $\nu 2f_{7/2}$, $\nu 3p_{3/2}$, $\nu 3p_{1/2}$, $\nu 1h_{9/2}$, $\nu 2f_{5/2}$, and $\nu 1i_{13/2}$. For these orbitals, experimental single-particle energies were used. Further improvements to the modified CW5082 interaction were obtained by the inclusion of updated experimental data in the ^{132}Sn region, which were used to change two-body matrix elements.

L. Y. Jia *et al.* performed calculations on low-lying states in ^{135}Sn by applying nucleon pair approximation of the shell model, in which only a few types of collective pairs, as building blocks of the model space, were considered [165]. In their work, further referred to as Jia2007, a separable phenomenological Hamiltonian including the monopole pairing, quadrupole pairing, plus quadrupole-quadrupole interactions between valence particles was used. The valence space consisted of proton and neutron orbitals in the 50-82 major shell: $3s_{1/2}$, $2d_{3/2}$, $2d_{5/2}$, $1g_{7/2}$, and $1h_{11/2}$ and additional neutron orbitals in the $N = 82 - 126$ major shell: $\nu 2f_{7/2}$, $\nu 3p_{3/2}$, $\nu 3p_{1/2}$, $\nu 1h_{9/2}$, $\nu 2f_{5/2}$, and $\nu 1i_{13/2}$. Single-particle energies were taken from experimental data available at that time.

7.2.3 Empirical calculations

There is an additional class of shell-model calculations for nuclei in the ^{132}Sn region, in which excitations are interpreted and predicted using empirical NN interactions. In this approach, excited states under consideration must have firmly determined spin and parity, and their dominant configurations should be identified. For that reason, experimental information on high-spin states is generally used. Typically, multiplet members with maximally aligned spin are considered so that the possible presence of admixtures from other configurations into the wave function is minimized.

In the ^{132}Sn region, there is still a lack of experimental data to calculate all the interactions. Their estimations can be made from corresponding empirical NN interactions known in the ^{208}Pb region for analogous nuclei with respect to the doubly magic core [34, 171–173]. This approach relies on the observed similarity of excitations in nuclei from regions of neutron-rich ^{132}Sn and stable ^{208}Pb, which was revealed in many studies [34, 93, 94, 146–148]. Among the tin isotopes under study, such calculations are available mainly for ^{133}Sn. In order to estimate the last missing neutron single-particle energy in this nucleus, the most recent data on empirical NN interactions in nuclei with a few valence particles or holes with respect to the doubly magic ^{132}Sn are used. This input information, if needed, is complemented by interactions estimated from experimental data on nuclei in the ^{208}Pb region. A renormalization due to the use of different shell-model cores, which in the simplest case leads to the inclusion of the mass scaling factor of $A^{-1/3}$, is included in such calculations.

7.2.4 Single-particle energies

Recognizing differences in valence spaces chosen in various theoretical approaches is essential to understand possible differences in predicted level schemes. Figure IV.15 shows a compilation of model spaces used in shell-model calculations for neutron-rich tin isotopes. Only neutron orbitals were compared because excitations involving proton orbitals are expected at high excitation energies, reflecting the size of the $Z = 50$ shell gap (see Figure IV.14). Such excitations were not considered in the theoretical studies on neutron-rich tin isotopes.

Single-particle energies adopted in shell-model calculations are presented in Figure IV.15 in such a way that the same positions have been fixed for the lowest $\nu 2f_{7/2}$ orbital above the $N = 82$ shell gap. Other single-particle states are presented with respect to this orbital. Not shown in Figure IV.15 are the valence spaces used in Naid2015 [155] and Yuan2016 [160]. In the former, experimental information available at that time for ^{133}Sn was briefly mentioned in this context. It can be assumed that single-particle energies reported in 2014 by J. M. Allmond *et al.* [32] were employed. However, it is not clear what value was used for the $\nu 1i_{13/2}$ orbital, because the identification of this single-particle state in ^{133}Sn was questioned in Ref. [32]. A general reference to the single-particle energies known at that time in the ^{132}Sn region was also given in Yuan2016 [160]. In this case, the specific single-particle energy adopted for the $\nu 1i_{13/2}$ orbital was stated. It is worth noting that the Hamiltonian used in the Yuan2016 calculation fixes the relative single-particle energies to the observed excited states. Final values of the single-particle energies, after modification by the residual proton-proton and proton-neutron interactions, were not provided.

Upon initial review of Figure IV.15, the valence space used in Jin2011 differs significantly from the others. Apart from the inclusion of the two neutron orbitals below the $N = 82$ shell gap and omission of the $\nu 1i_{13/2}$ orbital, there are larger energy gaps between orbital positions than in other variants of valence spaces.

Some differences in single-particle energies for two orbitals, namely $\nu 3p_{1/2}$ and $\nu 1i_{13/2}$, are visible in Figure IV.15. For the former, two values differing by about 290 keV were used. The experimental single-particle energy of the $1/2^-$ state in ^{133}Sn was measured in 2010 [17]. Prior to this, shell-model predictions employed a tentative value proposed in 1996, which was based on unassigned transition observed in the β decay of ^{134}In [19]. More recent calculations used the experimentally determined single-particle energy of the $\nu 3p_{1/2}$ state in ^{133}Sn, which was found to be 290 keV lower than that tentatively proposed. From a series of calculations made by A. Covello *et al.* [143, 161, 162], it is possible to trace how shell-model predictions on excited states in ^{134}Sn changed after updating the single-particle energy of the $\nu 3p_{1/2}$ orbital. Because the single-particle energy of the $\nu 1i_{13/2}$ orbital has not yet been confirmed experimentally, different values were adopted in theoretical studies. Most of them refer to the energy predicted by W. Urban *et al.* from empirical calculations [30] (more details in Section IV 7.3.1).

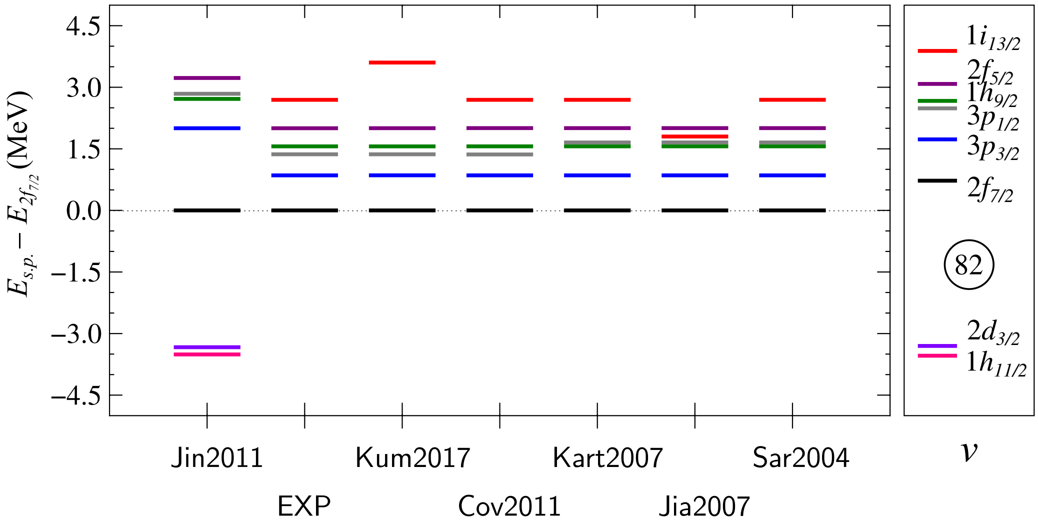

Figure IV.15: Comparison of neutron single-particle energies used in various shell-model calculations for neutron-rich tin isotopes. Normalization with respect to the single-particle energy of the $\nu 2f_{7/2}$ orbital, which was positioned at 0 MeV, was applied. Experimental neutron single-particle energies in ^{133}Sn are also shown (EXP) [32]. Note that the $\nu 1i_{13/2}$ orbital was not considered in Jin2011. On the other hand, only in this work, the two neutron orbitals below the $N = 82$ shell gap were included in the model space. See text and following Refs. for details: Jin2011 [134], Yuan2016 [160], Kum2017 [163], Cov2011 [162], Kart2007 [142], Jia2007 [165], and Sar2004 [166].

7.3 Predictions

Results of the different variants of the shell-model calculations for ^{133}Sn, ^{134}Sn, and ^{135}Sn are presented in this section. Predictions obtained from the individual theoretical approaches are generally limited to a discussion of one of the isotopes of interest. Special emphasis was given to the results presented in Jin2011 [134] and Yuan2016 [160]. The former is the only available theoretical study on neutron-rich tin isotopes in which excitations of the $N = 82$ ^{132}Sn core were considered. This type of excitation is shown in this thesis to be an important component of the deexcitation pattern observed in daughter nuclei following the β decay of neutron-rich indium isotopes. One of the most recent shell-model calculations employing neutron valence space commonly used in this mass region, which is suitable for investigating states at energies up to around 2 MeV, was reported in Yuan2016. New experimental data for nuclei in the ^{132}Sn region, including the recently identified isomer in ^{134}In [123, 160, 174], are faithfully reproduced by the shell-model predictions presented in this work. Therefore, the shell-model interactions used in Yuan2016 can be expected to describe well also low-energy excitations in neutron-rich tin isotopes.

7.3.1 ^{133}Sn

With only one neutron more than the doubly magic ^{132}Sn, ^{133}Sn allows the most straightforward interpretation of its ground and excited states. The shell-model approach provides us with a simple picture describing its structure consisting of a single-valence neutron in the $N = 82 - 126$ major shell, which occupies consecutive neutron orbitals above the $N = 82$ shell closure. Due to the excellent properties of the doubly magic ^{132}Sn as a core nucleus [17, 153, 175], the nature of these orbitals, and consequently, neutron-single-particle energies can be inferred from properties of low-energy excitations in ^{133}Sn. This means that this nucleus is a key system for calibrating theoretical models used to predict the properties of more complex nuclei in this mass region, including those relevant to r-process nucleosynthesis. Therefore, making shell-model predictions of low-energy levels in ^{133}Sn is not relevant, because their experimental energies are model calibration data. However, shell-model calculations are useful in studying states at high excitation energies in this nucleus, especially above its S_n. These may correspond to the last missing neutron single-particle state $\nu 1i_{13/2}$ or levels built on the couplings of valence neutrons to core excitations.

Recent theoretical studies on ^{133}Sn were motivated by one of two reasons. The first motivation was to investigate its high-energy states built on core excitations. This task poses a computational challenge because the opening of the core is required to allow for couplings of valence nucleons to core excitations. The second motivation was to estimate the last unknown neutron single-particle energy in ^{133}Sn. Its estimate was done by employing experimental data available for more complex nuclei in the ^{132}Sn region, in which states with a relatively pure configuration involving the $\nu 1i_{13/2}$ orbital are known. Such estimates are often referred to as empirical shell-model calculations.

Shell-model calculations with core excitations

Reconstruction of states at high excitation energies in ^{133}Sn poses a crucial test of the theoretical treatment of particle-hole excitations across the $N = 82$ shell gap. Shell-model calculations considering this type of excitations were reported for this nucleus so far only in one study, Jin2011 [134]. Results of these calculations are compared with experimental data in Figure IV.16. All levels with neutron $2p1h$ configuration are expected above S_n of this nucleus. Due to the adopted model space in Jin2011 (see Section IV 7.2.1), only two groups of such levels were predicted. Neutron-unbound states with negative parity correspond to a multiplet with a neutron hole in the $\nu 1h_{11/2}$ orbital, while those with positive parity belong to a multiplet with a neutron hole in the $\nu 2d_{3/2}$ orbital.

Experimental information on the neutron-unbound state identified at 3.6 MeV in ^{133}Sn, which was tentatively assigned as a $(11/2^-)$ state arising from the $\nu 2f^2_{7/2}1h^{-1}_{11/2}$ configuration [13], allowed the first verification of these calculations. The lowest state belonging to the $\nu 2f^2_{7/2}1h^{-1}_{11/2}$ multiplet is predicted at 3.6 MeV (see Figure IV.16), which is in excellent agreement with energies reported in two previous works, ~3700 MeV in Ref. [19] and 3570(50) keV in Ref. [13], as well as the more precise energy determined in this thesis, 3563.9(5) keV.

For new levels placed in the level scheme of ^{133}Sn at 3181 and 4110 keV, their attribution to one of the calculated states is more difficult. The lowest member of the $\nu 2f^2_{7/2}2d^{-1}_{3/2}$ multiplet is predicted at 3.4 MeV with spin and parity of $3/2^+$ (see Figure IV.16). The population of such a low-spin state following the β decay of the $(9/2^+)$ ground state of ^{133}In, from which these two levels were assigned to ^{133}Sn, is not expected. At higher energies, between 3.7 and 4.7 MeV, several states are predicted with a wide range of spin values. Those that can be populated following the β decay of the $(9/2^+)$ ground state of ^{133}In originate from the $\nu 2f^2_{7/2}2d^{-1}_{3/2}$ multiplet.

Shell-model calculations presented in Jin2011 do not provide predictions for levels above 5 MeV in ^{133}Sn where two neutron-unbound states were identified, one of which tentatively. This means that the used valence space is insufficient to describe such high-energy excitations in ^{133}Sn. The 6018- and 6088-keV levels must therefore originate from orbitals deeper bound in the ^{132}Sn core than the $\nu 1h_{11/2}$ and $\nu 2d_{3/2}$ orbitals. The expected configuration of these two levels involves the $\nu 1g_{7/2}$ orbital; hence, they cannot be reconstructed in the shell-model calculations presented in Jin2011 because this orbital was assumed to be frozen in the core.

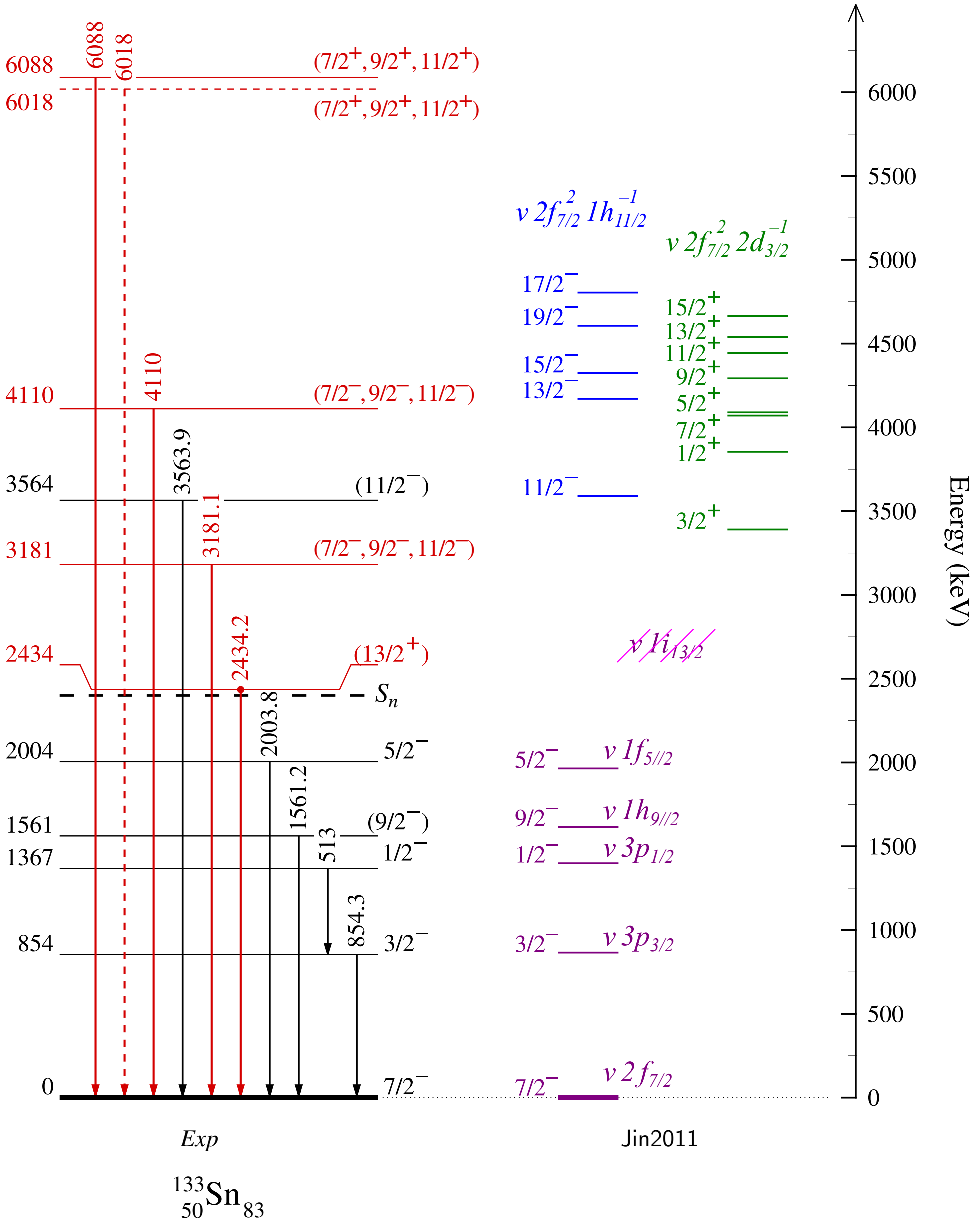

Figure IV.16: The level scheme of ^{133}Sn established experimentally (*Exp*) and predicted by the shell-model calculations with core excitations reported in Jin2011 [134]. The experimental spin-parity assignments for previously known excited states were taken from Refs. [17, 19, 32]. The S_n value was taken from Ref. [16]. Dominant configurations for predicted levels are indicated. Note that the $\nu 1i_{13/2}$ orbital was not considered in Jin2011.

Calculations of single-particle energy

On account of the fact that single-particle energies represent important inputs to the shell-model predictions, an overview of the calculations presented in Section IV 7.2.4 provides information about these energies as used in each variant of computations. When comparing level schemes established within different theoretical approaches, inspection of single-particle energies is valuable, because they may be the source of discrepancies between various shell-model results. Lack of knowledge of the experimental single-particle energy of the $\nu 1i_{13/2}$ orbital is therefore a hindrance in shell-model calculations, and it forces some assumptions to be made to estimate this missing energy.

Most of the shell-model calculations discussed in this thesis use single-particle energy of the $\nu 1i_{13/2}$ orbital estimated from experimental data on ^{134}Sb. W. Urban *et al.* calculated this energy in the ^{132}Sn core potential from the position of the 10^+ level in ^{134}Sb arising from the $\pi 1g_{7/2}\nu 1i_{13/2}$ configuration [30]. For this purpose, the corresponding proton-neutron interaction known for the analogous configuration in the ^{208}Pb region was scaled for use in the ^{132}Sn region [148]. Experimental single-particle energy of the $\pi 1g_{7/2}$ orbital contributing to the $\pi 1g_{7/2}\nu 1i_{13/2}$ multiplet in ^{134}Sb was also included. As a result, single-particle energy of 2694(200) keV was obtained for the $\nu 1i_{13/2}$ orbital. The uncertainty of this estimate includes the uncertainty of the energy of the scaled interaction as well as the accuracy of the reconstruction of excitation energies of other levels in ^{134}Sb for which dominant configurations were also identified.

The estimate provided by W. Urban *et al.* [30] was tested in Cor2002 [143], in which the position of the 10^+ state in ^{134}Sb was calculated employing the single-particle energy proposed for the $\nu 1i_{13/2}$ orbital. The energy of this state was well reproduced with Napoli interactions, supporting the use of the single-particle energy reported in Ref. [30].

Further empirical estimation of the last missing neutron single-particle energy in the ^{132}Sn region was reported by A. Korgul *et al.* [34] following the identification of new high-spin levels in ^{135}Sb. Their estimate was made in the same way as in the previous work by W. Urban *et al.* but using more recent experimental data for nuclei in the ^{132}Sn region, which allowed more empirical NN interactions to be established. Only one proton-neutron interaction energy had to be estimated from interaction known for the analogous configuration in the ^{208}Pb region. As a result, single-particle energy of 2669(70) keV was obtained for the $\nu 1i_{13/2}$ orbital, which is consistent with the value proposed earlier, but its uncertainty was reduced by three. With this new value, the excitation energy of the lowest $13/2^+$ level in ^{133}Sn was deduced to be 2511(80) keV. Interaction between two possible $13/2^+$ states in this nucleus, one corresponding to the pure single-particle $\nu 1i_{13/2}$ state and the other arising from the $(3^- \otimes \nu 2f_{7/2})$ configuration built on the octupole vibrational 3^- state in ^{132}Sn, was accounted for.

A more recent estimate of the single-particle energy of the $\nu 1i_{13/2}$ orbital was proposed by W. Reviol *et al.* following the identification of the second $13/2^+$ state in ^{137}Xe [99]. Experimental information on energies of two $13/2^+$ levels in this nucleus was employed to test their reproduction by shell-model calculations adopting estimates reported by W. Urban *et al.* [30] and independently by A. Korgul *et al.* [34]. Calculations were performed using the theoretical approach as presented in Cov2011, with Napoli interactions. It was evaluated that a better agreement between the calculated and experimental energies is obtained for both $13/2^+_1$ and $13/2^+_2$ levels when single-particle energy of the $\nu 1i_{13/2}$ orbital is assumed to be lower than that proposed by W. Urban *et al.* [30]. Calculations using a lower value of this energy were also tested for levels in ^{134}Sb and ^{135}Sb, which were employed in previously reported estimates. It was concluded that the last missing neutron single-particle energy in this mass region should be between 2360 and 2600 keV. The previous value estimated by A. Korgul *et al.* [34] is within this range.

Narrowing the energy range in which the single-particle $13/2^+$ state is expected in ^{133}Sn is of great help in its experimental identification. The 2434-keV transition observed in the β decay of both ^{134}In and ^{135}In is therefore a natural candidate for the transition deexciting the $13/2^+$ state that has been sought for over two decades. While experimental observations provide solid arguments for placement of the 2434-keV level in ^{133}Sn, proposing its spin-parity value is only possible by invoking theoretical considerations combined with empirical estimates. The purity of the lowest-lying $13/2^+$ level in ^{133}Sn is also an open question. Excitations corresponding to the single-particle $\nu 1i_{13/2}$ state as well as those built on octupole excitation can contribute to its structure.

7.3.2 ^{134}Sn

Reconstruction of measured properties of ^{134}Sn – the nucleus with only a pair of neutrons outside the core – is an important test of the shell-model interactions used to predict the properties of more complex nuclei in the ^{132}Sn region. Previously available experimental information on four excited states in ^{134}Sn [20, 35, 36] allowed the first verification of the theoretical predictions for this nucleus and assisted the development of empirical shell-model interactions used in this mass region [142, 143, 161, 166]. The low-lying yrast cascade in ^{134}Sn, built on the 6^+ isomer at 1247 keV [20], and the (8^+) state found at 2509 keV [35] were well reproduced by early shell-model calculations [142, 143, 161, 162, 165]. Identification of first transitions in more exotic even-A tin isotopes, ^{136}Sn and ^{138}Sn [18], acted as a trigger for improving NN interactions used in this mass region. This made it possible to systematically examine different interactions used to describe the structure of excited states in the three even-A tin isotopes beyond $N = 82$. Reproduction of the measured transition strengths, in particular for the $6^+ \rightarrow 4^+$ transition in ^{136}Sn, was a challenge for the theoretical description, and it motivated the development of improved variants of shell-model calculations, with modifications introduced to the NN interactions [18, 155, 160, 163, 164].

Shell-model predictions reported so far for ^{134}Sn can be grouped into two classes. One group focuses only on previously known low-lying levels and is aimed mainly at reconstructing the measured reduced transition probabilities of $E2$ transitions, designated by $B(E2)$, in three even-A tin isotopes beyond $N = 82$. The second class of calculations involves those that, in addition to discussing known transitions in ^{134}Sn in the context of the measured $B(E2)$ transition strengths, also predict new levels.

Previously known levels

Introducing modifications to the realistic NN interactions in order to reproduce experimental $B(E2)$ values determined for ^{134}Sn, ^{136}Sn, and ^{138}Sn can lead to changes in the predicted excitation energies of states in these isotopes. Such calculations were presented in Kum2017 [163] and Naid2015 [155] as well as by G. Simpson *et al.* in Ref. [18]. These theoretical studies were motivated primarily by an attempt to reproduce the $B(E2, 6^+ \rightarrow 4^+)$ transition strength in ^{136}Sn and were accompanied by an analysis of excitation energies in ^{134}Sn as well. Figure IV.17 shows the changes in the predicted excitation energies for the 2^+, 4^+, and 6^+ states in ^{134}Sn after applying the modifications to the interactions used in the three shell-model approaches.

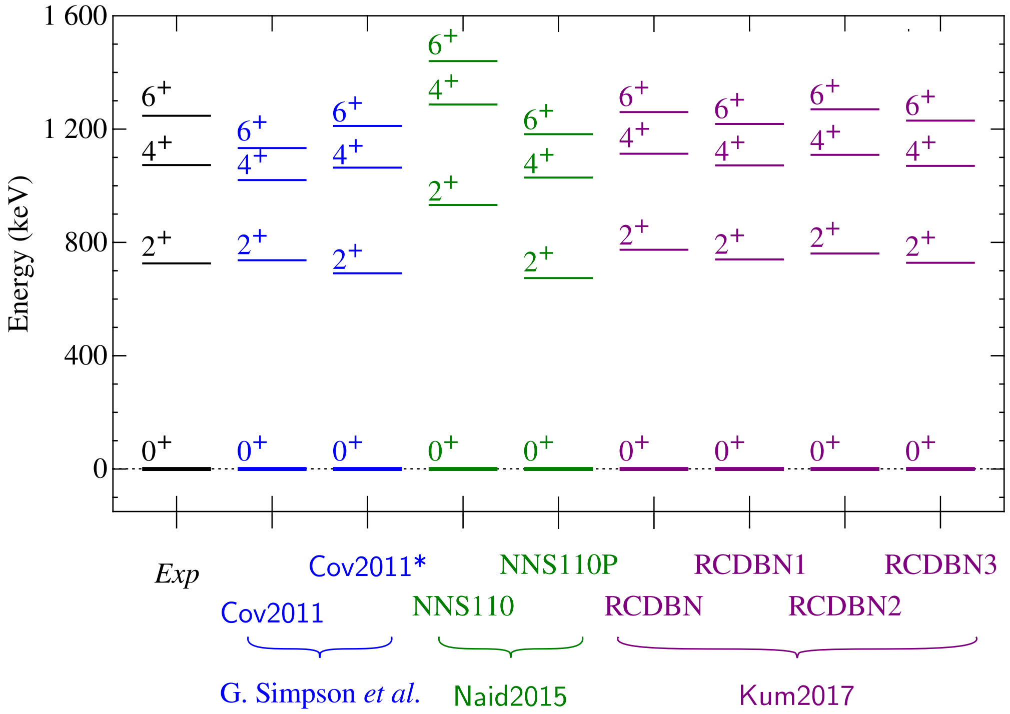

Figure IV.17: Experimental (*Exp*) and predicted energies of the low-lying 2^+, 4^+, and 6^+ levels in ^{134}Sn. Results of three independent approaches to shell-model calculations are presented from: work by G. Simpson *et al.* [18], Naid2015 [155], and Kum2017 [163]. For each approach, various modifications of the originally used interactions were tested. The NN interaction used by G. Simpson *et al.* was taken from Cov2011 [162]. Results obtained after introducing empirical modifications to this interaction are denoted by Cov2011*.

For a brief review of theoretical studies on reduced transition probabilities in ^{134}Sn, the reader is referred to Ref. [18] in which recent experimental information is compared with the results of different shell-model calculations. These include predictions from: Cov2011 [18], Kart2007 [142], and Sar2004 [166]. Results of additional calculations, with effective interactions derived in the same way as in Cov2011, but with smaller effective neutron charge, are presented in Ref. [18]. Empirical changes were independently applied to the initial interaction by partially opening of the ^{132}Sn core and by reducing the neutron pairing strength. The results of the calculations with the latter adjustment are indicated in Figure IV.17 as Cov2011*. Admittedly, the main focus of work by G. Simpson *et al.* was on reproducing the measured $B(E2, 6^+ \to 4^+)$ transition strength in ^{136}Sn. After some modifications were introduced in the NN interaction, the changes in the predictions for three even-A tin isotopes were studied, including variations in predicted excitation energies of the 2^+, 4^+, and 6^+ states in ^{134}Sn. With empirically modified $\nu 2f^2_{7/2}$ matrix elements, serving as an equivalent of a reduction in pairing, the calculated $B(E2, 6^+ \to 4^+)$ value for ^{136}Sn was found to be consistent with the measured one. This modification improved also the agreement in the excitation energies of the 2^+, 4^+, and 6^+ states in ^{134}Sn. The differences between calculated and measured values were below 40 keV. A similar study of the effect of including additional modifications to the NN interactions was performed in two other works [155, 163].

H. Naidja *et al.* carried out shell-model calculations for even-A tin isotopes beyond $N = 82$ using two versions of interactions [155]. In one of them, a reduction in the pairing strength was introduced. This modification resulted in the reconstruction of the experimental $B(E2, 6^+ \to 4^+)$ transition strength in ^{136}Sn and also improved the predicted excitation energies for the 2^+, 4^+, and 6^+ states in ^{134}Sn by lowering them. Findings consistent with those reported by G. Simpson *et al.* [18] were reported, indicating seniority mixing effect for the two lowest 4^+ states in ^{136}Sn.

A similar shell-model investigation of low-energy levels in ^{134}Sn, with various changes applied to the NN interaction, was performed by A. Kumar and B. Maheshwari [163]. Three independent modifications were introduced to the initial interaction (RCDB). One was to change the single-particle energy of the $\nu 1i_{13/2}$ orbital (RCDB1). It was positioned at energy 3.6 MeV higher than the $\nu 2f_{7/2}$ orbital, which corresponds to an increase of 0.8 MeV relative to RCDB. The second change was to reduce the $\nu 2f^2_{7/2}$ matrix elements (RCDB2). The last modification was to apply the two previous changes simultaneously (RCDB3). These changes led to minor variations in the calculated energies of the 2^+, 4^+, and 6^+ states in ^{134}Sn (see Figure IV.17), which were close to the experimental ones in all tested variants. Introducing the two changes simultaneously led to the best agreement, with a maximum difference between experimental and calculated values of the order of 20 keV.

After a recent half-life measurement for the 4^+ state in ^{134}Sn [176], a re-examination of predicted transition strengths for this nucleus should be performed. The experimentally determined $B(E2, 4^+ \to 2^+)$ value exceeds by a factor of two the transition strengths predicted in all available variants of shell-model calculations. One possible explanation for this difference could be the existence of the second 4^+_2 state close in energy to the first 4^+_1 state in ^{134}Sn, which has a different seniority component, in analogy to the effect reported for the 4^+_1 and 4^+_2 states in ^{136}Sn [18, 155]. In such a scenario, wave functions of the two 4^+ states can be mixed, and, as a result, deviations from the pure seniority scheme may occur. Interestingly, the seniority mixing effect was not revealed with previously measured transition strength $B(E2, 6^+ \to 4^+)$ in ^{134}Sn. Because measurements of the lifetimes of excited states in ^{134}Sn were part of another PhD thesis [63], in this work, only this brief review of the predicted $B(E2)$ values for ^{134}Sn is provided for the sake of completeness.

Predictive calculations

Shell-model calculations providing information on states not yet identified in ^{134}Sn are of particular interest here because the experimental information obtained in this thesis resulted in a significant expansion of its level scheme, including seven new states, of which one is tentatively proposed. The newly identified levels can be compared with those reported in theoretical studies: Jin2011 [134], Kart2007 [142], Yuan2016 [160], and Cov2011 [162]. Among them, only one shell-model approach, presented in Jin2011, includes an extended valence space. The other three shell-model approaches employ typical valence space used in the ^{132}Sn region.

Figure IV.18 shows a comparison of calculated and experimental level schemes of ^{134}Sn. At excitation energies between 2 and 3 MeV, where four new states were placed, several levels with a wide range of spin values are expected to exist. In the experimental level scheme of ^{134}Sn, an energy gap of about 1.5 MeV is visible between neutron-unbound and bound states. This separation of the two groups of levels is well reproduced by the shell-model calculations that provide information on high-energy levels.

Figure IV.19 presents dominant configurations of states calculated in four different shell-model approaches. The previously known $0^+_{g.s.}$, 2^+, 4^+, and 6^+ levels belong to the $\nu 2f^2_{7/2}$ multiplet. All shell-model calculations consistently reproduce their positions. In an energy range between 1.5 and 3 MeV, the existence of members of the $\nu 2f_{7/2}3p_{3/2}$, $\nu 2f_{7/2}3p_{1/2}$, $\nu 2f_{7/2}1h_{9/2}$, and $\nu 3p^2_{3/2}$ multiplets is expected. One of the states arising from the $\nu 2f_{7/2}1h_{9/2}$ configuration, the one with a maximum aligned spin of 8^+, was tentatively identified [35]. In an earlier version of shell-model calculations by A. Covello *et al.*, presented in Cov2007 [161], the 3^+_2 and 4^+_3 states belonging to the $\nu 2f_{7/2}3p_{1/2}$ multiplet were predicted above the 8^+ level. In their more recent work, Cov2011 [162], these two states are expected below the 8^+ level. Their lowering is due to the use of updated single-particle energy of the $\nu 3p_{1/2}$ orbital [17], which was found to be 290 keV lower than the previously adopted value, based on tentative assignment [19, 33].

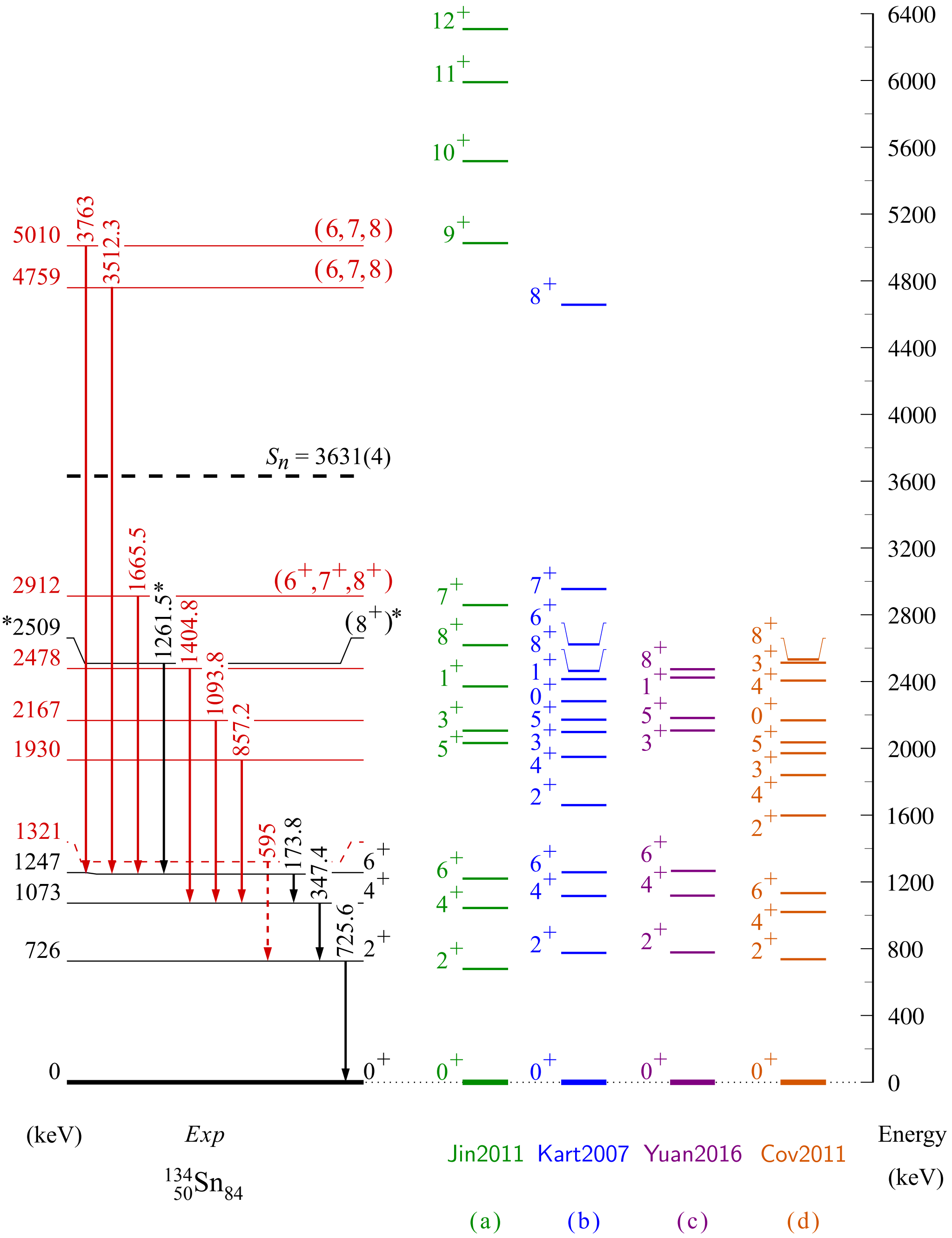

Figure IV.18: Experimental (*Exp*) level scheme of ^{134}Sn along with the results of four different approaches to shell-model calculations (a) considering neutron-core excitations, from Jin2011 [134], as well as employing ^{132}Sn as a closed core, from: (b) Kart2007 [142], (c) Yuan2016 [160], and (d) Cov2011 [162]. The newly identified states are indicated in red. The level shown by a dashed line is proposed tentatively. The (8^+) state at 2509 keV [35], which was not observed in the β decay of neutron-rich indium isotopes, is indicated with an asterisk. The experimental spin-parity assignments for previously known states were taken from Refs. [20, 35, 35]. The S_n value was taken from Ref. [16].

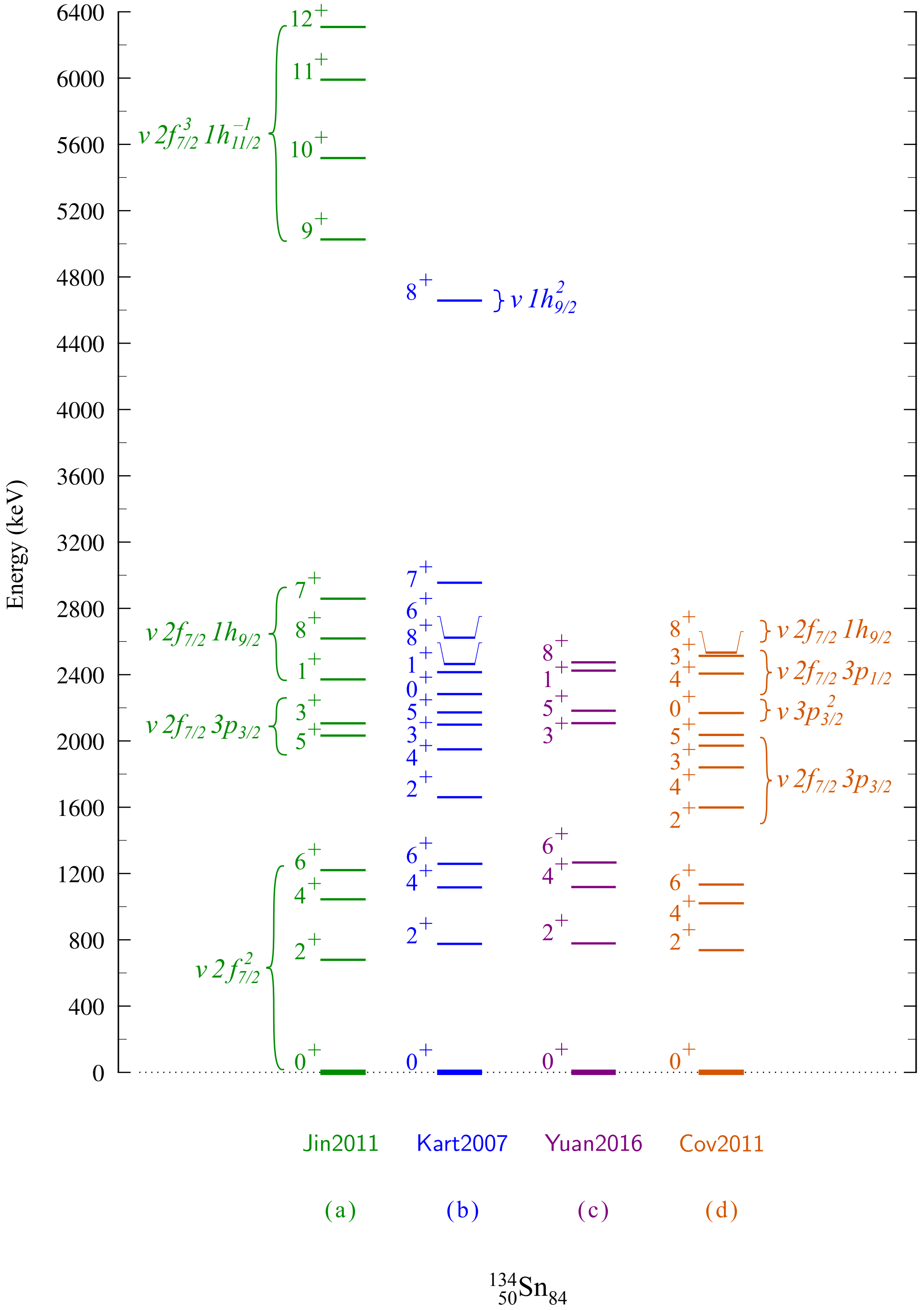

Figure IV.19: The dominant configurations of states predicted in ^{134}Sn. The data shown in this figure are compiled from Refs.: (a) Jin2011 [134], (b) Kart2007 [142], (c) Yuan2016 [160], and (d) Cov2011 [162].

The (8^+) state at 2509 keV attributed to the $\nu 2f_{7/2}1h_{9/2}$ configuration in ^{134}Sn was not observed in β decays of neutron-rich isotopes. In particular, it is worth noting that it was not identified in the ^{134}In β decay, in which its population can be expected to be favored due to the most probable ground-state spin and parity of 7^- for the parent nucleus. The lack of its observation can be explained by the little overlap of the wave functions of states involved in *ff* decays of ^{134}In resulting in a population of the level belonging to the $\nu 2f_{7/2}1h_{9/2}$ configuration. The ground-state wave function of the parent nucleus is dominated in 75% by the $\pi 1g^{-1}_{9/2}\nu 2f^{3}_{7/2}$ configuration [160, 177]. Among the other wave-function components, the highest contributions are from two configurations involving the $\nu 3p_{3/2}$ orbital. From this, it can be inferred that the state populated at 2912 keV in ^{134}Sn via *ff* decays of ^{134}In most likely arise from the $\nu 2f_{7/2}3p_{3/2}$ multiplet, whose population is favored due to admixtures present in the wave function of the ^{134}In ground state.

Interpretation of new levels at excitation energies around 5 MeV in ^{134}Sn differs for the various calculations. These differences are mainly due to the chosen model space. The shell-model calculations presented in Jin2011 [134], shown in Figures IV.18 and IV.19 in panel (a), do not include the $\nu 1i_{13/2}$ orbital in the valence space, but they do include neutron-core excitations by considering the $\nu 1h_{11/2}$ and $\nu 2d_{3/2}$ orbitals below the $N = 82$ shell gap (see Figure IV.15). Excited states predicted above 5 MeV correspond to couplings of the valence neutrons to neutron-core excitations with a dominant $\nu 2f^{3}_{7/2}h^{-1}_{11/2}$ configuration. These are not included in the model spaces of other theoretical studies on ^{134}Sn, which use neutron valence space consisting of orbitals above the $N = 82$ shell gap only (see Figure IV.15). At excitation energies exceeding 3.2 MeV [143] (Cor2002), 3.5 MeV [160] (Yuan2016), and 4 MeV [142] (Kart2007), respectively, states of negative parity arising from particle excitations, corresponding to the $\nu 2f_{7/2}1i_{13/2}$ configuration, are predicted. In contrast, multiplets involving the $\nu 1i_{13/2}$ orbital were not investigated in Jin2011, because this single-particle state was excluded from the model space.

Details on the structure of excited states in ^{134}Sn reported in Yuan2016 [160, 177] are presented in Figure IV.20. More levels are shown in this figure than presented in Ref. [160]. The predicted level density above 2.5 MeV is relatively high. Noteworthy is the identification of energies at which the first states belonging to subsequent multiplets appear in ^{134}Sn and evaluation of their purity.

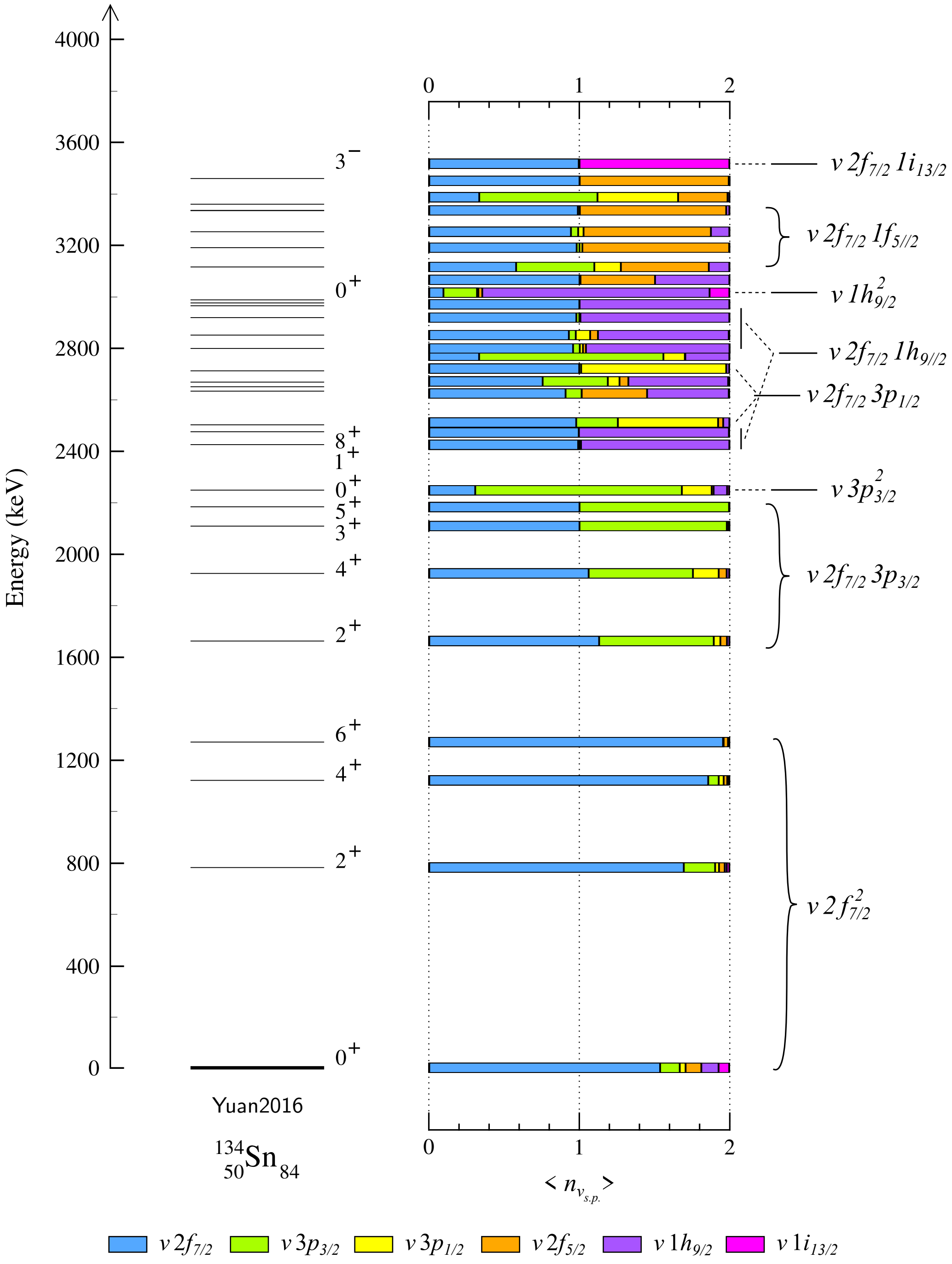

Figure IV.20: Results of the shell-model calculations for ^{134}Sn reported in Yuan2016 [160, 177]. Configurations of predicted states are indicated by showing occupation numbers of the neutron orbitals, $<n_{\nu_{s.p.}}>$ [177]. For readability, the spin-parity values for levels above 2.5 MeV are shown only for selected states, with distinctive configurations. For comparison with the experimental level scheme of ^{134}Sn, the reader is directed to Figure IV.18.

7.3.3 ^{135}Sn

Shell-model calculations for ^{135}Sn provide guidance in the interpretation of the first experimental results on excited states in this exotic nucleus. Predictions from five different shell-model approaches are available: Cor2002 [143], Sar2004 [166], Kart2007 [142], Jia2007 [165], and Yuan2016 [160, 177]. In all of these theoretical studies, only one type of excitation, the one involving valence neutrons outside the ^{132}Sn core, is included. Due to the low excitation energies of the states tentatively assigned to ^{135}Sn, the typical shell-model space in this mass region can be considered sufficient for their interpretation. In addition, when discussing the low-energy structure of ^{135}Sn, an analogy can be drawn with ^{133}Sn, having only a pair of neutrons less than the isotope of interest. A simple low-energy structure of this nucleus, which has been well studied experimentally, is helpful to establish the expected properties of states in ^{135}Sn.

Theoretical investigations of ^{135}Sn provide a consistent description of the structure of the lowest-lying levels in this nucleus. All variants of the shell-model calculations consistently predict a $7/2^-$ ground state, being a member of the $\nu 2f^3_{7/2}$ multiplet. Shell-model results presented in Yuan2016 indicate that the ground-state wave function is dominated by the $\nu 2f^3_{7/2}$ configuration, with 85% contribution. The $7/2^-$ ground-state spin-parity assignment is also supported by the systematics of excitation energies in the $N = 85$ isotones [178] as well as by the expected analogy to ^{133}Sn, with the $7/2^-$ ground state [17].

The $5/2^-$ and $3/2^-$ levels are predicted by all shell-model approaches to be the lowest-energy excited states in ^{135}Sn. These states are composed mainly of the $\nu 2f^3_{7/2}$ configuration, with its contribution to the total wave function of 87% and 82%, respectively [160, 177]. They are expected in the energy range between 200 and 450 keV. However, their population in the ^{135}In β decay is unlikely. Given the most probable $9/2^+$ ground-state spin and parity of ^{135}In, its *ff* decays populate the $7/2^-$, $9/2^-$, or $11/2^-$ states in ^{135}Sn. Therefore, the focus in the discussion is on levels with such spin-parity values. Figure IV.21 displays the calculated excitation energies for low-lying $7/2^-$, $9/2^-$, and $11/2^-$ levels in ^{135}Sn. The first $9/2^-$ and $11/2^-$ states are expected below 1 MeV. While the sequence of the low-lying levels in ^{135}Sn, namely: $7/2^-_{g.s.}$, $5/2^-$, and $3/2^-$, is reproduced in all available shell-model calculations, theoretical predictions tend to disagree at higher excitation energies, where states arising from the $\nu 2f^3_{7/2}$, $\nu 2f^2_{7/2} 3p_{3/2}$, and $\nu\, 2f^2_{7/2} 1h_{9/2}$ configurations are expected (see Figure IV.21).

The tentative assignment of the 950- and 1221-keV γ rays to ^{135}Sn as ground-state transitions is supported by shell-model calculations, which predict states with spin-parity values from $7/2^-$ to $11/2^-$ at comparable excitation energies (see Figure IV.21). Based on these predictions, it can be concluded that that there are more states decaying directly to the $7/2^-$ ground state, which can be populated via *ff* decays of ^{135}In. Several transitions observed in the ^{135}In β decay at energies higher than 1.2 MeV (see Section III 3.6 for discussion on this threshold energy for assignment), for which no $\gamma\gamma$ coincidences were observed, could also be associated with levels in ^{135}Sn. However, this is only one possible attribution, as there is no solid experimental argument for their assignment to the $\beta\gamma$-decay branch of ^{135}In. Among the low-lying levels predicted in ^{134}Sn, there is a second 2^+ state expected at around 1.6 MeV, which can deexcite directly to the 0^+ ground state (see Figure IV.18). Given that the βn emission with large orbital momentum occurs for ^{133}In and ^{134}In, the population of the predicted 2_2^+ state in ^{134}Sn is likely to proceed through the $\beta 1n$-decay branch of ^{135}In, with $(9/2^+)$ ground state. Therefore, alternative assignment to ^{134}Sn cannot be excluded for transitions seen in the ^{135}In β decay at energies higher than 1.2 MeV for which no $\gamma\gamma$ coincidences were observed. However, even if we consider possible overestimation of the predicted energy of the 2_2^+ state in ^{134}Sn by about 200 keV, the two transitions observed in the ^{135}In β decay at 1349 and 1373 keV remain plausible candidates for γ rays in ^{135}Sn.

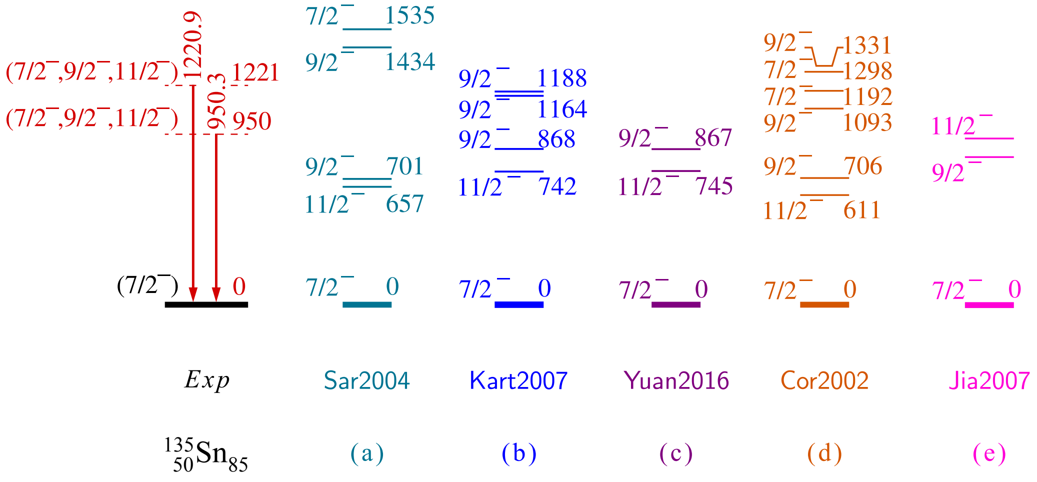

Figure IV.21: Excited states tentatively proposed in ^{135}Sn (*Exp*). Calculated excitation energies for the $7/2^-$, $9/2^-$, and $11/2^-$ levels in ^{135}Sn reported in: (a) Sar2004 [166], (b) Kart2007 [142], (c) Yuan2016 [160], (d) Cor2002 [143], and (e) Jia2007 [165] are also presented. Energies are given in keV. The ground-state spin-parity assignment is based on systematic trends in neighboring nuclei [29]. Exact excitation energies of states reported in Jia2007 were not available. The level scheme shown in panel (e) was reproduced from Figure 3 of Ref. [165].

Detailed interpretation of states predicted in ^{135}Sn with spin-parity values between $7/2^-$ and $11/2^-$ is provided in Figures IV.22 and IV.23. These figures present the results of shell-model calculations reported in Yuan2016 and Cor2002, respectively. More details are available from the former study, which provides average occupation numbers of the neutron orbitals for each state [177]. For levels below 1 MeV, their wave functions are dominated in 85% by the $2f_{7/2}^3$ configuration. At excitation energies above 1 MeV, the contribution of the multiplet involving the $3p_{3/2}$ orbital increases, in some cases reaching up to 36% of the total wave function.

The states with $\approx 30\%$ contribution of the wave-function component comprising the $\nu 1h_{9/2}$ orbital are predicted at around 1.2 MeV. Similar conclusions can be drawn from the shell-model results reported in Cor2002, in which dominant configurations are provided for states in ^{135}Sn (see Figure IV.23). Two levels predicted below 1 MeV arise from the $\nu 2f^{3}_{7/2}$ configuration. At higher excitation energies, from 1 to 1.3 MeV, three members of the $\nu 2f^{2}_{7/2}3p_{3/2}$ multiplet are expected. A state dominated by the $\nu 2f^{2}_{7/2}1h_{9/2}$ configuration is predicted above 1.3 MeV.

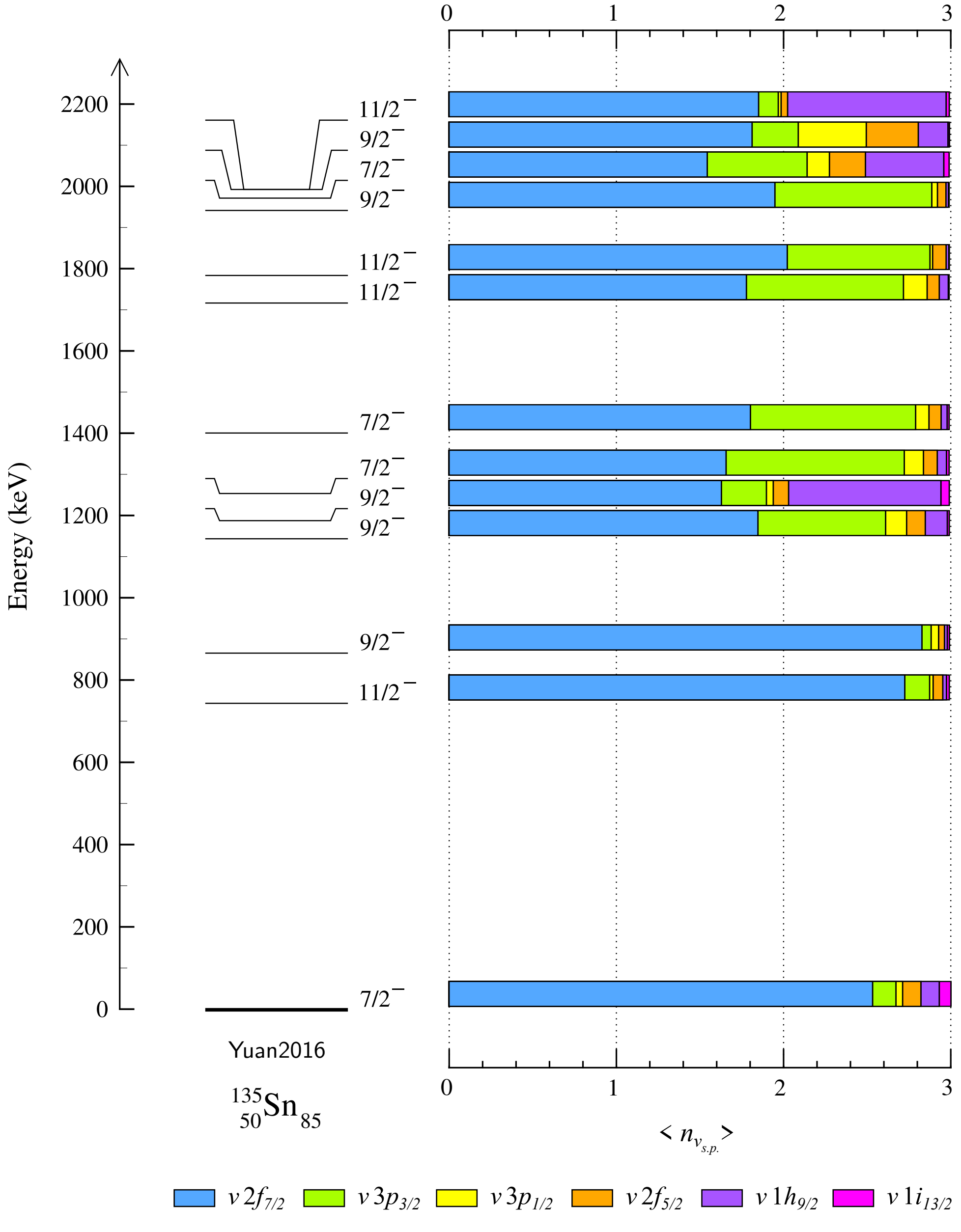

Figure IV.22: Results of the shell-model calculations for ^{135}Sn reported in Yuan2016 [160, 177]. Only states with spins and parities of $7/2^{-}$, $9/2^{-}$, and $11/2^{-}$ are shown. Configurations of these predicted states are indicated by showing occupation numbers of the neutron orbitals $< n_{\nu_{s.p.}} >$ [177].

A review of wave-function compositions for states calculated in ^{135}Sn is helpful in assessing which levels can be populated in the ^{135}In β decay by drawing an analogy to the ^{133g}In β decay. The ground-state configurations of these indium isotopes, $\pi 1g_{9/2}^{-1}\nu 2f_{7/2}^{2}$ and $\pi 1g_{9/2}^{-1}\nu 2f_{7/2}^{4}$, respectively, are similar in nature. Assuming that the *ff*-decay pattern of these nuclei is dominated by the same transitions, the population of states originating from the $\nu 2f_{7/2}^{3}$ and $\nu 2f_{7/2}^{2}1h_{9/2}$ configurations in ^{135}Sn is expected. The 950-keV γ ray observed in the ^{135}In β decay, having energy consistent with calculated energies of the $9/2^-$ and $11/2^-$ states arising from the $\nu 2f_{7/2}^{3}$ multiplet, is a candidate for transition deexciting one of its members. As for the configuration in ^{135}Sn corresponding to the analogous single-particle $\nu 1h_{9/2}$ state in ^{133}Sn (at 1561 keV), calculations predict the first level belonging to it at around 1.2 or 1.4 MeV. Three transitions have been observed in the ^{135}In β decay at consistent energies, at 1221, 1349, and 1373 keV. Therefore, they are candidates for transition deexciting states arising from the $\nu 2f_{7/2}^{3}1h_{9/2}$ multiplet in ^{135}Sn.

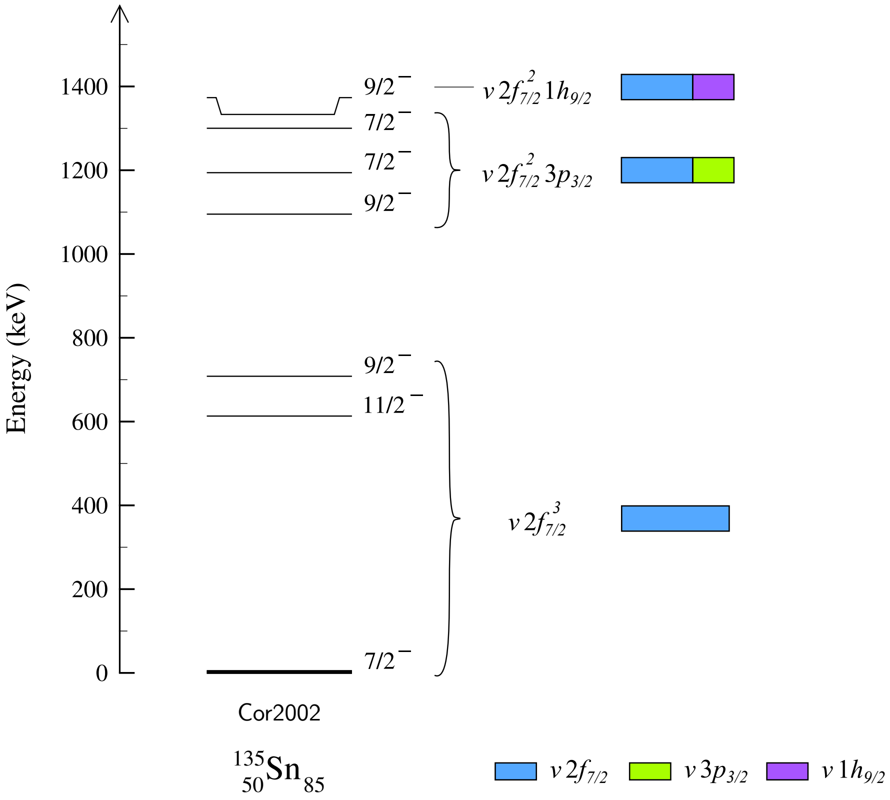

Figure IV.23: Results of the shell-model calculations for ^{135}Sn reported in Cor2002 [143]. Only low-lying states with spins and parities of $7/2^-$, $9/2^-$, and $11/2^-$ are shown. Dominant configurations of these states are indicated. To allow easy comparison with the Figure IV.22, the same colors were used to indicate neutron orbitals contributing to configurations.

SUMMARY

The presented thesis aims to address the most puzzling questions concerning the properties of nuclei in the vicinity of doubly magic ^{132}Sn by experimental investigation of neutron-rich tin isotopes above $N = 82$ populated in β decays of ^{133}In, ^{134}In, and ^{135}In. New experimental data for exotic nuclei around ^{132}Sn allow for a better understanding of phenomena that occur when the neutron-to-proton ratio becomes large, such as the β-delayed multiple-neutron emission. Properties of nuclei in that region are also important for r-process nucleosynthesis modeling, since the $A \approx 130$ peak in the r-process abundance pattern is linked to the $N = 82$ shell closure. Thanks to the robust nature of the ^{132}Sn core, tin isotopes above $N = 82$ offer a rare opportunity to investigate neutron-neutron components of shell-model interactions for heavy-mass nuclei with large neutron excess. The β decay of ^{133}In, ^{134}In, and ^{135}In provides unique conditions for the simultaneous investigation of one- and two-neutron excitations as well as states formed by couplings of valence neutrons to excitations of the ^{132}Sn core.

The β-delayed γ-ray spectroscopy measurement was performed at the CERN-ISOLDE facility, where ^{133}In, ^{134}In, and ^{135}In were selectively laser-ionized and on-line mass separated. Isomer-selective ionization was applied for ^{133}In, allowing its two β-decaying states to be studied independently. Indium ions were implanted on movable tape at the center of the detection setup consisting of β-particle and γ-ray detectors. Transitions following the β decay of indium isotopes were identified based on $\beta\gamma$ coincidences correlated with the beam implantation. Decay schemes of ^{133}In, ^{133m}In, ^{134}In, and ^{135}In were constructed from $\beta\gamma$, $\beta\gamma\gamma$, and $\gamma\gamma$ coincidence data. The βn-decay branching ratios of ^{133}In and ^{134}In were determined based on intensities of γ rays emitted in β decays of daughter nuclei.

Thanks to the large spin difference of the two β-decaying states of ^{133}In, it was possible to investigate separately the lower- and higher-spin states in ^{133}Sn, and thus to probe independently different single-particle states in this nucleus. New neutron-unbound states were identified in ^{133}Sn following the ground-state β decay of ^{133}In. Three β-decay branches of ^{134}In were established, two of which were observed for the first time. Transitions following the β decay of ^{135}In, including those belonging to the $\beta\gamma$-, $\beta 1n$-, and $\beta 2n$-decay branches, were also identified for the first time.

A significant contribution of γ-ray emission from neutron-unbound states populated in the two tin isotopes, ^{133}Sn and ^{134}Sn, at excitation energies exceeding S_n by 1 MeV was observed. The competition of γ-ray deexcitation with neutron emission well above S_n is explained by the weak overlap of the wave functions of states involved in the βn decay. Although the prevalent $\nu 1g_{7/2} \rightarrow \pi 1g_{9/2}$ GT decays of ^{134}In and ^{135}In feed neutron-unbound states at excitation energies exceeding S_{2n} of daughter nuclei, their β decays are dominated by one-neutron emission. In the energy range consistent with the predicted excitation energy of the $13/2^+$ state in ^{133}Sn, a 2434-keV transition was observed in β decays of both ^{134}In and ^{135}In. This transition is a candidate for a γ ray depopulating the missing single-particle $\nu 1i_{13/2}$ state in ^{133}Sn.

Based on information from the β decay of ^{133}In and ^{134}In, four new excited states were assigned to ^{133}Sn. The level scheme of ^{134}Sn was supplemented in total by six excited states, populated either through *ff* decays of ^{134}In or following neutron emission from neutron-unbound states in ^{135}Sn. Experimental level schemes of ^{133}Sn, ^{134}Sn, and ^{135}Sn were compared with shell-model calculations using various interactions, including predictions considering particle-hole excitations across the $N = 82$ shell gap. Experimental excitation energies of neutron-unbound states most likely populated via the $\nu 1h_{11/2} \rightarrow \pi 1g_{9/2}$ *ff* decays of ^{133}In and ^{134}In are well reproduced by shell-model calculations.

REFERENCES

[1] M. Thoennessen, *The Discovery of Isotopes: A Complete Compilation* (Springer International Publishing, Cham, 2016), ISBN 978-3-319-31763-2, URL https://link.springer.com/book/10.1007/978-3-319-31763-2.

[2] M. G. Mayer, Phys. Rev. **74**, 235 (1948), URL https://doi.org/10.1103/PhysRev.74.235.

[3] E. Feenberg and K. C. Hammack, Phys. Rev. **75**, 1877 (1949), URL https://doi.org/10.1103/PhysRev.75.1877.

[4] J. Suhonen, *From Nucleons to Nucleus* (Springer, Berlin, 2007), ISBN 978-3-540-48861-3, URL https://doi.org/10.1007%2F978-3-540-48861-3.

[5] T. L. Tang, B. P. Kay, C. R. Hoffman, J. P. Schiffer, D. K. Sharp, L. P. Gaffney, S. J. Freeman, M. R. Mumpower, A. Arokiaraj, E. F. Baader, et al., Phys. Rev. Lett. **124**, 062502 (2020), URL https://doi.org/10.1103/PhysRevLett.124.062502.

[6] P. F. A. Klinkenberg, Rev. Mod. Phys. **24**, 63 (1952), URL https://doi.org/10.1103/RevModPhys.24.63.

[7] M. G. Mayer, Phys. Rev. **75**, 1969 (1949), URL https://doi.org/10.1103/PhysRev.75.1969.

[8] O. Haxel, J. H. D. Jensen, and H. E. Suess, Phys. Rev. **75**, 1766 (1949), URL https://doi.org/10.1103/PhysRev.75.1766.2.

[9] R. F. Casten, *Nuclear Structure from a Simple Perspective* (Oxford University Press, Oxford, 2001), ISBN 9780198507246, URL https://doi.org/10.1093%2Facprof%3Aoso%2F9780198507246.001.0001.

[10] E. Caurier, G. Martínez-Pinedo, F. Nowacki, A. Poves, and A. P. Zuker, Rev. Mod. Phys. **77**, 427 (2005), URL https://doi.org/10.1103/RevModPhys.77.427.

[11] L. Coraggio, A. Covello, A. Gargano, N. Itaco, and T. Kuo, Prog. Part. Nucl. Phys. **62**, 135 (2009), URL https://doi.org/10.1016/j.ppnp.2008.06.001.

[12] B. Singh, J. Rodriguez, S. Wong, and J. Tuli, Nucl. Data Sheets **84**, 487 (1998), URL https://doi.org/10.1006/ndsh.1998.0015.

[13] V. Vaquero, A. Jungclaus, P. Doornenbal, K. Wimmer, A. Gargano, J. A. Tostevin, S. Chen, E. Nácher, E. Sahin, Y. Shiga, et al., Phys. Rev. Lett. **118**, 202502 (2017), URL https://doi.org/10.1103/PhysRevLett.118.202502.

[14] J. Erler, N. Birge, M. Kortelainen, W. Nazarewicz, E. Olsen, A. M. Perhac, and M. Stoitsov, Nature **486**, 509 (2012), URL https://doi.org/10.1038%2Fnature11188.

[15] C. Izzo, J. Bergmann, K. A. Dietrich, E. Dunling, D. Fusco, A. Jacobs, B. Kootte, G. Kripkó-Koncz, Y. Lan, E. Leistenschneider, et al., Phys. Rev. C **103**, 025811 (2021), URL https://doi.org/10.1103/PhysRevC.103.025811.

[16] M. Wang, W. Huang, F. Kondev, G. Audi, and S. Naimi, Chin. Phys. C **45**, 030003 (2021), URL https://doi.org/10.1088%2F1674-1137%2Fabddaf.

[17] K. L. Jones, A. S. Adekola, D. W. Bardayan, J. C. Blackmon, K. Y. Chae, K. A. Chipps, J. A. Cizewski, L. Erikson, C. Harlin, R. Hatarik, et al., Nature **465**, 454 (2010), URL https://doi.org/10.1038%2Fnature09048.

[18] G. Simpson, G. Gey, A. Jungclaus, J. Taprogge, S. Nishimura, K. Sieja, P. Doornenbal, G. Lorusso, P.-A. Söderström, T. Sumikama, et al., Phys. Rev. Lett. **113**, 132502 (2014), URL https://doi.org/10.1103%2Fphysrevlett.113.132502.

[19] P. Hoff, P. Baumann, A. Huck, A. Knipper, G. Walter, G. Marguier, B. Fogelberg, A. Lindroth, H. Mach, M. Sanchez-Vega, et al., Phys. Rev. Lett. **77**, 1020 (1996), URL https://doi.org/10.1103%2Fphysrevlett.77.1020.

[20] C. T. Zhang, P. Bhattacharyya, P. J. Daly, R. Broda, Z. W. Grabowski, D. Nisius, I. Ahmad, M. P. Carpenter, T. Lauritsen, L. R. Morss, et al., Z. Phys. A **358**, 9 (1997), URL https://doi.org/10.1007%2Fs002180050269.

[21] R. Taniuchi, C. Santamaria, P. Doornenbal, A. Obertelli, K. Yoneda, G. Authelet, H. Baba, D. Calvet, F. Château, A. Corsi, et al., Nature **569**, 53 (2019), URL https://doi.org/10.1038%2Fs41586-019-1155-x.

[22] NNDC – Brookhaven National Laboratory, NuDat 3.0 (2021), URL https://www.nndc.bnl.gov/nudat3/.

[23] J. L. Gross and M. Thoennessen, Atom. Data Nucl. Data Tabl. **97**, 383 (2011), URL https://doi.org/10.1016/j.adt.2011.03.001.

[24] P. G. Hansen, B. Jonson, H. J. Kluge, H. L. Ravn, and B. W. Allardyce, Tech. Rep., CERN-INTC-2020-027, INTC-P-554, CERN Geneva (1984), URL http://cds.cern.ch/record/152322.

[25] A. Sonzogni, Nucl. Data Sheets **103**, 1 (2004), URL https://doi.org/10.1016%2Fj.nds.2004.11.001.

[26] J. Liang, B. Singh, E. McCutchan, I. Dillmann, M. Birch, A. Sonzogni, X. Huang, M. Kang, J. Wang, G. Mukherjee, et al., Nucl. Data Sheets **168**, 1 (2020), URL https://doi.org/10.1016%2Fj.nds.2020.09.001.

[27] I. Dillmann, M. Hannawald, U. Köster, V. Fedoseyev, A. Wöhr, B. Pfeiffer, D. Fedorov, J. Shergur, L. Weissman, W. Walters, et al., Eur. Phys. J. A **13**, 281 (2002), URL https://doi.org/10.1007%2Fs10050-002-8756-7.

[28] G. Lorusso, S. Nishimura, Z. Xu, A. Jungclaus, Y. Shimizu, G. Simpson, P.-A. Söderström, H. Watanabe, F. Browne, P. Doornenbal, et al., Phys. Rev. Lett. **114**, 192501 (2015), URL https://doi.org/10.1103%2Fphysrevlett.114.192501.

[29] F. Kondev, M. Wang, W. Huang, S. Naimi, and G. Audi, Chin. Phys. C **45**, 030001 (2021), URL https://doi.org/10.1088%2F1674-1137%2Fabddae.

[30] W. Urban, W. Kurcewicz, A. Nowak, T. Rząca-Urban, J. Durell, M. Leddy, M. Jones, W. Phillips, A. Smith, B. Varley, et al., Eur. Phys. J. A **5**, 239 (1999), URL https://doi.org/10.1007%2Fs100500050280.

[31] K. L. Jones, F. M. Nunes, A. S. Adekola, D. W. Bardayan, J. C. Blackmon, K. Y. Chae, K. A. Chipps, J. A. Cizewski, L. Erikson, C. Harlin, et al., Phys. Rev. C **84**, 034601 (2011), URL https://doi.org/10.1103/PhysRevC.84.034601.

[32] J. M. Allmond, A. E. Stuchbery, J. R. Beene, A. Galindo-Uribarri, J. F. Liang, E. Padilla-Rodal, D. C. Radford, R. L. Varner, A. Ayres, J. C. Batchelder, et al., Phys. Rev. Lett. **112**, 172701 (2014), URL https://doi.org/10.1103/PhysRevLett.112.172701.

[33] P. Hoff, P. Baumann, A. Huck, A. Knipper, G. Walter, G. Marguier, B. Fogelberg, A. Lindroth, H. Mach, M. Sanchez-Vega, et al., Hyperfine Interact. **129**, 141 (2000), URL https://doi.org/10.1023%2Fa%3A1012661816716.

[34] A. Korgul, P. Bączyk, W. Urban, T. Rząca-Urban, A. G. Smith, and I. Ahmad, Phys. Rev. C **91**, 027303 (2015), URL https://doi.org/10.1103/PhysRevC.91.027303.

[35] A. Korgul, W. Urban, T. Rząca-Urban, M. Rejmund, J. Durell, M. Leddy, M. Jones, W. Phillips, A. Smith, B. Varley, et al., Eur. Phys. J. A **7**, 167 (2000), URL https://doi.org/10.1007%2Fpl00013594.

[36] D. Kameda, T. Kubo, T. Ohnishi, K. Kusaka, A. Yoshida, K. Yoshida, M. Ohtake, N. Fukuda, H. Takeda, K. Tanaka, et al., Phys. Rev. C **86**, 054319 (2012), URL https://doi.org/10.1103/PhysRevC.86.054319.

[37] M. Piersa, A. Korgul, L. M. Fraile, J. Benito, E. Adamska, A. N. Andreyev, R. Álvarez-Rodríguez, A. E. Barzakh, G. Benzoni, T. Berry, et al. (IDS Collaboration), Phys. Rev. C **99**, 024304 (2019), URL https://doi.org/10.1103/PhysRevC.99.024304.

[38] M. R. Mumpower, T. Kawano, and P. Möller, Phys. Rev. C **94**, 064317 (2016), URL https://doi.org/10.1103/PhysRevC.94.064317.

[39] T. Marketin, L. Huther, and G. Martínez-Pinedo, Phys. Rev. C **93**, 025805 (2016), URL https://doi.org/10.1103/PhysRevC.93.025805.

[40] P. Dimitriou, I. Dillmann, B. Singh, V. Piksaikin, K. Rykaczewski, J. Tain, A. Algora, K. Banerjee, I. Borzov, D. Cano-Ott, et al., Nucl. Data Sheets **173**, 144 (2021), URL https://doi.org/10.1016%2Fj.nds.2021.04.006.

[41] R. Caballero-Folch, I. Dillmann, J. Agramunt, J. L. Taín, A. Algora, J. Äystö, F. Calviño, L. Canete, G. Cortès, C. Domingo-Pardo, et al., Phys. Rev. C **98**, 034310 (2018), URL https://doi.org/10.1103/PhysRevC.98.034310.

[42] B. Moon, C.-B. Moon, P.-A. Söderström, A. Odahara, R. Lozeva, B. Hong, F. Browne, H. S. Jung, P. Lee, C. S. Lee, et al., Phys. Rev. C **95**, 044322 (2017), URL https://doi.org/10.1103/PhysRevC.95.044322.

[43] S. J. Smartt, T.-W. Chen, A. Jerkstrand, M. Coughlin, E. Kankare, S. A. Sim, M. Fraser, C. Inserra, K. Maguire, K. C. Chambers, et al., Nature **551**, 75 (2017), URL https://doi.org/10.1038%2Fnature24303.

[44] D. Watson, C. J. Hansen, J. Selsing, A. Koch, D. B. Malesani, A. C. Andersen, J. P. U. Fynbo, A. Arcones, A. Bauswein, S. Covino, et al., Nature **574**, 497 (2019), URL https://doi.org/10.1038%2Fs41586-019-1676-3.

[45] R. Surman, M. Mumpower, and A. Aprahamian, JPS Conf. Proc. **6**, 010010 (2015), URL https://doi.org/10.7566/JPSCP.6.010010.

[46] E. M. Burbidge, G. R. Burbidge, W. A. Fowler, and F. Hoyle, Rev. Mod. Phys. **29**, 547 (1957), URL https://doi.org/10.1103/RevModPhys.29.547.

[47] K. L. Kratz, , B. Pfeiffer, O. Arndt, S. Hennrich, and A. Wöhr, Eur. Phys. J. A **25**, 633 (2005), URL https://doi.org/10.1140%2Fepjad%2Fi2005-06-157-2.

[48] B. Pfeiffer, K. L. Kratz, F. K. Thielemann, and W. B. Walters, Nucl. Phys. A **693**, 282 (2001), URL https://doi.org/10.1016/S0375-9474(01)01141-1.

[49] M. Mumpower, R. Surman, G. McLaughlin, and A. Aprahamian, Prog. Part. Nucl. Phys. **86**, 86 (2016), URL https://doi.org/10.1016%2Fj.ppnp.2015.09.001.

[50] R. Catherall, W. Andreazza, M. Breitenfeldt, A. Dorsival, G. J. Focker, T. P. Gharsa, G. T. J, J.-L. Grenard, F. Locci, P. Martins, et al., J. Phys. G **44**, 094002 (2017), URL https://doi.org/10.1088%2F1361-6471%2Faa7eba.

[51] A. Gottberg, T. Mendonca, R. Luis, J. Ramos, C. Seiffert, S. Cimmino, S. Marzari, B. Crepieux, V. Manea, R. Wolf, et al., Nucl. Instrum. Methods Phys. Res. B **336**, 143 (2014), URL https://doi.org/10.1016%2Fj.nimb.2014.04.026.

[52] U. Köster, Eur. Phys. J. A **15**, 255 (2002), URL https://doi.org/10.1140%2Fepja%2Fi2001-10264-2.

[53] V. Fedosseev, K. Chrysalidis, T. D. Goodacre, B. Marsh, S. Rothe, C. Seiffert, and K. Wendt, J. Phys. G **44**, 084006 (2017), URL https://doi.org/10.1088%2F1361-6471%2Faa78e0.

[54] J. E. Sansonetti and W. C. Martin, J. Phys. Chem. Ref. Data **34**, 1559 (2005), URL https://doi.org/10.1063%2F1.1800011.

[55] M. L. Muchnik, Y. V. Orlov, G. D. Parshin, E. Y. Chernyak, V. S. Letokhov, and V. I. Mishin, Sov. J. Quantum Electron. **13**, 1515 (1983), URL https://doi.org/10.1070%2Fqe1983v013n11abeh004973.

[56] S. Rothe, V. Fedosseev, T. Kron, B. Marsh, R. Rossel, and K. Wendt, Nucl. Instrum. Methods Phys. Res. B **317**, 561 (2013), URL https://doi.org/10.1016%2Fj.nimb.2013.08.058.

[57] V. Fedosseev, D. Fedorov, R. Horn, G. Huber, U. Köster, J. Lassen, V. Mishin, M. Seliverstov, L. Weissman, and K. Wendt, Nucl. Instrum. Methods Phys. Res. B **204**, 353 (2003), URL https://doi.org/10.1016%2Fs0168-583x%2802%2901959-6.

[58] H. Fynbo, O. S. Kirseboom, and O. Tengblad, J. Phys. G **44**, 044005 (2017), URL https://doi.org/10.1088%2F1361-6471%2Faa5e09.

[59] ISOLDE Decay Station website (2021), URL https://isolde-ids.web.cern.ch/.

[60] H. Mach, R. Gill, and M. Moszyński, Nucl. Instrum. Methods Phys. Res. A **280**, 49 (1989), URL https://doi.org/10.1016%2F0168-9002%2889%2991272-2.

[61] M. Moszyński and H. Mach, Nucl. Instrum. Methods Phys. Res. A **277**, 407 (1989), URL https://doi.org/10.1016%2F0168-9002%2889%2990770-5.

[62] L. M. Fraile, J. Phys. G **44**, 094004 (2017), URL https://doi.org/10.1088%2F1361-6471%2Faa8217.

[63] J. Benito, Ph.D. thesis, Universidad Complutense de Madrid (2020), URL https://eprints.ucm.es/id/eprint/65223/.

[64] EUROBALL-type Clover Detector Specifications, Mirion Technologies (2021), URL https://www.mirion.com/products/clover-detectors-four-coaxial-germanium-detectors.

[65] G. Duchêne, F. Beck, P. Twin, G. de France, D. Curien, L. Han, C. Beausang, M. Bentley, P. Nolan, and J. Simpson, Nucl. Instrum. Methods Phys. Res. A **432**, 90 (1999), URL https://doi.org/10.1016%2Fs0168-9002%2899%2900277-6.

[66] R. Lica, Ph.D. thesis, University of Bucharest (2014), URL https://cds.cern.ch/record/2243047.

[67] Fast timing plastic scintillator EJ-232 Specifications, Eljen Technology (2021), URL https://eljentechnology.com/products/plastic-scintillators/ej-232-ej-232q.

[68] Photomultiplier Tube R5320 Specifications, Hamamatsu Photonics (2021), URL https://www.hamamatsu.com/resources/pdf/etd/R4998_R5320_TPMH1362E.pdf.

[69] Saint Gobain Brilliance 380 Brochure, Saint-Gobain Crystals (2021), URL www.crystals.saint-gobain.com/products/brillance-labr3-lanthanum-bromide.

[70] L. Fraile, H. Mach, B. Olaizola, V. Paziy, E. Picado, J. Sánchez, J. Udías, J. Vaquero, and V. Vedia, in *IEEE Nuclear Science Symposium Conference Record* (IEEE, 2011), p. 72, URL https://doi.org/10.1109/NSSMIC.2011.6154403.

[71] Lanthanum Bromide $LaBr_3$(Ce) scintillation material Specifications, Saint-Gobain Crystals (2021), URL https://www.crystals.saint-gobain.com/products/standard-and-enhanced-lanthanum-bromide.

[72] V. Vedia, M. Carmona-Gallardo, L. Fraile, H. Mach, and J. Udías, Nucl. Instrum. Methods Phys. Res. A **857**, 98 (2017), URL https://doi.org/10.1016%2Fj.nima.2017.03.030.

[73] Hamamatsu Photonic Systems R9779 Datasheet, Hamamatsu Photonic (2021), URL https://www.digchip.com/datasheets/download_datasheet.php?id=2541011&part-number=R9779.

[74] J. Benito, L. M. Fraile, A. Korgul, M. Piersa, E. Adamska, A. N. Andreyev, R. Álvarez-Rodríguez, A. E. Barzakh, G. Benzoni, T. Berry, et al. (IDS Collaboration), Phys. Rev. C **102**, 014328 (2020), URL https://doi.org/10.1103/PhysRevC.102.014328.

[75] Data Acquisition Systems Overview, Nutaq (2021), URL https://www.nutaq.com/wp-content/uploads/2015/07/VHS-ADC_Scientific_Nutaq_LowRes.pdf.

[76] Nutaq VHS-ADC Specification, Nutaq (2021), URL https://www.nutaq.com/wp-content/uploads/2015/07/VHS-ADC_Scientific_Nutaq_LowRes.pdf.

[77] I. Lazarus, E. Appelbe, P. Butler, P. Coleman-Smith, J. Cresswell, S. Freeman, R. Herzberg, I. Hibbert, D. Joss, S. Letts, et al., IEEE Trans. Nucl. Sci **48**, 567 (2001), URL https://doi.org/10.1109/23.940120.

[78] P. Rahkila, Nucl. Instrum. Methods Phys. Res. A **595**, 637 (2008), URL https://doi.org/10.1016/j.nima.2008.08.039.

[79] R. Lica, Nutaq Converter into ROOT and GASPware format for IDS (ISOLDE Decay Station) (2021), URL https://github.com/rlica/nutaq4ids.

[80] D. Bazzacco, GASP Data Analysis Program Package (2021), URL https://github.com/sztaylor89/GASPware-1/.

[81] *Update of X Ray and Gamma Ray Decay Data Standards for Detector Calibration and Other Applications* (International Atomic Energy Agency, Vienna, 2007), ISBN 92-0-113606-4, URL https://www.iaea.org/publications/7551/update-of-x-ray-and-gamma-ray-decay-data-standards-for-detector-calibration-and-other-applications.

[82] NNDC – Brookhaven National Laboratory, Evaluated Nuclear Structure Data File (2021), URL http://www.nndc.bnl.gov/ensarchivals/.

[83] G. Knoll, *Radiation Detection and Measurement* (John Wiley, New York, 2000), ISBN 0-471-07338-5, URL https://www.wiley.com/en-us/Radiation+Detection+and+Measurement%2C+4th+Edition-p-9781118026915.

[84] G. Audi, F. G. Kondev, M. Wang, W. Huang, and S. Naimi, Chin. Phys. C **41**, 030001 (2017), URL https://doi.org/10.1088%2F1674-1137%2F41%2F3%2F030001.

[85] T. Siiskonen and H. Toivonen, Nucl. Instrum. Methods Phys. Res. A **540**, 403 (2005), URL https://doi.org/10.1016%2Fj.nima.2004.11.021.

[86] I. Abt, A. Caldwell, K. Kröninger, J. Liu, X. Liu, and B. Majorovits, Eur. Phys. J. A **36**, 139 (2008), URL https://doi.org/10.1140%2Fepja%2Fi2007-10553-8.

[87] M. Anders, , D. Trezzi, A. Bellini, M. Aliotta, D. Bemmerer, C. Broggini, A. Caciolli, H. Costantini, P. Corvisiero, et al., Eur. Phys. J. A **49**, 28 (2013), URL https://doi.org/10.1140%2Fepja%2Fi2013-13028-5.

[88] J.-H. Chao, Appl. Radiat. Isot **44**, 605 (1993), URL https://doi.org/10.1016%2F0969-8043%2893%2990177-c.

[89] N. Jovančević, M. Krmar, D. Mrda, J. Slivka, and I. Bikit, Nucl. Instrum. Methods Phys. Res. A **612**, 303 (2010), URL https://doi.org/10.1016%2Fj.nima.2009.10.059.

[90] M. Baginova, P. Vojtyla, and P. Povinec, Appl. Radiat. Isot **166**, 109422 (2020), URL https://doi.org/10.1016%2Fj.apradiso.2020.109422.

[91] BrIcc Conversion Coefficient Calculator (2021), URL https://bricc.anu.edu.au/.

[92] P. D. I. Dillmann, B. Singh, Development of a Reference Database for Beta-delayed Neutron Emission Evaluation, International Atomic Energy Agency (2015), URL https://www-nds.iaea.org/publications/indc/indc-nds-0683/.

[93] J. Blomqvist, A. Kerek, and B. Fogelberg, Z. Phys. A **314**, 199 (1983), URL https://doi.org/10.1007%2Fbf01879878.

[94] M. Sanchez-Vega, B. Fogelberg, H. Mach, R. B. E. Taylor, A. Lindroth, J. Blomqvist, A. Covello, and A. Gargano, Phys. Rev. C **60**, 024303 (1999), URL https://doi.org/10.1103/PhysRevC.60.024303.

[95] C. A. Stone, S. H. Faller, and W. B. Walters, Phys. Rev. C **39**, 1963 (1989), URL https://doi.org/10.1103%2Fphysrevc.39.1963.

[96] The ISOLDE Yield Database, Version 0.2 (2021), URL https://cern.ch/isolde-yields.

[97] J. Ballof, J. Ramos, A. Molander, K. Johnston, S. Rothe, T. Stora, and C. Düllman, Nucl. Instrum. Methods Phys. Res. B **463**, 211 (2020), URL https://doi.org/10.1016/j.nimb.2019.05.044.

[98] K. Whitmore, C. Andreoiu, F. H. Garcia, K. Ortner, J. D. Holt, T. Miyagi, G. C. Ball, N. Bernier, H. Bidaman, V. Bildstein, et al., Phys. Rev. C **102**, 024327 (2020), URL https://doi.org/10.1103/PhysRevC.102.024327.

[99] W. Reviol, D. G. Sarantites, J. M. Elson, J. E. Kinnison, A. Gargano, S. Bottoni, R. V. F. Janssens, J. M. Allmond, A. D. Ayangeakaa, M. P. Carpenter, et al., Phys. Rev. C **94**, 034309 (2016), URL https://doi.org/10.1103/PhysRevC.94.034309.

[100] B. Fogelberg, M. Hellström, D. Jerrestam, H. Mach, J. Blomqvist, A. Kerek, L. O. Norlin, and J. P. Omtvedt, Phys. Rev. Lett. **73**, 2413 (1994), URL https://doi.org/10.1103%2Fphysrevlett.73.2413.

[101] A. Gottardo, D. Verney, I. Deloncle, S. Péru, C. Delafosse, S. Roccia, I. Matea, C. Sotty, C. Andreoiu, C. Costache, et al., Phys. Lett. B **772**, 359 (2017), URL https://doi.org/10.1016%2Fj.physletb.2017.06.050.

[102] B. Fogelberg, B. Ekström, L. Sihver, and G. Rudstam, Phys. Rev. C **41**, R1890 (1990), URL https://doi.org/10.1103%2Fphysrevc.41.r1890.

[103] Y. Khazov, A. Rodionov, S. Sakharov, and B. Singh, Nucl. Data Sheets **104**, 497 (2005), URL https://doi.org/10.1016%2Fj.nds.2005.03.001.

[104] The `mcerp` package – Monte Carlo Error Propagation (2021), URL https://pythonhosted.org/mcerp/.

[105] M. Asghar, J. Gautheron, G. Bailleul, J. Bocquet, J. Greif, H. Schrader, G. Siegert, C. Ristori, J. Crancon, and G. Crawford, Nucl. Phys. A **247**, 359 (1975), URL https://doi.org/10.1016%2F0375-9474%2875%2990642-9.

[106] I. Häller and B. Jung, Nucl. Phys. **52**, 524 (1964), URL https://doi.org/10.1016%2F0029-5582%2864%2990713-8.

[107] K. Wimmer, U. Köster, P. Hoff, T. Kröll, R. Krücken, R. Lutter, H. Mach, T. Morgan, S. Sarkar, M. S. Sarkar, et al., Phys. Rev. C **84**, 014329 (2011), URL https://doi.org/10.1103/PhysRevC.84.014329.

[108] W. G. Nettles, R. K. Scoggins, W. K. James, L. C. Whitlock, B. N. S. Rao, J. H. Hamilton, A. V. Ramayya, and R. Gunnink, Phys. Rev. C **18**, 2441 (1978), URL https://doi.org/10.1103%2Fphysrevc.18.2441.

[109] H. Warhanek, Nucl. Phys. **33**, 639 (1962), URL https://doi.org/10.1016%2F0029-5582%2862%2990555-2.

[110] G. H. Carlson, W. L. Talbert, and J. R. McConnell, Phys. Rev. C **9**, 283 (1974), URL https://doi.org/10.1103%2Fphysrevc.9.283.

[111] M. Stryjczyk, Y. Tsunoda, I. G. Darby, H. De Witte, J. Diriken, D. V. Fedorov, V. N. Fedosseev, L. M. Fraile, M. Huyse, U. Köster, et al., Phys. Rev. C **98**, 064326 (2018), URL https://doi.org/10.1103/PhysRevC.98.064326.

[112] A. K. Jain, B. Maheshwari, S. Garg, M. Patial, and B. Singh, Nucl. Data Sheets **128**, 1 (2015), URL https://doi.org/10.1016%2Fj.nds.2015.08.001.

[113] M. Stryjczyk, Y. Tsunoda, I. G. Darby, H. D. Witte, J. Diriken, D. V. Fedorov, V. N. Fedosseev, L. M. Fraile, M. Huyse, U. Köster, et al., Phys. Rev. C **98** (2018), URL https://doi.org/10.1103%2Fphysrevc.98.064326.

[114] M. Stryjczyk, Ph.D. thesis, KU Leuven (2021), URL https://lirias.kuleuven.be/retrieve/620472.

[115] J. Shergur, A. Wöhr, W. B. Walters, K.-L. Kratz, O. Arndt, B. A. Brown, J. Cederkall, I. Dillmann, L. M. Fraile, P. Hoff, et al., Phys. Rev. C **71**, 064321 (2005), URL https://doi.org/10.1103/PhysRevC.71.064321.

[116] T. Kibédi, T. Burrows, M. Trzhaskovskaya, P. Davidson, and C. Nestor, Nucl. Instrum. Methods Phys. Res. A **589**, 202 (2008), URL https://doi.org/10.1016%2Fj.nima.2008.02.051.

[117] M. Piersa, A. Korgul, L. Fraile, J. Benito, E. Adamska, R. Álvarez, A. Barzakh, G. Benzoni, T. Berry, M. Borge, et al., Acta Phys. Pol. B **49**, 523 (2018), URL https://doi.org/10.5506%2Faphyspolb.49.523.

[118] A. Vernon, Ph.D. thesis, University of Manchester (2019), URL http://cds.cern.ch/record/2723917.

[119] H. Grawe, K. Langanke, and G. Martínez-Pinedo, Rep. Prog. Phys. **70**, 1525 (2007), URL https://doi.org/10.1088%2F0034-4885%2F70%2F9%2Fr02.

[120] V. Paar, Nucl. Phys. A **331**, 16 (1979), URL https://doi.org/10.1016%2F0375-9474%2879%2990297-5.

[121] A. Jungclaus, A. Gargano, H. Grawe, J. Taprogge, S. Nishimura, P. Doornenbal, G. Lorusso, Y. Shimizu, G. S. Simpson, P.-A. Söderström, et al., Phys. Rev. C **93**, 041301 (2016), URL https://doi.org/10.1103/PhysRevC.93.041301.

[122] J. Hardy, L. Carraz, B. Jonson, and P. Hansen, Phys. Lett. B **71**, 307 (1977), URL https://doi.org/10.1016%2F0370-2693%2877%2990223-4.

[123] V. H. Phong, G. Lorusso, T. Davinson, A. Estrade, O. Hall, J. Liu, K. Matsui, F. Montes, S. Nishimura, A. Boso, et al., Phys. Rev. C **100**, 011302 (2019), URL https://doi.org/10.1103/PhysRevC.100.011302.

[124] I. N. Borzov, Phys. Rev. C **67**, 025802 (2003), URL https://doi.org/10.1103/PhysRevC.67.025802.

[125] M. Madurga and R. Grzywacz, Tech. Rep., CERN-INTC-2016-059, INTC-P-487, CERN Geneva (2016), URL https://cds.cern.ch/record/2223239.

[126] R. Grzywacz, M. Madurga, M. Karny, A. Algora, J. M. Allmond, D. Bardayan, J. Benito, N. Brewer, A. Fijałkowska, L. Gaffney, et al., Tech. Rep., CERN-INTC-2020-027, INTC-P-554, CERN Geneva (2020), URL http://cds.cern.ch/record/2717898.

[127] M. Mumpower, J. Cass, G. Passucci, R. Surman, and A. Aprahamian, AIP Adv. **4**, 041009 (2014), URL https://doi.org/10.1063%2F1.4867192.

[128] S. Yoshida, Y. Utsuno, N. Shimizu, and T. Otsuka, Phys. Rev. C **97**, 054321 (2018), URL https://doi.org/10.1103/PhysRevC.97.054321.

[129] T. Björnstad, M. Borge, J. Blomqvist, R. V. Dincklage, G. Ewan, P. Hoff, B. Jonson, K. Kawade, A. Kerek, O. Klepper, et al., Nucl. Phys. A **453**, 463 (1986), URL https://doi.org/10.1016%2F0375-9474%2886%2990447-1.

[130] A. Kerek, G. Holm, L.-E. D. Geer, and S. Borg, Phys. Lett. B **44**, 252 (1973), URL https://doi.org/10.1016%2F0370-2693%2873%2990217-7.

[131] B. Fogelberg, H. Gausemel, K. A. Mezilev, P. Hoff, H. Mach, M. Sanchez-Vega, A. Lindroth, E. Ramström, J. Genevey, J. A. Pinston, et al., Phys. Rev. C **70**, 034312 (2004), URL https://doi.org/10.1103/PhysRevC.70.034312.

[132] K. Aleklett, E. Lund, and G. Rudstam, Phys. Rev. C **18**, 462 (1978), URL https://doi.org/10.1103%2Fphysrevc.18.462.

[133] H. Gausemel, B. Fogelberg, T. Engeland, M. Hjorth-Jensen, P. Hoff, H. Mach, K. A. Mezilev, and J. P. Omtvedt, Phys. Rev. C **69**, 054307 (2004), URL https://doi.org/10.1103/PhysRevC.69.054307.

[134] H. Jin, M. Hasegawa, S. Tazaki, K. Kaneko, and Y. Sun, Phys. Rev. C **84**, 044324 (2011), URL https://doi.org/10.1103/PhysRevC.84.044324.

[135] P. Moller, J. R. Nix, and K. L. Kratz, At. Data Nucl. Data Tables **66**, 131 (1997), URL https://doi.org/10.1006/adnd.1997.0746.

[136] K. Miernik, Phys. Rev. C **88**, 041301 (2013), URL https://doi.org/10.1103/PhysRevC.88.041301.

[137] P. Möller, B. Pfeiffer, and K.-L. Kratz, Phys. Rev. C **67**, 055802 (2003), URL https://doi.org/10.1103/PhysRevC.67.055802.

[138] P. Möller, M. Mumpower, T. Kawano, and W. Myers, At. Data Nucl. Data Tables **125**, 1 (2019), URL https://doi.org/10.1016%2Fj.adt.2018.03.003.

[139] K. Miernik, Phys. Rev. C **90**, 054306 (2014), URL https://doi.org/10.1103/PhysRevC.90.054306.

[140] A. Spyrou, S. N. Liddick, F. Naqvi, B. P. Crider, A. C. Dombos, D. L. Bleuel, B. A. Brown, A. Couture, L. Crespo Campo, M. Guttormsen, et al., Phys. Rev. Lett. **117**, 142701 (2016), URL https://doi.org/10.1103/PhysRevLett.117.142701.

[141] E. Valencia, J. L. Tain, A. Algora, J. Agramunt, E. Estevez, M. D. Jordan, B. Rubio, S. Rice, P. Regan, W. Gelletly, et al., Phys. Rev. C **95**, 024320 (2017), URL https://doi.org/10.1103/PhysRevC.95.024320.

[142] M. P. Kartamyshev, T. Engeland, M. Hjorth-Jensen, and E. Osnes, Phys. Rev. C **76**, 024313 (2007), URL https://doi.org/10.1103/PhysRevC.76.024313.

[143] L. Coraggio, A. Covello, A. Gargano, and N. Itaco, Phys. Rev. C **65**, 051306 (2002), URL https://doi.org/10.1103/PhysRevC.65.051306.

[144] C. Ellegaard, J. Kantele, and P. Vedelsby, Phys. Lett. B **25**, 512 (1967), URL https://doi.org/10.1016%2F0370-2693%2867%2990224-9.

[145] J. Chen and F. Kondev, Nucl. Data Sheets **126**, 373 (2015), URL https://doi.org/10.1016%2Fj.nds.2015.05.003.

[146] M. Sanchez-Vega, B. Fogelberg, H. Mach, R. B. E. Taylor, A. Lindroth, and J. Blomqvist, Phys. Rev. Lett. **80**, 5504 (1998), URL https://doi.org/10.1103%2Fphysrevlett.80.5504.

[147] L. Coraggio, A. Covello, A. Gargano, and N. Itaco, Phys. Rev. C **80**, 021305 (2009), URL https://doi.org/10.1103/PhysRevC.80.021305.

[148] J. Blomqvist, in *Proceedings of the 4th International Conference on Nuclei Far from Stability* (European Organization for Nuclear Research CERN, 1981), p. 536, URL https://inis.iaea.org/search/search.aspx?orig_q=RN:13655415.

[149] M. Górska, L. Cáceres, H. Grawe, M. Pfützner, A. Jungclaus, S. Pietri, E. Werner-Malento, Z. Podolyák, P. Regan, D. Rudolph, et al., Phys. Lett. B **672**, 313 (2009), URL https://doi.org/10.1016%2Fj.physletb.2009.01.027.

[150] H.-K. Wang, Y. Sun, H. Jin, K. Kaneko, and S. Tazaki, Phys. Rev. C **88**, 054310 (2013), URL https://doi.org/10.1103/PhysRevC.88.054310.

[151] H.-K. Wang, S. K. Ghorui, K. Kaneko, Y. Sun, and Z. H. Li, Phys. Rev. C **96**, 054313 (2017), URL https://doi.org/10.1103/PhysRevC.96.054313.

[152] H. K. Wang, S. K. Ghorui, Z. Q. Chen, and Z. H. Li, Phys. Rev. C **102**, 054316 (2020), URL https://doi.org/10.1103/PhysRevC.102.054316.

[153] D. Rosiak, M. Seidlitz, P. Reiter, H. Naïdja, Y. Tsunoda, T. Togashi, F. Nowacki, T. Otsuka, G. Colò, K. Arnswald, et al. (MINIBALL and HIE-ISOLDE Collaborations), Phys. Rev. Lett. **121**, 252501 (2018), URL https://doi.org/10.1103/PhysRevLett.121.252501.

[154] T. Togashi, Y. Tsunoda, T. Otsuka, N. Shimizu, and M. Honma, Phys. Rev. Lett. **121**, 062501 (2018), URL https://doi.org/10.1103/PhysRevLett.121.062501.

[155] H. Naïdja, F. Nowacki, and K. Sieja, Acta Phys. Pol. B **46**, 669 (2015), URL https://doi.org/10.5506%2Faphyspolb.46.669.

[156] M. Hasegawa and K. Kaneko, Phys. Rev. C **59**, 1449 (1999), URL https://doi.org/10.1103%2Fphysrevc.59.1449.

[157] R. Machleidt, F. Sammarruca, and Y. Song, Phys. Rev. C **53**, R1483 (1996), URL https://doi.org/10.1103%2Fphysrevc.53.r1483.

[158] R. Machleidt, Phys. Rev. C **63**, 024001 (2001), URL https://doi.org/10.1103/PhysRevC.63.024001.

[159] S. Bogner, T. T. S. Kuo, L. Coraggio, A. Covello, and N. Itaco, Phys. Rev. C **65**, 051301 (2002), URL https://doi.org/10.1103/PhysRevC.65.051301.

[160] C. Yuan, Z. Liu, F. Xu, P. Walker, Z. Podolyák, C. Xu, Z. Ren, B. Ding, M. Liu, X. Liu, et al., Phys. Lett. B **762**, 237 (2016), URL https://doi.org/10.1016%2Fj.physletb.2016.09.030.

[161] A. Covello, L. Coraggio, A. Gargano, and N. Itaco, Eur. Phys. J.: Spec. Top. **150**, 93 (2007), URL https://doi.org/10.1140%2Fepjst%2Fe2007-00275-7.

[162] A. Covello, L. Coraggio, A. Gargano, and N. Itaco, J. Phys. Conf. Ser. **267**, 012019 (2011), URL https://doi.org/10.1088%2F1742-6596%2F267%2F1%2F012019.

[163] A. K. Jain and B. Maheshwari, Phys. Scr. **92**, 074004 (2017), URL https://doi.org/10.1088%2F1402-4896%2Faa7353.

[164] B. Maheshwari, A. K. Jain, and P. C. Srivastava, Phys. Rev. C **91**, 024321 (2015), URL https://doi.org/10.1103/PhysRevC.91.024321.

[165] L. Y. Jia, H. Zhang, and Y. M. Zhao, Phys. Rev. C **76**, 054305 (2007), URL https://doi.org/10.1103/PhysRevC.76.054305.

[166] S. Sarkar and M. S. Sarkar, Eur. Phys. J. A **21**, 61 (2004), URL https://doi.org/10.1140%2Fepja%2Fi2003-10198-7.

[167] M. Hjorth-Jensen, T. T. Kuo, and E. Osnes, Phys. Rep. **261**, 125 (1995), URL https://doi.org/10.1016%2F0370-1573%2895%2900012-6.

[168] T. Otsuka, T. Suzuki, M. Honma, Y. Utsuno, N. Tsunoda, K. Tsukiyama, and M. Hjorth-Jensen, Phys. Rev. Lett. **104**, 012501 (2010), URL https://doi.org/10.1103/PhysRevLett.104.012501.

[169] G. Bertsch, J. Borysowicz, H. McManus, and W. Love, Nucl. Phys. A **284**, 399 (1977), URL https://doi.org/10.1016%2F0375-9474%2877%2990392-x.

[170] W.-T. Chou and E. K. Warburton, Phys. Rev. C **45**, 1720 (1992), URL https://doi.org/10.1103%2Fphysrevc.45.1720.

[171] B. Fornal, R. Broda, P. J. Daly, P. Bhattacharyya, C. T. Zhang, Z. W. Grabowski, I. Ahmad, D. Seweryniak, I. Wiedenhöver, M. P. Carpenter, et al., Phys. Rev. C **63**, 024322 (2001), URL https://doi.org/10.1103/PhysRevC.63.024322.

[172] C. T. Zhang, P. Bhattacharyya, P. J. Daly, R. Broda, Z. W. Grabowski, D. Nisius, I. Ahmad, T. Ishii, M. P. Carpenter, L. R. Morss, et al., Phys. Rev. Lett. **77**, 3743 (1996), URL https://doi.org/10.1103%2Fphysrevlett.77.3743.

[173] A. Korgul, H. Mach, B. Fogelberg, W. Urban, W. Kurcewicz, T. Rząca-Urban, P. Hoff, H. Gausemel, J. Galy, J. Durell, et al., Eur. Phys. J. A **15**, 181 (2002), URL https://doi.org/10.1140%2Fepja%2Fi2001-10250-8.

[174] Z. Q. Chen, Z. H. Li, H. Hua, H. Watanabe, C. X. Yuan, S. Q. Zhang, G. Lorusso, S. Nishimura, H. Baba, F. Browne, et al., Phys. Rev. Lett. **122**, 212502 (2019), URL https://doi.org/10.1103/PhysRevLett.122.212502.

[175] M. Dworschak, G. Audi, K. Blaum, P. Delahaye, S. George, U. Hager, F. Herfurth, A. Herlert, A. Kellerbauer, H.-J. Kluge, et al., Phys. Rev. Lett. **100**, 072501 (2008), URL https://doi.org/10.1103/PhysRevLett.100.072501.

[176] M. Piersa-Siłkowska, A. Korgul, J. Benito, L. M. Fraile, E. Adamska, A. N. Andreyev, R. Álvarez-Rodríguez, A. E. Barzakh, G. Benzoni, T. Berry, et al. (IDS Collaboration), Phys. Rev. C **104**, 044328 (2021), URL https://doi.org/10.1103/PhysRevC.104.044328.

[177] C. Yuan, private communication (2021).

[178] W. Urban, W. R. Phillips, I. Ahmad, J. Rękawek, A. Korgul, T. Rząca-Urban, J. L. Durell, M. J. Leddy, A. G. Smith, B. J. Varley, et al., Phys. Rev. C **66**, 044302 (2002), URL https://doi.org/10.1103/PhysRevC.66.044302.